Digital Holographic Studies of Cloud and Precipitation Microphysics

Thomas Edward Chambers

School of Physical Sciences
University of Adelaide

This thesis is submitted for the degree of
Doctor of Philosophy

August 2022

I dedicate this thesis to my parents and family, whose endless love, support, and encouragement have made this possible

Declaration Of Originality

I certify that this work contains no material which has been accepted for the award of any other degree or diploma in my name, in any university or other tertiary institution and, to the best of my knowledge and belief, contains no material previously published or written by another person, except where due reference has been made in the text. In addition, I certify that no part of this work will, in the future, be used in a submission in my name, for any other degree or diploma in any university or other tertiary institution without the prior approval of the University of Adelaide and where applicable, any partner institution responsible for the joint award of this degree.

I give permission for the digital version of my thesis to be made available on the web, via the University's digital research repository, the Library Search and also through web search engines, unless permission has been granted by the University to restrict access for a period of time.

I acknowledge the support I have received for my research through the provision of an Australian Government Research Training Program Scholarship.

Signed: ... Date: 2022/08/30

Acknowledgements

On finding myself at the end of what has been rather an epic journey, I now face a final daunting challenge. The work undertaken and presented within this thesis comes as a result of the inputs of so many clever and wonderful people and to adequately express my gratitude would perhaps require a doubling of the page count. In the interests of avoiding excessive deforestation, I will here attempt to summarise the contributions that most readily occur to me at this time. To all those who I will inevitably omit, I look forward to the coming repercussions of my negligence; perhaps in the form of a shouted drink or a (temporary!) embargo on my bad puns!

First and foremost, I extend my deepest gratitude to Murray Hamilton as my principal supervisor. Your remarkable grasp over such a wide range of areas and excellent problem solving approaches have proven invaluable in this work. I am deeply grateful for the many excellent opportunities you have provided over this time along with your tireless support, particularly in the mitigation of some of my more overly-ambitious ideas. In short, I could not have hoped for a better mentor than you.

To my primary co-supervisor, Iain Reid. I have found your unique and insightful perspectives and shared experiences to be extremely helpful throughout this project and I have learnt a lot from your involvement. Your ongoing enthusiasm for this work along with your encouragement to view problems from different angles has proven especially useful to me and I am grateful for all the advice and experience you have provided.

I next acknowledge all those who have been so crucial in directly influencing the direction that this project has taken, including:

- Bob V: Your untiring commitment to determining my location at any given moment has been a surprisingly great source of motivation over the years and is genuinely appreciated. You have always made time – sometimes at the cost of Matlab training! – for discussing my work and your insights and guidance have been of great benefit to me. Your mastery of the English language has proven especially helpful through copious amounts of red ink over the past few months.

- Andrew M: Throughout this work you have been an unparalleled source of support, advice, and good humour which has been crucial in keeping me on track over this time and for that I am deeply grateful. Your valuable technical insights and comments are also gratefully acknowledged.

- Simon A, Alain P, Andrew K, Thom C, Andrew P, and Charmaine F: Through countless discussions and inputs of expert advice you have all been crucial in solidifying my understanding of the cloud physical processes at the core of this work. I gratefully acknowledge this support along with the provision and pre-processing of data from other instruments and logistical support in the Davis, Antarctica and Snowy Mountains field campaigns.

- Steve S and Yi H: I am grateful to you both for your useful insights and provision of data. I am particularly grateful to Steve S for your facilitation of my involvement in the Snowy Mountains field campaign and participation in the SOCRATES aircraft campaign.

- Gavin: I am grateful for your early enthusiasm in this work and for exploration of other potential applications of this research.

To those who have provided essential technical and logistical support, such as:

- Bob C and Evan J: Your expertise in machining and 3D printing proved invaluable in the development of the balloon instrument. I am particularly grateful for your enthusiasm in sharing your skills and knowledge over this time.

- Ramona, Adrian S, and Adrian G: Your professional support and creative ways of overcoming various computing and hardware issues have been very much appreciated.

- Mark J and the Amateur Radio Experimenters Group (AREG): Your enduring enthusiasm for this project was crucial in enabling one of the more significant aspects of this work; the holographic balloon launch. I gratefully acknowledge your logistical support and suggestions in undertaking this work.

- Luis A, Francisco L, Mike H, and John F: Your outstanding efforts and contributions towards the maintenance of my instruments during the field campaigns undertaken in this project are very much appreciated. I am particularly grateful to Luis for his technical insights and provision of the pre-processed Micro Rain Radar data during the Snowy Mountains field campaign.

- Bron, Richard M, Jonathan W, Chris A, Gary J, and Andrew J: It has been a pleasure working with the team from Atrad Pty Ltd over the years and I gratefully acknowledge your support and useful discussions over this time.

To those who have provided moral support and made this project such an enjoyable undertaking, including:

- The Space and Atmospheric Physics Group and Optics/Ozgrav Group members: To all past and present group members who have contributed their advice or companionship over this time, I extend a deep gratitude. The many board games nights, rogaine events, and dinners together have been essential for my sanity. I specifically acknowledge Adam G, Andrew H, Andrew S, Baden, Cao, Dan, Danielle, Lenard, Miftar, Ori, Simon C, and Tristan.

- Andrew S and Simon C: To Andrew S I am particularly grateful. Your relentless work ethic and logical manner have been an inspiration to me and our many long-winded discussions have been particularly useful in this project. Likewise to Simon C, you have always been a great sounding board for ideas and I am glad to have shared this experience with you from the beginning.

- Baden and Dan: You have both made this experience a particularly enjoyable one. Our nonlinear discussions and swapping of Simpsons lines was a particularly enjoyable aspect of this journey that was crucial in maintaining morale.

- Cao: I am grateful for the many fun discussions we have shared, Jaycar electronics adventures, and for your insightful inputs regarding the optics-related aspects of this work.

- Gary H, Steven S, Dave O, and Peter V: I have found my time demonstrating in the Second Year and Honours teaching laboratories to have been very rewarding. I extend my thanks to you all for sharing your experience and making this a particularly enjoyable process.

- Davis Crew: My time in Antarctica, as facilitated by Murray, proved to be a truly incredible experience for me. This was due in no small part to the people with whom I shared this adventure with and to whom I gratefully acknowledge here.

During the latter six months of this project I undertook a separate ionospheric internship project with the Australian Government Defence Science and Technology Group (DST). I am grateful to David H and Manny for facilitating this work and to Manny, Bruce W, David

H, Dave N, Andrew H, Lenard, and Trevor for making this project such an interesting and rewarding experience.

Logistical and financial support from the following organisations is gratefully acknowledged: The University of Adelaide's Institute for Photonics and Advanced Sensing (IPAS), Snowy Hydro Ltd, the Australian Antarctic Division (AAD), Atrad Pty Ltd, and the Australian Bureau of Meteorology (BoM).

To my parents, sister, extended family, and friends who have provided endless support and encouragement throughout this project. Put simply, this work would not have been possible without you. I extend my deepest gratitude to you and am particularly grateful for your patience and understanding regarding my reduced availability over this time.

To Danielle I am especially grateful. Meeting you over this time has been wonderful. You have been an excellent source of support and encouragement and I look forward to the many great adventures to come.

Abstract

This thesis describes the development and field testing of two in situ cloud observation instruments based on the principle of digital holography. These instruments have been designed to be both low cost and light weight, as suited for observations over wide areas as part of a network of sensors, and for vertical profiling of clouds from an untethered weather balloon. These capabilities are believed, by this author, to be unique to the instruments presented in this work and are intended to address the distinct lack of in situ cloud microphysical observations that are required for improving the understanding of cloud processes, calibration of climate and weather models, and validation of remote sensing observation methods.

A major challenge in the development of holographic instruments relates to their autonomous operation under field conditions. Methods are presented to overcome these issues, and aspects of the design process that allow significant reductions in cost and weight, as compared with standard instruments, are described. Automated analysis methods are an essential aspect of a holographic system, particularly for those presented in this work which are intended to be deployed under conditions in which they may be lost. Two automated analysis methods are presented in this work and are tested and optimised using field observations as well as a numerical model of a holographic system that was developed in this work.

One of the developed holographic instruments was deployed in a multi-month field campaign in the Australian Snowy Mountains alongside a range of standard instruments. An in-depth analysis of observations from all instruments for a range of different atmospheric events is undertaken, with a particular focus on assessing the performance of the developed holographic instrument. The holographic observations were found to be consistent with those of the other instruments within the overlapping resolution ranges that each were sensitive to. The potential for this instrument to classify atmospheric events was demonstrated using case studies, and holographic observations revealed biases in the microphysical outputs of a reanalysis model.

A world-first untethered balloon launch of a holographic microscope into clouds is described. Multiple bands of cloud were identified and the feasibility of this approach was demonstrated. Insights are presented relating to the microphysical structure of a post-drizzling warm stratus cloud, as well as cold clouds at higher altitudes. Microphysical

retrievals from an imaging satellite are evaluated using the in situ observations from this launch. The satellite retrievals were found to exhibit distinct biases, consistent with those identified in prior evaluation campaigns.

Table of contents

List of figures

List of tables

Nomenclature

Acronyms / Abbreviations

AAD	Australian Antarctic Division
BASTA	Bistatic rAdar SysTem for Atmospheric studies
BoM	Australian Bureau of Meteorology
C^{2}HOM	Compact Cloud-particle HOlographic Microscope
C^{2}HOM-B	C^{2}HOM–Balloon
C^{2}HOM-S	C^{2}HOM–Surface
CAPRICORN	Clouds, Aerosols, Precipitation, Radiation, and Atmospheric Composition over the Southern Ocean
CCN	Cloud Condensation Nuclei
CED	Cloud Effective Diameter
CER	Cloud Effective Radius
CT	Cloud Type
CTH	Cloud Top Height
CTT	Cloud Top Temperature
HYSPLIT	HYbrid Single-Particle Lagrangian Integrated Trajectory
INP	Ice Nucleating Particle
IPCC	International Panel on Climate Change
MARCUS	Measurements of Aerosols, Radiation and Clouds over the Southern Ocean

MPC	Mixed Phase Cloud
MRR	Micro Rain Radar Pro
Parsivel	Particle Size Velocity 2
PIP	Precipitation Imaging Probe
Polarsonde	Polarimetric Backscatter Sonde
RMAN	RMAN 510 Raman lidar
SLW	Supercooled Liquid Water
SOCRATES	Southern Ocean Cloud Radiation Aerosol Transport Experimental Study

Chapter 1

Introduction

1.1 Overview and Motivation

Clouds have been a source of fascination throughout human history, as evidenced by their prominence in art and literature over thousands of years [1]. Climatological review of satellite observations reveals that clouds cover approximately 70 % of the Earth's surface [2], and upwards of 80 % in areas such as the Southern Ocean [3]. The importance of clouds is difficult to overstate: they play a key role in the hydrological cycle, on which life on this planet depends, are a major contributing factor in extreme weather events, have implications for aviation safety and ground-based astronomy, and, perhaps of most direct relevance, a lack of understanding of clouds and precipitation has been identified by the International Panel on Climate Change (IPCC) as the leading source of uncertainty in climate and weather modelling [4]. The importance of clouds is elaborated on in this section to provide motivation for this work, and a more in-depth discussion of their role in climate modelling is provided in the following chapter.

Human prosperity depends directly on clouds through their role in the hydrological cycle. Accurate rainfall forecasting is a crucial aspect of agricultural planning, yet model performance is significantly impaired by a lack of understanding of clouds and precipitation [5, 6]. Understanding of rainfall processes is expected to become increasingly important over the coming years as increased drought frequency is suggested by climate models [7, 8]. Cloud Seeding (the attempt to artificially generate precipitation) is one mitigation approach being considered to address this issue that has been tested throughout the world for decades [9, 10]. Under certain conditions this approach has been found to be effective at enhancing precipitation [11, 12], yet much remains poorly understood due to the complexity of the underlying processes [13]. A stronger understanding of clouds is crucial in determining the environmental impacts of approaches such as this, as is required in determining viable strategies for overcoming these climate challenges sustainably.

Clouds also play a very important role in extreme weather events and aviation hazards [14], such as hurricanes, thunderstorms, hail events, floods, and aircraft icing. The societal and economic impacts of these events are severe. The global economic loss from weather-related disasters in the period from 2001 to 2010 has been estimated at around US$1.7 trillion [15]. The losses over the following decade have been estimated at around US$2.5 trillion, and climate modelling suggests that the frequency and intensity of extreme events may increase over the coming years [7]. Forecasting of extreme weather events is currently impaired by a lack of understanding of cloud microphysical processes [16, 17], and further observations are necessary to resolve these uncertainties.

Clouds have important implications for other fields of research, such as astronomy and astrophysics. The clouds of Earth offer a convenient natural laboratory for the study of clouds of other planetary atmospheres. The presence of clouds has been identified as a key signature in the search for extra-terrestrial life [18], and a strong understanding of the clouds of Earth can assist with such searches. Clouds are also a key component in the observation process of ground-based astrophysical observatories [19]. Measurements of the microphysical properties of clouds could allow for the correction of high-energy astrophysical observations obscured by cloud that would otherwise be discarded [20, 21]. Such measurements are expected to be of particular importance to the detection of transient phenomena, such as gamma-ray bursts [22], that may only be observable during times of cloud cover.

Beyond the importance to applied problems, there are many open questions within the field of cloud physics of a more fundamental nature. The physics of thunderstorms is particularly poorly understood [23], as a result of the many complicated and interacting processes observed to occur. The basic questions regarding lightning, for example, are only beginning to be addressed [24], and there is no accepted overarching theory describing the observed generation of gamma rays [25] and anti-matter [26] within these storm systems. Other open problems relate to the generation of gravity waves within convective clouds [27], the nature of small-scale turbulent processes within clouds [28], believed to be of particular importance in climate modelling [29], and the role of cosmic rays in the formation of clouds [30, 31].

Despite extensive research efforts, even theories regarding fundamental processes, such as the growth and breakup of cloud droplets by collision and coalescence, and the growth and splintering processes of ice crystals, have been found to be insufficient for accurate description and modelling of clouds [6]. These processes occur at the microscopic scale of cloud particles.

The low-cost in situ instruments presented in this work should be particularly useful in resolving these issues due to their capability for dramatically increasing the availability of cloud observations at these critical scales.

1.2 Challenges in the Understanding of Clouds

Given their importance, it is perhaps surprising that scientific progress towards the understanding of clouds is considered to have largely occurred over just the past few hundred years [32, 33]. Significant progress has been made over this time, as outlined in Chapter 2, yet much still remains unknown [6]. This is particularly so within the field of cloud microphysics [34], which is focussed on the physical processes involving individual cloud and precipitation particles. The work presented in this thesis relates most directly to this area of research.

Challenges in the understanding of clouds are primarily born from the vast complexity and range of scales over which their underlying physical processes are found to occur [34, 35]. Cloud particles typically can grow from nanometre-sized aerosols into precipitation particles with sizes of up to a few centimetres (about 7 orders of magnitude). Particle interactions are determined over spatial scales of sub-millimetres, and global cloud extents can cover thousands of kilometres (about 10 orders of magnitude). The electrification of clouds has been found to be of importance to their evolution [36], and typical electric field values within clouds range from around 10^2 V m^{-1} to 10^6 V m^{-1} (about 4 orders of magnitude). Similar ranges of scales are found for other key parameters such as particle charges, number densities of chemical constituents, and thermodynamic variables.

This underlying complexity necessitates a multi-scale approach to resolving this problem of understanding. Whilst significant progress in modelling is being made as a result of increasing computational resources, a fundamental lack of field observations of clouds remains a limiting factor [6]. Remote sensing instruments, such as lidar and radar, allow for widespread observations with high temporal resolution; however, the inversion algorithms used to relate bulk observed properties to the underlying microphysical parameters require calibration and validation from direct in situ observations [37].

A range of sampling methods are currently employed in a complementary fashion to perform these in situ observations, each with their advantages and limitations. Aircraft flights through clouds are useful as they allow targeted studies throughout the 3D cloud extent in a controlled fashion. They are fundamentally limited by the large costs involved, and consequently cannot provide global measurements throughout the year, as is required for capturing the large variability of clouds. Tethered balloons are another effective sampling method with the key advantage of long-term observations at a fixed location, though their deployment is limited to certain locations and atmospheric conditions. The status of current observational methods is discussed in greater detail in the following chapter.

This thesis describes the development and field testing of two new in situ cloud-sampling instruments. The instruments are based on the principle of digital holography [38] and allow for 3D imaging of cloud particles at micron-scale resolution. Automated methods are presented in this work to extract particle counts, sizes, and shapes. Such measurements have been identified as being of particular importance for improving climate models.

The instruments were designed to be both low cost and light weight to address the issue of limited in situ cloud observations. This allows for widespread observations via deployment over a network of towers. One of the instruments is sufficiently light weight so as to be deployed on an untethered balloon or Unmanned Aerial Vehicle (UAV). This offers the unique capability of routine vertical profiles of cloud microphysics from most locations around the world, at a fraction of the cost of aircraft observations. The results of an untethered balloon launch of a holographic instrument are presented in this thesis.

The developed holographic microscope designed for deployment on the ground or on tower structures is referred to hereafter as the Compact Cloud-particle HOlographic Microscope – Surface (C^2HOM–S). The lighter-weight instrument, suitable for deployment on an untethered weather balloon, is referred to as the C^2HOM – Balloon (C^2HOM–B).

1.3 Thesis Organisation

The first chapter of this thesis presents a brief overview of the motivations for this work, along with a summary of the thesis structure. Chapter 2 provides a theoretical overview of the cloud and precipitation microphysical processes relevant to this work, a summary of the role of cloud microphysical observations in improving climate models, as well as an assessment of current observational techniques. Chapter 3 describes the experimental methods and analysis routines developed for the autonomous operation of holographic instruments under field conditions. A description and results of a Monte Carlo model of a holographic instrument is presented in chapter 4, with a focus on the application of this model for testing of an automated holographic analysis method. A summary of the instruments deployed in the field campaigns undertaken in this project is provided in Chapter 5. Chapter 6 presents the results of the field deployment of a newly developed holographic instrument, alongside a range of widely used instruments, in the Australian Snowy Mountains. Chapter 7 describes an untethered balloon launch of a holographic microscope into clouds. In chapter 8, the key conclusions are summarised along with a discussion of future work.

Chapter 2

Cloud Microphysics and Observation Techniques

2.1 Introduction

This thesis primarily describes the development and field deployment of two new in situ cloud observation instruments based on the principle of digital holography. These instruments were developed to be low cost and light weight to significantly increase the availability of observations of cloud microphysical processes. This chapter provides a summary of the relevant cloud background theory and existing observation techniques to outline the context and relevance of the work presented in this thesis.

The chapter begins with a summary of the current understanding regarding cloud microphysical processes. Much remains to be understood about these underlying processes, particularly at the microscopic scales to which the presented instruments are sensitive to, and specific gaps in the current knowledge are outlined here. A brief discussion of the role of microphysical observations in improving the predictions of climate models is next provided, as this is one of the primary motivations for this work. The chapter concludes with an overview of the advantages and limitations of existing methods used for observing cloud microphysical processes, with an emphasis on the manner in which the instruments presented in this work can overcome existing observational challenges.

2.2 Cloud Microphysics

The field of cloud microphysics concerns the physical processes relating to the formation and evolution of individual cloud and precipitation particles. These processes occur over scales of sub-micrometres to centimetres and the key processes are summarised in Figure 2.1. Cloud processes occurring over larger scales are addressed by the field of cloud dynamics [39], but this area is outside the scope of this discussion.

A standard convention in the field of cloud microphysics is to classify and separately study clouds based on the thermodynamic phase of their constituent particles. In this work the standard distinction will be made between warm clouds, consisting solely of liquid water droplets, and cold clouds which contain ice, either solely or in mixture with liquid water droplets. Clouds and processes of both types were observed in the field campaigns presented in this thesis, and so a summary of both types is presented in this section for reference. The following discussion is based on the textbooks of Pruppacher and Klett [34], Lohmann, Lüönd, and Mahrt [35], and Rogers and Yau [40]. The reader is encouraged to consult these sources, along with the references contained therein, for additional detail if desired.

2.2.1 Warm Clouds

Warm clouds are formed from the conversion of atmospheric water vapour into liquid water droplets. Formation of water droplets from pure water vapour requires the collision and aggregation of water molecules. For a stable equilibrium mixture of water vapour over a planar surface of water to exist, the rate of water molecules leaving the liquid phase (evaporation) and the rate entering the liquid phase (condensation) must be equal. This state is referred to as saturation and the pressure of the water vapour in this state is referred to as the saturation vapour pressure (e_*). The ratio of the water vapour pressure (e) in an air mass to the saturation vapour pressure is defined as the relative humidity (RH) or saturation ratio. Values of this ratio that are larger than the saturation value are referred to as supersaturation.

The equilibrium vapour pressure with respect to a spherical water droplet as a function of droplet radius is described by the Köhler equation [34]:

$$e_s'(a) = e_* \exp\left(\frac{2M_w\sigma}{a\rho_w R_v T} - \frac{\nu\Phi_s m_s \frac{M_w}{M_s}}{\frac{4}{3}\pi a^3 \rho_s - m_s} \right), \tag{2.1}$$

where e_s' is the equilibrium vapour pressure over the droplet surface, a is the droplet radius, e_* is the saturation vapour pressure relative to a planar surface of water, M_w is the molar mass of water, σ is the droplet surface tension, ρ_w is the density of water, R_v is the water vapour gas constant, T is temperature, ν is the chemical dissassociativity, Φ_s is the practical osmotic coefficient, m_s is the mass of constituent salt, M_s is the molar mass of constituent salt, and ρ_s is the density of salt. The first term in the exponent of this equation describes the effects of surface tension, which tend to increase e_s' relative to e_*, and the second term

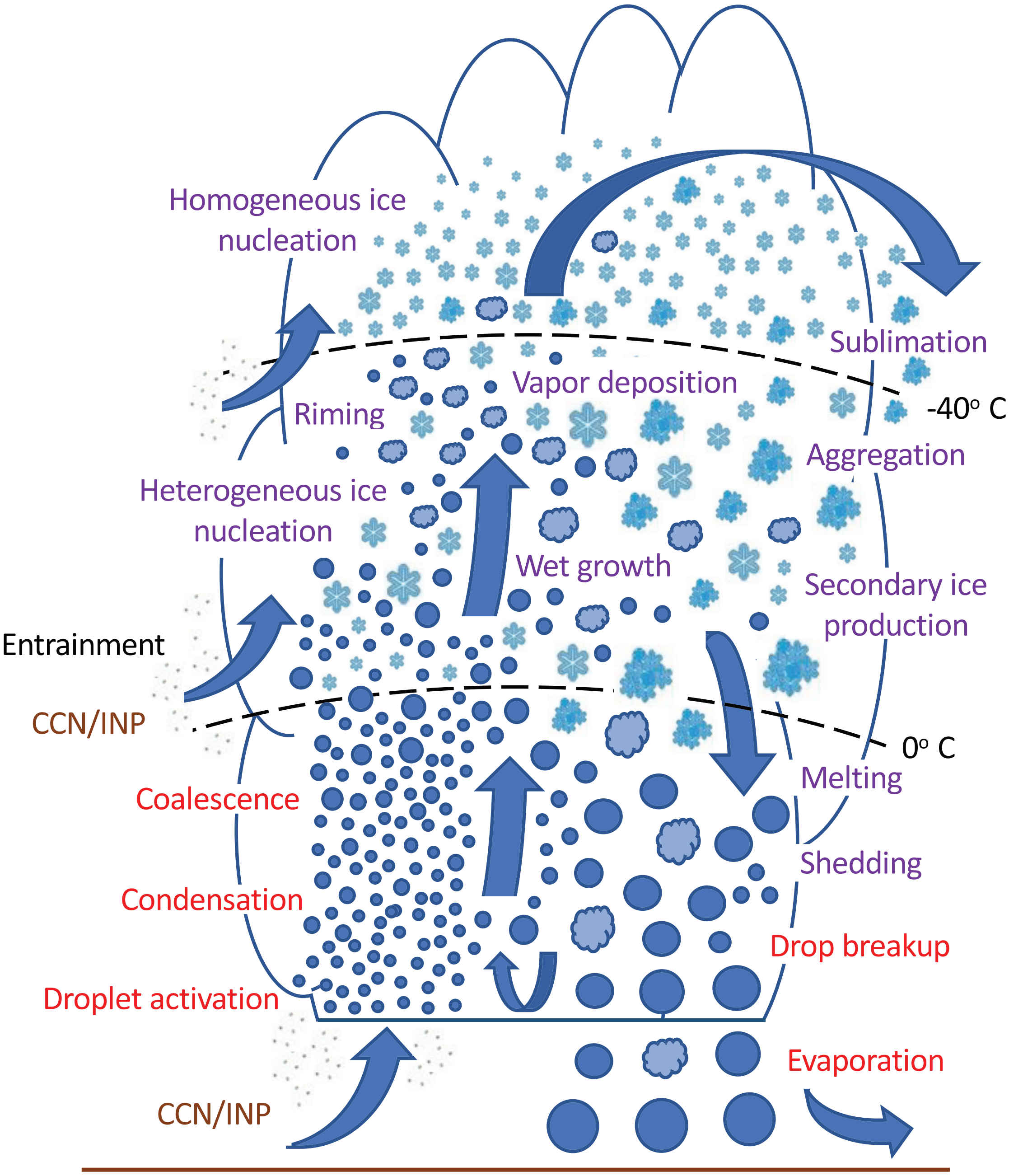

Fig. 2.1 Summary of the key cloud microphysical processes discussed in this section. Reprinted from Morrison et al (2020) [6].

describes the hygroscopic effects of salt solution within the droplet, which tend to decrease e'_s relative to that of a pure water droplet.

The formation and growth of cloud droplets via the diffusion of water vapour can be understood directly from the Köhler theory [34]. If the supersaturation adjacent to a water droplet is less than the supersaturation of the surrounding air mass, there will be a net diffusion of water vapour towards the droplet. If the supersaturation of the surrounding air mass is greater than the maximum supersaturation adjacent to the droplet, as predicted by Equation 2.1, the droplet will freely grow in radius without the need for further increases in the supersaturation and is referred to as an activated droplet. If at some droplet radius the supersaturation around the droplet is greater than the supersaturation of the air mass, then the droplet will remain at this fixed radius and is referred to as a haze particle. If the relative humidity drops below 100 %, droplets will begin to evaporate and decrease in size.

Air masses are generally subsaturated but can attain the necessary supersaturation values required for cloud formation through a number of mechanisms [39]. This includes adiabatic lifting and cooling, addition of water vapour, and nonlinear mixing of subsaturated air masses. Adiabatic lifting can occur from free and forced convection processes, such as via orographic lifting in a mountainous region. Larger updraft velocities lead to larger supersaturation values and hence larger numbers of activated cloud droplets. The adiabatic lifting theory predicts that supersaturation values reach a maximum value at the base of clouds, and then decrease monotonically with height [41]. Deviations from this simplified model are expected with the inclusion of processes such as turbulence and strong convection that remain poorly understood [42, 43].

A key prediction of the Köhler theory is that the formation of water droplets from pure water vapour would require supersaturation values on the order of a few hundred percent [35]. Supersaturation values in the atmosphere rarely exceed more than a few percent [43], and so this process of homogeneous nucleation does not produce clouds on Earth. Cloud formation instead proceeds via the process of heterogeneous nucleation which requires an aerosol particle to reduce the necessary supersaturation through a combination of increasing the initial size of the droplet and increasing the hygroscopicity relative to pure water.

Aerosols are solid and liquid particles suspended in the atmosphere. They include clusters of a few molecules through to giant aerosols with sizes on the order of a few hundred microns [44]. There are many types of aerosols including black carbon, dust, pollen, volcanic emissions, charged particles produced by cosmic rays, and sea spray. Aerosols can also be produced directly within the atmosphere through the chemical interaction of constituents such as sulphuric acid. The subset of aerosols that can become activated cloud droplets, for a given supersaturation, are referred to as Cloud Condensation Nuclei (CCN).

There are typically more sources of aerosols and greater observed number densities over continental regions, as compared with ocean regions [45]. This leads to a distinct observed difference in the properties of clouds formed from air masses of continental or oceanic origin, and the resultant clouds are correspondingly classified as being either continental or marine. Continental clouds are typically found to have a greater number density of CCN, and hence activated water droplets, than marine clouds. The lower number density of marine cloud droplets tend to have a larger size distribution than continental clouds, as the fixed available water vapour mass can be distributed to the fewer available particles. The composition and sources of aerosols, and the resultant cloud-aerosol interactions, remain particularly poorly understand, especially in regions such as the Southern Ocean due to a lack of in situ observations [46, 47].

The rate at which a cloud droplet grows via condensation is determined by factors such as supersaturation, droplet curvature, solute inclusions, the diffusivity of water vapour in air, conductivity and amount of heat flow by condensation and evaporation, gas-kinetic effects, and the ventilation of the droplet as it moves through the air. This growth is described by the droplet growth equation, the form of which can be found in standard textbooks [35]. This theory predicts that for typical cloud conditions, cloud droplets can grow rapidly via condensation to a diameter of around 40 microns [48]. Subsequent growth takes considerably longer and the process of condensation alone cannot explain the observed formation of rain, nor even drizzle defined as precipitation droplets with sizes less than 500 microns, in warm clouds over timescales of less than 20 minutes [49].

Growth of droplets to sizes larger than around 40 microns over such short timescales requires the additional growth processes of collision and coalescence [35]. Droplets larger than around 40 microns in diameter have appreciable fall velocities due to gravity. Droplets of differing sizes have different fall velocities and hence collision and coalescence becomes possible. Condensational growth leads to a narrowing of the droplet size, and hence velocity, distributions. Therefore, additional processes are required to prepare the population of droplets for collisional growth mechanisms.

Broadening of the droplet size distribution can occur through the presence of Giant CCN (GCCN) [50]. Pollen particles have been identified as potential candidates for GCCN with sizes of up to around 200 microns [51], and modelling studies suggest that GCCN can be an important factor in the formation of rain in warm continental clouds [52]. The role of GCCN is expected to be less important for marine clouds due to their lower number densities of cloud droplets. Radiative effects can also play a role in broadening the droplet size distribution [53], and are also important in the formation of fog.

Micro-scale turbulence is believed to play an important role in initiating the collision and coalescence growth mechanisms since turbulent fluctuations at millimetre to centimetre scales can enhance the probability of droplet collisions [54]. There is much remaining to be understood regarding the detail of these turbulent processes. Simulations including the effects of turbulence in a homogeneous environment show relatively small broadening of the droplet size distribution [55, 56]. Specification for inhomogeneous mixing of clouds at centimetre scales significantly increases the broadening effect, as particles can cluster in regions of low vorticity [28] and regions of enhanced supersaturation are produced.

Field observations of these processes are limited by the lack of instrumentation available that can provide statistically significant measurements over such small scales [28, 42]. The holographic instruments developed in this work are well suited to addressing this particular problem, as 3D images of centimetre-scale sampling volumes are produced at micron-scale resolution. Recent holographic observations of clouds from an aircraft campaign reveal that inhomogeneous mixing does occur over these small scales [57], but significantly more observations are required to better understand these processes. Details regarding the design and limitations of the holographic instruments developed in this work are discussed further in the following chapter.

The efficiency of droplet growth by collision and coalescence is a function of the probability of collision of droplets, as well as the probability of coalescence [34]. This depends on factors such as the droplet sizes, turbulence, and electric field conditions. Holographic observations of the 3D trajectories [58] of cloud particles during these processes would be particularly useful in furthering understanding for the improvement of climate and weather models.

Stochastic models of collision and coalescence processes suggest that for sufficiently broad droplet size distributions, these processes can be effective at producing droplets large enough to leave the cloud as precipitation [34]. Droplets large enough to reach the ground due to the force of gravity are referred to as rain, and hydrometeors that evaporate before reaching the ground are referred to as virga. Rain droplets become unstable as they grow larger, leading to droplet breakup [59], and droplets are rarely seen with diameters greater than around 10 mm for this reason [60].

The adiabatic theory of warm cloud formation described in this section leads to a number of basic predictions that can be experimentally tested by the instruments developed in this work. Aerosols will deliquesce and grow via condensation to an equilibrium size in subsaturated air, as determined by Equation 2.1. Adiabatic cooling of this parcel of air as it is lifted can then provide the necessary supersaturation to convert some fraction of the aerosols, acting as CCN, to activated water droplets beginning at the base of the cloud. The number density of activated water droplets should then remain approximately constant with height within a few hundred metres from cloud base. The median diameter of these particles is expected to increase with height in this height range as they grow via the processes of condensation.

Additional growth processes may become dominant above these heights, depending on the supersaturation, aerosol, and turbulence conditions within the cloud. For clouds that produce rain, or drizzle, the processes of collision and coalescence are expected to contribute to the growth of particles beyond around 40 microns in diameter. The profiles of number density and particle diameter above these heights are expected to strongly depend on processes such as the entrainment and mixing of air masses [61], micro-scale turbulence [28], and cloud electricity effects [62]. A detailed observational study of a warm cloud system, as measured by a holographic microscope on an untethered balloon, is presented in Chapter 7.

2.2.2 Cold Clouds

The defining property of cold clouds is the presence of ice crystals, which can be formed via the processes of homogeneous ice nucleation and heterogeneous ice nucleation at temperatures below 0 °C [34]. Homogeneous ice nucleation describes the process of pure water droplets freezing into ice crystals. Unlike the analogous homogeneous nucleation of water droplets from water vapour, the conditions required for this process to occur are frequently observed in the troposphere in high-altitude clouds – the coldest of which have been observed with temperatures of around -111 °C [63]. Liquid water droplets of micron-scale sizes can exist in a supercooled state to temperatures as low as around -38 °C [64]. Below such temperatures the spontaneous freezing of these droplets becomes energetically favoured. The supercooled droplet state is highly unstable and the introduction of a nucleating surface, such as an aeroplane flying through a cloud of supercooled water droplets, can lead to rapid freezing of the water and significant aviation hazards as a result [14]. Low-cost methods for routinely identifying the presence of supercooled water droplets in clouds, such as the Polarsonde instrument [65] discussed in later chapters, are therefore of interest.

Heterogeneous nucleation of ice is believed to be the dominant ice formation process for temperatures warmer than around -38 °C [35]. The theory of this process describes the formation of ice crystals as nucleated by a subset of aerosols, referred to as Ice Nucleating Particles (INP), which significantly reduce the energy barrier for ice crystal formation. One of the most important types of INP are mineral dust particles, due to their effectiveness [66] and abundance in the atmosphere [67], but many other types have been identified. Much remains to be understood regarding what properties make for a suitable INP [68], though it is believed that factors such as the crystalline structure and surface properties are important.

The growth of ice crystals in a cloud proceeds via the same fundamental methods as for water droplets: vapour deposition and collision-based methods [35]. Growth by vapour deposition is significantly more complicated for ice crystals, and depends on a range of factors such as the ambient temperature, supersaturation with respect to ice, atmospheric pressure, ice crystal shape, and underlying crystal structure. This complexity is poorly understood, and leads to a wide range of ice crystal shapes, or habits, that have been observed within clouds [69, 70]. A review of many ice crystal observations from in situ field campaigns and laboratory studies has highlighted the strong dependence of their growth on temperature and supersaturation in particular [71], as summarised by the 2D ice crystal images in Figure 2.2a and habit diagram in Figure 2.2b. The shape of ice crystals has a significant impact on the radiative properties of clouds [72], and a lack of in situ ice crystal observations around the world is a primary source of uncertainty in climate and weather modelling [6].

Collisional growth mechanisms are also more complicated for ice crystals than for water droplets since collisions with both water droplets and ice crystals are possible in cold clouds [35]. The probability of colliding particles remaining attached to each other is particularly difficult to model for ice particles. Ice crystals are found to have a layer of melted liquid water on their surface that affects their ability to stick to other particles [73]. This layer becomes thicker at warmer temperatures and observations suggest that temperatures of larger than around -5 °C [74] are optimal for colliding ice crystals to stick together. This process is referred to as aggregation and can result in the formation of large snowflakes. Collision of an ice crystal with a supercooled water droplet is referred to as riming. Unlike aggregation, this process is energetically favourable for all temperatures below 0 °C.

Mixed Phase Clouds (MPC), consisting of water vapour, supercooled water droplets, and ice crystals, are found throughout the planet and play a key role in precipitation and radiative transfer processes [75]. Such clouds are inherently unstable, since the saturation vapour pressure for ice is lower than for liquid. Consequently, liquid droplets will evaporate and ice crystals will grow via vapour deposition, unless there is sufficient cooling or moistening of the cloud to preserve liquid saturation. This mechanism is referred to as the Wegener–Bergeron–Findeisen (WBF) mechanism [76] and can convert all liquid to ice, referred to as glaciation, in a matter of hours. However, MPC have been observed to persist for days to weeks [77], and much remains to be understood regarding their underlying processes. It is believed that turbulence and updrafts are crucial in explaining this longevity [41, 78]. Holographic observations over these scales should prove particularly useful in improving this understanding, as is required to overcome modelling challenges [79] for these processes.

Ice processes in clouds have been found to contribute to around 60 % of the Earth's precipitation [80], mostly from the melting of ice crystals as opposed to snow that reaches the

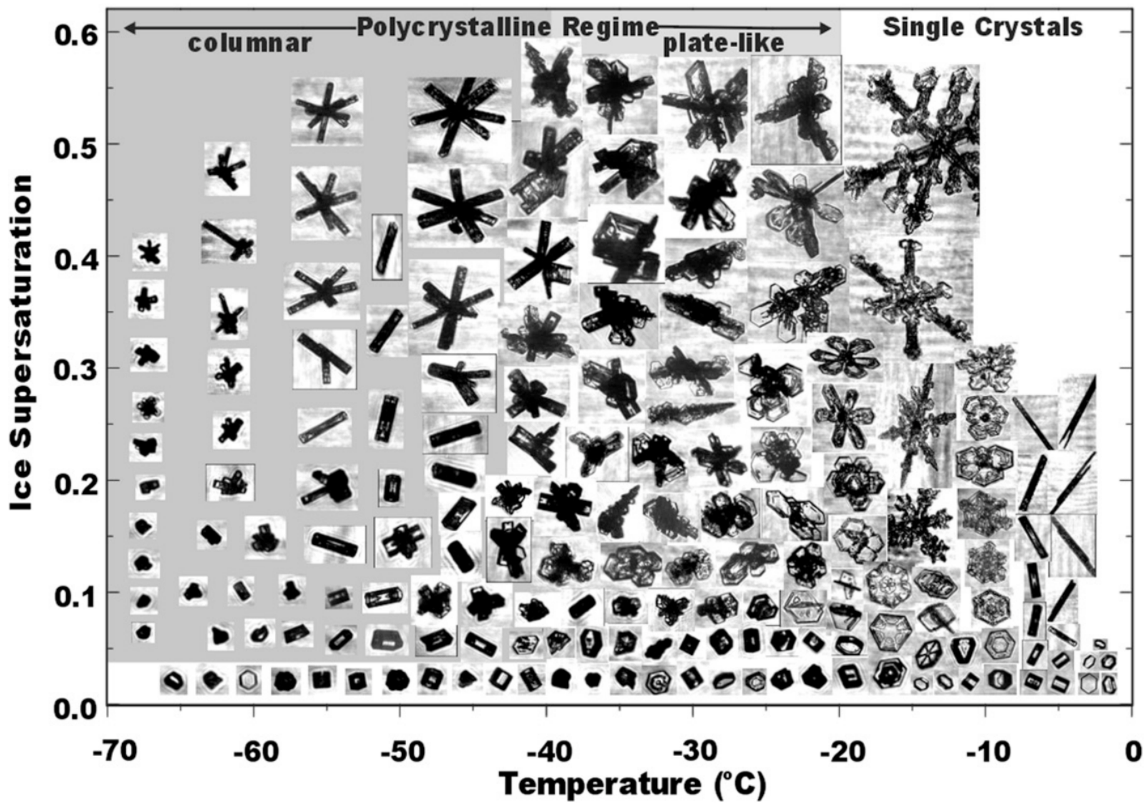

(a)

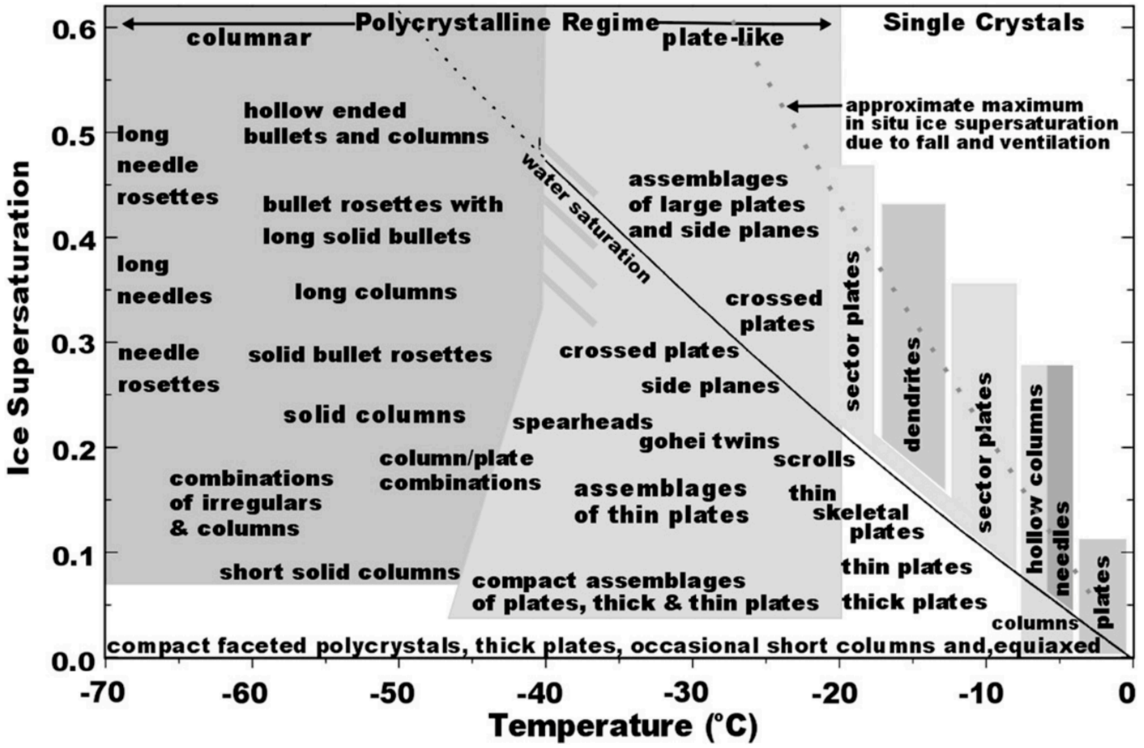

(b)

Fig. 2.2 Summary of in situ field observations and laboratory studies of ice crystals. Dependence of ice crystal shape on temeprature and ice supersaturation is shown in a) by grouping of 2D cloud particle images and b) by the derived habit diagram. Figures are reproduced from Bailey et al (2009) [71].

surface. Snowflakes can become significantly larger than rain droplets due to their reduced aerodynamic drag, and hence, greater time available for collisional growth mechanisms within the cloud [35]. Growth by riming tends to produce particles with lower densities than via the process of aggregation. Growth by riming tends to produce graupel, if sizes are below 2.5 mm, and if sufficient convective updrafts are present, hail stones of larger sizes can be produced [81].

The discussion so far has introduced the concepts of primary ice production: homogeneous and heterogeneous ice nucleation. A major challenge in cloud physics is in the understanding of Secondary Ice Production (SIP) processes, which involve the generation of additional ice particles from those formed via primary processes [82]. In situ observations within clouds reveal that the amount of ice crystals can exceed that of the Ice Nucleating Particles (INP) by almost four orders of magnitude [83], suggesting that SIP processes must occur within some clouds.

A recent review into laboratory studies of SIP processes [82], referred to hereafter as K20, describes six distinct mechanisms by which the phenomenon may occur. One such method involves the freezing of water droplets. Large internal pressures are observed during this process that can cause cracking as the droplet freezes. Liquid water that fills these cracks will then expand on freezing, and the droplet can shatter. This causes ice multiplication through fragmentation, and also deformations to the droplet shape in the form of spikes, bulges, and splits. Such deformations of particle shape, as well as the fragments themselves, could potentially be observed directly and classified using in situ holographic measurements.

Another process believed to be important is termed rime splintering, otherwise known as the Hallett–Mossop process [84]. The proposed mechanism describes ice crystals that are exposed to a flow of supercooled water droplets. It is suggested that this leads to the formation of splinters and hence ice multiplication downstream of the ice crystal from the fragments. This process is believed to be particularly efficient in the temperature range from -3 °C to -8 °C. Other proposed processes include fragmentation due to ice collisions, ice particle fragmentation due to the thermal shock of freezing droplets, fragmentation of sublimating particles, and the activation of INP from regions of enhanced supersaturation surrounding a freezing droplet [82].

The K20 review of SIP processes highlights the complexity in these processes. A wide range in the efficiency of these processes is reported between experiments, and consistent conclusions are difficult to draw. One area of broad agreement is in the importance of particle properties in these processes, such as their size, shape, and number density. The processes are also highly sensitive to atmospheric conditions, such as the temperature and pressure, requiring the need for further laboratory and in situ observational studies under a range of conditions to draw general conclusions.

Due to the complexity of SIP processes and the challenges in their observation, understanding of these processes remains highly limited [82]. Climate and weather models often do not parametrise these processes at all, and those that do tend to focus on only the Hallet-Mossop mechanism. In situ observation campaigns dedicated towards understanding of SIP processes are challenging due to issues in identifying which particles have been produced via SIP processes. Methods have been proposed to classify particles based on their size and environmental conditions, and recent field campaigns using these methods have been undertaken [85, 86].

The holographic instruments proposed in this work are particularly well suited to overcoming the challenges in the understanding of both primary and secondary ice production processes. Holographic instruments have the capability for large volumetric sampling rates [57], allowing statistically significant observations over the relevant small spatial scales. The 3D images obtained from holography allow for observation of the key parameters of particle size, shape, and number density. Holographic instruments also have the capability for measuring the 3D trajectory of particles [58], which may be particularly useful in the understanding of dynamic SIP processes.

Frequent deployment of low-cost holographic instruments, for example on an untethered weather balloon or Unmanned Aerial Vehicle (UAV), has the potential to greatly increase the available observations of these processes. Such observations are crucial in determining the conditions under which SIP processes occur, and for development of physical theories that can be incorporated into climate and weather models. The results of an untethered balloon launch of a holographic instrument into warm and cold clouds are presented in Chapter 7. Detailed observations of cold clouds and processes, as measured by a holographic microscope deployed alongside standard cloud instrumentation in the Australian Snowy Mountains, are presented in Chapter 6.

2.3 Parameterisation of Cloud and Precipitation Microphysics in Climate Modelling

One of the key motivations for the development of the instruments presented in this work is for the improvement of climate and Numerical Weather Prediction (NWP) models. A full review of climate and weather modelling is outside the scope of this work, but a basic description is provided to put the outcomes of this thesis into context. This includes a discussion of how in situ cloud observations are incorporated into these models, areas in which significant uncertainties remain, and a brief discussion of the impacts of those uncertainties on bulk predictions.

It is not computationally feasible to numerically simulate every cloud and aerosol particle in the atmosphere. Climate and NWP models must, therefore, incorporate sub-grid-scale parameterisation methods when modelling the effects of clouds and aerosols. Three main approaches are used in current climate and NWP models for parameterising cloud microphysics [87]: bulk models, spectral bin models, and Lagrangian super-particle models. In each case, models evolve by describing the flow of energy and mass between a set of hydrometeor classes such as liquid droplets, rain, ice particles, and snow. These models tend to predict one or two moments of the particle size distribution for each hydrometeor class. Double-moment schemes, predicting both particle mass mixing ratio and particle number mixing ratio from which the mean particle sizes and bulk cloud radiative properties can be derived, have been found to be more accurate than single-moment schemes [88] and are becoming more common as computational resources improve. Direct Numerical Simulation (DNS) models are an additional method of simulation that allows for resolution of individual particles, as suited to studies of micro-scale turbulence [89], but computational burdens limit these to only the smallest of scales [90].

Bulk models that predict one or two parameters for each hydrometeor class are the simplest of the three approaches and are most commonly utilised in operational models due to their low computational costs [91]. Spectral bin models describe the evolution of the size distributions directly over a specified set of size bins. This is significantly more computationally expensive, but is regarded as being more accurate and a useful tool for assessing the performance of bulk models [92].

The accuracy of the Eulerian approaches is fundamentally limited by the discrete manner in which hydrometeor classes are converted, as distinct from the continuous manner in which clouds are observed to evolve [87]. Additionally, the rates of hydrometeor conversion processes, such as aggregation and riming, are poorly understood and contribute additional uncertainty [6]. Despite the expectation that spectral bin models should be generally more reliable than bulk models, recent comparisons with observations indicate significant errors and spread in model outputs of both kinds [6, 93]. Lagrangian super-particle modelling is a more recent approach that follows the evolution of a subset of particles that act as a proxy for a specified number of additional particles [94]. This approach is becoming more popular and is expected to be useful in overcoming the fundamental limitations of Eulerian methods as it is significantly less computationally expensive to model a range of particle properties, such as aerosol composition and ice crystal shape, in this way.

None of these model types directly resolve individual cloud particles, and so assumptions must be made to define their basic parameters [6]. The choice of these parameters is guided by in situ observations of cloud particles. Inputs that must be determined by in situ observations include the shape of the particle size distribution [95, 96], the homogeneity of particle mixing at small scales [57], and information regarding the shape properties of ice crystals [69]. The holographic instruments developed in this work can directly measure each of these properties and it is in this way that the work presented in this thesis is of direct importance to the improvement of climate and NWP models.

The most common way in which in situ ice crystal shape information is incorporated into these models is through power law relations between their mass and size [69]. This allows for simple parameterisation of processes that depend on the terminal velocity of the particles, such as growth by coalescence. Particle mass can be derived from the 2D projected area that is measured by an imaging probe using standard methods [97, 98]. The fitting coefficients of this power law relationship have been found to vary significantly [99] between clouds formed from different processes, such as cirrus clouds vs orographic clouds, and also between different field campaigns. The coefficients also depend strongly on the particle habit, which is highly variable due to the complexity in the underlying physical processes. Adequately capturing this variability is a major existing challenge in the parameterisation of modelled ice clouds [100].

In situ observations are also crucial in modelling the bulk optical and radiative properties of clouds, such as the optical depth, single scattering albedo, and asymmetry parameter [100]. These bulk properties are parameterised as a function of the outputs of the underlying microphysics scheme [101], such as the cloud temperature, and the ice and liquid water contents. Cloud optical parameterisations of varying complexities have been developed [102], but generally require the inclusion of modelled particle single-scattering properties and in situ observations of clouds. Single-scattering properties are determined using electromagnetic scattering models and reference tables have been produced [103] for a range of electromagnetic wavelengths and particle parameters such as size, shape, and surface roughness. In situ observations of relevance include the relative frequency of occurrence of ice crystal habits and particle size distributions as a function of temperature [100].

It is ultimately the large variability and complexity in microphysical parameters that leads to the wide spread in the predictions of climate models [4], as highlighted in the following section. The instruments presented in this work have the potential to significantly increase the availability of in situ microphysical observations, as required to better constrain the variability in these parameters, and to better understand the underlying physical processes.

2.3.1 Sensitivity of Climate Model Predictions to Microphysical Observations

One of the most fundamental questions to be answered through climate modelling is the prediction of future temperatures at the surface of the Earth. A standard metric for assessing temperature rise is referred to as the Equilibrium Climate Sensitivity (ECS) [104]. This metric is defined as the change in the global mean surface temperature of a system that is equilibrated to the radiative forcing arising from a doubling of CO2. The ECS is described by the following relationship:

$$\Delta T_s = -\lambda F_{2\mathrm{x}}, \tag{2.2}$$

where ΔT_s is the ECS, λ is referred to as the climate sensitivity parameter, and $F_{2\mathrm{x}}$ is the radiative forcing due to a doubling of CO2. The climate sensitivity parameter represents the contributions of feedback mechanisms that affect the radiative balance such as water vapour, ocean warming, and clouds. Clouds contribute the largest variability to this parameter [105], and hence are the largest source of variability in global mean surface temperature predictions since the variability due to $F_{2\mathrm{x}}$ is relatively small [4]. The spread of ECS predictions from current climate models is between 1.8 °C and 5.6 °C, and this is attributed directly to a lack of understanding of cloud processes [106].

The contribution to the climate sensitivity parameter due to clouds is directly related to the Cloud Radiative Forcing (CF) [107]. The CF describes the net impact from clouds on the top-of-atmosphere balance between incoming short-wave solar radiation and long-wave thermal radiation from the Earth. The CF depends on the bulk radiative properties of modelled clouds which are determined from the underlying microphysical parameterisations, as described in the previous section.

The large variability in cloud microphysical properties and the lack of understanding of the underlying processes results in large biases in modelled CF [108]. This is demonstrated in Figure 2.3 which shows the global distribution of differences between modelled and observed CF, using the Community Atmosphere Model 5 (CAM5) [109] climate model and satellite observations [110]. Distinct biases are found, particularly in both the short-wave CF (SWCF) and long-wave CF (LWCF) in the equatorial regions and in the SWCF over the Southern Ocean.

Observations over the Southern Ocean reveal an abundance of supercooled liquid water [46, 111] and discrepancies between modelled and observed supercooled liquid water properties in clouds [112], likely because model parameters are biased by the significantly greater number of observations from the northern hemisphere [46]. The optical and radiative

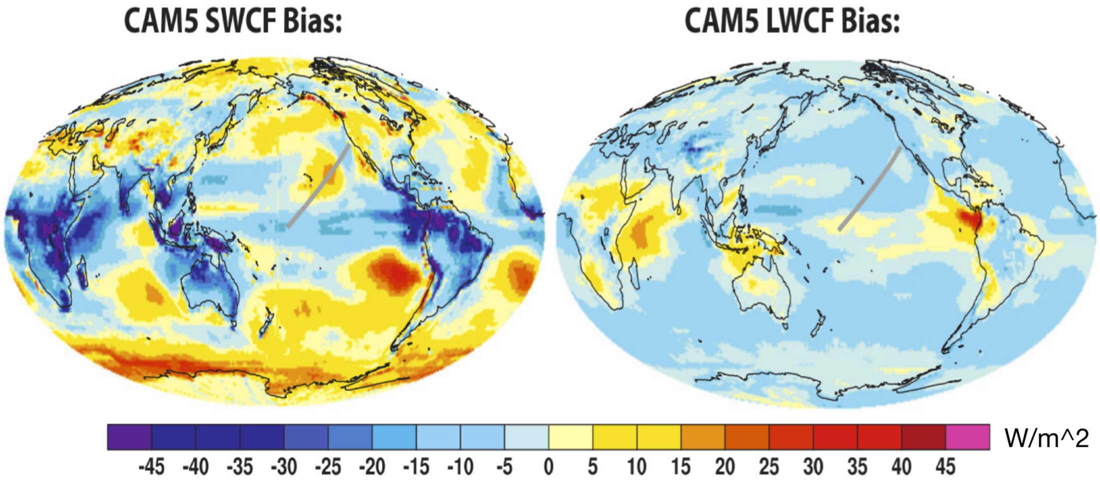

Fig. 2.3 Global biases between modelling and satellite observations of cloud radiative forcing. Note the large short-wave biases over the Southern Ocean. Figure adapted from Kay et al (2012) [108].

properties of cloud particles differ considerably for liquid and ice [113] and the large radiative biases over the Southern Ocean are commonly attributed to this [114], along with a poor representation of low-level clouds [115]. A recent study [116] investigated the impacts of reducing radiative biases by increasing the modelled supercooled liquid water fraction in clouds. This led to a rise in the ECS from 4.1 °C to 5.6 °C, directly highlighting the importance of cloud microphysical observations in the predictions of climate models.

Satellite-based observations of clouds are crucial for the evaluation of climate models due to their large spatial and temporal coverage [117]. Satellites cannot resolve individual cloud particles and so parameterisations of the bulk optical properties must be utilised, with methodologies similar to those used for climate models [100], for remote sensing of microphysical parameters. In situ observations are therefore of added importance for the calibration and validation of satellite retrievals of cloud microphysics [101].

Predicted adverse effects of global mean surface temperature rise include mean sea level rise [118], increased risks of agricultural drought [8], and reductions in the Earth's habitability [119]. Quantitative assessments of these impacts are challenging, but significant efforts are being made [4, 120]. One such study [121] has predicted that an increase in global mean surface temperature rise from 2 °C to 3 °C, which is a small fraction of the range of predicted ECS values in current climate models, can increase the reduction in future suitable climate area for flora and fauna from 35 % to 50 %. Better constraints on the range of ECS predictions, through the increase of understanding and parameterisation of cloud microphysics, is essential for mitigating risks and predicting future outcomes.

2.4 Observations of Cloud and Precipitation Microphysics

Instruments to observe the microphysical properties of clouds and precipitation have been developed for decades, with significant advances taking place from around the time of the Second World War and onwards [6, 122]. Techniques broadly fall into the categories of remote sensing instruments, which observe clouds from a distance, and in situ instruments which make observations from inside of the clouds. This section provides a broad overview of these methods, with a focus on the advantages and limitations of the approaches used in this work. Particular attention is given towards the areas in which the instruments presented in this thesis can overcome existing observational challenges.

It is outside the scope of this work to comprehensively review the performance of the many individual instruments currently used in this field, but specific details regarding the instruments used in the presented field campaigns are provided in Chapter 5. Standard reviews on the current state of remote sensing [123] and in situ [124] instruments should be consulted for a more detailed assessment of individual cloud instruments.

2.4.1 Remote Sensing Measurement Techniques

Remote sensing observations are the most effective means of determining cloud microphysical properties over large temporal and spatial scales [125], and instruments have been deployed around the world in ground-based installations, aircraft, ships, and satellites. Cloud-sensing instruments deployed on satellites in polar orbits can obtain observations over large spatial scales, though the temporal resolution is typically limited at a given location to at most two over-passes per day [126]. Instruments deployed on satellites in geostationary orbit and in ground-based installations allow observations with high temporal resolution, but are limited to a fixed geographical extent. Remote sensing instruments are deployed in each of these configurations and are used as the primary means of evaluating the performance of climate and Numerical Weather Prediction (NWP) models.

Remote sensing instruments are not able to resolve individual cloud particles, and so inversion methods based on models of the bulk optical properties of clouds are required for retrievals of microphysical properties [102]. Such models are described in the previous section, but notably require in situ observations of clouds to parameterise and constrain the underlying microphysical properties used in the inversion algorithms. In situ observations are also crucial for the validation and evaluation of remote sensing observations [127].

Remote sensing instruments used for cloud microphysical observations largely fall into the following categories: lidar, radar, and passive sensors [6]. Each approach utilises information resulting from the interaction of electromagnetic energy with a cloud system. Lidar and radar are active systems that transmit energy into the cloud and receive the signal returning from the cloud, whereas passive systems do not directly transmit energy into the cloud system, but instead derive information from interactions with external sources of energy such as sunlight. The merits and challenges of each method are briefly summarised as follows.

2.4.1.1 Lidar

Lidar instruments are used to infer the vertical structure of clouds and aerosols. A pulsed laser transmits electromagnetic energy into clouds and a receiver system detects the returning scattered light within the field-of-view of the instrument. The arrival times of the light returning to the receiver are used to infer the heights of scattering targets and the amplitudes of the returning signals are used to infer properties such as the ice water content [128].

Elastic scattering lidars, those that record scattered light at the same wavelength as the transmitted light, allow for vertical profiling of aerosol backscatter [129]. Determination of aerosol extinction requires assumptions in the inversion algorithm that can lead to significant uncertainties [130]. Raman lidar systems utilise inelastic scattering to overcome this limitation [131], though their deployment is limited due to the added complexity and they can only be operated at night due to the relatively weak inelastic signals [132]. Raman systems can also be used to obtain vertical profiles of water vapour [133].

Lidar systems that can determine the change in polarisation of light scattering from cloud particles can be used to obtain information about the underlying particle shapes [134]. Such approaches are useful in differentiating spherical supercooled liquid water droplets from ice crystals with more complicated shapes, though the inversion methods require assumptions regarding the underlying ice crystal properties [135]. Quantitative interpretation of depolarisation measurements can be complicated due to issues such as instrument calibration and the effects of multiple scattering in optically thick clouds [136].

A key limitation of the lidar technique is that the optical wavelengths used are strongly attenuated by clouds, particularly by liquid water [137]. Such signals can be fully attenuated after approximately 3 optical depths, limiting observations to a few tens of metres into typical cumulus clouds [138]. Clouds with multiple layers of supercooled liquid water are ubiquitous in regions such as the Southern Ocean [46], which limits the applicability of this technique.

2.4.1.2 Radar

Radar instruments are conceptually similarly to lidar, though the transmitted energy is notably at significantly larger wavelengths. This limits their application to cloud and precipitation observations [139], rather than for smaller aerosol particles. The increased wavelength also results in reduced signal attenuation, such that radar instruments can observe clouds with larger optical thicknesses than is possible with lidar [140]. Large uncertainties still result from particularly optically thick clouds [141], but dual-wavelength radar systems can be effective in reducing these errors [142].

Radar observations are strongly sensitive to the particle diameter [143]. This means that returns in a mixed phase cloud can be dominated by large ice crystals and can complicate the identification of small water droplets [144]. Optically thin clouds consisting of small water droplets can be particularly challenging to measure with this approach [145]. Furthermore, the strong dependence on particle diameter results in a large sensitivity to the assumed ice crystal properties used for retrieving microphysical parameters such as the ice water content [141].

Radar observations from satellite-based instruments have been recorded for many years [139] and such long-term datasets are particularly useful in validating climate models. These observations are less reliable below around 1.2 km [146] due to the impacts of surface clutter. This is especially problematic since low-level clouds around this height range are poorly represented in climate models [115]. Observations from radar instruments on aircraft, ship, and ground-based installations, along with in situ observations, are therefore crucial in better understanding the properties of low-level clouds.

2.4.1.3 Passive Sensors

Passive sensors derive information about clouds and aerosols through the detection of electromagnetic energy originating from sources that are external to the instrument, such as the sun. Most systems in use are either hyper-spectral imaging instruments or radiometric instruments [123]. A key advantage of passive sensors is that they tend to have significantly larger field-of-views as compared with active instruments, providing a greater global coverage of observations

Observations within multiple electromagnetic wavelength bands are commonly used by passive instruments to infer properties such as the cloud optical thickness and effective particle size [100]. Inversion methods require an assumed ice cloud model to be used based on in situ observations [147]. Significant variability in the outputs of these inversion methods has been attributed to different assumptions in the underlying ice cloud models [125], highlighting the need for improved ice cloud models based on in situ observations under a range of global conditions.

Passive instruments suffer from similar limitations as active systems, such as reduced reliability for observations of optically thick clouds and low-level clouds [148]. Satellite-based passive techniques also become less reliable for optically thin clouds [149] due to the impact of reflections from the Earth's surface. The quality of observations into optically thick clouds can be improved using tomographic techniques [150], though additional assumptions must be made in the retrieval of microphysical properties. Instruments that utilise sunlight are also notably limited to day-time observations.

2.4.2 In Situ Measurement Techniques

In situ instruments provide the highest resolution observations of cloud microphysical processes and are essential in the validation and calibration of climate models and remote sensing techniques [6]. The majority of in situ instruments used for cloud particle observations fall into the following categories: impaction, optical scattering, and imaging [124]. The advantages and limitations of each method are outlined in this section, though it is noted that all approaches should be considered useful and complementary in obtaining a comprehensive understanding of cloud processes.

A key challenge in the development of in situ instruments is the harsh conditions encountered within the clouds in which they are deployed. Challenges include robust operation under turbulent conditions, moisture ingress, and extreme temperatures. A discussion of the designs of the instruments presented in this thesis is to be found in Chapter 3.

Additional challenges unique to in situ instruments arise due to the interaction of the instrument with cloud particles. For example, significant shattering of ice crystals has been identified for aircraft observations that do not utilise specially designed anti-shattering probe tips [151]. This results in large overestimates in the total number concentration of particles [152] and draws into question the validity of aircraft observations undertaken before the adoption of anti-shattering probe tips. Biases in parameters derived from higher moments of the particle size distribution, such as the ice water content, have been found to be less affected by shattering, with assumptions regarding ice crystal habits having a significantly greater impact on the overall biases [153]. Adjustment algorithms have been developed to reduce the impacts of shattering [154, 155], though their implementation can lead to additional biases [156].

A wide range of in situ instruments have been developed for cloud observations, as summarised in Table 2.1 along with their respective measurement ranges. The measurement ranges of the holographic instruments presented in this thesis are provided in Table 3.1

Parameter measured	Measurement technique	Instrument	Measurement range	Manufacturer	Primary references
Particle size	Impaction	Video ice particle sampler (VIPS)	5–200 μm	NCAR	Heymsfield and McFarquhar (1996)
	Light scattering and interference	FSSP-100	2–50 μm	Formerly Particle Measuring Systems, Inc. (PMS), no longer available	Knollenberg (1976, 1981)
		Fast FSSP-100 (FFSSP)	1–50 μm	SPEC	www.specinc.com
		CDP	2–50 μm	DMT	Lance et al. (2010)
		FCDP	1–50 μm	SPEC	www.specinc.com
		CAS	0.5–50 μm	DMT	Baumgardner et al. (2001)
		CAS-POL	0.5–50 μm	DMT	Glen and Brooks (2013)
		BCP	5.0–75 μm	DMT	Beswick et al. (2014)
		CPSPD	0.5–50 μm	DMT	Baumgardner et al. (2014)
		SID-2/3	2–70 μm/2–140 μm	University of Hertfordshire	Cotton et al. (2010), Ulanowski et al. (2014)
		Phase Doppler interferometer (PDI)	1–2000 μm	Artium	Bachalo (1980)
		HOLODEC	5–2000 μm	NCAR	Fugal and Shaw (2009)
	Imaging probes	2D-C/2DG	25–800 μm/25–1600 μm	formerly PMS, no longer available	Knollenberg (1970, 1976, 1981)
		2D-P	200–6400 μm	formerly PMS, no longer available	Knollenberg (1970, 1976, 1981)
		260-X	10–620 μm	formerly PMS, no longer available	Knollenberg (1970, 1976, 1981)
		CIP	25–1550 μm	DMT	Baumgardner et al. (2001)
		CIP-GS	15–900 μm	DMT	Baumgardner et al. (2001)
		PIP	100–6400 μm	DMT	Baumgardner et al. (2001)
		CPI	2.3–>2000 μm	SPEC	Lawson et al. (2001)
		2D-S	10–1280 μm	SPEC	Lawson et al. (2006)
		HVPS-3	150–19 200 μm	SPEC	Lawson et al. (1998)
		3V-CPI	4.6–1280 μm	SPEC	www.specinc.com
		PHIPS-HALO	5–800 μm	Karlsruhe Institute of technology (KIT)	Abdelmonem et al. (2011, 2016)
		HSI	5–1250 μm	Artium	http://www.artium.com
Optical properties	Light scattering	PN		Laboratoire de Météorologie Physique (LaMP)	Gayet et al. (1997)
		CIN		Gerber Scientific, Inc. (GSI)	Gerber (2000)
		CEP		Environment and Climate Change Canada (ECCC)	Korolev et al. (2014)
		PHIPS-HALO		KIT	Abdelmonem et al. (2011, 2016)
Water content	Hot wires and evaporators	King LWC probe and LWC-100/300	0.05–3.0 g m^{-3} @ 100 m s^{-1}	Formerly PMS (no longer available), and DMT	King et al. (1978)
		Nevzorov LWC/TWC	0.002–>3.0 g m^{-3} @ 100 m s^{-1}	SkyPhysTech, Inc.	Korolev et al. (1998b)
		TWP	0–20 g kg^{-1}	Met Office	Nicholls et al. (1990)
		HTW isokinetic evaporator	5–2500 ppmv	Harvard University	Weinstock et al. (2006)
		CLH	0.005–1 g m^{-3}	University of Colorado	Davis et al. (2007)
		FISH	0.5–1000 ppmv condensed + vapor	Forschungszentrum Jülich (FSJ)	Schiller et al. (2008)
		CVI	0.003–2 g m^{-3} @ 100 m s^{-1}	NCAR, DMT	Noone et al. (1988)
		IKP	0–10 g m^{-3}	Science Engineering Associates (SEA)	Davison et al. (2009, 2011)
	Light scattering	PVM-100A	0.002–3 g m^{-3}	GSI	Gerber et al. (1994)

Table 2.1 Summary of in situ instrument measurement ranges from a recent review of in situ cloud instrumentation. This table is adapted from Baumgardner et al (2017) [124] and definitions of the abbreviated instrument names are also to be found in this reference.

with a maximum range of 3.1 microns up to 3000 microns, as discussed in Chapter 3. This relatively large particle measurement range is one of the key advantages of these instruments as compared with other existing approaches.

2.4.2.1 Impaction Instruments

Impaction instruments directly capture and analyse cloud, aerosol, and precipitation particles impacted onto an adhesive-coated surface. This method overcomes the challenges of measuring airborne particles with large velocities in a 3D volume. This allows for particularly high-resolution observations using 2D microscopy methods.

Impaction probes have been used to capture cloud particles both from the ground [157, 158] and in the air using aircraft [159] and balloons [160]. Impacted particles can be cryogenically preserved and then studied in great detail under laboratory conditions [157]. Such studies have utilised Scanning Electron Microscopy (SEM) to provide unique insights into the surface roughness properties of naturally formed hydrometeors [160].

Ice crystals larger than around 150 microns are prone to shattering on impact with aircraft-based impaction instruments [161] and so this method is limited to relatively small particles. Information about the 3D spatial distribution of particles is lost with this approach and manual analysis methods tend to be necessary, though automated systems have been developed [162], which limits the amount of available observations. Additional challenges arise due to the coalescence of particles on the surface of microscope slides.

2.4.2.2 Optical Scattering Probes

Optical scattering probes have provided microphysical observations for decades [163] and their performance has been studied extensively over this time [164]. Instruments operate by scattering light from cloud particles and Mie scattering theory [165] is used to infer the particle sizes from the intensity of scattered light within certain angular detection ranges. The Mie scattering theory is suited for retrievals of spherical particle properties, but with appropriate assumptions the technique has also been used for ice crystal measurements [156]. Ice crystal measurements by scattering instruments can be improved through the use of polarisation information [166]. Testing of a low-cost polarimetric backscattering instrument is presented in this thesis.

Determination of particle sizes using single-particle scattering instruments has been found to be reasonably accurate for spherical particles with sizes of less than around 50 microns [164]. Ambiguities in defining the sizes of aspherical ice crystals is a major challenge for this technique that can result in large uncertainties [167]. Issues such as detector saturation tend to limit the usage of these sensors to the observation of particles smaller than a few hundred microns [168].

Another significant source of uncertainty in single-particle scattering probe measurements is the issue of coincidence in which multiple particles are detected at once. This issue can result in errors due to the misclassification of multiple water droplets as ice crystals [169], as well as significant sizing uncertainties [170]. The probability of coincident detections has been estimated to be around 12 % for a typical cloud particle number density of around 300 cm^{-3} [169].

2.4.2.3 Imaging Probes: 2D and Stereoscopic Imagers

Imaging probes require less assumptions than scattering probes for the retrieval of microphysical parameters through the direct imaging of cloud particles. Instruments utilising this approach can be divided into Optical Array Probes (OAPs), that image particles by progressively scanning the signals along a linear array of photodiodes [171], and higher-resolution imagers utilising camera sensors [172]. Imaging probes have larger sampling volumes than for scattering probes [164], though this comes with the downside of an increased sensitivity to biases from ice crystal shattering in aircraft deployments.

OAPs are commonly used due to their relatively simple design and many processing algorithms have been developed to improve their accuracy [156]. Imaging probes using camera sensors provide higher-resolution observations, though processing algorithms tend to be more specialised. Imaging probes typically utilise a binary threshold to define the presence of cloud particles. Grayscale imaging probes have been developed with multiple intensity thresholds, though methods for interpreting their observations are lacking [164].

The sampling volume of imaging probes is effectively limited by the particle-size dependent depth of field, which is challenging to quantify for aspherical ice crystals due to ambiguities in defining their sizes [173]. If the depth of field is smaller than the spacing between probe arms, out-of-focus particle images can be recorded which are a large source of uncertainty [174]. A correction algorithm has been developed to infer the true size of out-of-focus spherical particles by relating the sizes of the particle shadow and Poisson spot features in their recorded diffraction patterns to Fresnel diffraction simulations [175]. Aspherical particles have significantly more complicated diffraction patterns and there is currently no accepted method for correcting the observations of these particles [156].

Stereoscopic imaging probes produce images of particles from multiple angles. As compared with OAPs, this approach has a reduced ambiguity in the depth of field [176], and hence sampling volume [173], and an improved capability for measuring particles smaller than around 100 microns [177]. Stereoscopic imagers also have the potential to improve the determination of 3D cloud particle properties, though algorithms are yet to be developed to perform this analysis routinely [176].

2.4.2.4 Imaging Probes: Holographic Imagers

Digital holography is a wavefront sensing technique that allows micron-scale measurements of cloud particle number densities, sizes, and shapes within a well-defined sampling volume [178]. A distinct advantage of holographic imagers is their significantly larger sampling volumes as compared with 2D and stereoscopic imagers [57]. Furthermore, this approach has the potential for nanometre-scale particle measurements through the retrieval of optical phase information [179], as discussed further in Chapter 4. This principle forms the basis for the in situ instruments developed in this work and the details of this method are discussed in Chapter 3.

Holographic imagers are effective at measuring particles with a wide range of sizes, typically on the order of a few microns up to a few millimetres as outlined in Chapter 3. These instruments are notably capable of measuring ice crystals with sizes smaller than around 100 microns. This size range is poorly covered by the majority of in situ sensors and a lack of these observations has been identified as a limiting factor in the understanding of ice crystal processes [124]. Holographic instruments also have the useful capability to identify ice crystal shattering by inspection of the spatial distribution of particles within the 3D sampling region [180].

Holographic instruments have a long history of deployment for cloud particle studies including from aircraft [57, 178, 181, 182], ground-based [183–185], cable-car [186], and tethered-balloon [187] platforms. Despite these efforts, few systems remain in operation today. One potential reason for this is due to the challenges in analysing the large datasets which can quickly grow to the order of terabytes. Sophisticated automated analysis methods are, therefore, required to extract particle number density, size, and shape information from 3D images. The ongoing development of the HoloSuite [188, 189] software represents an important step towards overcoming this limitation, though challenges remain in areas such as the automated separation of small ice crystals from artefacts [190]. Two new automated analysis methods are presented and tested in this thesis.

Another challenge towards the wide-spread deployment of holographic imagers is their complexity of design which has tended towards systems that are expensive and heavy. Such systems have been used to provide unique insights into cloud processes with unprecedented detail [57]; however, their deployment has been limited to only a handful of field campaigns over the years. Furthermore, the risk of instrument loss prohibits their deployment using platforms such as untethered balloons. Overcoming these limitations is the core motivation for the development of the low-cost and light-weight holographic instruments presented in this thesis.

2.4.3 Cloud Sampling Strategies

An important aspect of in situ instruments is the means by which they gain access to a cloud. A range of methods are currently used including aircraft, Unmanned Aerial Vehicle (UAV), dropsonde, high-altitude, tethered balloon, and untethered balloon platforms. Each approach has advantages and limitations, and a combination of all methods is important in obtaining a full understanding of clouds over a wide range of spatial and temporal scales.

Aircraft flights provide the greatest control over the sampling path through clouds as their flight paths can be carefully controlled. This is an effective way of obtaining a large number of vertical cloud profiles within a given field campaign. However, the cost of aircraft field campaigns is large and this has significantly limited the availability of observations of this kind.

The large relative velocities between cloud particles and aircraft result in significant amounts of ice crystal shattering [151], as discussed previously in this section. This issue is less problematic for other deployment methods where typical relative velocities between the instruments and cloud particles are an order of magnitude smaller. Large aircraft velocities also require additional assumptions to be made regarding the stationarity and ergodicity of clouds in order to obtain statistically significant observations with commonly used instruments that have relatively small sampling volumes [57].

Thunderstorm clouds and those with large amounts of supercooled liquid water are generally too dangerous to fly into, which produces further sampling biases for these cloud types [6]. These issues could potentially be overcome through the use of Unmanned Aerial Vehicles (UAVs) and dropsondes, and the low-cost and light-weight instruments presented in this work should be well suited to this approach.

Deployment of in situ sensors on high-altitude structures is an effective means for obtaining long-term observations of microphysical processes. Cloud observations are limited to mountainous regions where clouds can naturally pass through the instrument sampling volumes and at lower altitudes the approach can be used for observations of low-lying fog and precipitation. The spatial scale of such observations is limited, though low-cost instruments have the potential to resolve this issue through deployment over a widespread network.

Tethered balloon systems are an extension to ground-based deployments that allow for the routine vertical profiling of cloud microphysical properties [191]. Such systems can be automated and deployed over relatively long durations to produce more frequent in situ cloud profiles than is feasible with other methods. A notable limitation of tethered systems is that vertical profiles are typically limited to just a few kilometres in altitude. Their deployment is also restricted to wind speeds of below around 10 m s^{-1} [192], which is particularly problematic for deployments over the ocean from ships. A tethered system using a kytoon has recently been developed that relaxes these wind restrictions [187].

Untethered balloons have been used for the deployment of a range of in situ cloud instruments, such as impaction instruments [160, 193, 194], scattering probes [65, 195], and 2D particle imagers [196–201]. The primary advantage of untethered balloons is their capability to retrieve vertical profiles of atmospheric observations throughout the troposphere. They can also be used for long-term stratospheric measurements using super-pressure balloons [202]. The relative ease of deployment also allows for unique observations. For example, observations within clouds that would be too dangerous to fly an aircraft into, and balloon launches from ships over the ocean where the logistics of tethering a balloon are particularly challenging and in situ cloud observations are crucially lacking.

A major challenge for untethered balloon deployments is the significant risk of losing the payloads. Large volumes of data recorded during flights can be received from the ground using high-speed radio transmission methods [203], but the risk of loss of the instrument itself can be cost prohibitive. The low-cost and light-weight holographic instruments presented in this thesis have been designed to specifically overcome this challenge to significantly increase the availability of cloud microphysical observations. The results of a world-first untethered balloon launch of a holographic microscope into clouds are presented in Chapter 7.

Chapter 3

Holographic Microscope Design and Automated Holographic Analysis

3.1 Introduction

The developed Compact Cloud-particle HOlographic Microscope – Surface (C^2HOM–S) and C^2HOM – Balloon (C^2HOM–B) instruments operate based on the principle of digital holography. This is a wavefront-sensing technique allowing both the amplitude and phase of a coherent electromagnetic wavefront to be measured using interferometric methods. Scalar diffraction theory is used along with this information to reconstruct a 3D image of scattering objects, in this case cloud particles, from which the particle counts, sizes, and shape information can be extracted. The holographic theory relevant to the development and operation of the instruments used in this work will be outlined further in the following sections as well as in Appendix A.

The holographic instruments presented in this project were initially developed by this author as part of a Master of Philosophy project [204, 205] and the published thesis is hereafter referred to as C17. Much of the details of the initial design, electro-optical testing, characterisation, and laboratory validation of the instruments are presented in that reference, and so rather than duplicating those results, the reader is directed to that thesis for further clarification. Laboratory calibration measurements and instrument specifications that are of particular relevance to the research presented within this thesis will be presented in this chapter, particularly work undertaken in this project subsequently to C17, and as required for the interpretation of field results.

The C^2HOM–S instrument is suited to deployment on the ground on a tower structure and was developed based on the findings of C17. The C^2HOM–B instrument was designed to be suited to deployment on a weather balloon. The requirements for the instrument to be light weight and cost effective, to mitigate the risk of potentially losing the instrument, were therefore particularly strict. The design process and impacts on the sampling volume of the new mounting design are discussed in this chapter.

A key development since the work presented in C17 is the improvement of the automated analysis algorithms for processing field data and identifying cloud particles within the reconstructed 3D images. Previous algorithms were found to work effectively in a laboratory environment, but a host of challenges can arise under field conditions such as a varying optical quality of the sampling windows, shaking instrument mounts under heavy winds, and a variable saturation effect due to sunlight. These issues have largely been resolved with the improved algorithms and methods presented in this chapter. The automated methods developed for extracting particle properties such as size and shape are compared with manually analysed data from the Snowy Mountains and balloon launch field campaigns, discussed further in subsequent chapters.

3.2 Holography Background

Holography is fundamentally a technique for reconstructing a coherent wavefront through direct measurement of the amplitude and phase via interferometric methods. The invention of holography is attributed to Dennis Gabor [206–208] for which he was awarded the Nobel Prize in Physics in 1971. This research was originally motivated by the work of W. L. Bragg [209] as a means of reducing aberration in electron microscopy of atomic structures, and remains an important technique within that field of research [210]. The principle of holography can be applied to any wave phenomena and has subsequently found applications throughout the electromagnetic spectrum [211–214], as well as in other areas such as acoustics [215], atom optics [216], and helioseismology [217].

A key application of holography is optical 3D imaging of a field of objects. The technique requires the formation and measurement of a stable interference pattern between light scattered from the field of objects to be imaged and a known reference wavefront. This interference pattern is hereafter referred to as a hologram. The invention of the laser [218] significantly extended the applicability of this method through the introduction of light sources with suitably large coherence lengths, as discussed further in Section 3.3. Significant progress [219–221] in the decades following the initial invention of holography led to the routine application of this technique by recording of the interference pattern on light-sensitive emulsions, and reconstruction of the 3D image in free space by illumination of the recording with the original reference wavefront. This approach is referred to as analogue holography.

The next major development in this field was introduced by Schnars and Jüptner [222] with the recording of a holographic interference pattern on a Charge-Coupled Device (CCD). This development marked the beginning of the technique referred to as digital holography in which the hologram is recorded on an electronic sensor and the object wavefront is reconstructed numerically using scalar diffraction theory. The wavefront, when reconstructed at a range of longitudinal positions in this way, is hereafter referred to as a 3D image. The transverse dimensions of this 3D image are defined by those of the camera sensor and the notion of depth is defined as the distance along the longitudinal axis of this 3D image relative to the camera sensor. This technique forms the basis for the holographic instruments presented in this thesis and the theory of operation is outlined in greater detail in Appendix A for reference.

3.3 Resolution and Sampling Constraints of a Holographic Microscope

The resolution and sampling constraints of a holographic imaging instrument depend on many factors, particularly when operated under field conditions as with the instruments used in this work. The major fundamental constraints are discussed in this section, though in practice the true resolution can only be determined through laboratory testing. A summary of such laboratory results are presented in C17 but key results will also be presented in this section.

3.3.1 Instrument Configuration

The basic configuration of the holographic instruments used in this work is illustrated in Figure 3.1 and is referred to as an in-line geometry. This setup is defined by having the laser, scattering objects, and camera collinear along the optical axis. The primary motivation for using this setup is that it results in the shortest optical path differences between the scattered object wavefronts and unscattered reference wavefront. This is essential due to the relatively poor coherence length of the low-cost laser diodes used in this work. The coherence length is defined as the path difference between wavefronts that results in a drop in interference fringe visibility by a factor of 1/e and is defined by the relation

$$L_c = \frac{\lambda^2}{\pi \Delta \lambda}, \tag{3.1}$$

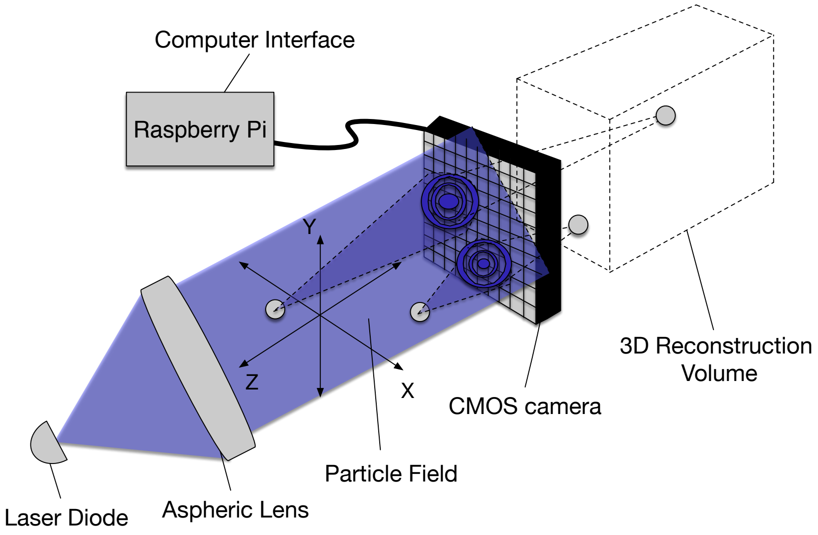

Fig. 3.1 Illustration of the in-line geometry employed in the holographic instruments used in this work. An aspheric lens is used to collimate the diverging laser diode light and interference patterns are recorded on a CMOS sensor.

where λ is the peak laser wavelength and $\Delta\lambda$ is the Full Width Half Maximum (FWHM) of the laser spectrum. The coherence length for the lasers used in this work is on the order of only 20 μm, necessitating such a setup. A secondary advantage of the in-line setup is that the hologram will have lower spatial frequencies than for an equivalent off-axis setup. This is important in digital holography as the resolution of the coarse camera pixel array is orders of magnitude worse than for the photographic films used in analogue holography.

A notable disadvantage of the in-line setup relative to off-axis configurations is that the twin image wavefront, as defined in Appendix A, is overlaid with the object wavefront in Fourier space and cannot be simply filtered out. However, this does not represent a significant issue for the particular application of imaging cloud and precipitation particles as understood by the following argument [223, 224]. Such particles are small relative to the distances by which the wavefronts are propagated in the reconstruction process and the scattered wavefronts diverge relatively quickly. When the wavefront emerging from the hologram is propagated to the depth at which the image of the object comes into focus it can be shown that due to diffraction the virtual image term becomes spread over a significantly larger extent than the object extent. This slowly varying background variation is then relatively simple to differentiate from the sharply focussed and localised particle image. Extracting the phase of the wavefront under such a configuration remains challenging, but various phase retrieval techniques have been developed [225–227]. Only amplitude reconstructions are considered in this work but such methods may prove useful in upgraded instruments that are currently being considered.

3.3.2 Resolution

The lateral resolution of a holographic imager is determined by the fidelity to which the interference fringes are measured on the recording sensor [228, 229]. By requiring that at least the zeroth and first order maxima of the interference pattern are recorded the following relationship can be derived [185, 223]:

$$\begin{aligned} D_{\text{res}} &\geq \frac{\lambda}{2\,(\text{NA})} \\ &\gtrsim \frac{2.44\lambda z}{D_{\text{sensor}}}, \end{aligned} \tag{3.2}$$

where D_{res} is the smallest resolvable particle diameter, λ is the peak laser wavelength, NA is the numerical aperture of the camera sensor, z is the depth relative to the camera sensor, and D_{sensor} is the camera sensor size along a given dimension. A similar expression can be derived for the longitudinal resolution

$$Z_{\text{res}} \geq \frac{\lambda}{2\,(\text{NA})^2}, \tag{3.3}$$

where Z_{res} is the longitudinal resolution and the other terms are as defined in Equation 3.2.

These relations describe a theoretical depth dependence for the transverse resolution that is linear whereas the depth dependence of the longitudinal resolution is quadratic. This results in a longitudinal resolution that is significantly poorer than in the transverse dimension and in practice it is only the 2D outlines of the scattering particles at their depth of best focus that are measured. These theoretical resolution constraints are plotted as a function of depth in Figure 3.2 for the holographic instruments used in this work. Horizontal and vertical cases are plotted since the camera used in these instruments has a rectangular sensor. Magnification is not intended in the chosen configuration and therefore the pixel size of the camera sensor of 2.2 microns also imposes a fundamental resolution constraint that is plotted for reference.

The Compact Cloud-particle HOlographic Microscope – Surface (C^{2}HOM–S) and C^{2}HOM– Balloon (C^{2}HOM–B) holographic instruments used in this work have slightly different spacings between the optical components that results in differing resolution capabilities. The C^{2}HOM–S instrument has a sampling volume that begins from approximately 26 mm from the camera sensor and extends to around 85 mm. This corresponds to a lateral resolution that theoretically varies between approximately 2.3 microns and 7.4 microns. The

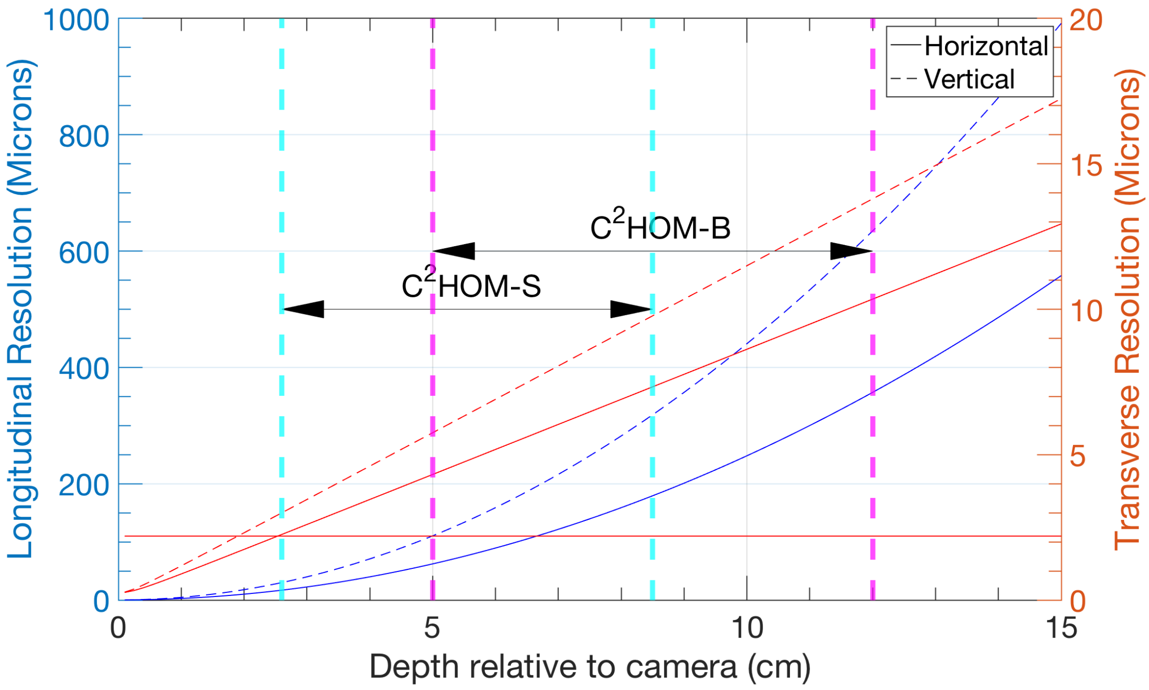

Fig. 3.2 Theoretical diffraction-limited transverse and longitudinal resolution as a function of depth relative to the camera sensor. The sampling depth range of each of the holographic instruments used in this work is annotated. The pixel size resolution limit is also shown for reference.

design of the C^{2}HOM–B instrument was significantly different, as discussed in Section 3.5, and notably had the camera sensor further from the sampling window to reduce sunlight saturation effects. This led to a sampling depth starting at around 50 mm from the sensor up to 120 mm. The corresponding transverse resolution varies between roughly 4.4 microns and 10.3 microns. These sampling depth and resolution properties are indicated on Figure 3.2 for reference.

The actual resolution of a holographic instrument is likely to deviate from the theoretical limits outlined above due to issues such as chromatic aberration, laser power fluctuations, sensor noise, and degradation of sampling window quality in the field. The resolutions of the holographic instruments used in this work were determined by laboratory measurements using calibration test spheres as well as a United States Air Force (USAF) resolution test chart. This procedure is described further in C17 but a brief summary of the preferred USAF-chart method is provided here for reference. This method is preferred as it allows finer control over the object locations and is simpler to replicate in future.

The USAF-chart was placed at a range of depths in the holographic sampling volumes to characterise the varying resolutions. At each depth the hologram was reconstructed and bounding boxes were manually drawn over each of the resolved chart elements, as shown in Figure 3.3a for the C^2HOM–B instrument. The mean of each group of three bars was then taken and compared with the true bar width provided by the manufacturer of the chart.

The bias between the measured and true element widths is plotted as a function of element width in Figure 3.3b for the C^2HOM–B instrument. The bias was found to increase with the size of the chart element, suggesting magnification. Measurements are shown for both the horizontal and vertical dimensions since the resolution along each dimension is different due to the rectangular camera sensor, as described by Equation 3.2.

A relationship for the magnification in a holographic system can be derived under the paraxial regime, in which spherical waves are approximated with a quadratic phase term, with the following form [230, 231]:

$$M_t = \left| 1 - \frac{z_o}{z_r} - \frac{\lambda_1 z_o}{\lambda_2 z_p} \right|^{-1}, \tag{3.4}$$

where M_t is the transverse magnification factor, z_o is the object location, z_r is the source of the reference wavefront which is modelled as a spherical wavefront with a quadratic phase function, λ_1 is the laser wavelength, λ_2 is the wavelength of the numerical reference wavefront used in the reconstruction, and z_p is the focus depth of the reconstructed image. By measuring each of these terms and iteratively refining the depth of the reference wavefront, this relationship was used to correct for the magnification arising from the imperfectly collimated reference wavefront. This resulted in the magnification-corrected measurements shown in the bottom panel of Figure 3.3b. No such magnification corrections were required for the C^2HOM–S instrument, suggestive of a better collimated beam than for the C^2HOM–B instrument. These resolution tests and magnification corrections were repeated before and after each of the field campaigns presented in this work.

The transverse resolution of the C^2HOM–S instrument was measured to be 3.5 microns at the camera side of the sampling volume and 7.8 microns at the laser side. This is relatively close to the theoretical diffraction limited resolution for this system. The resolution of the C^2HOM–B instrument varied from 3.1 microns on the camera side up to 3.9 microns on the laser side. This relatively constant resolution throughout the sampling volume was unexpected but is likely due to the magnification introduced into this setup by the imperfectly collimated reference wavefront. The upper resolvable particle diameter for both instruments is limited to around 3 mm which is governed by the size of the camera sensor, which has

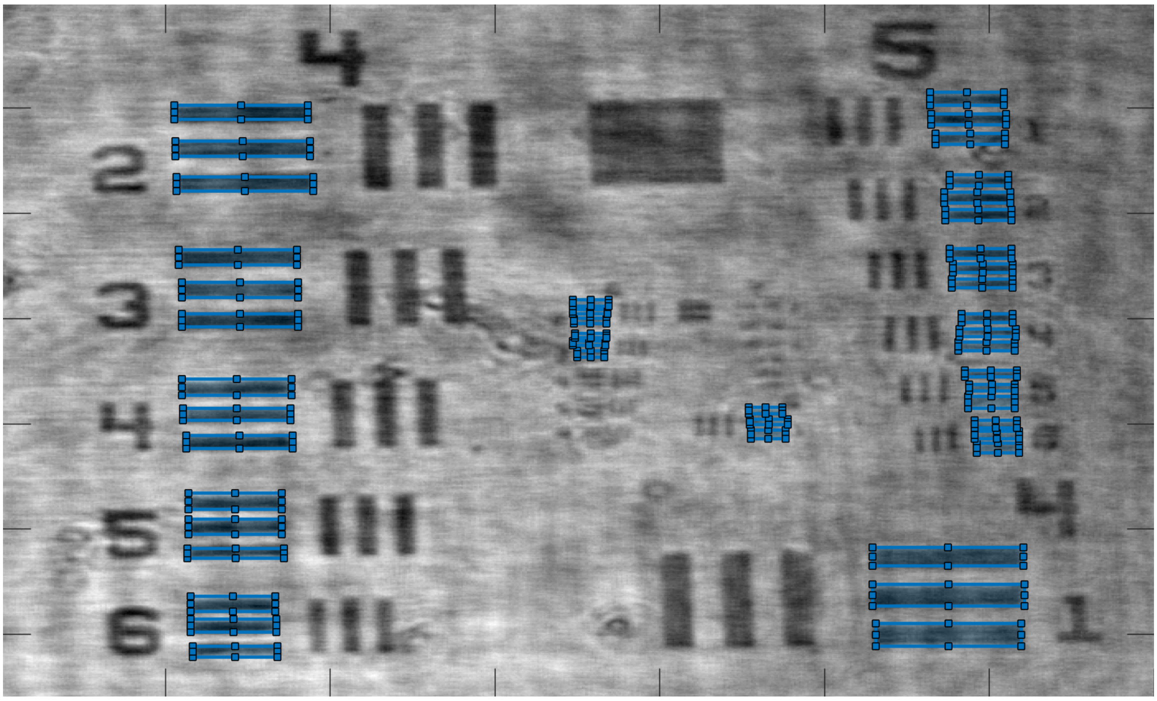

(a)

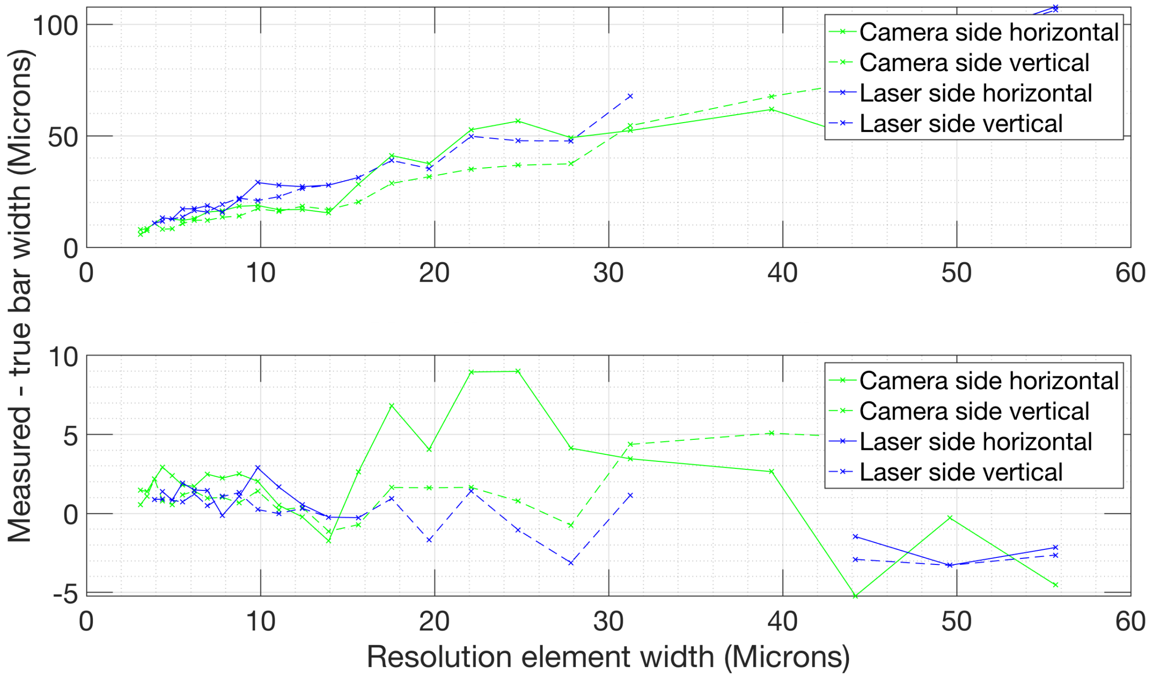

(b)

Fig. 3.3 a) USAF resolution test chart used to measure the resolution of the holographic instruments used in this work and to correct for magnification effects arising from an imperfect beam collimation in the C^{2}HOM–B instrument. b) Holographic sizing errors without (top) and with (bottom) magnification corrections applied. Measurements are shown for the case of placing the USAF test chart at the depth of the sampling window closest to the camera (camera side) and at the depth of the window closest to the laser (laser side).

	C^2HOM–S	C^2HOM–B
Sampling volume	0.9 cm^3	1.2 cm^3
Transverse resolution (Camera-side, Laser-side)	(3.5 μm, 7.8 μm)	(3.1 μm, 3.9 μm)
3D reconstruction depth spacing	1.5 mm	1.8 mm

Table 3.1 Summary of key measured instrument parameters for the holographic instruments used in this work.

dimensions of 5.7 mm by 4.3 mm, and the requirement of recording multiple interference fringes.

3.3.3 Cloud Particle Sampling Constraints

There are a number of sampling constraints that must be considered in the design of a holographic instrument intended for cloud particle detections. The aspects discussed in this section are separate from the fundamental resolution limits described in the previous section and must also be considered in the design of such an instrument. Only the major constraints are summarised here, and the reader is again directed to C17 for a more detailed discussion of this matter as relevant to the holographic instruments used in this work. Key resolution and sampling parameters for the holographic instruments used in this work are summarised in Table 3.1.

Cloud particles will have a velocity relative to the camera sensor that can lead to blurring of the recorded hologram and a subsequent loss in resolution. This issue is mitigated by choosing a suitably short laser pulse duration so as to reduce the detected particle movement during the camera exposure time. An approximate relationship describing this condition is as follows:

$$\delta t \simeq \frac{D}{fv}, \tag{3.5}$$

where δt is the required laser pulse duration, D is the particle diameter, f is the specified particle displacement as a fraction of particle diameter, and v is the relative speed between the camera sensor and the particle.

For sampling of cloud particles on a weather balloon, or with a fixed installation under moderate wind conditions, a relative speed of 5 ms^{-1} can be used as a representative value. Using this relationship it is found that a pulse duration of less than 400 ns is required to measure a typical cloud particle with a diameter of 20 microns [232] and an acceptable particle displacement of 10 % of the diameter. The holographic instruments used in this work used a laser pulse duration of approximately 150 ns and laboratory testing with calibration objects moving at such speeds did not reveal significant blurring artefacts.

The 3D image reconstruction is obtained by propagating a numerical reference wavefront through the recorded hologram using scalar diffraction theory. The number of depths used in this reconstruction imposes an additional sampling constraint that is more difficult to quantify than the previous relationships. One means of estimating the impact of this sampling spacing along the depth axis is to consider the holographic depth of focus. The depth of focus in this context is interpreted as the approximate range of depths over which the reconstructed wavefield resembles the scattering object, with the optimal focus depth being at the centre of this range. An approximate expression for this property can be derived with the following form [233, 234]:

$$\delta_I \simeq \frac{(2a)^2}{\lambda}, \tag{3.6}$$

where δ_I is the holographic depth of focus, a is the particle radius, and λ is the laser wavelength. For reliable sizing of the reconstructed particle it is argued that the reconstruction depth spacing should not be significantly larger than this depth of focus metric. Such an argument is only approximate but does provide some guidance for system design, particularly regarding the impacts of wavelength choice.

For a 20 micron particle, Equation 3.6 leads to a depth of focus of approximately 1 mm. The holographic datasets studied in this work were reconstructed over 40 depth slices with a corresponding depth spacing of 1.5 mm for the C^2HOM–S instrument and 1.8 mm for the C^2HOM–B instrument. These spacings are close to the approximate depth of focus required, and visual inspection of reconstructed images of objects as small as 3 microns indicated that they were suitably focussed. Laboratory measurements using calibration test spheres and a USAF-chart suggest that the sizing uncertainty due to the chosen depth spacing is approximately 4 microns. The larger source of sizing uncertainty was associated with the automated analysis methods used to extract particle size, as discussed further in Section 3.6.

The choice of 40 sampling depths was motivated by a balance between maintaining resolution and reducing the size of the reconstructed 3D images in computer Random Access Memory (RAM). The automated methods developed to identify particles, discussed further in Section 3.6, require two 3D images to be reconstructed and manipulated per hologram. With the chosen number of sampling depths and a bit depth of 12 bits, this resulted in 6 gigabytes (GB) of RAM usage which could reasonably be processed with the available computing resources. The ability to directly reconstruct multiple 3D images at once is a distinct benefit of using the chosen camera sensor with a relatively low pixel count of 5 megapixels (MP). This point is elaborated on in Section 3.6.

A large number density of cloud particles within the sampling volume can represent a significant source of noise in the reconstructed image. This arises due to obscuration of the reference wavefront as well as additional intensity variations from scattering between particles. An approximate expression for the number density beyond which this issue starts to become significant can be derived with the following form [57]:

$$n_c \simeq \frac{0.04}{\pi d^2 l}, \tag{3.7}$$

where n_c is the number density threshold, d is the mean particle diameter, and l is the depth of the sampling volume. For a mean particle diameter of 20 microns and the sampling depth used in the C^{2}HOM–B instrument, this number density threshold is approximately 450 cm^{-3}. The estimated threshold is relatively conservative and so for typical cloud droplet number densities of around 100 cm^{-3} [232] it is not expected that this issue will significantly impact the holographic instruments used in this work.

The number density of cloud or precipitation particles can be measured directly from a single hologram since the sampling volume can be measured and the number of particles can be counted directly. The sampling volume of the holographic instruments was determined by measuring the overlapping area of the collimated beam on the camera sensor using a polygon outline and multiplying this by the depth between the sampling windows. This gave a maximum sampling volume of approximately 0.9 cm^3 for the C^{2}HOM–S instrument and 1.2 cm^3 for the C^{2}HOM–B instrument.

In practice the effective sampling volume was less than these values as some pixels become saturated by sunlight when deployed in the field. It was identified that the saturated pixels occurred at the bottom of the camera sensor and linearly rose to higher rows as a function of the position of the sun. This allowed the saturated pixel rows to be automatically removed from the analysis and the effective sampling volume can be recalculated on a frame-by-frame basis.

For a typical cloud droplet number density of 100 cm^{-3} it is then expected that around 100 particles will be measured within a single hologram with the holographic instruments used in this work. The counting uncertainties follow Poisson statistics which gives a relative counting uncertainty of 10 %. This uncertainty is relatively large and so the size and shape measurements are considered more reliable than the number density measurements. The primary motivation for the developed holographic instruments was for them to be both cost effective and light weight such that they can be deployed on a weather balloon or in a network over large areas. The larger counting uncertainty was a necessary trade-off in attaining these goals, though an upgraded version of the instrument is in development that resolves this limitation through use of a larger camera sensor and faster computer.

3.4 Data Processing

The discussion in previous sections has been centred around the theoretical constraints on the capabilities of a holographic imager as well as laboratory testing and calibration results. Such an analysis provides a baseline expected performance and is useful in the design phase of a holographic instrument. In this section the methods used to process the data from such an instrument for subsequent automated analysis will be presented. Particular attention will be given towards the reduction of noise sources arising from the field deployment of such an instrument. It should be noted that some of these issues are specifically due to long-term deployment in the field and are, therefore, less relevant to the C^2HOM–B instrument due to the short duration of a typical balloon launch.

3.4.1 Sampling Window Quality

One of the major sources of noise in a hologram recorded in the field arises from the optical quality of the sampling windows. This issue is manifested via two main mechanisms, the first of which is through the direct impaction of cloud particles and dust on the sampling windows. This issue is demonstrated in Figure 3.4a which shows a hologram recorded in the laboratory without any objects placed in the sampling volume. A relatively smoothly varying background intensity is noted which is the unscattered laser diode light which has an elliptical beam shape that is characteristic of such devices [235]. Overlaid on this background are the interference patterns formed from light scattered from particles on the sampling windows. These window particles have the effect of partially blocking the reference wavefront and the out of focus diffraction patterns of these particles represent a noise source against which airborne particles within the sampling volume must be distinguished.

The other way in which the sampling window quality can be degraded is demonstrated in Figure 3.4b and occurs over longer timescales. This shows a hologram recorded from the C^2HOM–S instrument after 3 months of field deployment in the Snowy Mountains during the field campaign discussed in Chapter 6. This was over a period of time during which the sampling windows were not regularly cleaned. Many water droplets impacted the windows over this time and deposited a permanent layer of dirt as the droplets evaporated. This build-up of small dirt particles effectively acts as a distorting screen through which the laser

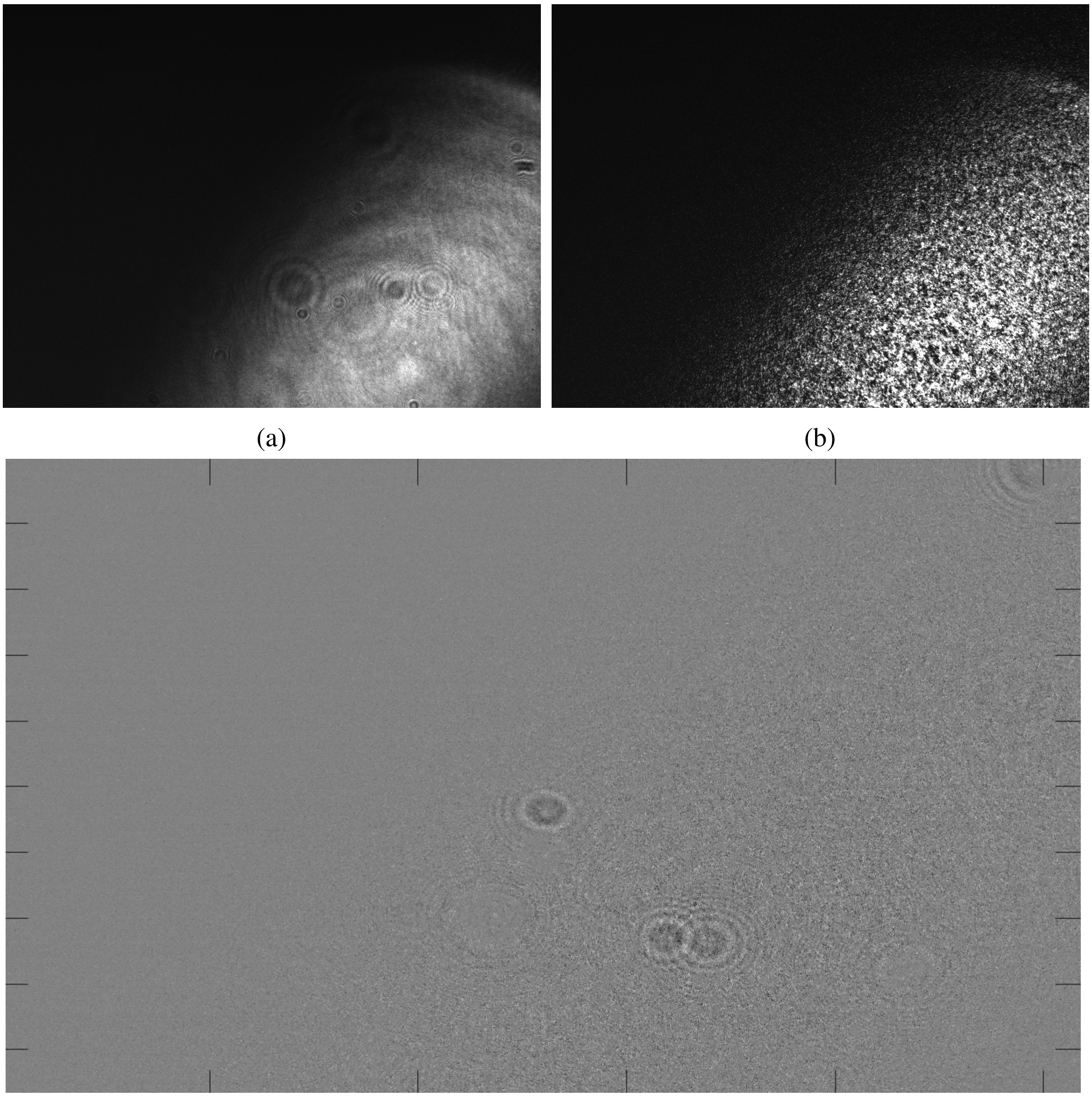

(a) (b)

(c)

Fig. 3.4 a) Raw hologram recorded in the laboratory before a field campaign. b) Raw hologram recorded after 3 months of field deployment in the Snowy Mountains. c) Background-subtracted hologram obtained during field deployment revealing the presence of three airborne particles in the centre of the beam.

beam must propagate and significant degradation of the wavefront quality is seen in this hologram relative to the hologram recorded in the laboratory.

Various approaches to mitigating these issues were attempted in this work. It was found that Fourier filtering methods were not suitable since the interference fringes of interest from light scattered from airborne particles consisted of spatial frequencies that were too similar to those arising from particles on the windows. Another method used in other holographic instruments [178] is to divide the hologram of interest by the median of temporally adjacent holograms. This approach proved more effective than Fourier filtering, particularly when three holograms either side of the central frame were used in the average. Despite the improvement, significant background noise was still present with this method due to particles impacting and leaving the windows over the averaging time frame.

The most effective method found for mitigating the window quality issues was through background subtraction. This method simply subtracts the previously measured hologram from the hologram of interest and the results of this are shown in Figure 3.4c as applied to the hologram in Figure 3.4b. A hologram is recorded every 10 seconds for the C^2HOM–S instrument and every 1-second for the C^2HOM–B instrument for the field campaigns discussed in this work. Over these timescales it is expected that for typical particle velocities that airborne particles passing through the sampling volume will only be detected in a single frame, whereas particles impacted on the windows will be present in both frames and hence will be subtracted out. In this example it is seen that much of the noisy background is removed in this way and three airborne particles in the centre of the hologram can be identified that were previously hidden in the noise. The background subtraction method is also effective in removing other sources of noise in the hologram that remain relatively constant between frames. This includes irregularly spaced bad pixels, and non-uniformly distributed sunlight on the sensor.

A limitation of the background subtraction method is that it requires the consecutive frames to be recorded with the same relative alignment between the camera and laser. This can be an issue for the C^2HOM–S instrument since the metal plate on which the camera and laser boxes are mounted can flex under significant wind or vibration conditions. Such a limitation was due to a trade-off in optimising the design for cost effectiveness and weight considerations. The C^2HOM–B instrument avoids this issue by mounting the optical components on a rail system made from carbon fibre rods, as discussed further in Section 3.5.

To resolve the issue of variations in optical alignment due to strong winds, a computational correction method was developed in this work. The pixelwise cross correlation is first calculated between temporally adjacent holograms. The mean displacement between intensity features is then computed which corresponds to the uniform shift in the positions of the particles impacted on the sampling windows due to the relative change in alignment between the camera and laser. One of the holograms is then cropped and each pixel is shifted by the mean displacement to match the adjacent hologram. The cropped hologram is then resampled to the original size using linear interpolation which causes a slight reduction in the resolution but with the advantage that it is then suitable for background subtraction with the adjacent hologram.

The issue of varying optical alignment between temporally adjacent holograms was identified during preliminary testing of the C^2HOM–S instrument on the railings of the Research Survey Vessel (RSV) Aurora Australis. The developed correction method was found to perform well, though a reduction in system resolution on the order of around 10 microns was noted. Use of the algorithm also significantly increased the data processing time. Such alignment issues were not identified in the Snowy Mountains field campaign, despite relatively large wind speeds encountered at times, and so the correction method was not used in the presented results. Due to this observation, it is interpreted that this alignment issue was likely due to vibration of the ships railings rather than flexing induced by wind motions.

3.4.2 Laser Fluctuations

The laser diode used in the holographic instruments in this work is not temperature stabilised and hence variations in the output power are observed over time. The wavelength temperature dependence of a similar laser diode was found in C17 to be around 0.1 nm $^{\circ}\mathrm{C}^{-1}$. This wavelength variation can lead to a reduction in output power as the wavelength shifts outside of the pass band of the 10 nm bandpass filter used to reduce sunlight on the camera sensor. This variation is significant enough to decrease the measured laser power by more than a factor of two, as seen in the balloon launch campaign presented in this work where temperature changes of nearly 60 °C were encountered. This causes a reduction in the signal to noise ratio since the primary noise sources encountered in the field, such as sunlight, do not vary with temperature.

Shorter-timescale intensity fluctuations also occur as energy shifts between different spatial modes of the laser. These variations represent only a small fraction of the total beam power and laboratory testing did not show a noticeable impact on reconstruction quality due to this effect. A temperature stabilisation system would reduce the impact of both of these issues, but would significantly add to the system complexity and remains the topic of future research.

3.5 C^{2}HOM–B Instrument Design

The Compact Cloud-particle HOlographic Microscope – Balloon (C^{2}HOM–B) featured a significantly different design to the C^{2}HOM – Surface (C^{2}HOM–S) instrument. The latter is based closely on the design of the instrument presented in C17, whereas the C^{2}HOM–B instrument was specifically designed to be deployed on a weather balloon. This design choice imposed significantly more stringent demands on the requirements for the instrument to be both light weight and cost effective, such that the risk of losing the instrument was mitigated. The instrument design and assembly process is briefly discussed in this section, and the results of an untethered balloon launch of this instrument into clouds are presented in Chapter 7.

3.5.1 Instrument Assembly

The core assembly of the C^{2}HOM–B instrument is shown in Figure 3.5a. The laser and pulse amplifier electronics are housed within the smaller box that is aligned with the camera sensor using carbon fibre rods. Control electronics are attached to the main aluminium plate using 3D-printed mounts. An aluminium plate with a thickness of 1 mm was chosen to provide a balance between the weight of the instrument and in maintaining optical alignment.

The system is powered using 8 AA batteries which can provide power for approximately an hour under standard sampling modes. A temperature-corrected real-time clock is used along with the Raspberry Pi computer to provide accurate timing. The pulse width and repetition frequency are controlled by an Arduino Uno microcontroller, and the system can be remotely operated and reprogrammed using a Wi-Fi interface. Further details on the electro-optical design of the instrument are described in C17.

The final version of the instrument is shown in Figure 3.5b. The larger instrument box was constructed from polystyrene panels which were attached around the aluminium mounting plate. The instrument was sealed to protect from the ingress of water and wrapped in multiple layers of aluminium sheets to block sunlight from reaching the camera sensor. The physical dimensions of the instrument are indicated on the figure, and the total weight of the instrument was around 1.5 kg. The majority of the weight came from the aluminium mounting plate and subsequent testing suggests that this could be significantly reduced in future with a smaller plate whilst still maintaining sufficient optical alignment. The instrument is attached to the payload train of a balloon using string and a fishing swivel.

The Computer Aided Design (CAD) model and assembly of the optical mounting setup is shown in Figure 3.6a. The assembly allows for the alignment of the laser diode, collimating aspheric lens, neutral density filter, bandpass filter, and camera. The optical mounts were

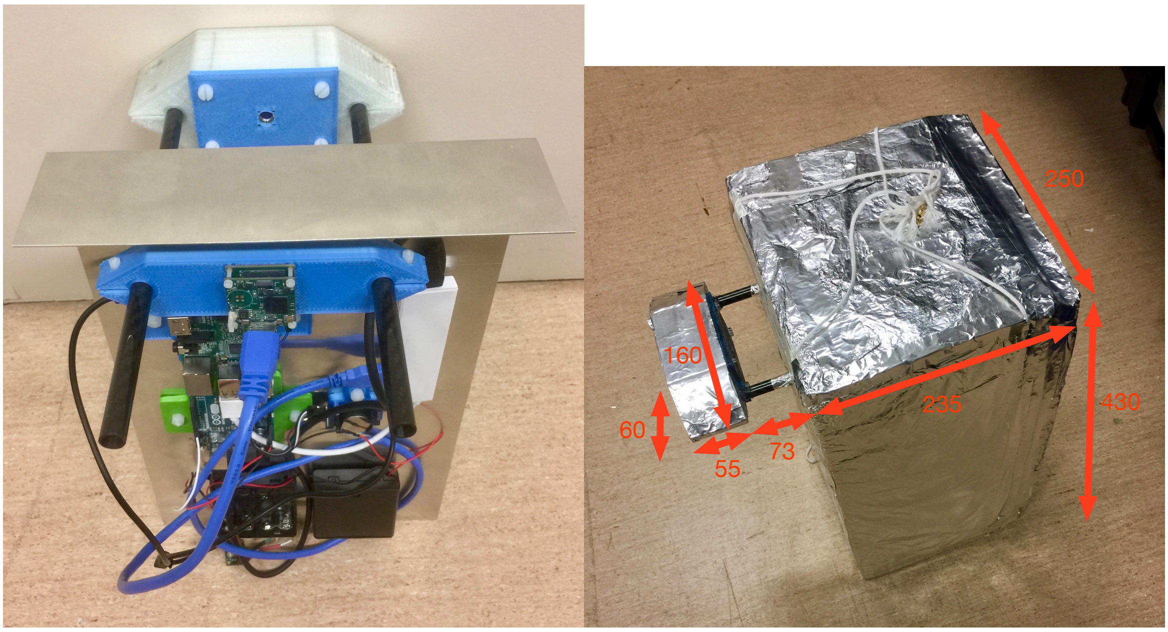

(a) (b)

Fig. 3.5 a) Core assembly of the C^{2}HOM–B instrument showing the aluminium mounting plate, control electronics, carbon fiber spacing rods, and 3D printed laser mount. b) Finalised C^{2}HOM–B payload before launch with physical measurements overlaid in units of millimetres.

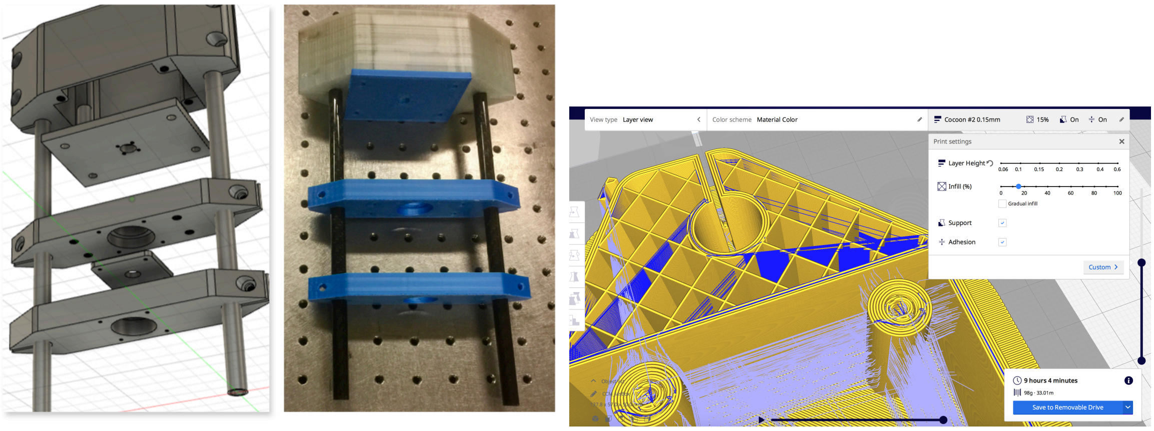
View type Layer view

Color scheme Material Color

Cocoon #2 0.15mm 15% On On

Print settings

Layer Height

Infill (%)

☐ Gradual infill

Support ☑

Adhesion ☑

9 hours 4 minutes

98g · 33.01m

(a) (b)

Fig. 3.6 a) CAD model and 3D printed optical mounts. b) Fill factor specification during 3D printing.

3D printed using polylactic acid (PLA) due to the balance between rigidity and weight. The weight was further reduced by using a hollow lattice structure within the walls of the mounts, as shown in Figure 3.6b.

3.5.2 Computational Fluid Dynamics Simulation

A key difference in the C^{2}HOM–S and C^{2}HOM–B instrument designs relates to the sampling volumes. The former instrument has the laser and camera mounted on a metal plate with a cut-out between them that allows air to pass freely into the sampling volume. The C^{2}HOM–B instrument separates these components using carbon fibre rods that can potentially interrupt the natural flow of air into the sampling volume. It is important to minimise and characterise such disturbances to the flow of air entering the sampling volume as they can result in sampling biases when determining the number density of particles. Obstructions to the air flow can also cause ice crystal shattering which is a particular problem for aircraft instruments [154].

Computational Fluid Dynamics (CFD) modelling using Autodesk CFD [236] software was carried out to address this problem for a range of instrument designs. The simulation geometry for assessing the air-flow impact of the number of carbon fibre rods used to support the optical components is summarised in Figure 3.7a. Designs with between zero and four rods were compared, in each case with the rods placed so as to avoid direct blockage of the sampling volume from the direction of travel of the balloon. A simulation with no rods was performed to determine the impact on the flow due to the rest of the instrument structure.

The disturbance to the flow for each design is visualised in Figure 3.7b with streamlines and a heatmap of the flow speed. A background flow speed of 5 ms^{-1} was chosen to simulate the typical ascent rate of a balloon. The bottom row of figures shows the variation in the flow speed within the centre of the sampling volume along the direction of travel of the balloon. Comparison between these visualisations indicates that the majority of the flow disruption arises from the instrument boxes rather than the rods, and also that the mean flow is relatively uniform under all rod configurations.

A comparison of the flow speed transects within the centre of the sampling volume along the direction of travel of the balloon for each design is compared in Figure 3.8a. The average profile for each of the rod configurations is relatively similar to the case of no rods, again suggesting that the majority of the flow disturbance arises from the box structures. The use of four rods shows significantly more perturbation to the flow speed than when using two rods, with localised speed variations of up to around 2 m s^{-1} within certain regions. The flow speed when using two rods remains relatively uniform and does not exhibit such significant variations.

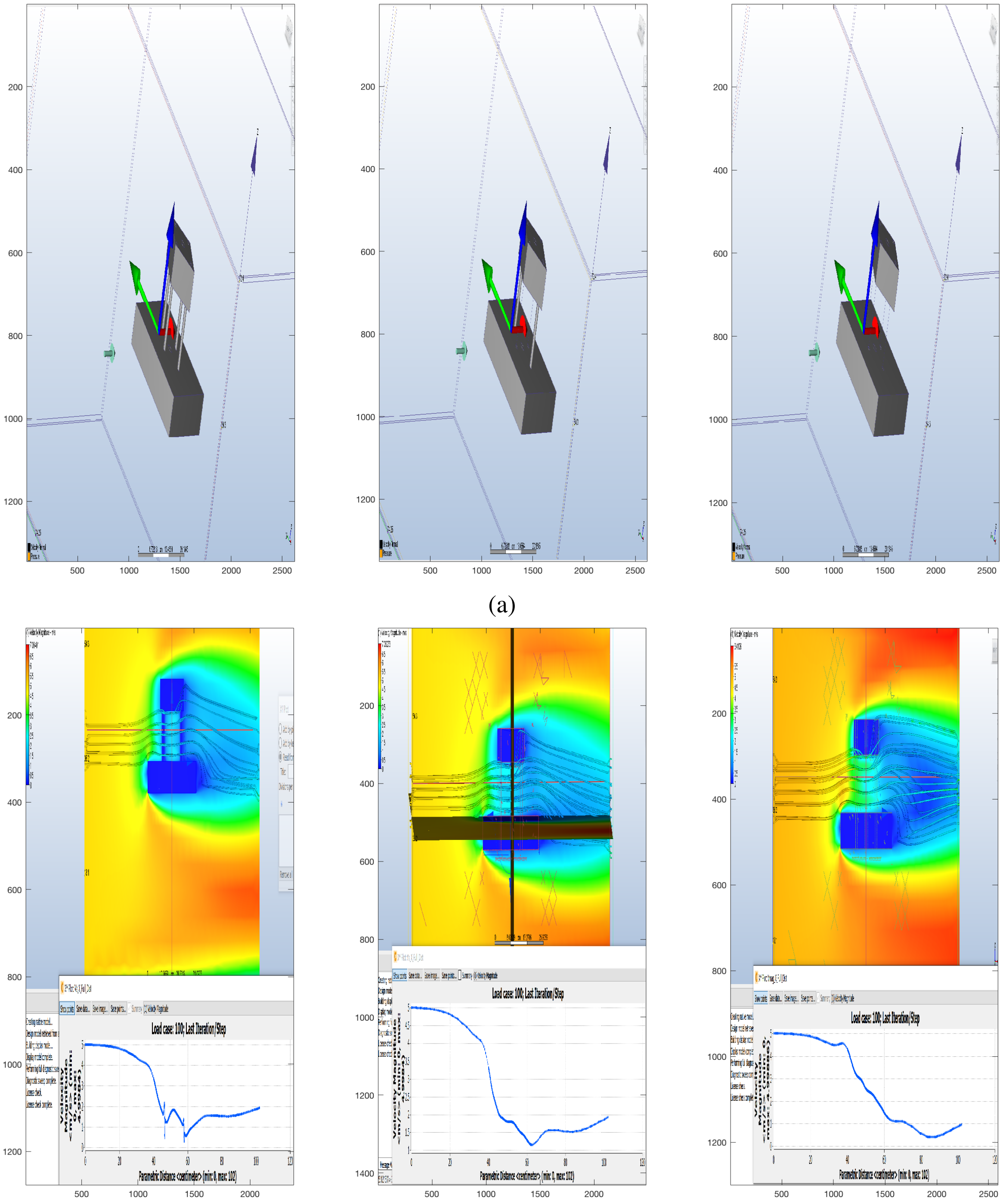

(a)

(b)

Fig. 3.7 a) Instrument configurations tested in the CFD simulation. The number of rods connecting the instrument boxes varies from zero to four. b) Flow speed heatmap indicating the flow disruption introduced by the boxes and rods.

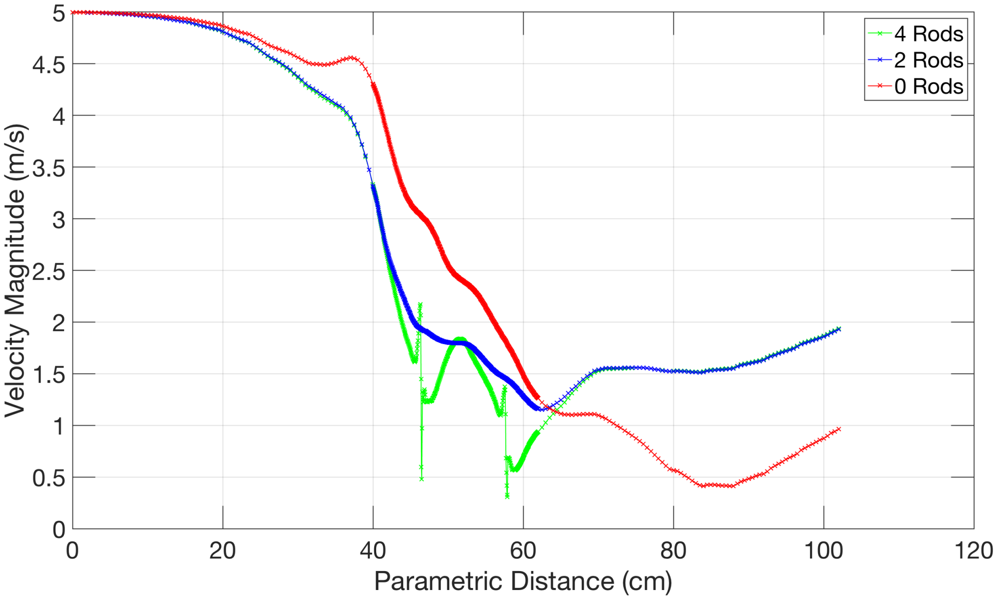

(a)

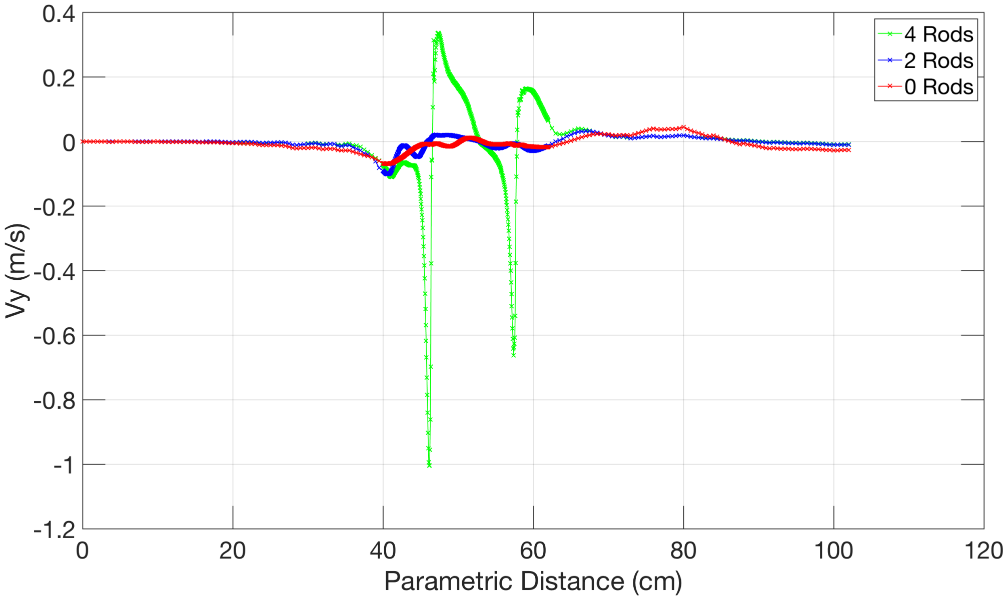

(b)

Fig. 3.8 a) Transect of the flow speed through the center of the sampling volume between the camera and laser. b) Transect of the velocity component perpendicular to the direction of travel of the balloon.

Transects of the velocity component orthogonal to the direction of travel of the balloon are plotted in Figure 3.8b. Similar localised perturbations are seen in this flow metric for the case of four rods but not when using two rods. The relatively uniform flow distribution and minimal disruptions observed in these simulations motivated the chosen design of using two rods to support the optical components. Testing in the laboratory indicated that the chosen geometry was sufficient to avoid flexing and potential misalignment of the optical system when using the combination of 3D printed PLA and carbon fibre rods. Improvements to future designs could be made by reducing the physical size of the instrument enclosures, though it was considered that the relatively uniform flow obtained with the current design was sufficient for the measurements undertaken in this work.

A larger source of potential flow disruption is expected from the balloon itself. For the balloon launch of this instrument presented in Chapter 7 the instruments were positioned approximately 9 m below the balloon in an attempt to minimise this source of disruption on the air sampled by the instruments. Due to the significantly lower relative velocities involved in a balloon launch as compared with an aircraft experiment it is assumed that this disruption will not present a significant bias in the interpretations. This assumption should be tested in future with laboratory experiments, perhaps within a wind tunnel or large cloud chamber.

3.6 Automated Holographic Analysis

Automated methods for processing holograms obtained under field conditions and extracting properties of interest, such as the particle count, size, and shape metrics, are an essential part of a functioning holographic instrument. Such methods have been developed specifically for the instruments used in this work and are summarised in this section. A comparison and optimisation of these methods is presented as compared with manually analysed data from the field campaigns presented in this thesis. A brief comparison is also provided between these methods and the widely used HoloSuite [188, 189] holographic software.

3.6.1 Algorithm Overview and Computational Requirements

The automated analysis methods developed can be separated into two main components: (i) the identification of airborne particles, and (ii) the retrieval of particle geometric and morphological parameters. These methods are computationally demanding and are currently performed after a field campaign is completed using dedicated computing resources. This has the limitation that many terabytes of raw holograms must be recorded, of which the actual information relating to airborne particles may constitute only a few megabytes. Efforts have been made to optimise these methods through vectorisation, Graphics Processing Unit (GPU) acceleration, and functional modularity. Future versions of these instruments will likely perform these operations using optimised Field-Programmable Gate Array (FPGA) units which should allow for real-time processing. This is of particular interest for the C^{2}HOM–B instrument as there is a risk that the instrument will be lost on an untethered balloon and so real-time data transmission is appealing, but such developments remain the topic of future research.

3.6.1.1 Identification of Airborne Particles

A conceptual diagram and flowchart describing the automated analysis methods are presented in Figure 3.9. Two background-subtracted holograms are first produced between the hologram of interest and the temporally adjacent holograms. This stage removes much of the fixed noise in the holograms, as discussed in Section 3.4.1, as well as particles that are impacted on the windows for each of the raw holograms. Information about airborne particles and particles on the window for just two of the raw holograms is still retained at this stage.

Each hologram is then normalised between zero and one using the extreme pixel values of each. Holograms can then be edge-padded at this stage to reduce edge effects due to the Fast Fourier Transform (FFT) based reconstruction methods, as discussed further in Section 4.5.1. The holograms are then reconstructed at 40 depths to produce two 3D amplitude images using the Angular Spectrum method, as described in the previous sections.

The mean and standard deviation of pixel values for each 3D image is next calculated. A histogram of pixel values for a typical 3D image is shown in Figure 3.10 and it is noted that this distribution is tightly distributed around the mean background value. It is at this stage that it is possible to discriminate between airborne particles and particles that have been impacted on the windows but were not present in all three of the raw holograms. An airborne particle present in the hologram of interest will appear dark when in focus in one of the 3D images and bright in the other. A window particle present in only two of the raw holograms will appear in only one of the 3D images. It is also noted that the intensity of the reconstructed object wavefront tends to be most extreme within the bounds of the focussed particle image [237, 238].

These properties motivate the next stage of the method which is to binarise each of the 3D images based on a specified number of standard deviations from the mean pixel value. The number of standard deviations is a key free parameter of this method and optimisation of this value using field observations is discussed in Section 3.6.3. Optimal values of this parameter will lead to a clear separation between background pixels and those with extreme values associated with focussed particles. At this stage there still may be pixels that attain

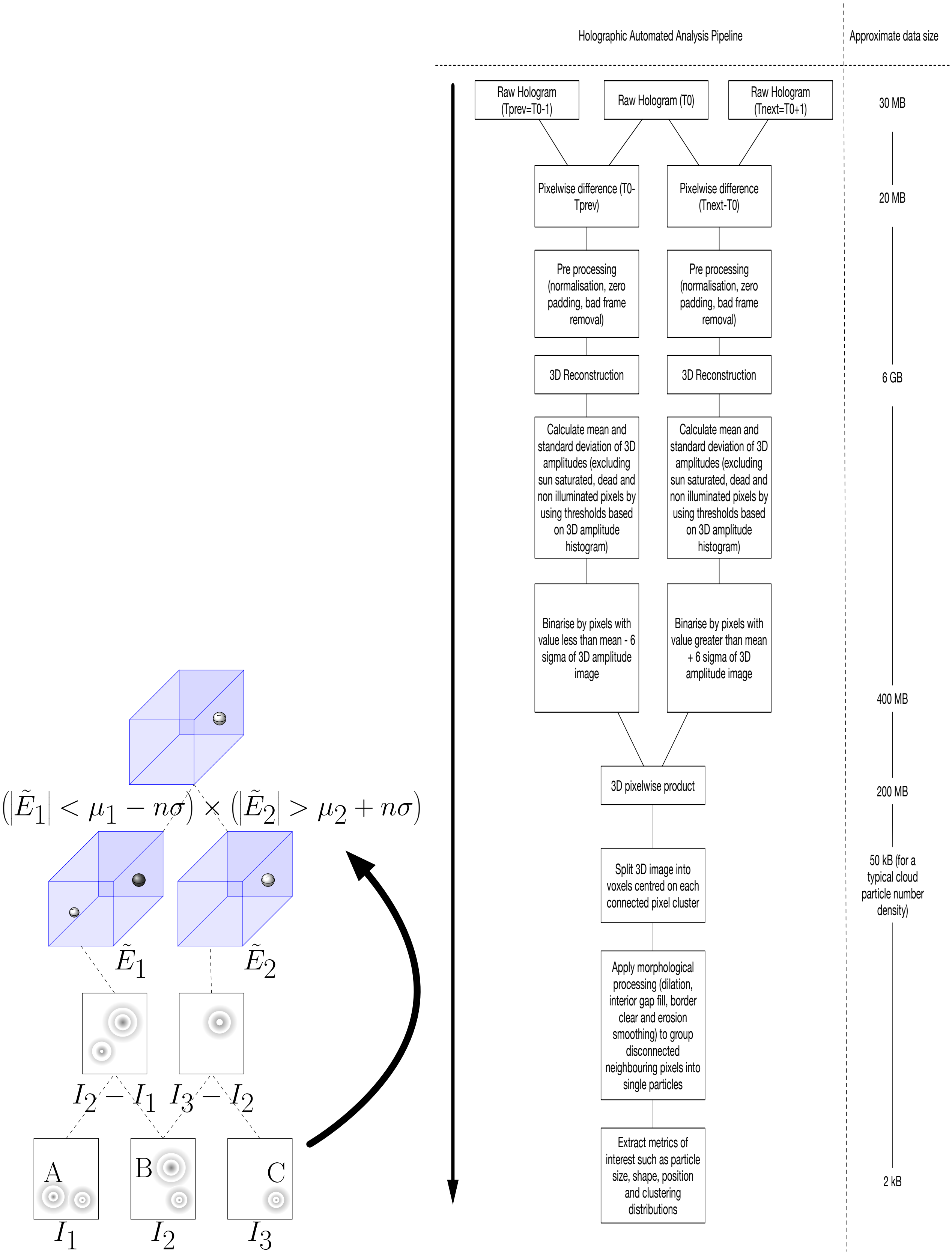

(a) (b)

Fig. 3.9 a) Visualisation of the automated analysis algorithm stages from recording of holograms to the generation of a binarised reconstructed 3D image. b) Flowchart of the automated analysis algorithm along with indicative memory requirements at each stage. Note that both diagrams describe the same algorithm, but the flow direction is reversed in the flowchart relative to the diagram in a).

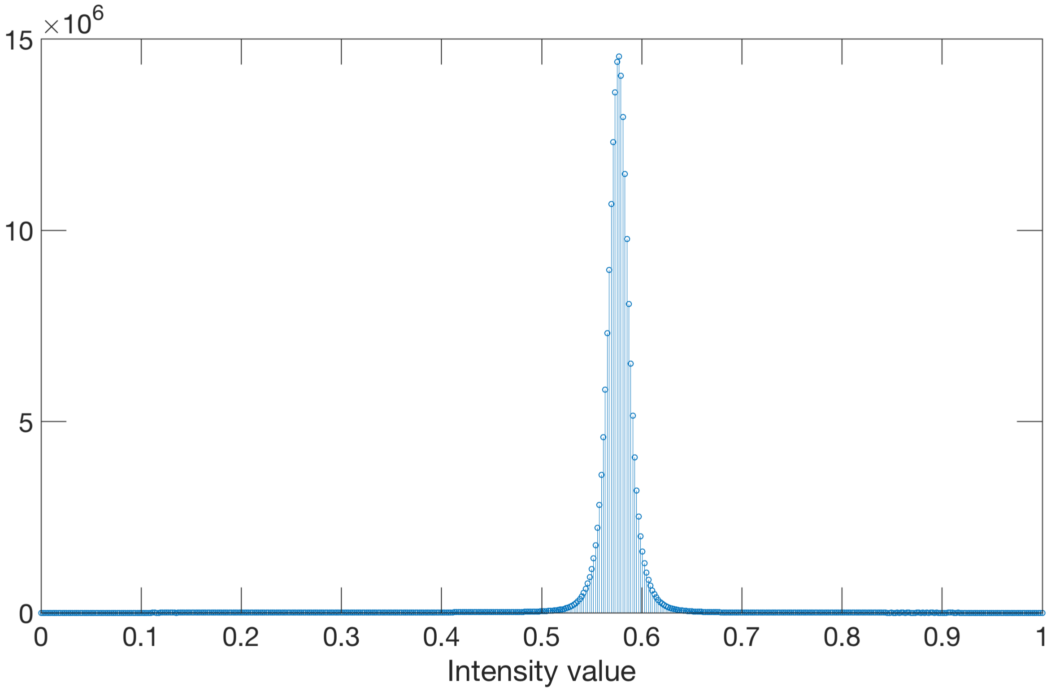

Fig. 3.10 Histogram of normalised pixel values for a typical 3D image reconstruction.

extreme values for other reasons, such as those particularly affected by sunlight. The final stage of the automated particle detection technique is to take the product of the binarised 3D images. Pixels associated with airborne particles that are present in both images are retained in this way and those associated with noise are unlikely to be present in both, and are thus rejected.

The method described above in which two 3D images are utilised will now be referred to as the DoubleNSigma method, where the N denotes the number of standard deviations used in the binarisation stage. This is in contrast to the simpler approach of just using a single 3D image, referred to as the SingleNSigma method. The performance of the two methods was directly compared using field data from the Snowy Mountains campaign, discussed further in Chapter 6. Figure 3.11a shows the number of detected particles from each method during a time for which manual analysis revealed approximately six airborne particles per minute. It is seen that the DoubleNSigma method reports counts that agree well with the manual observations, whereas the SingleNSigma method reported counts that were orders of magnitude greater than this. Inspection of the data revealed that this was due to many spurious classifications due to noise sources in the holograms.

Figure 3.11b shows the derived particle diameter from each method with a binarisation threshold of six standard deviations from the mean pixel value. Manual inspection again

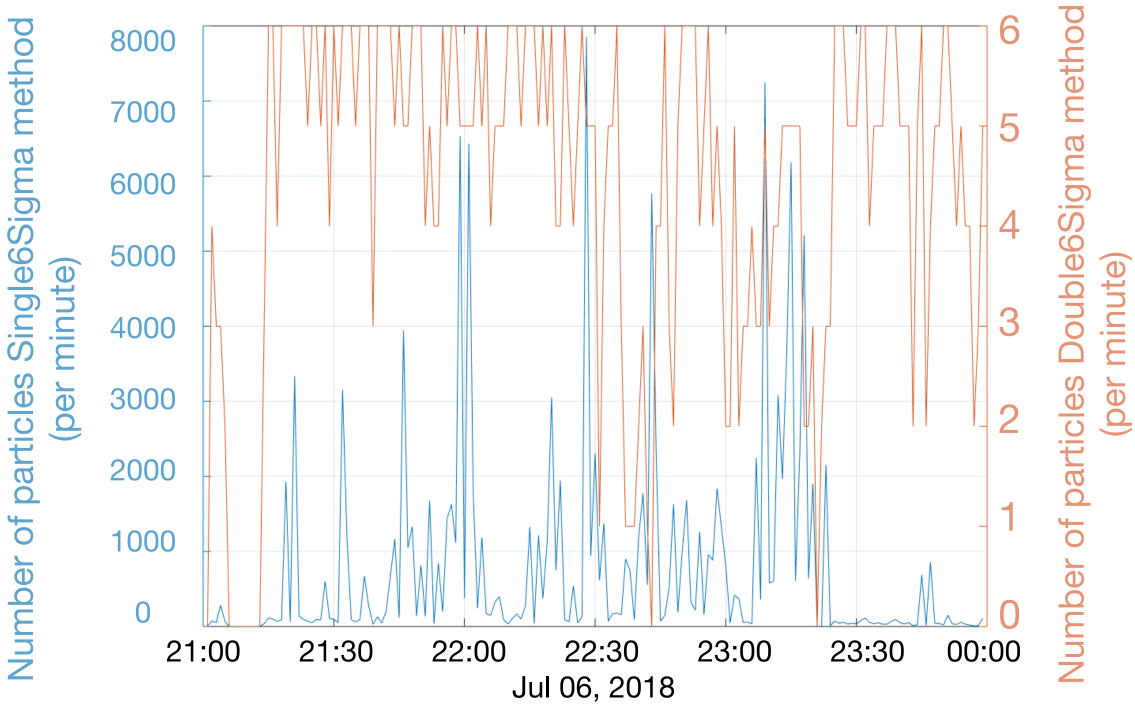

(a)

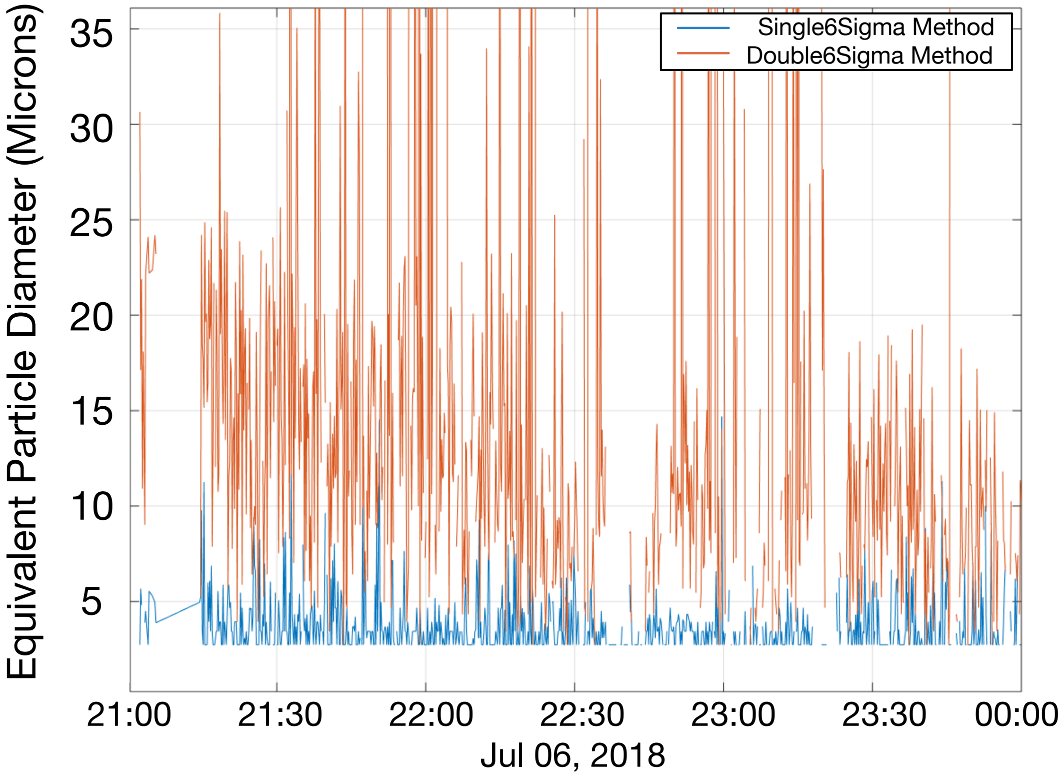

(b)

Fig. 3.11 a) Number of particle counts for single and double sigma methods. b) Particle sizes for single and double sigma methods.

indicated that the DoubleNSigma method was performing more accurately with the majority of detections from the SingleNSigma method corresponding to individual noisy pixels. A more rigorous assessment of the DoubleNSigma method compared to manual analysis is presented in Section 3.6.3.

The DoubleNSigma method was also briefly compared with the HoloSuite [188, 189] holographic software that is commonly used in this field. Reconstructions of the same holograms from both methods produced similar outputs, which is not surprising given that they both fundamentally utilise exact scalar diffraction methods. This comparison was useful as an additional sanity check that the developed software was working correctly.

A key difference between these methods is that the DoubleNSigma method presented in this work performs an adaptive intensity threshold in the binarisation stage to locate airborne particles using the product of two 3D images, whereas the HoloSuite software uses only a single 3D reconstruction per hologram, as with the SingleNSigma method. Similarly to the comparison between NSigma methods, it was found that the HoloSuite software tended to produce orders of magnitude more particle outputs that were associated with noise. Attempts were made to optimise the thresholding in these tests, though it is noted that this is only a preliminary comparison and more rigorous testing should be undertaken to better compare the algorithm performances.

It is not suggested in this preliminary comparison that this is a limitation of the HoloSuite method since the particle classification methods used in this software have been demonstrated to effectively remove much of these noise detections using neural network methods [190]. As an avenue of future research it would be interesting to incorporate the DoubleNSigma method into the HoloSuite software to assess the potential benefits offered through improved noise rejection. However, this would potentially come at the cost of rejecting real airborne particles if the sigma parameter is not optimised appropriately.

An important limitation of the DoubleNSigma method to note is that it is computationally demanding since it requires the reconstruction of two 3D images per hologram. For reconstructing a 5 MP hologram at 40 reconstruction depths, as with the instruments used in this work, this required only 6 GB of RAM per hologram. Camera sensors with significantly more pixels would quickly exceed the RAM available in standard computers, limiting the scope for applying this method. This limitation could potentially be overcome by distributing the work over a number of computers in a cluster. The issue could also be overcome by downsampling the hologram, but this would cause a corresponding decrease in resolution. Such methods may still prove useful with larger camera sensors if the improvement in noise rejection is considered to be more important than these limitations.

3.6.1.2 Retrieval of Particle Parameters

The second key stage of the automated analysis methods is the retrieval of particle geometric and morphological properties such as size, number density, and shape metrics. The airborne particles identified in the previous stage first undergo some minor preprocessing. A threshold number of pixels is defined below which particles are considered to be noise. Testing suggests that reconstructions are reliable for particles consisting of at least two pixels, which is consistent with the resolution constraints defined for the instruments in the previous sections.

Since the longitudinal resolution is significantly poorer than the transverse resolution, the 3D binarised image is then summed and rebinarised to produce a 2D projection. Internal amplitude variations within the particles are lost in this way but this approach offers significantly improved computational performance in defining particle extents. This method cannot resolve particles that are overlapping in the transverse dimension at different depths, but this is a standard issue in any holographic analysis. This issue is unlikely to occur for the relatively low number densities of typical cloud and precipitation events.

In the next analysis stage a set of morphological operators are applied to the particle images to better identify their spatial extents. A morphological dilation operation is first performed using two linear structuring elements (strel) arranged in the shape of a cross. This is used to better determine the outer boundary of the particle as there are often gaps in the binarised images due to amplitude fluctuations and noise. The strel length is a key free parameter of this method and an optimisation of this parameter is undertaken using field campaign data in Section 3.6.3. A filling operation is then performed to remove internal holes in the pixel structures within particles. The definition of strel here should not be confused with the similarly named concept of Strehl ratio that relates to optical image quality.

Particles connected to the edges of the image are next removed. This reduces the effective sampling volume of the system slightly, but presents the significant advantage that the retrieved statistics relate only to entire particles. The final processing step is to apply two consecutive erosion operations using a diamond shaped strel with a size of one pixel. This final erosion smooths the particle boundary and removes any remaining isolated pixels near to the particle.

The projected particle images are then counted and ellipses are fitted to parameterise the particle geometric and morphological properties. The key parameters used in this work are the eccentricity of the fitted ellipse and the equivalent diameter, which is defined as the diameter of a circle with the same area as the pixel region. The morphological analysis process is visualised in Figure 3.12 for a typical cloud particle measured in the field. The same in-focus amplitude image of the particle is shown in gray in each frame for reference.

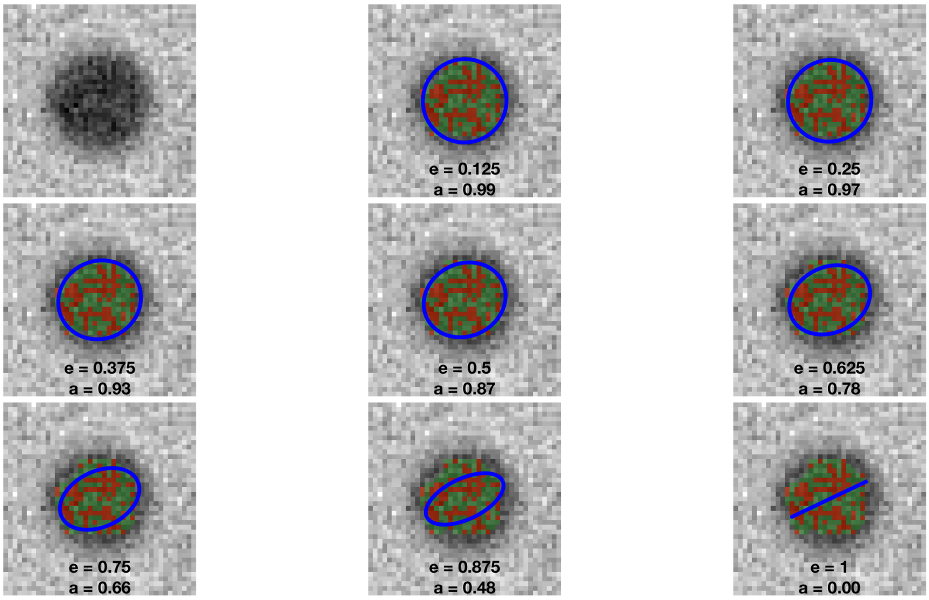

Fig. 3.12 Effect of varying eccentricity (e) of a fitted ellipse for a typical detected cloud particle. Each image shows the same in-focus particle measured in the field (gray), automatically determined particle pixels (red), morphologically processed particle extents (green) and fitted ellipses (blue). Aspect ratio (a) is also shown for reference.

The red pixels indicate those outputted from the automated airborne particle determination stage, and the green pixels are the output of the morphological processing stage. A blue ellipse is overlaid over each frame with a varying eccentricity. It is seen that the particle detection analysis stage is effective in identifying pixels within the particle extent and that the morphological processing stage is essential in identifying the particle bounds. Without the latter stage the single particle here would instead be erroneously reported as multiple smaller particles.

This example also demonstrates one of the limitations of using eccentricity as a shape metric. Visual inspection of the image suggests that this particle is relatively circular in the projected image, yet the ellipses appear to fit relatively well even with an eccentricity of up to around 0.5. For the results presented in this work this shape metric is used only as a relatively crude indication of changes in the mean shape properties rather than for specific habit classification. In practice it was concluded that eccentricities greater than around 0.7 are indicative of irregularly-shaped particles, and values below 0.5 are consistent with a spherical particle.

This metric is also overly simplistic for classifying complex ice crystal shapes which may have significant crystal structure despite being relatively symmetric. For example, a hexagonal ice crystal may be best fit by a low eccentricity ellipse despite being clearly aspherical. Attempts were made in this work to develop a more reliable shape metric. It was found that a metric based on the average of various independent shape metrics was most effective. Such properties included the eccentricity, mean edge sharpness, and geometric metrics like the circularity which are based on the particle area and perimeter. Despite the improvement in performance, it was decided that the eccentricity was preferable for the analyses presented in this work due to the more straightforward interpretation of this metric. Further development and testing of more sophisticated shape metrics is recommended as an avenue of future research.

3.6.2 Manual Analysis Tools

Observations from each of the presented field campaigns have been analysed manually and this quality-controlled dataset is one of the key contributions arising from this work. The manual analysis process is slow, so it is desirable to develop automated methods that can be relied on in future. The manual analysis methods are presented in this section and the manual datasets are then compared with the automated methods to optimise the free parameters. This dataset is also planned for use in the training of neural network-based approaches in future.

The first stage of the manual analysis software requires the user to inspect the background-subtracted holograms for airborne particle candidates. This is determined by the condition that airborne particles must not be present in temporally adjacent holograms, otherwise the particles are tagged as window particles. Holograms with airborne particle candidates are then reconstructed using 40 reconstruction depths between the sampling windows, as with the automated methods.

Particles that are not in focus at the window depths are considered to be airborne and undergo the next analysis stage. The user interface for this next stage is shown in Figure 3.13. The user can scroll through each depth in the 3D reconstruction and is prompted to draw a rectangular bounding box around each particle as shown in Figure 3.13a. The depth of focus for each particle is specified using the interface shown in Figure 3.13b, and a polygon is hand drawn around the particle extent to provide a binary particle image with use of the interface shown in Figure 3.13c. Particle size and shape properties are then retrieved by fitting of an ellipse. This process is repeated for each particle within the 3D image and each hologram from the observation times of interest.

The manually analysed observations are primarily presented in the following chapters as laboratory testing suggests that they are more reliable than the automated methods, despite the relatively good agreement between methods. A potential limitation of the manual method is that particularly small particles can be missed due to human error, and this may introduce

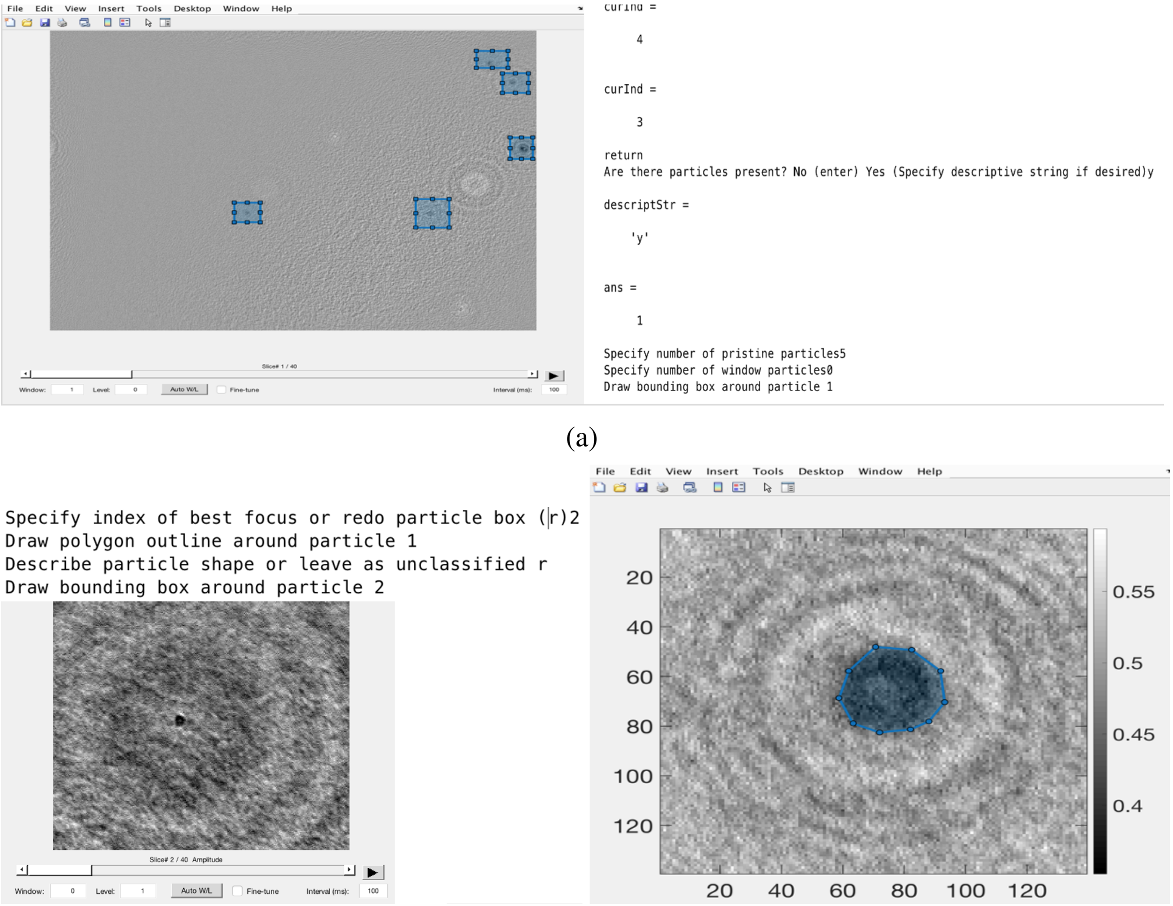

```
curInd =

     4


curInd =

     3

return
Are there particles present? No (enter) Yes (Specify descriptive string if desired)y

descriptStr =

    'y'


ans =

     1

Specify number of pristine particles5
Specify number of window particles0
Draw bounding box around particle 1
```

(a)

```
Specify index of best focus or redo particle box (r)2
Draw polygon outline around particle 1
Describe particle shape or leave as unclassified r
Draw bounding box around particle 2
```

(b) (c)

Fig. 3.13 Summary of the manual analysis interface. The user is prompted to (a) identify the locations of airborne particles using rectangular bounding boxes, as shown in blue, and then (b) identify the depths of best focus and (c) draw a polygon around each particle to precisely indicate particle extents.

a bias that tends to underestimate the true particle number densities. Significant effort went towards carefully searching for particles in each frame, though due to the time-consuming nature of this approach it is acknowledged that these potentially missed particles represent a limitation of this method.

3.6.3 Comparison to Manually Analysed Data

The performance of the automated analysis methods used in retrieving particle count, size, and shape properties represents a key limiting factor in the operation of a holographic system. The automated methods presented in this work have two key parameters that must be optimised: (i) the number of standard deviations used in binarisation of the 3D image

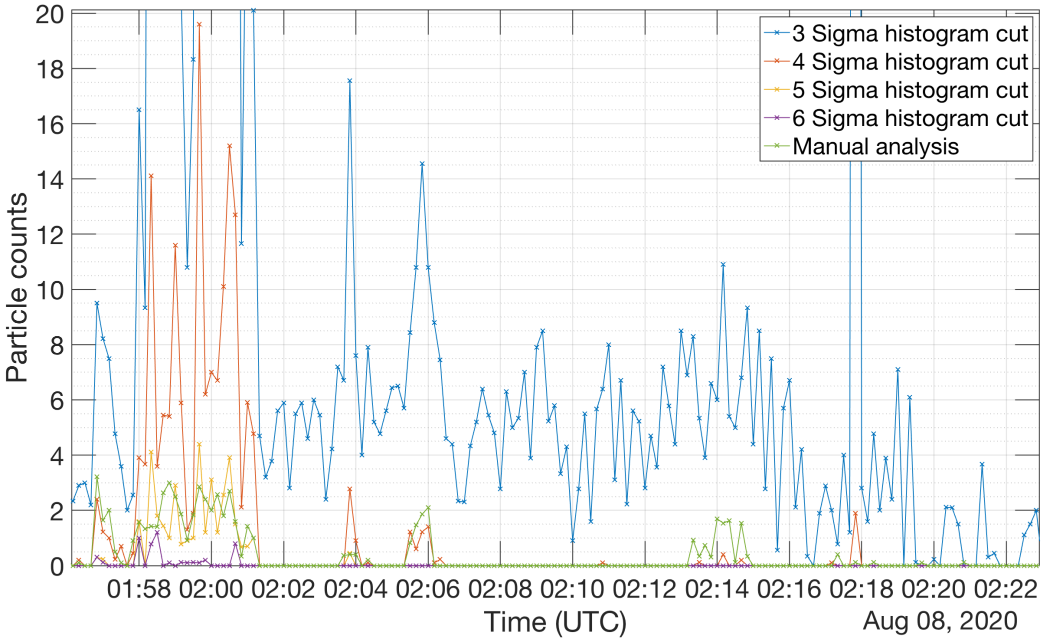

Fig. 3.14 Comparison of particle counts obtained from automated analysis runs with varying N-sigma parameter and manual analysis. Observations are from the balloon launch campaign, as discussed further in Chapter 7, and are averaged on a 10-second basis.

(N-sigma), and (ii) the number of pixels used in the linear morphological dilation structuring element (strel). These parameters are varied and the automated methods are compared with manually analysed observations in an attempt to optimise their values. Similar results were found with data from the Snowy Mountains and balloon launch field campaigns, and so only the balloon launch analysis is presented in this section. A comprehensive summary of each field campaign is presented in subsequent chapters.

Figure 3.14 provides a comparison between the manually determined particle counts during the launch and those derived from the automated analysis software. The manual counts are shown in green and the other traces indicate the effect of varying the N-sigma parameter in the automated retrievals. Each trace has been averaged on a 10-second basis. The automated counts have not yet had the morphological processing stage applied such that the N-sigma parameter can be independently optimised.

An optimal N-sigma choice provides a balance between a large enough value such that noise is not counted as a particle, yet still small enough that airborne particles are not missed. A value of three is too low since counts are reported throughout the sampling duration, whereas periods of no particle counts are seen in the manual analysis. Values of five and six are effective at rejecting noise, but this comes at the cost of sensitivity to real particles. This is particularly noticeable for particles sampled after around 2:05Z at which time none of the manually detected particles are identified. This drop in sensitivity at later times is likely due to the decreasing signal to noise ratio as a result of increasing sunlight saturation during the launch, as discussed further in Chapter 7. A value of four was determined to give the optimal balance for this parameter. Good agreement is seen in the occurrence of particle detections; however, the automated method significantly overestimates the number of particles before the morphological stage is applied.

The impact of strel length on counting error, defined relative to the manual counts, is shown in Figure 3.15a. With no morphological processing applied the 10-second averaged particle counts are significantly higher than the manually obtained values, resulting in a large counting error. A strel length of five was found to be optimal in reducing error by connecting pixels throughout the extent of the focussed particles. Using values significantly larger than five gave little improvement in counting of small particles, though a reduction in sizing error for particles larger than around 50 microns was observed when using a strel length of 100. Such a large strel length comes with the downside of a significantly reduced resolution. Multiple automated analyses with different strel lengths could be undertaken simultaneously to target both small and large particles as a future improvement to this method.

The sizing error is shown in Figure 3.15b. This parameter was found to be significantly more sensitive to strel length, though there was seemingly less size dependence. A strel length of five was found to minimise the sizing error, as with the counting error, leading to the optimised parameter choice of a strel length of five and an N-sigma value of four. This optimised combination was used in the automated analysis results presented in Chapter 6 for the Snowy Mountains campaign.

The performance of the optimised automated parameters is compared with the manual analysis in Figure 3.16a for raw particle counts. With no morphological processing applied, a relatively flat counting distribution is reported which extends significantly beyond the range of the manually analysed data. The optimised automated counts agree well with the range of manual particle counts, but the shape of the distribution is skewed towards low particle counts. The reduction in larger particle count values may be an indication that the N-sigma parameter is missing airborne particles. A more adaptive threshold that makes use of other metrics, such as edge sharpness, is recommended in future.

A comparison of the automated and manually derived size distributions is presented in Figure 3.16b. An anomalous number of particles are reported with a size of one pixel when morphological processing is not used. This is due to the clusters of disconnected pixels within a particle, as demonstrated previously in Figure 3.12. The optimised automated processing gives a size distribution that matches well with the extent of the manually obtained

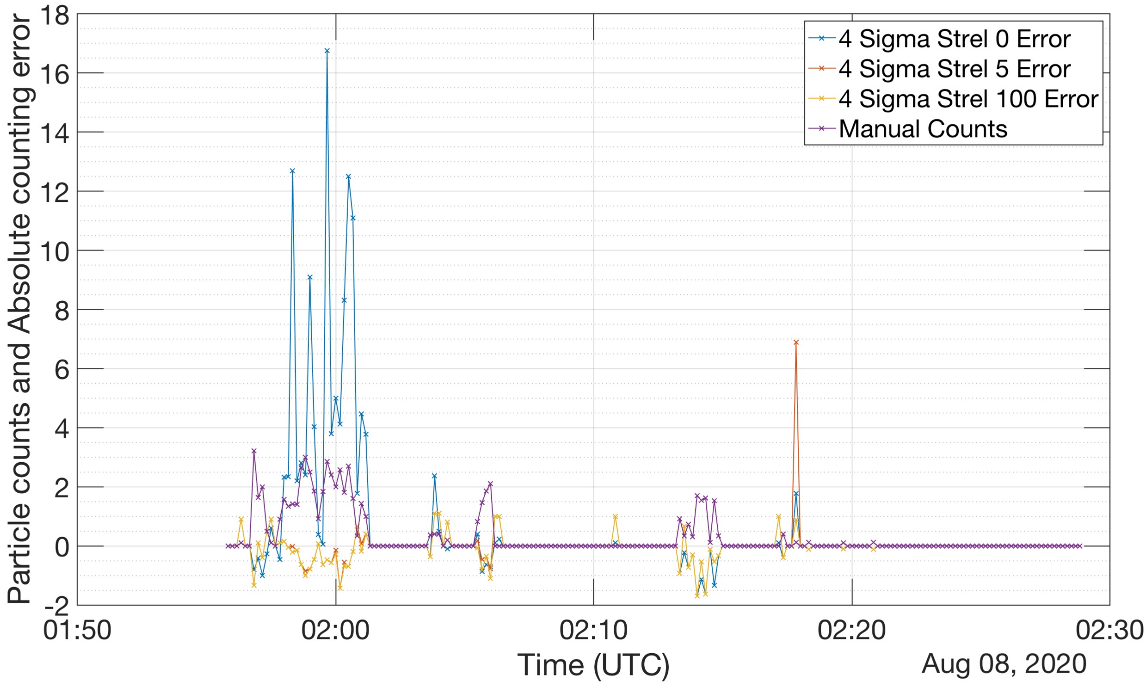

(a)

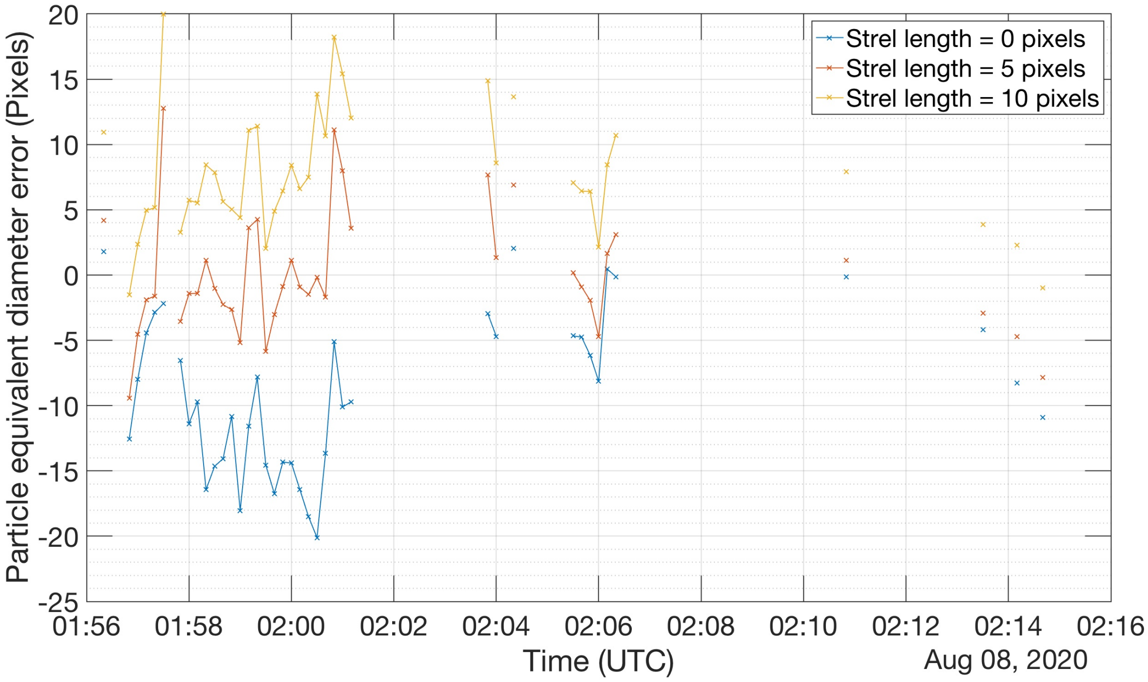

(b)

Fig. 3.15 Errors in the automatically retrieved particle counts (a) and median sizes (b) as a function of morphological structuring element (strel) length. Errors are defined relative to the results of manual analysis.

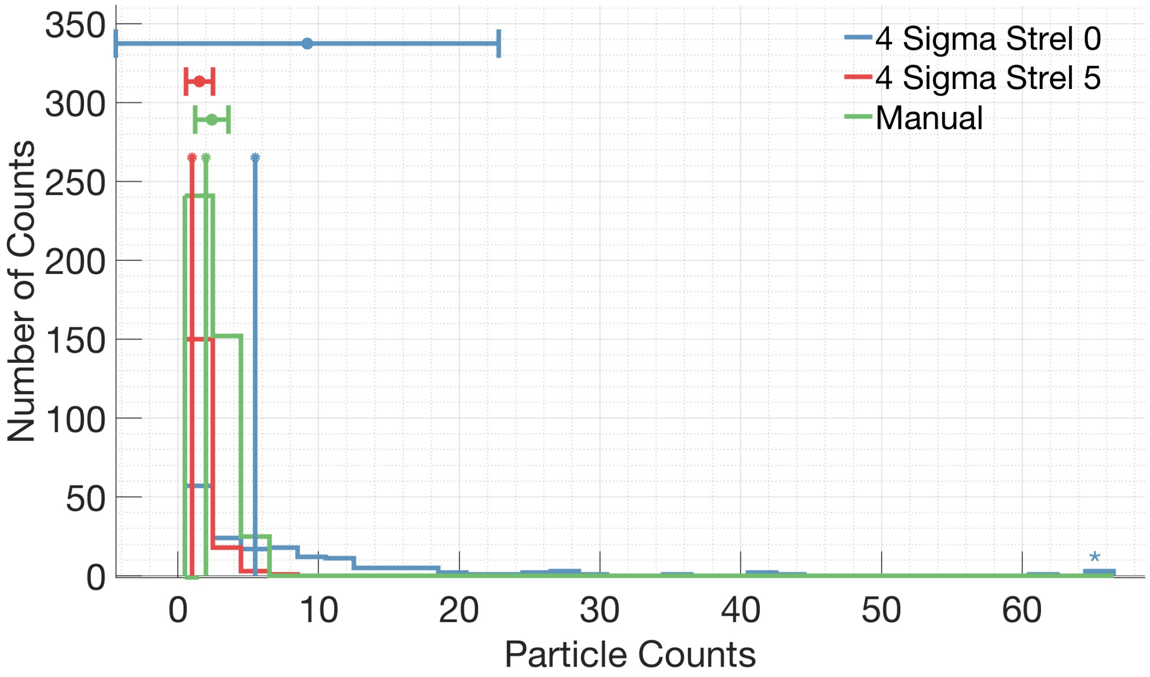

(a)

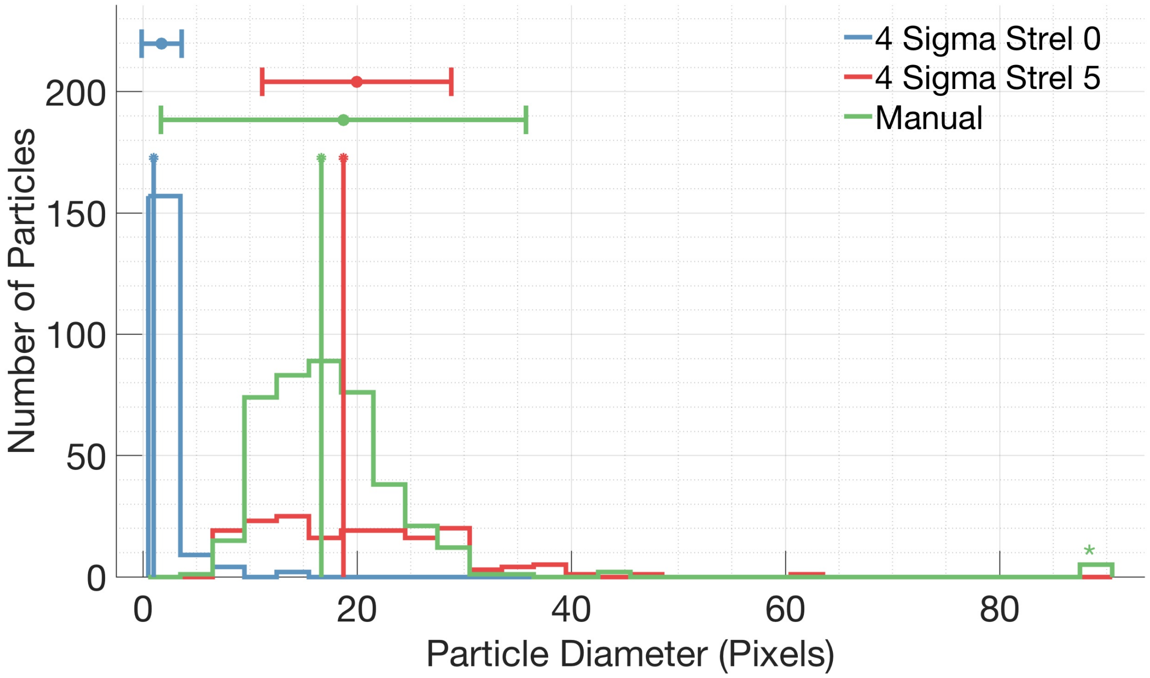

(b)

Fig. 3.16 a) Distribution of manually determined particle counts (green) compared to automated count distributions with optimal (red) and without (blue) morphological processing. Error bars indicate the mean and standard deviations of each histogram, and the stem plots indicate the median values. The star above the far-right column signifies that this column includes contributions from all data points with value larger than or equal to the bin range. The bin width for this plot is two counts. b) As in a) but for particle size distribution. The bin width in this case is three microns.

distribution. As identified with the particle count distributions, the automated size distribution underestimates the total number of particles and notably does not identify the manually-observed particles with diameters larger than 80 microns.

These comparisons highlight some of the strengths of the automated methods in reporting mean particle sizes and counts, and the limitations in accurately reporting the exact distributions of these parameters. The optimised automated methods were found to compare well with manual analysis for observations from both of the field campaigns presented in this thesis. Future analyses of this kind should be undertaken to test the performance of these methods on datasets from other field campaigns without the need for significant human intervention.

More sophisticated automated methods should also be pursued in future to overcome the limitations of the current methods, for example those that make use of the phase information, as discussed further in Chapter 4. Neural network-based methods should also be investigated as an alternative approach. The manually labelled training datasets obtained from both of the field campaigns presented in this work are expected to be a valuable resource for training and evaluating such methods.

3.7 Summary

In this chapter the practical issues and fundamental constraints that guide the design and performance of a holographic microscope are summarised. The theoretical resolution limits were derived and experimentally determined for both of the holographic instruments used in this work. Consideration of these performance constraints led to the conclusion that the holographic instruments used in this work are well suited to measuring cloud and precipitation particle size and shape properties. Particle number density measurements from these instruments were determined to be less accurate, though still sufficient for the level of analysis presented within this work. Use of a larger camera sensor to increase the sampling volume in future designs is expected to overcome this limitation whilst still maintaining the key design criteria of being light weight and cost effective.

A summary of the practical methods developed for autonomous operation of a holographic instrument under long-term field deployment was presented. A key issue with such deployments is the varying optical quality of the sampling windows. Background subtraction was determined to be the optimal solution to this problem. Methods of applying background subtraction during conditions that cause a relative flexing between the camera and laser were presented, as was required for automated analysis of observations obtained whilst the instrument was mounted to the railings of the Aurora Australis research vessel.

An overview of the design of the C^2HOM–B instrument, suited for deployment on a weather balloon, is provided in this chapter. This instrument represents the first of its kind for cloud measurements from an untethered balloon. The key design decisions regarding weight and cost are outlined. CFD simulations are summarised which suggest that the airflow within the sampling volume is not significantly disrupted by the instrument structures.

The automated methods developed to identify airborne particles and extract their geometric and morphological parameters of interest are presented. These methods are adaptive and ideally do not require significant human interaction once the free parameters have been optimised. Comparison of these methods with manual analysis of observations from both of the field campaigns presented in this thesis suggested that the algorithms can be effective in retrieving mean particle sizes and counts, but also that they tended to underestimate the total number of particles. More sophisticated algorithms, perhaps incorporating the phase information or neural network-based methods, should be pursued in future to overcome this limitation. It is expected that the manually analysed dataset produced in this work will be a valuable source of training and validation for such methods.

Preliminary comparisons with the HoloSuite holographic software suggest a potential improvement in noise rejection when using the automated methods presented in this work. Key limitations of the methods presented in this work include the previously mentioned under-counting issue as well as the significant computational burdens of the approach. Future comparisons between these methods should be undertaken in an attempt to combine the strengths of each approach.

Chapter 4

Monte Carlo Modelling of a Holographic Microscope

4.1 Introduction

The previous chapter presented some of the key limiting factors in the performance of a holographic imaging system. It was identified that analytical constraints are useful in designing such systems, but that the performance is most significantly constrained by the ability for the automated analysis methods to operate under field conditions. Such conditions vary significantly and include the optical quality of the sampling windows, fluctuations in laser outputs, varying sunlight saturation on the camera sensor, and the morphological properties of the particles being measured.

The most direct way in which the system performance can be assessed is by comparing the outputs of the automated analysis methods with manually analysed field observations. This style of comparison was presented in the previous chapter and arguably gives the most relevant performance metrics since it is based on real field data. A key limitation of this method is the accuracy of the manual analysis methods, which are susceptible to human error. This evaluation method is also slow which further limits the applicability.

An alternative method for assessing the performance of a holographic system is through numerical modelling techniques. The Monte-carlo Holographic Imager SimulaTion (MHIST) software was developed in this project to provide this capability and is presented in this chapter. This software allows full specification of holographic system parameters, as well as particle morphological properties, from which synthetic holograms can be generated. Monte Carlo methods are used to generate large datasets in this way to which automated analysis methods can be applied and tested.

The chapter begins with an assessment of the performance of various methods for automatically determining the longitudinal position, referred to hereafter as the depth, of a particle in a reconstructed 3D image using the MHIST software. An alternative method to that presented in the previous chapter for automated particle analysis is then assessed with this tool. It is also used to highlight some of the holographic microscope performance limitations that are difficult to constrain analytically, such as the edge artefacts in the reconstruction process. The chapter concludes with a brief discussion of the potential for this model to be used in the in situ retrieval of high-resolution particle surface roughness and refractive index information.

4.2 Holographic Monte Carlo Model Overview

The Monte-carlo Holographic Imager SimulaTion (MHIST) software consists of three main model aspects that can be specified by the user: (i) the hardware parameters of the holographic microscope, (ii) the cloud particle properties, and (iii) the internal model parameters, such as the choice of wavefront propagation method used for the simulation of holograms. These key aspects of the MHIST software are visualised in Figure 4.1 with the yellow planes indicating the locations of the laser, sampling windows, scattering particles, and camera sensor. The outputs of the software are synthetic holograms along with the simulated particle properties, as required for the testing and validation of automated analysis methods.

The wavefront simulation and propagation is carried out using scalar diffraction theory, as outlined in Appendix A. The laser wavelength, transverse noise profile, and complex transverse wavefront profile are specified and the wavefront is propagated between interaction planes using either the Angular Spectrum, Fresnel, or Rayleigh-Sommerfield diffraction formulae. A combination of these methods can be used to ensure that the Nyquist sampling limits are maintained, as discussed in Appendix A.2.

The surfaces of the instrument sampling windows are approximated as 2D apertures with a complex transmittance mask. This allows for the parameterisation of the optical quality of the windows to simulate effects such as the build-up of dirt during a long-term field deployment. The refractive index and thickness of the windows can also be specified to investigate the potential for aberration and magnification introduced by the optical components.

Scattering particles are also defined using complex 2D transmittance masks. Particle properties can either be manually specified, or distributed randomly between a user-specified range of particle size, shape, number, orientation, and position values. Particle shapes can be manually specified using hand-drawn polygons, or simpler structures can be parametrically

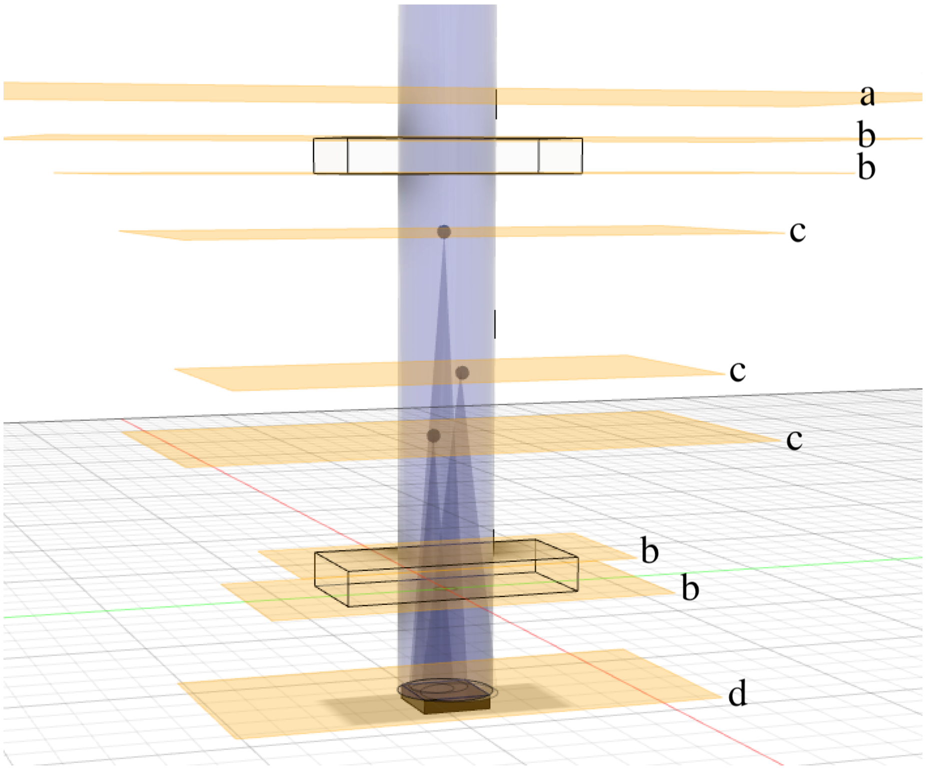

Fig. 4.1 Visualisation of the MHIST simulation geometry. Yellow planes indicate the locations of the: (a) laser source, (b) sampling window surfaces, (c) scattering particles, and (d) camera sensor.

defined which include circles, hexagons, and rectangles to approximate simple cloud droplets and ice crystals.

The hologram is simulated by propagating the wavefront from the last interaction surface to the depth of the simulated camera sensor. The intensity at this depth is then sampled using a grid with the physical dimensions, bit depth, and pixel size of the camera sensor. Additional noise sources can be specified at this stage. This includes saturated pixels to simulate dead pixels and sunlight effects, and more generalised noise models such as Gaussian white noise.

The developed software has been tested against laboratory measurements using a range of calibration objects. Targets were placed at known positions and a hologram was recorded. A synthetic hologram of the same targets was then generated by hand-drawing polygons with the same sizes, shapes, and positions as the calibration objects. Comparison of the holograms and reconstructed 3D images indicated that the synthetic holograms were sufficiently accurate such that the particle properties retrieved from the simulation agreed with the measured values to within the experimental uncertainties outlined in Chapter 3.

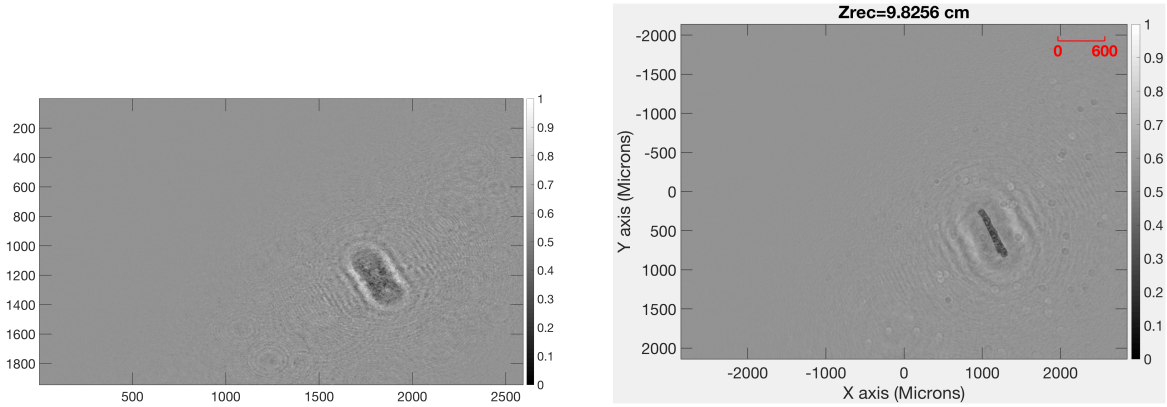

(a) Measured Hologram (b) Measured Focus

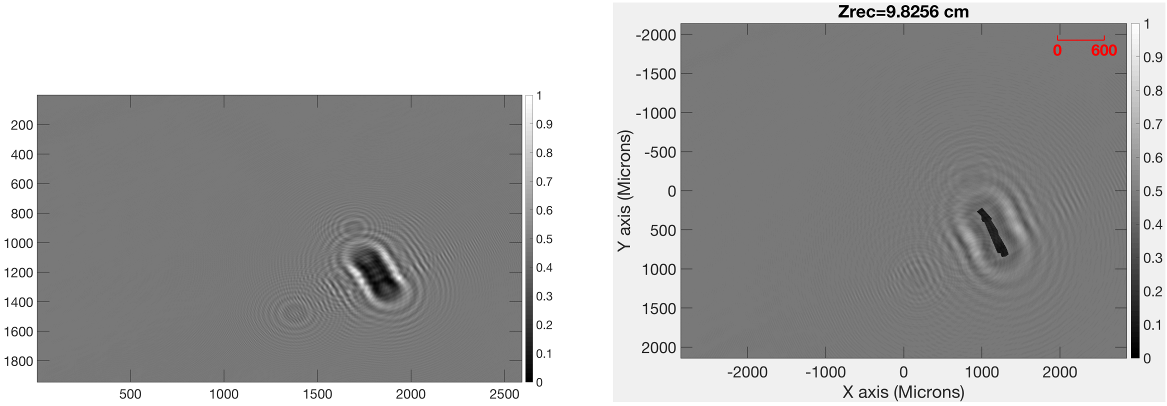

(c) Simulated Hologram (d) Simulated Focus

Fig. 4.2 Comparison of recorded and simulated holograms and focussed particle reconstructions.

The accuracy of the software is demonstrated in Figure 4.2 through a comparison with field observations. A hologram recorded during the Snowy Mountains field campaign is shown in Figure 4.2a and a reconstructed image of a column-like particle is seen in Figure 4.2b. This reconstruction was used to determine the shapes of particles present which then allowed a synthetic hologram to be generated based on hand-drawn polygons of the outlines of some of the focussed particles. The resultant synthetic hologram is shown in Figure 4.2c and the reconstructed column-like particle is seen in Figure 4.2d. Good agreement was again seen between the recorded and synthetic holograms and in the retrieval of particle properties, providing further confidence in the simulation outputs.

The MHIST software is still in a relatively early stage of development and so only limited testing of the model accuracy has been undertaken so far. It is recommended that a more comprehensive range of tests be carried out and for the model accuracy to be quantified as a function of particle size, and shape, using a statistically significant number of calibration objects. One potential line of investigation would be to test the performance of each of the diffraction methods to determine their exact range of applicability and to identify the specific impacts of under-sampling of the propagation functions.

The software is modular and readily extendible such that more sophisticated simulations can be undertaken in future. Efforts have been made to optimise the software through approaches such as vectorisation and processing of images using a Graphics Processing Unit (GPU) to reduce processing times. Recommended future enhancements include the use of higher-resolution regions around particles to better capture internal structure, allowance for specification of non-monochromatic light sources in considering beam coherence impacts, and incorporation of the effects of motion blur by overlaying holograms from particles moving at a specified velocity within the camera exposure duration.

Preliminary efforts have also been made towards a GPU-accelerated N-body simulation of cloud particles interacting under electrostatic and turbulent forces. Coalescence is parameterised crudely based on the particle proximity and a probabilistic interaction term. It would be of particular interest to incorporate this model into the MHIST software for generating more realistic spatial distributions of cloud particles that can evolve with time. Such a model may allow direct retrieval of properties such as micro-scale turbulence through comparison between modelled particle distributions and the spatial distributions measured within a holographic 3D image. It is expected, for example, that cloud particles would cluster around regions of lower vorticity [89] and such clustering can be directly measured by holographic instruments [57].

4.3 Particle Focus Depth Metrics

One of the key applications of the MHIST software is in assessing the performance of automated analysis methods. An important component of such methods is the approach used to determine the depth within the reconstructed 3D image, as defined in Section 3.2, at which particles are at their best focus. The focus determination methods tested in this section depend on the property of reconstructed holographic images to attain extreme amplitude and phase values at the depth of best focus for a given object [237, 238]. The rates of change of these properties as a function of depth in the 3D reconstruction were also found during the testing to be effective and independent focus determination metrics. Particles simulated in the following tests are approximated as opaque 2D diffracting apertures.

An example of these focus depth determination metrics is shown in Figure 4.3 which can be assessed based on their ability to separate particles from the background. Each panel shows the pixelwise minima as a function of depth for a given metric which has been

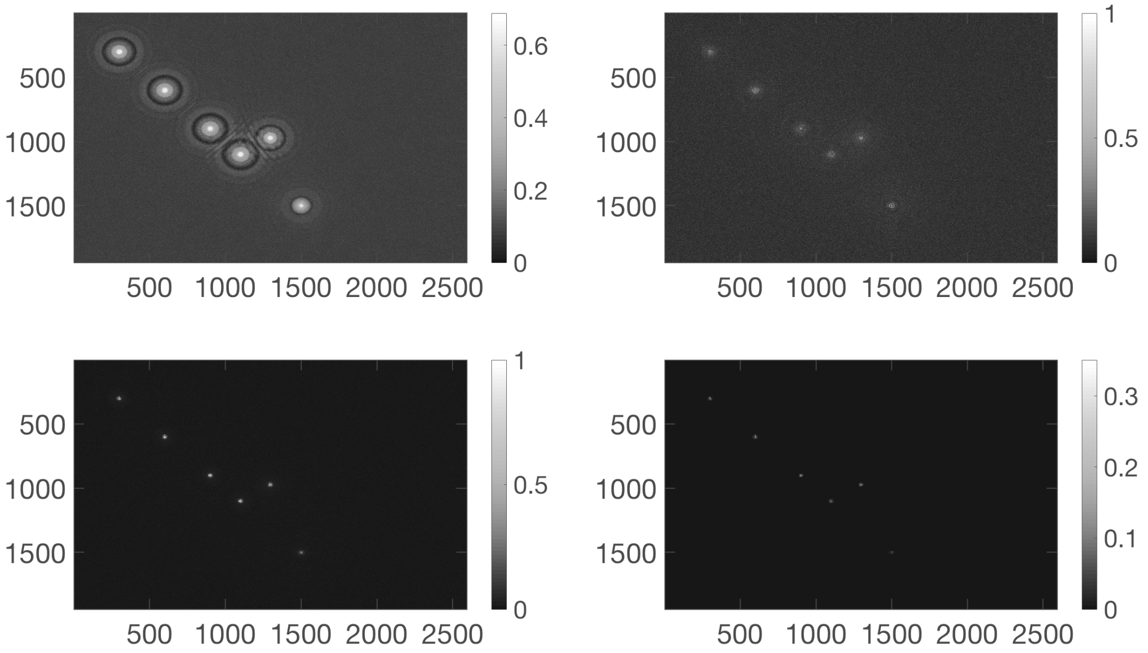

Fig. 4.3 Four different metrics for determining the depths of 6 circular particles, each with a diameter of 20 microns, within a 3D reconstructed image. Counter-clockwise from the top right panel shows 2D maps of the pixelwise minima with depth of the: Longitudinal amplitude gradient, amplitude, and longitudinal phase gradient. The product of all listed metrics is shown in the bottom right panel.

normalised between zero and one. Each metric is effective at distinguishing the six particles from the background pixels, though there is significant variation in the number of pixels that are associated with the particles. The longitudinal phase gradient minima is seen to give the best separation from the background pixels, though only with relatively few pixels within the centre of the particle extent. The amplitude minima covers more of the particle extent but has relatively large values for the diffraction fringes surrounding the particle which complicates the interpretation. The product of each of these metrics is seen to give good contrast between particles and background values, though this is only for a small number of pixels in the centre of the particles. The product method incorporates information from each of the three independent metrics and was found to be the most robust depth metric throughout the testing.

A more detailed comparison of these metrics is shown in Figure 4.4a in which ten circular particles, each with a diameter of 20 microns, are positioned randomly throughout the 3D sampling volume of a holographic instrument with the same specifications as those used in this work. The longitudinal profiles of each metric for the central pixel in each particle show extreme values around the particle focus depths. The phase difference is seen to give the best

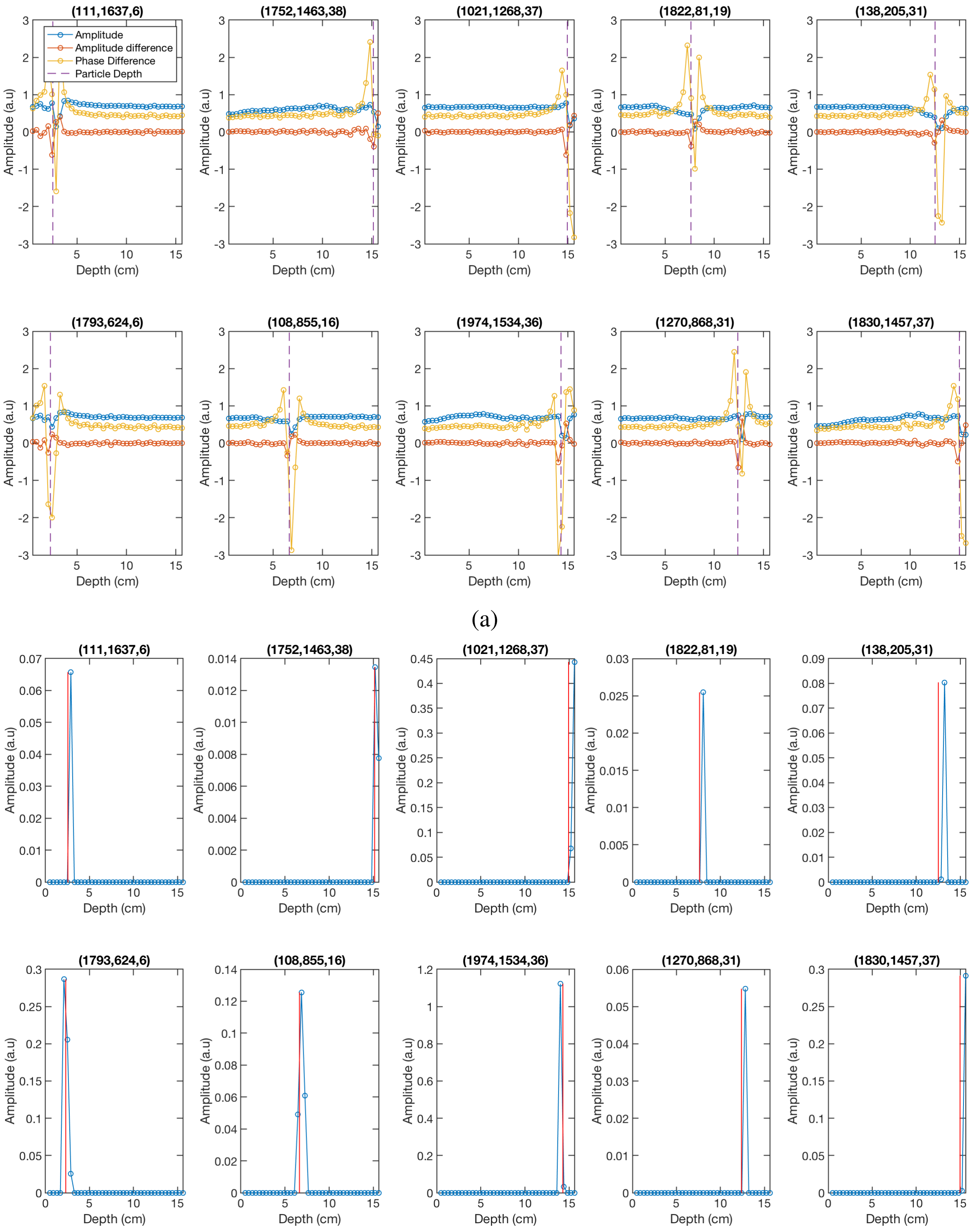

(a)

(b)

Fig. 4.4 a) Comparison of particle depth metrics for ten circular particles, each with a diameter of 20 microns. Each panel shows the longitudinal dependence of depth metrics for the central pixel of each particle. 3D pixel indices of each particle are indicated on the top of each panel and the particle depth is indicated by a purple dashed line. b) Longitudinal dependence of the product of the normalised metrics shown in Figure a) for each particle. Particle depth is indicated by the solid red line.

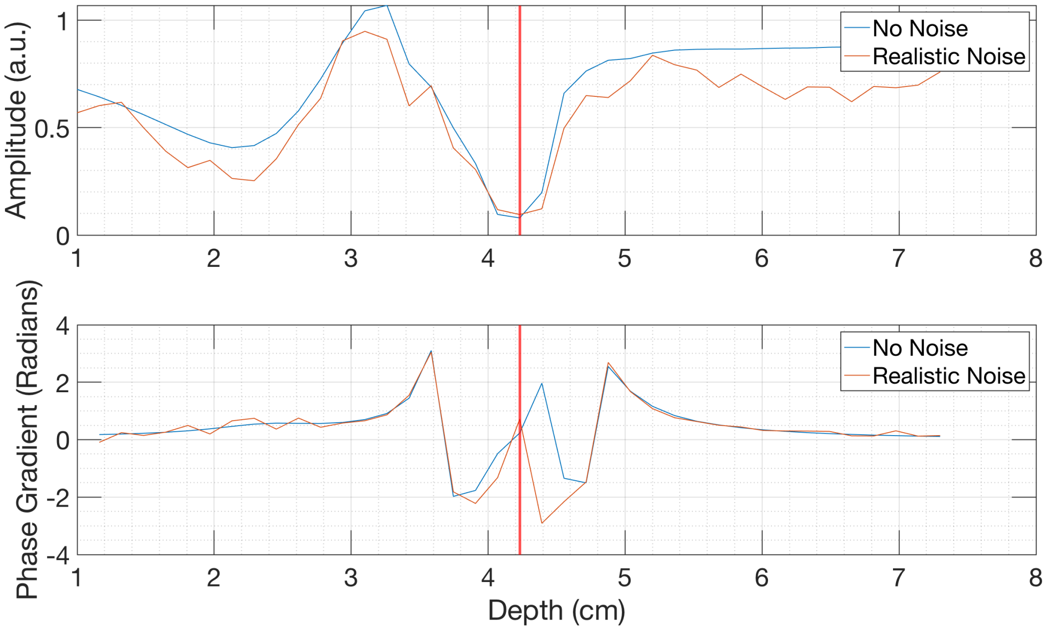

Fig. 4.5 Longitudinal amplitude (top) and phase gradient (bottom) profiles centred on a 160 micron particle for a case with no noise (blue) and Gaussian white noise (red) applied in the simulation.

contrast relative to the background values, though the minima of the amplitude traces tend to be closer to the true particle depths. The product of these normalised metrics was again found to be the most robust method for determining particle depth, as indicated in Figure 4.4b.

The performance of the product method is most limited by the inclusion of the longitudinal phase difference. This metric is especially sensitive to noise in the hologram which leads to significant variability in the phase gradient profile within the transverse extent of the particle. Profiles of the amplitude and phase gradient metrics are plotted in Figure 4.5 for a case with no noise and a case with Gaussian white noise applied that approximates values measured in the laboratory for the holographic systems used in this work.

The inclusion of this amount of noise did not significantly impact the interpretation of the amplitude profile in this case and the contrast in the phase gradient profile around the focus depth remained reasonably large. This suggests that such an approach is potentially viable in practice. Preliminary testing of this method on holograms recorded during the Snowy Mountains field campaign also indicated that the technique can be effective under a range of conditions, but it was found to be unreliable when applied to holograms taken with a large build-up of dirt on the sampling windows and sunlight saturation. A rigorous evaluation of this method using field observations remains the topic of future work.

Whilst small particles are observed to have a singular extrema at the particle focus depth in their longitudinal profiles of amplitude and phase metrics, this is not always the case for larger particles. The secondary minima at a depth of around 2 cm in the amplitude profile for the 160 micron particle shown in Figure 4.5 is an example of this complicating factor. The variability in the phase gradient profile within the transverse extent of this particle is a further complicating issue. For the instruments used in this work, such issues were found to became significant for circular particles larger than around 100 microns in diameter.

Various methods have been proposed in the literature to overcome the challenges for automated depth determination of larger particles [188, 239, 240]. The approach used in the widely used HoloSuite [188, 189] software, for example, has been shown to be particularly effective and is based on an edge sharpness metric that is resilient to noise. An evaluation and comparison of these automated methods using the MHIST software is recommended as an avenue for future research.

4.4 Automated Analysis Testing

The primary motivation for development of the MHIST software is for the testing of automated analysis algorithms using large synthetic datasets. An automated analysis method, referred to as the DoubleNSigma method, was presented in Chapter 3 that was based on 3D amplitude metrics. This approach was chosen as it was found to perform well under the noise conditions encountered during the field deployments discussed in this work.

It was demonstrated in the previous section that inclusion of phase information can improve automated identification of particles under certain noise conditions. A preliminary evaluation of an automated analysis method that incorporates phase information, hereafter referred to as the Complex LOngitudinal Gradient (CLOG) method, is presented in this section using the MHIST software. These results are primarily included as a demonstration of the utility of the MHIST software, though insights obtained from this approach regarding the algorithm performance are also of relevance to this work.

4.4.1 Algorithm Overview

The first stage of the CLOG method is to automatically identify particles and determine their longitudinal positions within the instrument sampling volume. A single 3D image is reconstructed from a background-subtracted hologram and the pixelwise minima with depth is calculated for the longitudinal profiles of amplitude, longitudinal amplitude gradient, and longitudinal phase gradient. The 2D grids of these parameters are normalised between zero and one and the product of these grids is obtained. This product of three independent metrics was found to give robust contrast between pixels associated with particles and those for background or noise values. Otsu's method [241] is applied to the grid of multiplied values to automatically determine the threshold between background and particles and this threshold is used to binarise the 2D grid.

A standard set of morphological processing operations are next performed on the binarised 2D grid to improve the identification of particles. This includes rejection of pixel clusters below a threshold size, filling of gaps within structures, and removal of particles on the edges of the hologram. Each remaining cluster of pixels in the binarised grid is considered to be a particle and bounding boxes are recorded as an approximate indication of the particle extents.

Particles are individually processed to determine the focus depths using each of the bounding boxes. When the pixelwise minima of the amplitude, longitudinal amplitude gradient, and longitudinal phase gradient profiles are computed, corresponding maps of the depths of these minima are also recorded. The most common minima depth value within each particle extent is determined for each depth metric and the median of the three values is taken to be the best estimate of the particle depth position.

A Canny edge detection filter [242] is applied to each of the particle amplitude reconstructions at their corresponding depths of focus. This takes advantage of the sharp edge between the focussed particles and the background pixels. A morphological filling operation is applied to remove internal pixel gaps in the particles and ellipses are fitted to each particle to extract their size and shape metrics.

4.4.2 Simulation Results

The performance of the CLOG method was assessed using MHIST simulations of holograms from randomised distributions of particles and a holographic microscope with the same parameters as those described in Chapter 3. This simulation process is summarised in Figure 4.6 for a case consisting of randomly distributed particles with circular, hexagonal, and rectangular shapes and a fixed size. Particle outlines are shown in Figure 4.6a and the simulated hologram is seen in Figure 4.6b.

The automatically identified particle extents obtained from the CLOG method are shown in Figure 4.6c. Comparison with Figure 4.6a indicates that none of the particles were missed in this case, nor were there any incorrect classifications of noise as particles. The retrieved particle sizes are also within the theoretical uncertainty bounds for the majority of particles, regardless of shape or orientation.

Despite the generally good performance of the algorithm in this case, a number of issues are still noted. The two overlapping rectangular particles at different depths that

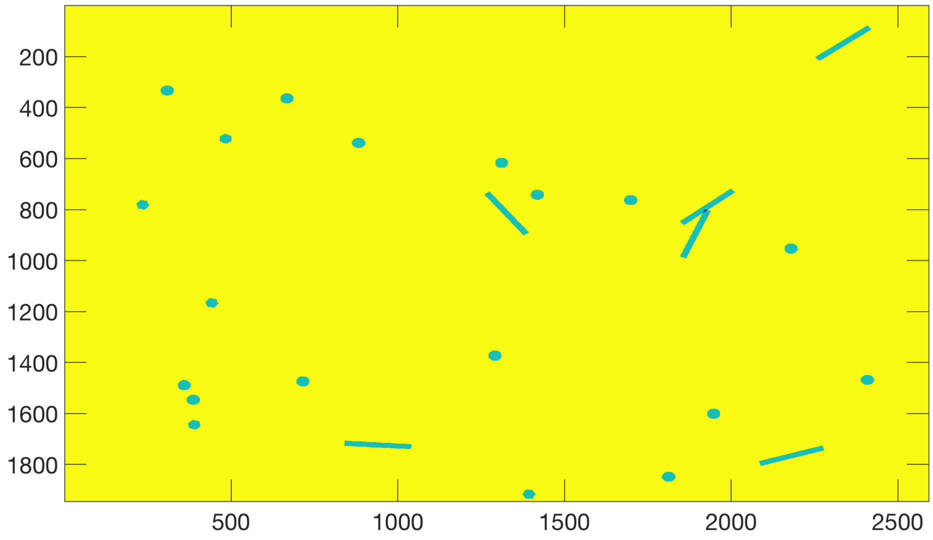

(a) Simulated particle positions

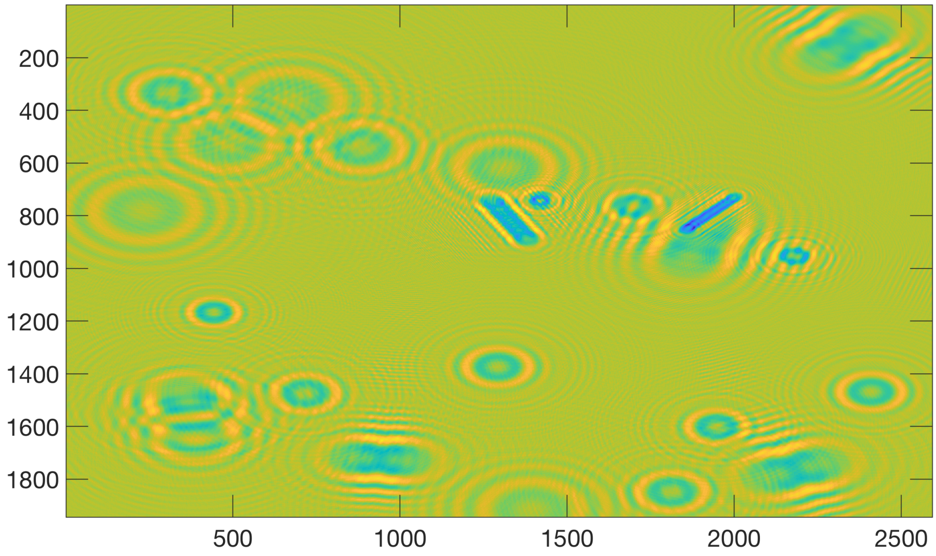

(b) Simulated hologram

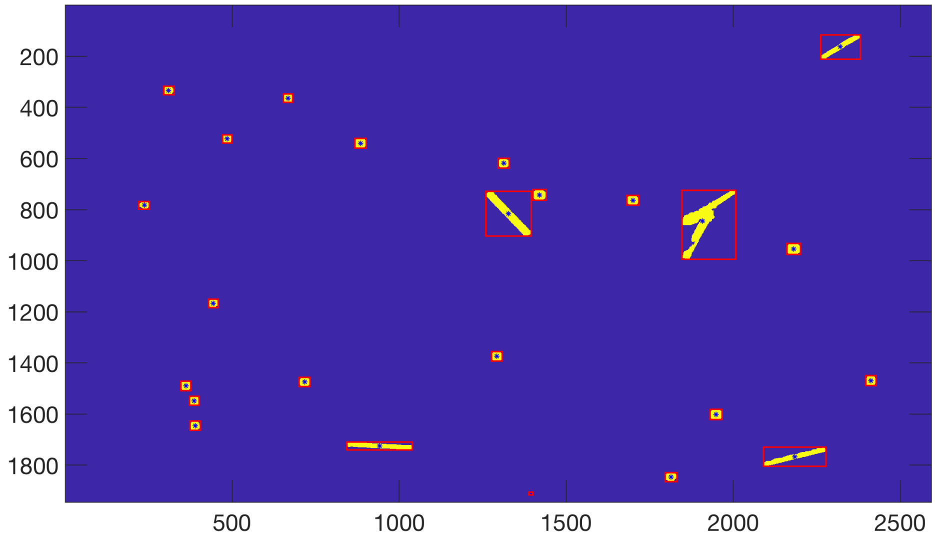

(c) Automatically identified particles

Fig. 4.6 Summary of the a) particle placement, b) hologram simulation, and c) automated detection processes for testing of the CLOG algorithm.

are seen on the right-hand side of Figure 4.6a were identified as a single large particle. The outlines of these particles are also significantly more distorted than those of the single rectangles. The current algorithm acts to group overlapping particles together and a focus depth corresponding to the average of each of the particles is found, resulting in a particle measurement from an out-of-focus reconstruction. This issue could be avoided in future by checking for multiple peaks in the distribution of particle depths within a particle cluster.

The algorithm was found to underestimate the sizes of particles towards the edge of the hologram, despite multiple interference fringes still being recorded. This motivates the approach of excluding particles within a specified number of pixels from the edge of the hologram. This comes at the cost of a reduced sampling volume and so a future optimisation of this value would be useful. This could be based on the minimum number of interference fringes required for a targeted particle size resolution and particle shape sensitivity, as determined using the MHIST software. It may also be possible to use this software to determine a numerical correction such that particles on the edge of the hologram can still be retained under certain conditions.

A more quantitative assessment of the CLOG method is presented in Figure 4.7 which shows the results of three sets of simulations with differing particle distributions. A comparison is made between the absolute and relative errors in retrieved particle counts and median sizes for each case. Particle counts, positions, sizes, and shapes are varied randomly between ranges that are defined for each simulation set and 1000 simulations runs are used in each case.

Figure 4.7a shows the relative errors in retrieved particle count for distributions of between 1 and 50 particles with a fixed equivalent size of 80 microns. The red trace shows the results for a mixture of circular and hexagonal particles and the blue trace is for circular particles only. The algorithm is found to perform reasonably well for these scenarios with a mean relative counting error of around 3 %, regardless of whether hexagons are included or not. A large relative error was seen in a few of the simulation runs and it was identified that this was for cases with only a few particles in total that were either on the edge of the hologram or spatially overlapping.

Similarly low average relative errors in retrieved median particle size are seen in Figure 4.7b for both cases. A slight systematic bias towards overestimating the size of hexagonal particles is noted. No such bias is observed for circular particles. A comprehensive investigation into the performance of automated analysis algorithms as a function of particle shape is recommended as future work.

Errors in retrieved median particle size for a more realistic simulation configuration are shown in Figure 4.7c. Each simulation run consists of a distribution of between 1 and 50

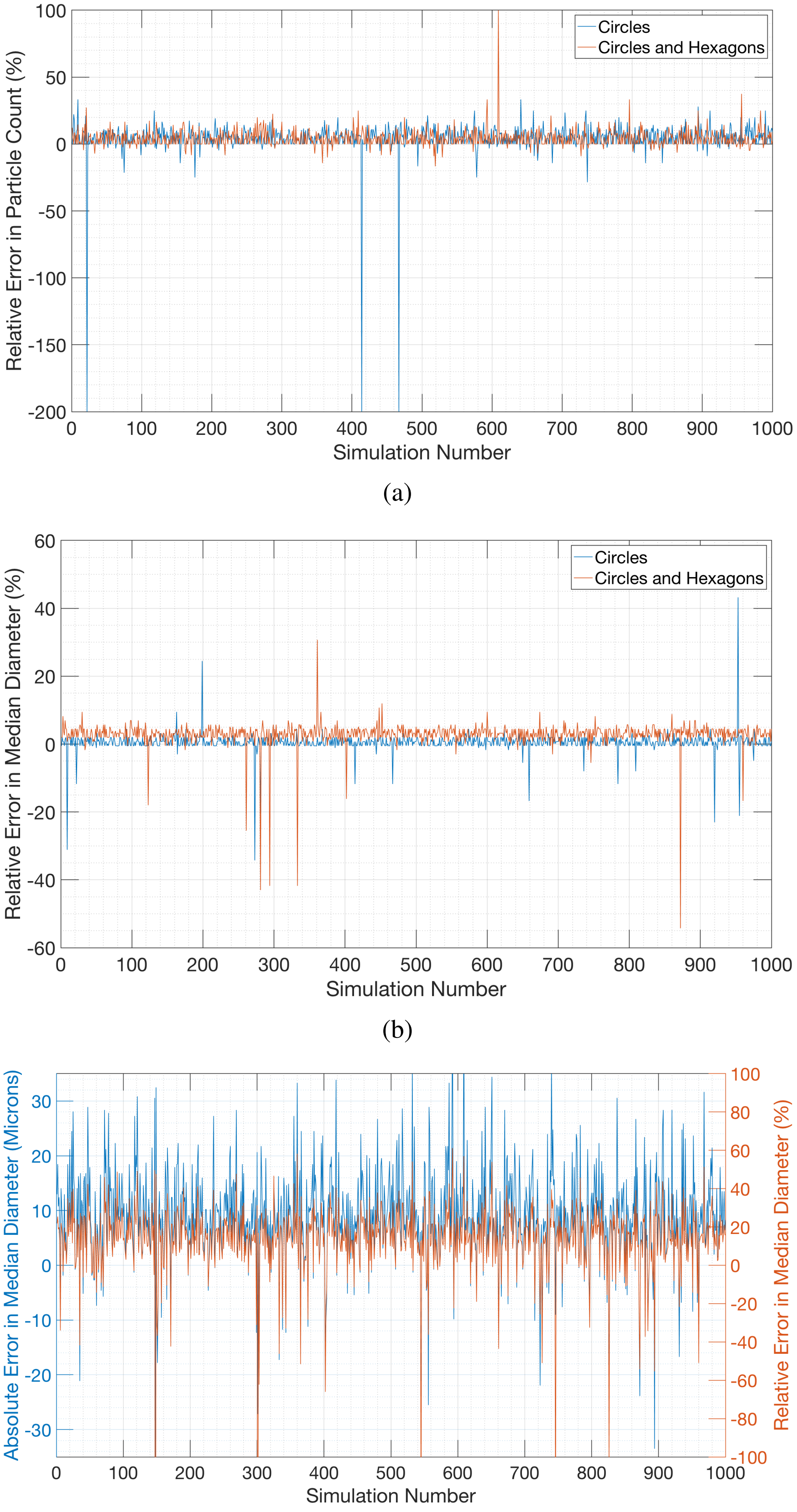

(a)

(b)

(c)

Fig. 4.7 CLOG automated analysis results from simulation runs with randomly varying distributions of particle number, size, and shape. Plotted are the relative errors for distributions of between 1 and 50 particles with a) & b) a fixed particle size of 80 microns, and c) circular and hexagonal particles with sizes varying between 1 and 200 microns.

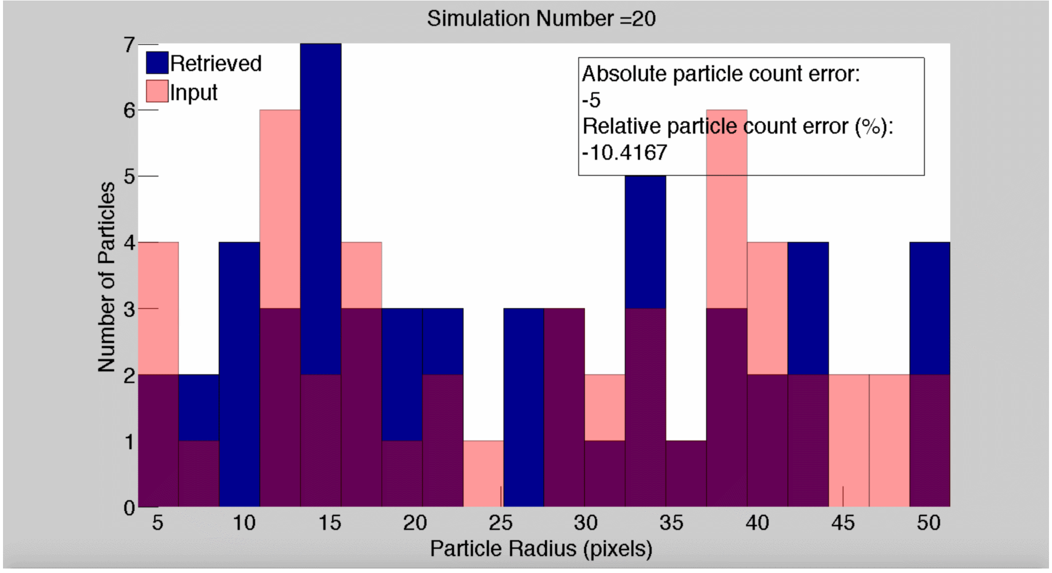

Fig. 4.8 An example of a typical input and output particle size distribution from one of the 1000 simulation runs used for automated analysis testing. Particle radius is quoted in pixels which have a size of 2.2 microns.

circular and hexagonal particles with sizes randomly varying between 1 and 200 microns. This simulation run is considered as a crude approximation of the spherical water droplets and irregularly shaped ice crystals of varying sizes that are observed in real clouds. The algorithm is again found to perform reasonably well, though a larger relative sizing uncertainty of around 20 % is identified in this case along with greater variability between simulation runs.

The larger systematic bias in the relative error indicates that the algorithm performance is more significantly impacted by the size of the particles than by their number, or whether they are circular or hexagonal. This is consistent with the findings in Section 4.3 where an automatically-determined focus depth was found to be challenging to obtain for particles larger than around 100 microns. This effect tends to overestimate the size of particles, as is seen in this testing, as the out-of-focus diffraction fringes will appear larger than the focussed particle.

An example of a typical input and output particle size distribution for one of the simulation runs used in the results presented in Figure 4.7c is shown in Figure 4.8. It is seen that whilst the relative sizing error of approximately 10 % is relatively large, the range and approximate shape of the distribution are still retrieved reliably by the automated method.

These tests suggest that the CLOG algorithm can perform reliably for the laboratory conditions simulated in these cases. When applied to particles larger than around 100 microns, or when larger sources of noise are included, the algorithm performance is seen to degrade. Future investigations should be undertaken using the MHIST software to assess the performance of more sophisticated algorithms suited to unattended analysis of field observations.

4.5 Holographic Microscope Sampling Biases

Another application of the MHIST software is in the determination of biases in a holographic system. Fundamental limitations were described in Chapter 3 that were simple enough to model analytically. The advantage of the numerical MHIST software is that more complicated processes can be modelled as well as the impact of coupled effects. In this section the impacts of edge effects are investigated using the MHIST software.

4.5.1 Reconstruction Edge Effects

Discrete Fourier Transforms (DFTs) are utilised in the 3D holographic reconstruction process, as described in Appendix A. The DFT algorithm assumes that the signal to which it is applied is both of finite length and cyclic. This cyclic property of the DFT manifests as edge effects in the reconstructed 3D image which can represent a significant disturbance against which automated methods must attempt to identify particles.

An amplitude reconstruction for a particle on the edge of the frame is shown in Figure 4.9a at a depth slightly beyond that of the simulated hologram. Diffraction fringes are noted around the particle location at the bottom-left of the frame as expected. Edge effects are seen at the opposite sides of the frame due to the cyclic nature of the DFT. As the amplitude is reconstructed at further depths, these fringe artefacts are seen to progress further towards the centre of the frame which can become a significant issue for automated analysis methods.

One method of mitigating these edge effects is to pad the edges of the hologram with a matrix of zeros. This approach is demonstrated in Figure 4.9b. This method creates a sharp discontinuity in the edges of the hologram which causes significant ringing artefacts in the reconstruction. Whilst these artefacts are more substantial than the unpadded case, they are more uniform in nature and potentially easier to mitigate via additional processing methods such as filtering.

An alternative method for addressing this issue is shown in Figure 4.9c. The pixel values in the edge regions are replicated and used as a padding matrix which has a less-sharp discontinuity than that of the zero-padding method. This approach was found to be effective at reducing artefacts on opposite edges of the hologram, though a slight corruption of the reconstruction is noted around edge regions that are not uniform, such as around the particle

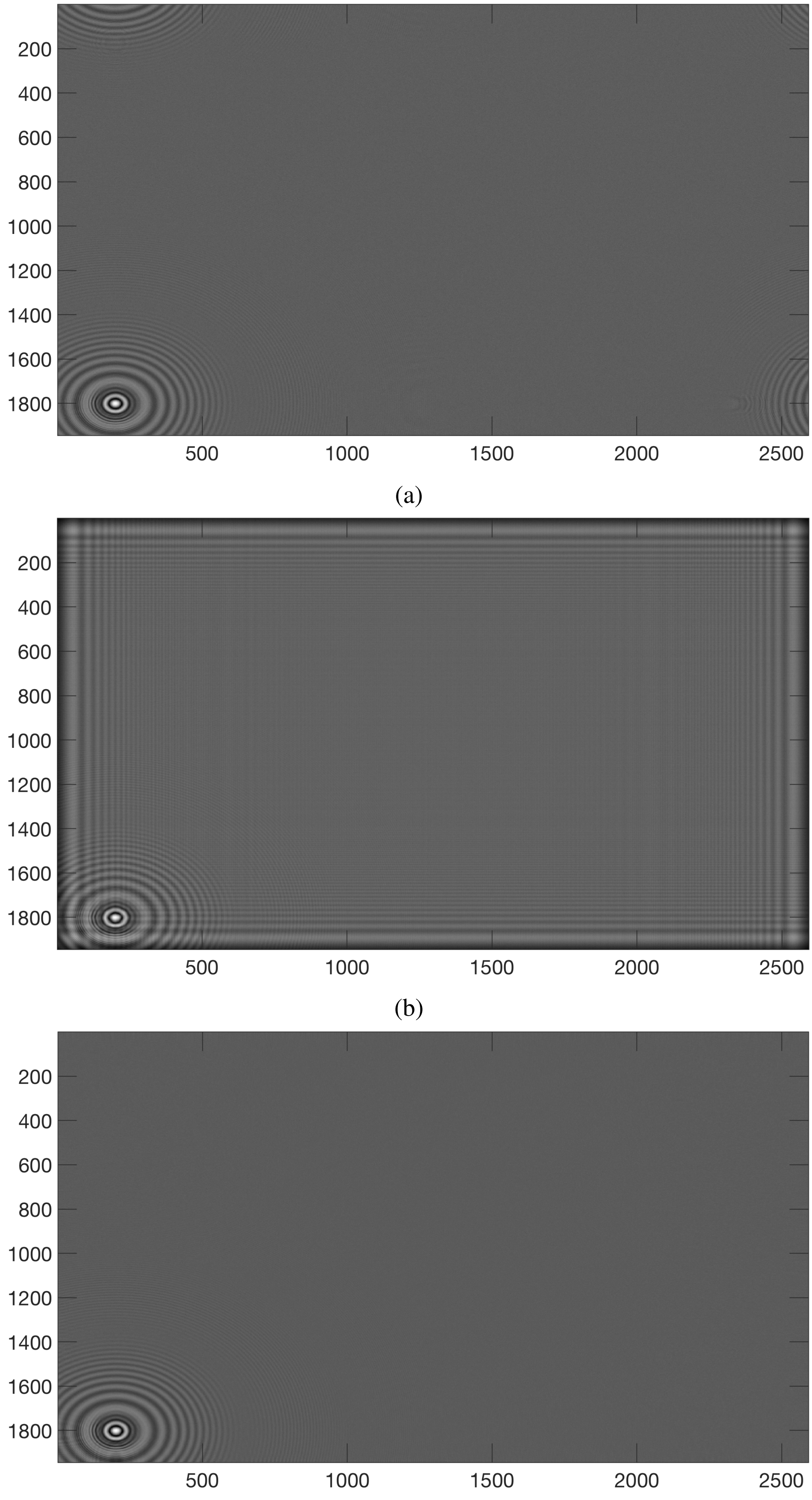

(a)

(b)

(c)

Fig. 4.9 a) Edge effects when reconstructing without padding. b) Artefacts introduced by zero padding. c) Replication padding gives best compromise between artefacts and edge effects.

location in this case. This issue is particularly problematic for retrieving particle properties on the edges of the hologram when significant amplitude variations exist at the edges.

Various other methods have been proposed for mitigating edge effects in the reconstruction process. Apodisation is an effective method [243], though this comes at the cost of reduced intensity towards the edges of the reconstruction. Padding the hologram with artificial values that minimise high spatial frequencies is also effective [244], but this suffers from the same disadvantage of the replication method of introduction of artificial information into the reconstruction.

Holographic reconstructions for the field observations presented in this thesis were constrained to exclude particles on the edges of the hologram. This was primarily decided to avoid the automated measurement of particles with incomplete outlines. It was found that by excluding the edge regions in this way, the edge artefacts were significantly reduced and so no edge-padding method is used for these results. This approach has the notable downside of reducing the overall sampling volume of the instrument, but significantly decreases the computation times as compared with padding. Selection of a given method will likely depend on the application of interest but it is important to understand the impacts in each case using simulations such as those presented here.

4.6 Retrieval of Particle Surface Roughness and Refractive Index

The technique of digital holography allows for the reconstruction of both the amplitude and the phase of light scattered from a field of objects. The discussions so far have focussed on the retrieval of amplitude information and the subsequent reconstruction of a 3D image. In this section a new method is proposed for the retrieval of particle surface roughness and refractive index at nanometre-scale resolution using the holographic phase information.

Light propagating through a transparent object will experience a phase change of the form

$$\Delta\phi = \frac{2\pi\Delta n\Delta L}{\lambda} \tag{4.1}$$

where Δn is the difference in refractive index between the object and the surrounding medium, ΔL is the geometric thickness, and λ is the laser wavelength. Previous observations of ice crystals within clouds suggest that these particles may be transparent enough to preserve phase information [245], though this remains uncertain and should be directly tested in future.

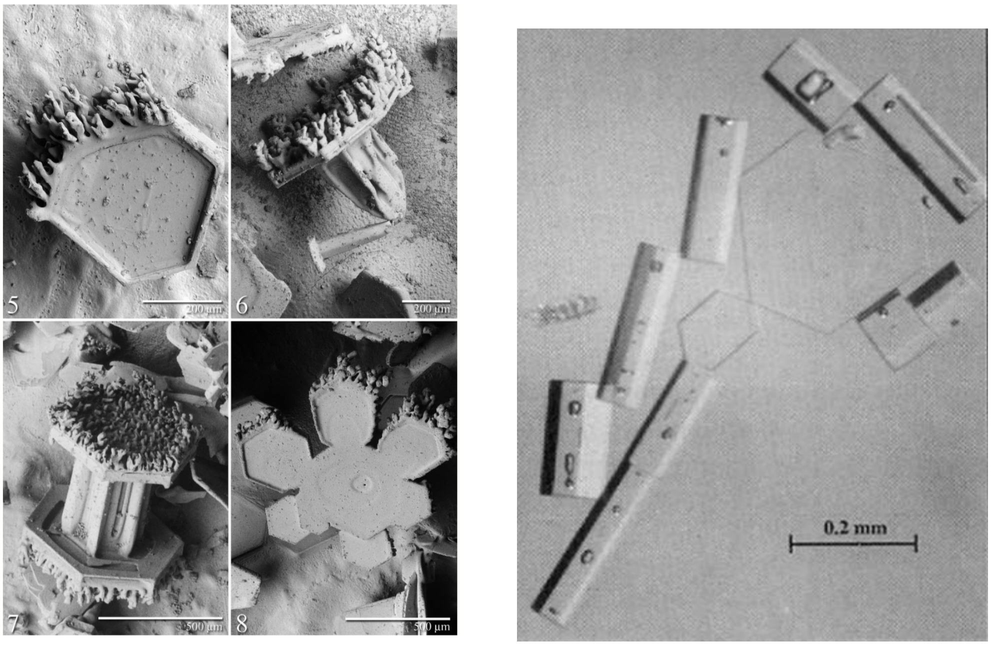

(a) (b)

Fig. 4.10 A selection of observed snowflakes indicating the variability in a) particle surface roughness and b) internal air bubbles. Figures reproduced from Rango (2003) [157] and Tape (1994) [158].

This phase information is directly recorded in the digital holographic method; however, phase measurements are ambiguous for phase changes greater than 2π which complicates the interpretation of this parameter. An effective method for resolving the 2π ambiguity issue is referred to as multi-wavelength digital holography [179, 246, 247]. The simultaneous recording of holograms at slightly different wavelengths allows the physical range of depths for the 2π phase interval to be extended to beyond the size of micron-scale cloud particles. Phase-unwrapping algorithms can also be effective for systems utilising only a single wavelength [248, 249], though these approaches are typically less robust to noise.

An additional challenge in the interpretation of phase information is that the contribution to a change in phase from either refractive index variations or geometric depth variations, due to particle surface roughness, cannot be directly distinguished from Equation 4.1. This issue is particularly problematic for the case of ice crystals within a cloud as these can exhibit complicated refractive index variations, due to the inclusion of air bubbles for example [158, 250], and the surface roughness variations are also highly variable between particles [157]. Examples of the complex surface roughnesses of snowflakes, as recorded using a scanning electron microscope, are shown in Figure 4.10a and optical images of ice crystals with internal air bubbles are shown in Figure 4.10b.

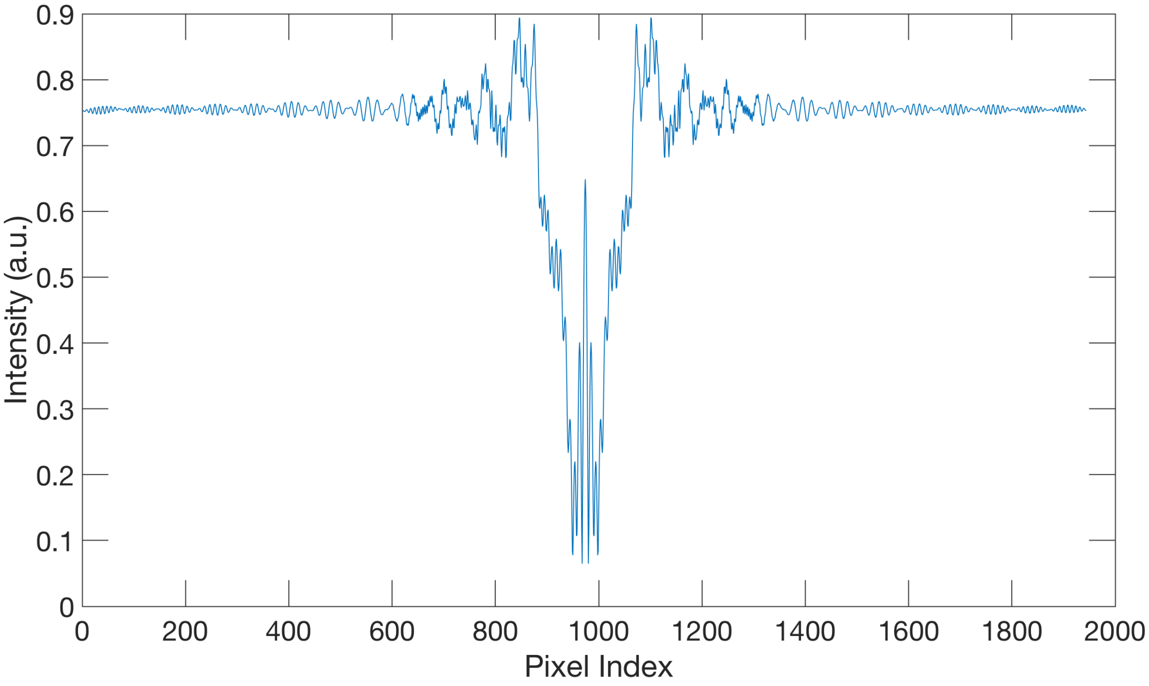

Fig. 4.11 Horizontal cross section of a simulated diffraction pattern from a 200 micron circular particle. Note the intensity spike within the center of the particle shadow, referred to as the Poisson spot.

An independent method of retrieving particle surface roughness would allow the phase measurements to be directly inverted to obtain refractive index measurements. A method for such measurements using a holographic microscope along with the MHIST software, hereafter referred to as the Resolution Enhanced Digital HOlography using Poisson's Spot (REDHOPS) technique, is proposed as follows. A key aspect of the technique is the measurement of a distinctive feature found in the diffraction patterns of particles in the Fresnel diffraction regime that is referred to as Poisson's spot [230]. This feature is due to the constructive interference of light scattered from the edges of a particle and appears as a bright spot within the particle shadow. This feature is simulated in Figure 4.11 for a 200 micron circular particle.

The shape and intensity of Poisson's spot depend directly on the particle shape and surface roughness [251]. Holographic recordings with the instruments presented in this thesis allow the reconstruction of the particle shape to micron-scale resolution, but the nanometre-scale surface roughness is not directly resolved. The first stage of the REDHOPS technique requires the simulation of a particle reconstructed from a recorded hologram, as was demonstrated in Figure 4.2. The Poisson spot intensity from the reconstruction of the recorded hologram is then compared to that simulated using the MHIST software. The surface roughness of the simulated particle is then iteratively varied to minimise the difference between the recorded and simulated Poisson spot intensity. When this difference is minimised it is determined that the modelled surface roughness provides a representative approximation of the true particle surface roughness as all other free parameters are measured directly.

This independent method of measuring particle surface roughness could then be used with Equation 4.1 to determine the refractive index changes within the particle. This may be precise enough to test for the presence of air bubbles with differing refractive index within the particle extent. Further comparison to MHIST simulations including air bubbles may allow for more precise measurements such as the position and size of air bubbles within the particle.

The validity of this proposed technique remains speculative and follow-up investigations are recommended to implement and test the approach. The technique notably requires the assumption that the surface roughness on the edges of the particle is representative of the roughness on the back and front of the particle. This degree of symmetry may only be found in a subset of ice crystals which limits the applicability. There are also questions as to the fidelity with which surface roughness can be modelled and the uniqueness of the relationship between surface roughness and Poisson spot intensity which may further limit the applicability of the method.

Cloud particle surface roughness and refractive index variations have been found to significantly change the predictions of climate models [252], as discussed in greater detail in Chapter 2. These properties cannot currently be measured in situ within clouds and so this technique would represent a significant contribution to climate studies. This technique could be applied to historical observations from any holographic field campaign which would greatly increase the availability of these parameters. The demonstration in this thesis of holographic instruments that are suited to deployment on weather balloons or tower structures, in combination with the REDHOPS technique, could allow routine observation of these parameters in future.

4.7 Summary

This chapter presented the Monte-carlo Holographic Imager SimulaTion (MHIST) software for use in simulating holographic microscope systems and in the testing of automated analysis methods using synthetic holograms. The software allows specification of the hardware parameters of a holographic microscope, cloud particle properties and distributions, and internal model parameters such as the choice of wavefront propagation method. Preliminary efforts have also been made towards a GPU-accelerated N-body cloud particle simulation for studying more realistic cloud conditions of particles interacting under electrostatic and turbulent forces.

The MHIST software was first used to test the performance of various methods for automatically determining the focus depth of particles within reconstructed 3D images. Metrics based on the amplitude, longitudinal amplitude gradient, and longitudinal phase gradient were found to be effective. The normalised product of each of these independent metrics was identified as the most robust metric for determining particle depth. These depth-determination metrics were found to perform reliably for typical amounts of Gaussian noise that were based on that measured in the laboratory for the holographic instruments used in this thesis. The methods were found to perform less reliably for particles larger than around 100 microns in diameter, motivating the development of more sophisticated methods in future.

An automated analysis method utilising the previously mentioned depth-determination metrics, referred to as the Complex LOngitudinal Gradient (CLOG) method, was developed and tested using the MHIST software. The algorithm was generally found to perform well for the retrieval of particle counts and median sizes, though significant biases were found for particles larger than around 100 microns. This is consistent with the limitations found for the depth-determination metrics and tended towards an overestimation in particle size since the out-of-focus diffraction fringes appear larger than the focussed particles. Significant errors were also seen for overlapping particles and particles on the edges of the hologram. Suggestions were made for overcoming these limitations in future, such as by testing for multiple clusters of determined focus depths within the extent of a particle candidate.

For more complicated noise conditions, such as those arising from the variable optical quality of the sampling windows in a field deployment of the instrument, it was determined that the simpler amplitude-based automated analysis method, presented in Chapter 3, was more robust and so this was used for the field campaigns discussed in this thesis. Development and testing of more sophisticated automated analysis methods using the MHIST software is recommended as an avenue for future research.

A brief investigation into the impact of reconstruction edge effects was presented using the MHIST software. A replication method of edge padding was found to give reduced artefacts in the holographic reconstruction as compared with zero-padding methods, though this approach was found to be less reliable for significant amplitude variations on the edge of the hologram. Simulations of this kind are helpful in motivating a given edge-effect mitigation approach, and may also be useful in future for interpretation of particle observations at the edges of holograms that are currently discarded by the automated analysis methods used in this work.

A new method was proposed for retrieving nanometre-scale in situ measurements of ice crystal surface roughness and refractive index variations using the holographic phase information and the MHIST software. The approach, referred to as the Resolution Enhanced Digital HOlography using Poisson's Spot (REDHOPS) technique, could theoretically be applied to any holographic dataset which would greatly improve the understanding of these parameters, as required for climate modelling. Further investigation into this method is considered a particularly interesting avenue for future research.

Chapter 5

Field Instrumentation and Model Summary

5.1 Introduction

The design, development, and testing of two holographic imaging instruments, the Compact Cloud-particle HOlographic Microscope – Surface (C^2HOM–S) and C^2HOM – Balloon (C^2HOM–B) instruments, is presented in the previous chapters of this thesis. Development and testing of automated analysis methods intended for application to field observations is also presented. The remainder of this thesis is devoted to the field deployment of these instruments in two major field campaigns: (i) a high-altitude deployment of the C^2HOM–S instrument in the Australian Snowy Mountains and (ii) an untethered balloon deployment of the C^2HOM–B instrument near Adelaide, South Australia.

A primary goal of the Snowy Mountains field campaign was to assess the performance of the C^2HOM–S instrument alongside standard cloud and precipitation measurement instruments. These instruments included a Polarsonde, Particle Size Velocity 2 (Parsivel) disdrometer, Precipitation Imaging Probe (PIP), Bistatic Radar System for Atmospheric Studies (BASTA) radar, Micro Rain Radar Pro (MRR) radar, RMAN 510 (RMAN) lidar, and HIMAWARI-8 imaging satellite. Comparisons were also made with the The Bureau of Meteorology Atmospheric high-resolution Regional Reanalysis for Australia (BARRA) reanalysis. The instruments deployed in the untethered balloon campaign were limited by weight requirements and consisted of the C^2HOM–B instrument, Polarsonde, an outwards-facing camera, and a set of standard meteorological sensors.

A brief summary of the instruments used in these field campaigns is presented in this chapter. Aspects relating to the specific deployment of these instruments in the field are discussed in the relevant subsequent chapters. For a more general discussion of the advantages and limitations of both in situ and remote sensing techniques, Chapter 2 of this thesis should be consulted along with the references contained within.

5.2 In Situ Instruments

A summary of the in situ instruments used in the field campaigns presented in this thesis is provided in this section. Images of each instrument are shown in Figure 5.1.

5.2.1 C^2HOM–S and C^2HOM–B Instruments

The development, testing, and field deployment of the C^2HOM–S and C^2HOM–B Instruments forms the core focus of this thesis. The main aspects of the design, laboratory testing, and fundamental limitations of these instruments are described in the Master of Philosophy thesis in which the C^2HOM–S instrument was originally presented [204, 205]. The subsequent development and testing of these instruments undertaken during this project is described in Chapter 3. A summary of the measured resolution and sampling parameters for each instrument is provided in Table 3.1.

5.2.2 Polarsonde

The Polarsonde [65, 253] is a polarimetric backscatter sonde, suitable for deployment on a weather balloon or tower structure, developed as a cost-effective method for discriminating spherical water droplets from aspherical ice crystals in a cloud or fog. The instrument consists of two polarised LEDs, each of which is mounted collinearly with two photodiodes. Each photodiode in a pair is overlaid with parallel and perpendicularly oriented polaroids, respectively, such that the depolarisation of the signal backscattered from cloud particles can be measured for each transmitted polarisation channel. In this case, the depolarisation is simply defined as the ratio of the perpendicular and parallel backscatter components for a given channel. The two transmitted polarisations are oriented at 90 degrees and 45 degrees, respectively, with regard to the scattering plane and will be referred to as Lin90 and Lin45 in accordance with previous publications involving this instrument [65, 253].

The use of two polarisation channels was motivated by Monte Carlo modelling of the Polarsonde, using an ice scattering matrix database [103], as a function of cloud particle size, shape, surface roughness, mean free scattering path, and detector geometry [253]. The model also takes into account effects such as multiple scattering and the fact that the instrument does not measure exact backscatter. It was found that the Lin90 channel is expected to give

(a) (b)

(c) (d)

Fig. 5.1 Images of the in situ instruments used in the field campaigns presented in this thesis: a) C^2HOM–S instrument, b) Polarsonde, c) Parsivel disdrometer, and d) PIP 2D imager. Images of the C^2HOM–B instrument are shown in Figure 3.5.

a high depolarisation value for aspherical ice crystals and a low value for spherical water droplets. A low value was also found for large hexagonal plates due to specular reflection from aligned facets. The Lin45 channel nominally reports large depolarisation values for spherical water droplets and low values for ice crystals, and so by analysis of both channels, the instrument should ideally allow discrimination between water droplets and aspherical ice crystals.

The Polarsonde is in an early stage of development and so the testing of this instrument was a secondary motivation for the field campaigns presented in this work. Previous balloon measurements at Macquarie Island suggest that the instrument is sensitive to both aerosols and cloud particles [65]. Attempts can be made at separating the contributions from each particle population by comparison with other observations and modelling, though this is a non-trivial procedure and further study is required into this matter. It is also shown in Chapter 6 that long-term observations from this instrument in the field can be challenging to interpret due to the accumulation of dirt and varying amounts of water on the sampling window. By comparison with collocated instruments, and with new metrics presented in this thesis, it is shown that these issues can be mitigated and that this instrument may be used for classifying different atmospheric events. A quantitative evaluation of the performance of this instrument in a balloon launch, as compared with holographic and meteorological observations, is presented in Section 7.5.

A standard calibration procedure [65] was carried out for each of the Polarsondes used in this project. This included measurement of the relative sensitivity of the parallel and perpendicular backscatter receivers using an unpolarised light source, as required for depolarisation measurements. The temperature dependence of the electrical background noise and the scattered signal was measured in a temperature controlled chamber operated between -30 °C and 5 °C . No dependence was observed in this range, though previous launches have indicated a slight drift at temperatures significantly colder than -30 °C, as encountered at high altitudes.

5.2.3 Parsivel Disdrometer

The Particle Size Velocity 2 (Parsivel) [254] is a laser disdrometer – shown in Figure 5.1c – that measures precipitation particle size and velocity, from which various parameters can be inferred such as the precipitation intensity and classification. A 180 x 30 x 1 mm laser sheet is emitted from one arm of the instrument and then focussed onto a single photodiode in the opposite arm. As a particle passes through the laser sheet, the attenuation of the beam and duration of blocking is recorded to infer size and velocity. This instrument has undergone extensive field testing [255–261] alongside other instruments considered reliable such as the 2 Dimensional Video Disdrometer (2DVD) [262] and standard rain gauges. Comparisons with the C^2HOM–S was therefore a primary motivation for this field campaign.

The Parsivel nominally measures liquid particles in a size range from 0.2 to 8 mm and solid particles from 0.2 to 25 mm with the size resolution varying from 125 to 3000 microns over this observation range. It is also quoted as operating in rain rates from 0.001 to 1200 mmh^{-1}. In practice it has been found that a lower limit for reliable size measurements is closer to 300 microns [257] and it tends to overestimate the number of small drops (<0.8 mm) [258]. In the size range from 0.6 to 4 mm the instrument was found to agree well with a 2DVD disdrometer and at rain rates >20 mm/h it was found to overestimate large drops (>4 mm) [259]. It should be noted that the 2DVD instrument used for comparison also has large uncertainties for drops <0.8 mm [263]. The majority of rain drops are considered small

(<3 mm) [264] and so care should be taken in interpreting these observations, particularly under light precipitation conditions.

The reason for the observed sampling biases are likely due to the assumptions and limitations of the laser sheet technique. The method assumes particles to have an oblate spheroid shape and uses only a single dimension to classify the size. This can result in large errors for aspherical snow particles and for small droplets for which the size is difficult to measure [256]. Border effects are present due to particles measured at the edge of the relatively small sampling area of the laser sheet and coincidence effects have also been reported whereby multiple particles passing through the beam simultaneously can be treated as a single large particle [255].

5.2.4 Precipitation Imaging Probe (PIP)

The Precipitation Imaging Probe (PIP) [265], shown in Figure 5.1d, is an optical array probe [266] consisting of a linear array of 62 sizing photodiodes and a collimated laser beam. The shadow of a particle intersecting the beam is recorded on the array from which an image can be reconstructed by combining observations from consecutive timesteps. The instrument is reported to operate under particle number densities of up to 100 cm^{-3} with a size range between 100 microns and 6.2 mm. This instrument has been used extensively in the field [267–273], predominantly in aircraft campaigns.

Despite extensive usage, a number of unconstrained biases and limitations remain and must be considered when retrieving quantitative parameters such as particle size and shape distributions [274]. Since the particle image is not recorded simultaneously, the instrument has a variable sampling volume that depends on particle size and velocity [275]; this further results in velocity-dependent sampling biases for particles smaller than approximately 75 microns [274]. Shattering of ice crystals on the sampling inlet produces significant over-counting of small particles and adjustment algorithms should be applied [154, 155]. Retrieval of parameters for spherical particles on the edge of the detector is possible but independent verification of particle shape must be introduced to avoid further significant uncertainties [275]. The issue of measuring aspherical particle sizes is particularly challenging as the extent of the measured diffraction pattern does not depend simply on the particle size. Sizes of spherical particles can be inferred by assuming Fresnel diffraction but methods for aspherical particles remain elusive [156] .

5.3 Remote Sensing Instruments

A summary of the remote sensing instruments used in the Snowy Mountains field campaign is provided in this section. Images of each instrument are shown in Figure 5.2.

5.3.1 BASTA

The Bistatic Radar System for Atmospheric Studies (BASTA) is a vertically-pointing W-band 95 GHz FMCW Doppler radar intended for measurements of cloud and fog [140]. This instrument has been tested in the field alongside other remote sensing and in situ techniques and found to be reliable under a range of atmospheric conditions [126, 138, 276]. The BASTA has a maximum vertical resolution available of 12.5 m, with a minimum usable range of 40 m and a Nyquist limit of 10 m s^{-1} for the Doppler velocity. A known limitation of W-band radar is in distinguishing light precipitation from cloud [138] and so comparison with in situ instruments is useful in calibrating such observations.

The instrument is particularly sensitive to small scattering particles, due to the high radio frequency transmitted; however, this also results in significantly more attenuation, which complicates interpretations during heavy rain [277]. Attenuation by atmospheric gases in the tropics can reach values of 0.35 dB km^{-1} at 35 GHz and 2.0 dB km^{-1} at 94 GHz [278]. Attenuation by a 1 g m^{-3} distribution of rain droplets can reach values of 0.8 dB km^{-1} at 35 GHz and 4.0 dB km^{-1} at 94 GHz. Attenuation by ice is significantly lower, at around 0.03 dB km^{-1} at 94 GHz, and so W-band radar is an effective method for measuring mixed phase clouds consisting of ice and water droplets.

In situ observations are necessary for calibrating microphysical retrievals of parameters such as the Liquid Water Content (LWC) from the measured reflectivity (Z). This relationship is particularly sensitive to the shape of the Droplet Size Distribution (DSD) as, in the Rayleigh approximation that applies to small droplets, Z is proportional to the sixth moment of the DSD and LWC to the third moment. Previous collocated in situ and BASTA observations have been made to this end [279] but further observations are required to generalise such results due to the complexity of cloud and fog microphysics [280]. Such corrections are particularly important [281] as calibration errors on the order of just 1 dB can introduce uncertainties on the order of 20% in retrievals of LWC [282].

5.3.2 Micro Rain Radar

A Micro Rain Radar Pro (MRR) [283], a vertically pointing K-band FMCW Doppler radar operating at 24 GHz, was also deployed in this study. The system has been used extensively

(a) (b)

(c)

Fig. 5.2 Images of the remote sensing instruments used in the Snowy Mountains field campaign: a) 95 GHz BASTA radar, b) 24 GHz MRR radar, and c) 355nm RMAN lidar.

for studies of both precipitation [284, 285] and wind-blown snow [286]. The instrument was operated in this work with 128 equally-sized range gates of 35 m in length. The resulting height coverage was between 30 m and 4480 m.

Radars operating at 95 GHz and 24 GHz were deployed in this study to obtain targeted measurements of both cloud and precipitation respectively. For radar scattering in the Rayleigh regime, when particles are significantly smaller than the radar wavelength, the radar reflectivity is independent of wavelength and the radar backscattering cross section goes as λ^{-4} [277, 278]. For a cloud of small spheres (<100 microns) a change from the BASTA's frequency of 95 GHz to the MRR's 24 GHz results in a reduction in radar reflectivity of approximately 24 dB. The reduced frequency also means less attenuation, though heavy rain is still challenging to measure. Due to this significant loss in sensitivity for small particles and reduced attenuation, the MRR is better suited to studies of larger precipitation particles such as rain and snow, rather than cloud or fog for which the BASTA is more appropriate. The manufacturer reports that particles with a fall velocity of less than 0.75 m s^{-1} are not included in the standard analysed products which limits observations in still air to particles larger than around 250 microns in diameter at ground level.

Retrievals of properties, such as the precipitation rate, from reflectivity depends on look-up tables determined from field campaigns alongside in situ instruments. For microphysical conditions that are significantly different from the calibration studies, significant errors can arise [287]. This is especially problematic for the complicated geometries of snow and ice particles. Due to differences in the dielectric constant for ice and liquid water, attenuation by ice is negligible at K-band but significant for liquid. The reflectivity approximately goes as the sixth power of diameter for liquid droplets and the fourth power of diameter for snow [143]. Reflectivity is linear with number density for both phases and so returns are especially sensitive to the particle size. Despite these factors, reliable snow measurements have been made with a MRR for reflectivities as low as -14 dBZ [288]. MRR observations for moderate vertical wind velocities greater than around 1 ms^{-1} can also be corrupted by aliasing effects which further complicates interpretations [289].

5.3.3 RMAN Lidar

An RMAN 510 (RMAN) [290] Raman UV polarisation lidar, transmitting at a wavelength of 355 nm, was deployed in this campaign. The system detects elastic Rayleigh backscatter at 355 nm as well as inelastic Raman backscatter at 387 nm, with a height resolution of 15 m. Two wavelengths are required to retrieve both aerosol backscatter and aerosol extinction without introducing significant uncertainties due to an assumed lidar ratio [131]; however, such retrievals must be carefully calibrated [130] and can only be performed at night since the Raman backscatter is orders of magnitude weaker than the elastic backscatter and sunlight backgrounds [132].

The instrument has proven effective at discriminating supercooled liquid water from ice within clouds [291–293] based on depolarisation and this is the primary motivation for using the instrument in this work. Previous field campaigns with this instrument suggest a depolarisation threshold of around 0.3 can be effective in discriminating ice from liquid [293], consistent with values for the satellite-based CALIPSO depolarisation lidar [294]. Care must be taken in quantitative studies of depolarisation due to instrumental calibration factors and the effects of multiple scattering in optically thick clouds [136] and so these observations are considered alongside those from other instruments in this study. The lidar is tilted at 4 degrees off zenith to avoid specular reflection from aligned plate ice crystals and to help rain to run off the sampling window.

To summarise the previous discussion, radar is effective at measuring large particles, such as ice crystals, but struggles with measuring small particles such as water droplets, even in relatively large number densities, due to the strong sensitivity to particle size. Depolarisation lidar is more effective at measuring liquid cloud layers; however, the signal can attenuate fully after as few as around three optical depths and so cannot penetrate more than in the order of tens of meters into a typical cumulus cloud [138]. For these reasons, a merged RMAN lidar and BASTA radar product is analysed here at a height resolution of 15 m, where observations from either the lidar or the radar are retained to maximise data availability. Both instruments are utilised by the cloud classification algorithm used in this thesis, as described in previous works [117].

5.3.4 HIMAWARI-8

HIMAWARI-8 is a geostationary atmospheric monitoring satellite that allows high-resolution observations of the Asia-Oceania region [295]. The primary observation instrument is the Advanced Himawari Imager (AHI) which is a 16-channel hyperspectral imager targeting the visible and infrared wavebands. Observations are made with a spatial resolution of 0.5 to 2 km at a temporal resolution of 10 minutes. Cloud microphysical properties used in this study, such as Cloud Optical Thickness (COT), Cloud particle Effective Radius (CER) and Cloud Type (CT), are derived from a combination of look-up tables of cloud properties and the raw spectral observations – as obtained directly from the Japanese Meteorological Agency (JMA) using a standard retrieval algorithm [296].

Geostationary microphysical observations provide high temporal and spatial coverage, beyond what is feasible with other methods, yet suffer from some key limitations. Derived products depend on assumptions regarding the vertical profile of thermodynamic variables and therefore have difficulty under disturbed atmospheric conditions [126]. Reflectance measurements are also overly sensitive to the tops of clouds and so measurements of multi-layered and patchy clouds can be especially challenging [297]. Previous comparisons with in situ microphysics observations over the Southern Ocean suggest that discrepancies in CER and droplet number density can be on the order of 30% [298]. In situ observations are therefore necessary in both the calibration and validation of these satellite products and such comparisons were one of the motivations for this research.

5.4 BARRA Reanalysis

The Bureau of Meteorology Atmospheric high-resolution Regional Reanalysis for Australia (BARRA) [299] is a data-constrained reanalysis utilising the UK Met Office Unified Model (UM) [300] and Australian Community Climate and Earth-System Simulator (ACCESS) [301] models. BARRA-R is a regional-scale model at 12 km spatial resolution and is used to produce the down-scaled BARRA-SY [302] reanalysis that was used in this study. BARRA-SY includes the Snowy Mountains region with a spatial resolution of 1.5 km, 70 vertical height levels spaced non-linearly up to 40 km, and a temporal resolution of 10 minutes.

A key point of difference between BARRA-R and BARRA-SY is in how each reanalysis handles precipitation, though rainfall observations are notably not assimilated into either method. BARRA-R uses a microphysics scheme [303] and a subgrid-scale parametrisation of cumulus clouds to simulate the atmospheric processes by which water changes thermodynamic phase. Convection is modelled independently between grid points and an area-averaged rainfall is produced that is expected to perform worse for subgrid-scale precipitation than at larger scales. BARRA-SY does not use such a convection parametrisation scheme and instead utilises model dynamics to generate convective motions directly due to the finer spatial resolution.

Both the BARRA-R and BARRA-SY reanalyses are relatively new and therefore have not been extensively validated with targeted observation campaigns of clouds and precipitation. Comparisons with the ERA-Interim [304] global reanalysis and the Australian Water Availability Project (AWAP) [305] interpolated precipitation product suggest that BARRA-R performs reasonably well for daily precipitation estimates [306]. Early comparisons between the BARRA models for intra-daily performance suggest that BARRA-SY performs better than BARRA-R for extreme rainfall events and in coastal and mountainous regions [302]. Despite general improvements, BARRA-SY tends to initiate precipitation too early and rapidly whilst also overestimating heavy rain and underestimating light rain. Such biases are expected to be even larger in high-altitude regions such as the Snowy Mountains where unresolved orographic processes can significantly influence precipitation. Targeted microphysical observations, such as those undertaken in this work, should prove useful in resolving these issues through better parametrisation of cloud and precipitation processes within the models.

Chapter 6

Snowy Mountains Field Campaign

6.1 Introduction

The Compact Cloud-particle HOlographic Microscope – Surface (C^2HOM–S) and Polarsonde were deployed in the Australian Snowy Mountains as part of a multi-instrument study of wintertime precipitation from June to August 2018. The instruments were deployed on a dedicated observation tower at an altitude of approximately 1480 m above sea level, allowing measurements of precipitation, low-level cloud, and fog. The observations were part of a broader ARC-funded campaign to investigate the impacts of cloud seeding in an orographically influenced environment [307].

A primary motivation for including the C^2HOM–S instrument in this campaign was to assess the performance of the instrument in the field alongside other instruments that have been more extensively field tested and validated. The deployment of holographic instruments in general is still uncommon in cloud studies, yet they offer unique insights into microphysical processes, as discussed in Chapter 2. The observations are, therefore, of intrinsic interest from a cloud physics perspective. The campaign also provided an opportunity to assess the performance of the developed automated analysis methods as compared with manually analysed data under field conditions.

The chapter begins with an overview of the field site and instrumentation. A summary of observations from the full campaign is then presented along with a more detailed analysis of case events encompassing a range of atmospheric conditions. The chapter concludes with an assessment of the capability of the C^2HOM–S and Polarsonde instruments to automatically classify types of cloud and precipitation events, and to validate and calibrate remote sensing observations and climate models.

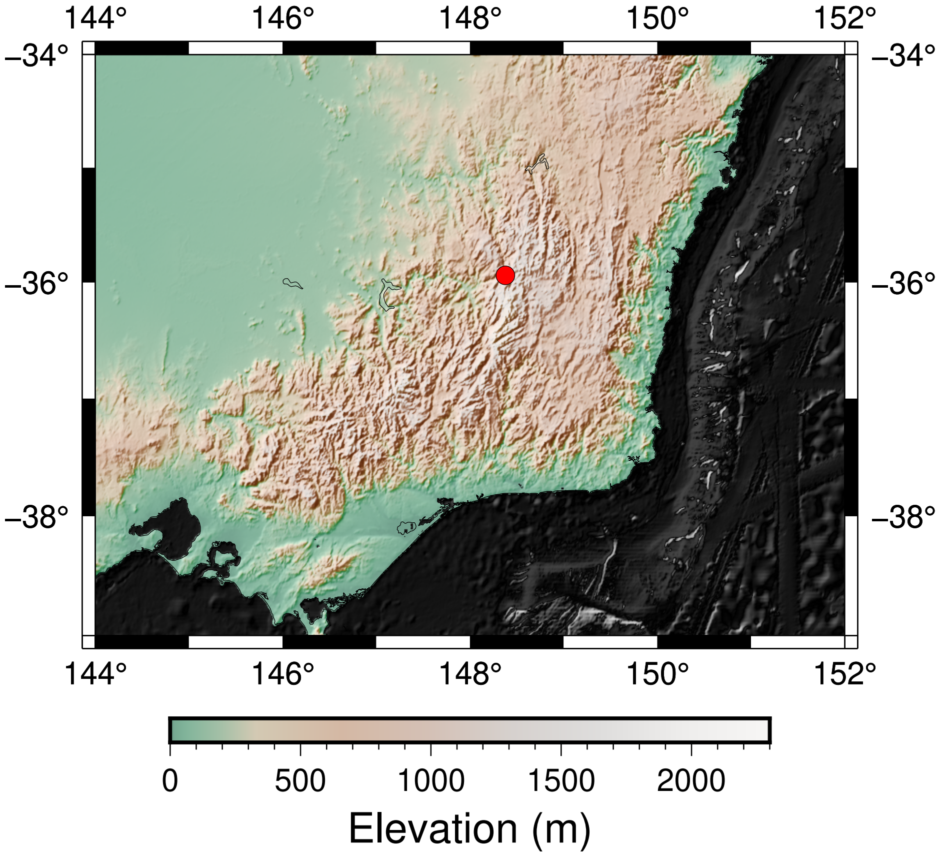

Fig. 6.1 Topography of the field site within the Australian Snowy Mountains and surrounding regions. Instrument tower location indicated by the red circle.

6.2 Field Campaign Overview

The field site is located within the Australian Snowy Mountains near the town of Cabramurra at 35.94°S, 148.38°E, as indicated on Figure 6.1. Precipitation processes within the Snowy Mountains contribute significantly to the supply of national water resources via natural flow into the Murray and Murrumbidgee rivers and are of further economic interest due to the Snowy Hydro power project. Climatological forecasts of precipitation within this region are, therefore, of significant interest, yet accurate modelling remains challenging [308].

A key modelling challenge for this region is in understanding the role of orographic effects on clouds [309], due to the extended mountain range, with peaks on the order of 2 km in altitude. An observed prevalence of Supercooled Liquid Water (SLW) in this region is noted, as compared with other mountainous regions of the world [310]. Past surface-based radiometer observations indicate SLW occurrence frequencies as high as 53% from April to September [311]. A significant fraction of precipitation events over this region are driven by

(a) (b)

Fig. 6.2 a) Platform on which field instruments were mounted. The Polarsonde is highlighted by the red circle on the southern railing. b) C^2HOM–S mounted on the western railing as indicated by the red circle.

air masses coming from the Southern Ocean [312], a region which is also poorly represented in models [114]. Much remains to be understood about the interplay between these processes and further observations are required to better constrain model outputs.

The C^2HOM–S and Polarsonde instruments were mounted on the railings of an observation tower, as shown in Figure 6.2, at approximately 4 m above ground level. The prevailing winter wind at Cabramurra is eastward and hence the C^2HOM–S was mounted on the western handrail to minimise obstruction of particles passing through the sampling volume. The Polarsonde was mounted on the southern railing, to reduce the accumulation of particles on the sampling window. The tower itself was at a height of approximately 1480 m above sea level.

The C^2HOM–S and Polarsonde instruments were deployed from the 27th of June to the 16th of August 2018, and an intensive observation period with all instruments operating occurred between the 24th of July and the 11th of August. During this time the instruments were monitored by on-site researchers and daily cleaning of the sampling windows was carried out. The instruments operated essentially continuously through the campaign, with only occasional drop outs due to power supply issues and hard drive swaps.

It should be noted that cloud seeding operations were undertaken by Snowy Hydro around the field site area at intermittent times throughout this observation campaign. Assessment of the impacts of these operations was one of the motivations for this campaign, but is outside of the scope of this research project.

6.2.1 Instrumentation Summary

A summary of the instrument deployments and sampling characteristics specific to this field campaign, with an emphasis on the newly developed C^2HOM–S and Polarsonde instruments, is provided in this section. A more detailed summary of the operating principles and limitations for each of the instruments used in this campaign is presented in Chapter 5. The operational parameters for the in situ instruments most relevant for comparison with the C^2HOM–S are presented in Table 6.1.

6.2.1.1 C^2HOM–S

The C^2HOM–S is described in detail in Chapter 3 of this thesis and deployment of this instrument was the primary motivation for this observation campaign. A sampling rate of 0.1 Hz was chosen for this campaign as a compromise between sampling statistically significant numbers of particles whilst not requiring the 4 TB hard drive to be replaced too frequently for the multi-month campaign. A pulse width of around 150 ns was chosen as a compromise between laser beam intensity, and blurring due to particle motion during an exposure. The volume is defined by the transverse extent of the collimated laser beam and the spacing between the sampling windows on the boxes containing the camera and laser, respectively. For this campaign a spacing of 6 cm was chosen which resulted in a maximum sampling volume of 0.9 cm^3.

The instrument can resolve particles with diameters ranging from approximately 3.5 microns at the depth of the sampling window closest to the camera, to 7.8 microns at the depth of the further sampling window. An upper resolvable particle diameter of around 3 millimetres is imposed by the size of the camera sensor, making it suitable for detection of cloud particles as well as small precipitation particles.

On deployment at the field site it was discovered that the existing measures to avoid sunlight saturation of the CMOS sensor were insufficient during times of intense sunlight. Prior testing did not indicate such an issue and the problem was likely due to reflections off the white enclosures of nearby instruments and metal structures. To mitigate this problem, an aluminium shield was constructed and placed on top of the sampling volume at the start of the campaign, as visible in Figure 5.1a. The presence of clouds and precipitation further acts

Instrument Name	**Diameter Resolution** μm	**Sizing Uncertainty** μm	**Sampling Rate** Hz	**Sampling Volume** cm^3	**Velocity Range** m s^{-1}
C^{2}HOM–S	3.5 - 3000	2	0.1	0.9	0 - 15
Parsivel Disdrometer	200 - 25000	125 - 3000	0.03	-	0.2 - 20
Precipitation Imaging Probe (PIP)	100 - 6200	100	1	-	10 - 200

Table 6.1 Summary of key in situ instrument measurement parameters.

to block sunlight incident on the sensor and so observations of actual interest are significantly less impacted by this problem.

Manual inspection of the data revealed that saturation mostly occurred between the times of 00Z and 05Z when the sun was directly above the instrument. This issue was fixed during the latter half of the campaign but in the interests of consistency, all holographic observations between these times have been discarded in the subsequent analysis. Future analyses could benefit from the inclusion of these observations, perhaps by using adaptive correction methods similar to those described in Section 7.1.2.1 for the untethered balloon campaign.

The sunlight shield presents an unquantified potential sampling bias. The path for particles entering the sampling volume from directly above is blocked and it would be expected that precipitation observations would be limited to particles that are being sufficiently wind blown so as to pass through the sampling volume from the sides. It is expected that this would effectively reduce the maximum detectable particle size since larger particles should be advected less for a given wind magnitude.

The instrument was mounted such that low-lying cloud particles would pass through the sampling volume due to the prevailing winds without obstruction from the instrument boxes and so these observations should be less impacted. No clear sampling bias into the sampling volume from the sides was identified with wind direction or magnitude, suggesting that the obstructions to the air flow did not significantly impede the detection of cloud particles, despite the limitations noted above.

The instrument was heated with approximately 30 W of resistive power in an attempt to avoid condensation and icing of the sampling windows without significantly impacting the electronics housed in the compact instrument boxes. This was usually sufficient to avoid condensation, but icing was still occasionally noted by observers on site. Icing was continuously monitored during the intensive observation campaign and ice was removed before it could grow large enough to block the sampling volume. Future unmonitored deployments will require significantly more heating to resolve this issue. The sampling windows were cleaned daily during the intensive observation period and the window quality throughout the campaign was sufficient for reliable holographic reconstruction and subsequent automated analysis.

The instrument was sampling reliably for the majority of the observation campaign and outages were mainly due to rare power supply issues at the site. A 10 MB image was recorded every 10 seconds and so the 4 TB hard drive was swapped out once every approximately 1.5 months, but this procedure only resulted in a few minutes of overall dead time. The data were moved to the external hard drive from the SD card every 3 hours, which was a significant burden on the processor of the low-cost Raspberry Pi used. This resulted in a $\sim$4-minute down time at the start of each 3-hour sampling period.

6.2.1.2 Polarsonde

The Polarsonde was operated at a sampling rate of 1 Hz and averaged to 1-minute resolution to reduce the impact of noise. The standard calibration routine for this instrument was applied including channel sensitivity correction and initial offset of backgrounds due to electrical pickup.

A significantly greater challenge for long-term field deployment arises from the variable optical quality of the glass window through which the light enters and exits the weather-protected instrument box. Icing, condensation, and deposited dirt from evaporating water droplets on the sampling window contribute a time-varying mean backscatter component with a variable depolarisation. A weather shield was placed upwind of the instrument to somewhat mitigate this effect, as shown in Figure 5.1b, and window quality monitoring and cleaning was carried out daily by the on-site observers.

Despite these efforts, a varying background contribution is evident in all detectors. Local background subtraction using a running mean can be helpful in correcting these offsets but without more knowledge of the window quality, quantitative conclusions are challenging. This thesis presents new methods based on the covariance between channel signals and signal variance that are less sensitive to the mean window optical quality. It is shown in Section 6.6 that these metrics are useful for classification of different atmospheric events.

6.2.1.3 Other In Situ Instruments

C^{2}HOM–S and Polarsonde observations were analysed alongside those from a suite of in situ instruments that have been more extensively tested in the field. This included standard meteorological sensors for ground and infrared sky temperature, relative humidity, and a sonic anemometer for wind measurements. A Parsivel disdrometer was mounted next to the C^{2}HOM–S instrument just above the railing on which that instrument was mounted. This allowed for direct comparisons with holographic observations of particle number density and diameter, though differences in the sampling constraints of each instrument must be accounted for, as discussed in Section 6.3.2. The Parsivel instrument reports a rain mask based on measurements of particle size and velocity which was used for assessing the capability for classification of atmospheric events using the C^{2}HOM–S instrument.

A PIP 2D particle imager was deployed for direct comparison with the holographic particle images. The majority of validation campaigns and developed corrections for this instrument have been based on observations from aircraft campaigns, rather than surface deployment. The instrument was mounted on a short mast reaching 2 m above the platform floor and experienced significantly different conditions than in an aircraft campaign, including snow accumulation, significantly slower particle velocities, and an abundance of large irregularly shaped snow particles. For this reason the PIP data were not analysed quantitatively and instead images were used to provide a qualitative indication of the shapes and sizes of particles observed through the key case study events.

6.2.1.4 Remote Sensing Instruments

Remote sensing instruments were deployed to aid in the classification of atmospheric events and were used to evaluate the capability of the C^2HOM–S instrument to calibrate and validate remote sensing observations. A 355 nm RMAN depolarisation lidar was operated at 15 m vertical resolution to identify and classify cloud layers. The observations were sampled at approximately 0.1 Hz and depolarisation is calculated by taking the ratio of the perpendicular and parallel backscatter channels. A merged lidar and BASTA cloud classification product was supplied by the Australian Bureau of Meteorology (BoM) and Australian Antarctic Division (AAD) collaborators, as described in previous works [117].

A 95 GHz BASTA cloud radar and a 24 GHz MRR Pro precipitation radar were deployed for reflectivity and Doppler velocity observations. The BASTA was operated at its maximum vertical resolution of 12.5 m with a sampling rate of approximately 0.1 Hz. The MRR was operated at a vertical resolution of 35 m at a rate of about $1/60$ Hz.

It is expected that BASTA observations below approximately 240 m are less reliable as they are within the near-field regime [140], but such observations appeared realistic by manual inspection and were necessary in this study for directly comparing with the in situ instruments. MRR observations near the ground are similarly affected by this issue, though again, no noticeable artefacts were identified. Regardless, this is a notable limitation of this method. Post-processing was applied by the BoM and Monash University collaborators to the radar observations to remove clutter and calibrate the returns.

6.3 Full Campaign Observations

In this section the observations from the C^2HOM–S instrument are summarised and compared with observations from the Parsivel disdrometer, since both instruments are capable of measuring particle diameter, number density, and precipitation type. Observations during the times when both instruments were operational are compared, and a number of representative

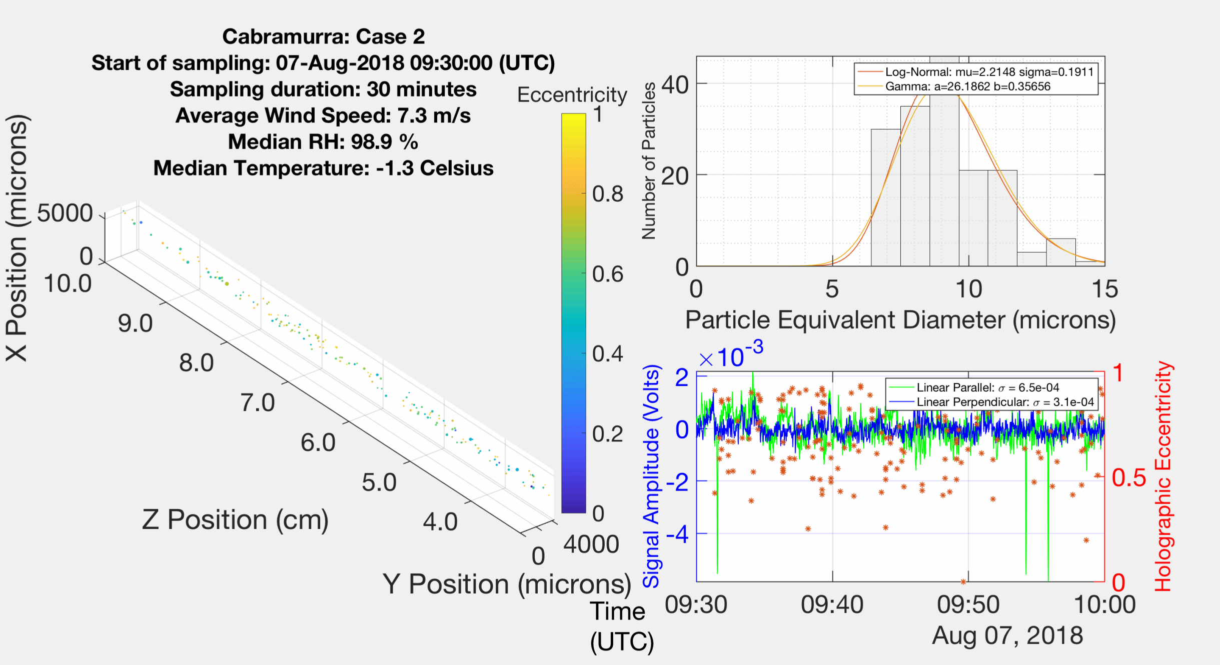

Fig. 6.3 Summary of 30 minutes of holographic observations showing particle 3D positions, size distribution, and eccentricity along with averaged meteorological parameters and Polarsonde backscatter signals. The z-axis on the 3D plot indicates the depth within the sampling volume relative to the camera sensor, and the transverse dimensions are in the plane of the camera sensor.

case events are identified within the full dataset that cover a range of atmospheric conditions that are studied in greater detail in the following section.

6.3.1 Representative Holographic Observations

A representative snapshot of automated holographic observations is presented in Figure 6.3 for a 30-minute observation period during what is subsequently argued in this section to be a mixed phase cloud event. A visualisation of the particle locations within the sampling volume is shown in the left half of the figure which demonstrates that the spatial sampling of particles was uniform. The particles are colour coded by their eccentricity and both high and low values are seen, suggestive of a mixture of both spherical and irregularly shaped small particles. The mean meteorological values are listed in the top left of the figure and the large relative humidity is consistent with this being a cloud detection.

The size distribution is shown in the top right of the figure and Log-Normal and Gamma fits are overlaid to highlight that the distribution follows the typical form for a cloud [34].

The Log-Normal distribution is defined with the standard form of:

$$f(x|\mu,\sigma) = \frac{1}{x\sigma\sqrt{2\pi}} e^{\frac{-\left(\log(x)-\mu\right)^2}{2\sigma^2}}, \tag{6.1}$$

where x is the particle diameter, μ is the mean of logarithmic values, and σ is the standard deviation of logarithmic values. The Gamma distribution is defined with the standard form of:

$$f(x|a,b) = \frac{1}{b^a\Gamma(a)} x^{a-1} e^{\frac{-x}{b}}, \tag{6.2}$$

where x is the particle diameter, a is the shape parameter, b is the scale parameter, and Γ is the Gamma function. The fit parameters for each of these distributions are included in the top right legend.

The sharp cut off in the particle size distribution at approximately 7 microns indicates the resolution limit of the automated analysis method which is described in Chapter 3. The narrow distribution and mean particle diameter of approximately 8 microns is further consistent with this being a detection of cloud, as opposed to precipitation which would have significantly larger particle sizes.

The bottom right of the figure shows the Lin90 parallel and perpendicularly polarised Polarsonde backscatter signals as the blue and green traces and overlaid are the holographic eccentricity values in red. The mean backscatter does not vary significantly over this event and small-scale fluctuations are seen in both channels, supporting the interpretation of a mixture of both ice and water droplets. As discussed earlier, the eccentricity values are not expected to go to zero with this method as would intuitively be expected but it will be seen later that values of up to approximately 0.5 are consistent with spherical particles and those greater than approximately 0.7 are more likely to be irregularly shaped. This metric can be used for crude particle classification but a more sophisticated method should be pursued in future, perhaps based on machine learning methods.

6.3.2 Holographic Microscope and Parsivel Comparison

Comparing the C^{2}HOM–S observations to those from the Parsivel disdrometer was one of the key goals of this field campaign, as the Parsivel has undergone extensive field testing in other campaigns and produces comparable measurements of particle size, number density, and precipitation classification. Despite the similar outputs, it is important to note that the operating principles of the instruments are fundamentally quite different, with the holographic microscope sensitive to particles as small as micron-scale cloud particles and the Parsivel better suited to larger precipitation particles with low number density due to its significantly higher volumetric sampling rate. Strong agreement between these methods is therefore only expected for precipitating clouds that pass through the instrument sampling volumes, but the aim of this study is to investigate how these complementary techniques perform under a range of atmospheric conditions as classified using data from all of the deployed instruments.

6.3.2.1 Particle Diameter

Particle diameter observations from both instruments over a number of case events are presented in Figure 6.4. The blue and green crosses indicate the individual automatically extracted holographic particle diameters for small (<100 microns) and large (>100 microns) particles, respectively, and the hourly running mean values are overlaid as indicated by the solid lines and triangle markers. This delineation between small and large particles, which will be maintained throughout this chapter, is made to emphasise the presence of two distinct populations of particles in certain events; cloud particles (<100 microns) and larger aspherical ice crystals & small rain droplets (>100 microns). Manually analysed holographic measurements are shown as purple crosses and these agree well with those reported by the automated method, as discussed in further detail in Section 3.6.3.

Over this observation period the Parsivel recorded a large number of particles with sizes ranging between approximately 300 microns and 10 mm. This is in contrast to the holographic size distribution which is between roughly 7 microns and 1 mm. To better visualise the trends in these measurements, as relevant to the discussion in the following sections, the 1-minute and 1-hour mean particle diameters are also plotted.

The majority of the holographic observations are smaller than around 400 microns, which is close to the reliable sampling size limit of the Parsivel that is reported to be approximately 300 microns [257]. The Parsivel size resolution in this range is 125 microns, in contrast to the maximum holographic diameter resolution of approximately 7 microns and so the holographic observations are expected to be more reliable in this range.

During the shown times the Parsivel reported a mean number density of approximately 5×10^{-3} cm^{-3} for particles larger than 300 microns. This is argued to be the primary reason for the holographic microscope not seeing the larger particles as the volumetric sampling rate of $\sim$0.1 cm^{3}s^{-1} would lead to only a few tens of particle detections of these sizes per day, as confirmed by manual analysis. The sampling rate can be significantly increased in future campaigns as it is largely constrained by the small CMOS sensor and relatively slow mini-computer used, but was considered an acceptable trade off in reducing the cost and weight since the primary focus was on cloud observations for which number densities of hundreds per cubic centimetre can be observed.

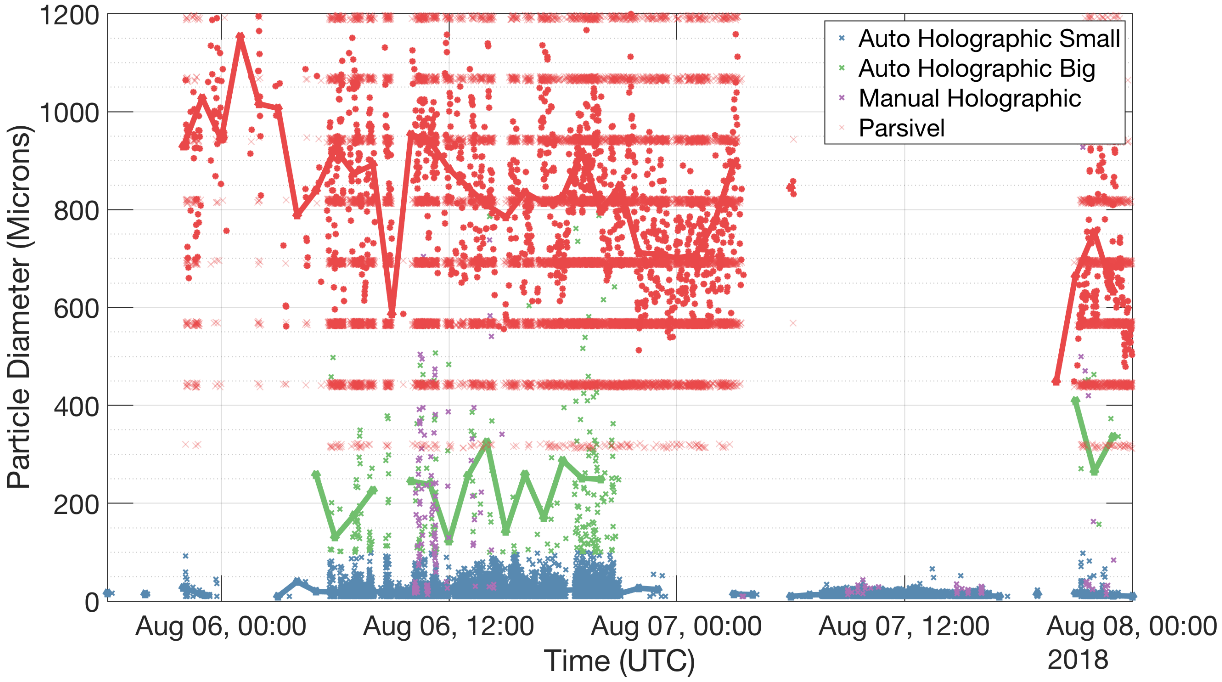

Fig. 6.4 Comparison of particle diameter observations between the holographic microscope and Parsivel disdrometer. Individual particle measurements are indicated by cross markers, and the 1-minute and 1-hour running mean data are indicated by star markers and triangle markers, respectively. Manually analysed holographic observations are included for validation and automated holographic observations are grouped into large (>100 microns) and small (<100 microns) categories to emphasise the significantly different statistics of these populations. Raw Parsivel observations have been decimated for ease of viewing.

In the size range between 300 and 400 microns, where both instruments can produce reliable observations, there is reasonable agreement in the reported raw particle sizes throughout the field campaign. A case of poor agreement in this time range is seen around 00Z on August 7th on Figure 6.4. This was during a time of significant sunlight saturation during which the automated holographic analysis software was unable to reliably extract particle properties.

6.3.2.2 Particle Number Density

Despite the relatively narrow overlapping observation range of the C^2HOM–S and Parsivel instruments, as established in the previous section, it is still of interest to compare the particle number densities reported by these instruments. Absolute agreement is not expected, but their relative agreement was investigated to determine whether there may be a link between the

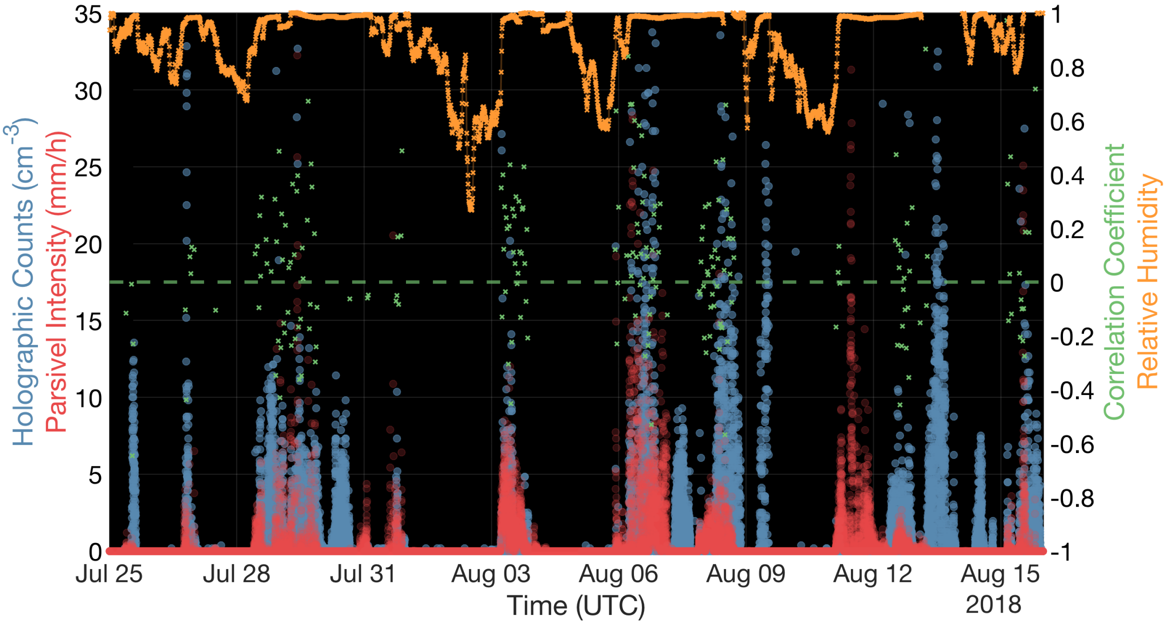

Fig. 6.5 Holographic counts, Parsivel intensity, and 30-minute windowed correlation coefficient during the intensive observation period. Relative humidity measurements between 0 and 1 are included to indicate the times for which the instruments are likely within cloud.

small particles observed by the C^{2}HOM–S and the larger particles measured by the Parsivel. Such correlations may prove useful in understanding the dynamics of a microphysical event as it evolves. For atmospheric conditions that have a mixture of both small and large particles, such comparisons provide validation that the holographic microscope can reliably operate under field conditions.

The 1-minute averaged mean holographic number density and Parsivel intensity measurements during the time period when both instruments were operational is shown in Figure 6.5. In this case precipitation intensity is used instead of number density for the Parsivel as it was found to correlate slightly better with the holographic number densities in general and, as discussed, the absolute count values were not expected to agree. A 30-minute moving window was applied to these observations within which the Pearson correlation coefficient [313] was calculated and is plotted in green.

The instruments agree on the onset time and duration of the majority of events observed. Despite this general agreement it is clear that there are numerous events where only the holographic microscope observes particles as well as, less commonly, cases where only the Parsivel does. Manual inspection of the raw holographic data reveals that the latter scenario occurs during times when the holographic microscope was experiencing significant sunlight saturation on the sensor, impairing the performance of the automated methods.

The instruments are expected to agree best for precipitating clouds that pass through the instrument sampling volumes and so the relative humidity is also plotted to indicate cases for which the instruments are likely to be within cloud.

The observed agreement for most events suggests that there is a link between the populations of small and large particles for the measured precipitation events and hence that the holographic microscope is able to provide useful information despite not measuring the larger particles. The cases where only the holographic microscope measures something were found to be cases with only a population of small particles that the Parsivel was unable to resolve, suggestive of a low-level cloud or fog event, as discussed further in Section 6.4.1.3.

Despite the broad agreement between these instruments, the 30-minute windowed correlation coefficient is not overly strong with an average value of around 0.2 that rarely exceeds 0.6. There are even times when the correlation coefficient goes negative, suggesting an inverse relationship. This lack of correlation may be a sign of spatial inhomogeneities in the cloud over the scale of the few meters that physically separated the instruments. This particular field site is high enough that cloud frequently intersects the observation tower; however, it is also common for the tower to only just be intersecting the cloud base height causing clouds to intermittently pass in and out of the instrument sampling volumes (A. Peace, private communication). Such behaviour is identified and discussed in Section 6.4.1.2, and is consistent with the relatively small holographic number densities and low correlations between the small and large particle populations that each instrument is better sensitive to.

To test whether the relatively weak correlation may be due solely to sampling inhomogeneities, this analysis was carried out for a range of window lengths and averaging. Figure 6.6 shows the result of using a 6-hourly moving average by plotting the time series of observations along with their scatter. Despite again broadly agreeing reasonably well, and even with the longer averaging window, there is still relatively poor correlation between these values. This further demonstrates the complementary nature of these observations and their relative strengths and limitations for the measurement of small and large particles.

6.4 Case Studies Overview

A representative selection of case study events was identified during the intensive observation period that encompassed a range of atmospheric conditions. This allowed a full comparison between all deployed instruments to be carried out in the interests of validating the C^2HOM–S instrument alongside reliable instruments and to study the microphysics measurements obtained from the complementary sensors. A key question to be asked is whether the holographic microscope is able to classify atmospheric events based solely on

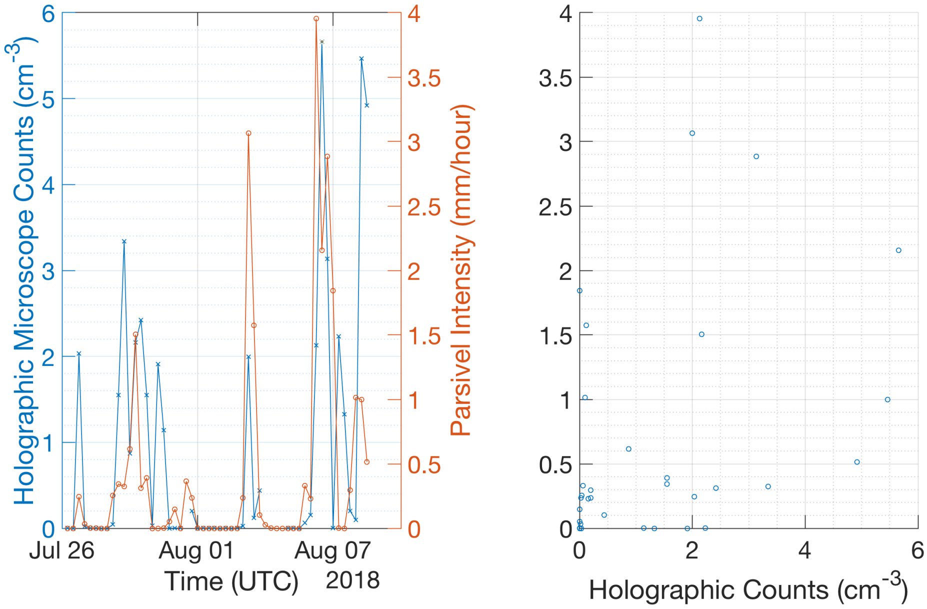

Fig. 6.6 Time series (left) and scatter plot (right) of mean holographic counts and Parsivel intensity with a 6-hourly moving window.

measurements of the number density, size, and shape information. By comparison with the other instruments this will be investigated with a potential application in calibration of remote sensing instruments and for climate model validation.

The case study period extends between August 3rd and August 8th and observations from the key instruments are plotted in Figure 6.7. The in situ observations from the C^{2}HOM–S and Parsivel are displayed along with those from the BASTA and MRR radars. A metric for comparing the remote and in situ observations was found by taking the mean radar reflectivities from the ground up to 100 m altitude, as shown by the green and orange traces. Observations in these lowest height bins are considered less reliable as they are within the near-field regime, yet visual inspection suggests reasonably good agreement with the in situ observations regardless. There will also be cases where significant backscatter is returned in this height range without any particles reaching the ground for the in situ sensors to measure, so complete agreement between these parameters is not expected and the metric is to be used as yet another complementary observation in understanding the events. The Parsivel outputs a rain mask based on the measured size and velocity information which is indicated by the magenta shading.

The four case events of interest are indicated and labelled by letter on this plot. The four instruments agree as to the onset and duration of event A. The rain mask suggests a transition

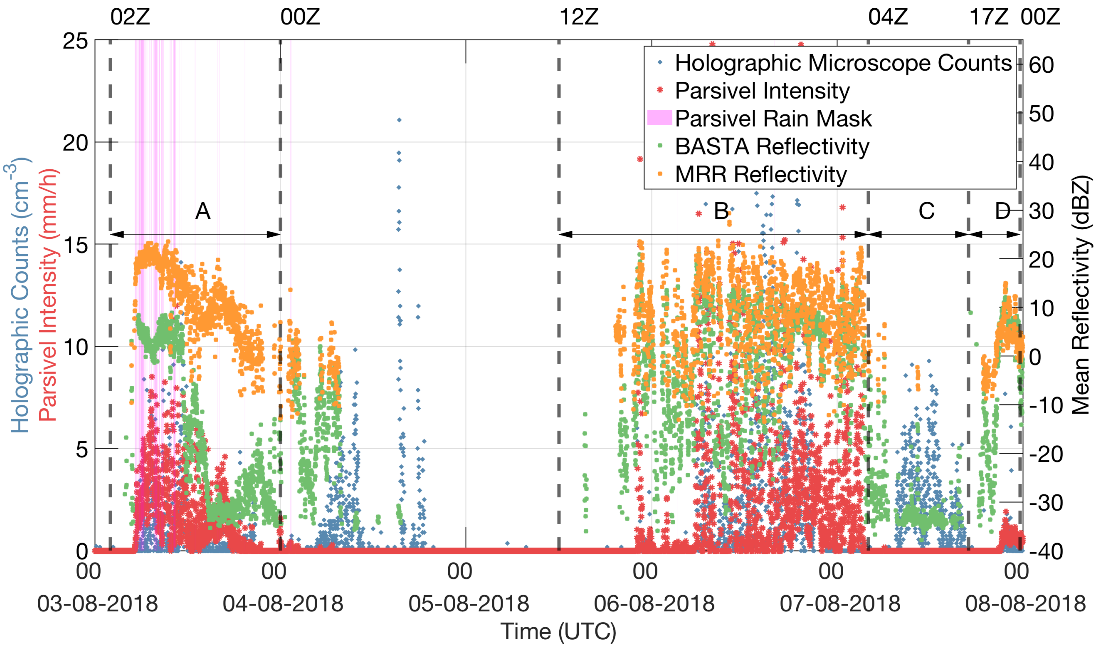

Fig. 6.7 Summary of key observations for the case study period with individual events labelled by letter. Plotted is the holographic microscope number density, Parsivel intensity & rain mask, and ground-to-100 m averages of BASTA and MRR reflectivities.

from liquid to solid precipitation during the event which coincides with a distinct drop in reflectivity from the BASTA but not the MRR. It was noted by observers during this time that the BASTA was experiencing significant icing so it is expected that this is the cause of the sudden discrepancy between radars.

Cases B and D have similarly good agreement between instruments regarding the onset and duration of events. The key difference from case A is that the Parsivel does not report rain during this observation time and the radars tend to agree better throughout the events. Case C is an example of the C^{2}HOM–S detecting particles when the Parsivel does not. The BASTA reports a reflectivity of just -30 dBZ which, whilst low, is above the background noise level, in contrast to times of no atmospheric scatterers such as around August 5th 00Z. The MRR does not measure returns during this event. The BASTA, with a frequency of 95 GHz, has greater sensitivity to small scattering particles than the MRR with a frequency of 24 GHz. This greater sensitivity comes with greater attenuation and so is less suited to the measurement of heavy precipitation events, so observations from both instruments are useful in classifying these events.

A more comprehensive overview of these events is presented in Figure 6.8 which will be studied in more detail over the following sections. The top three panels show the RMAN lidar

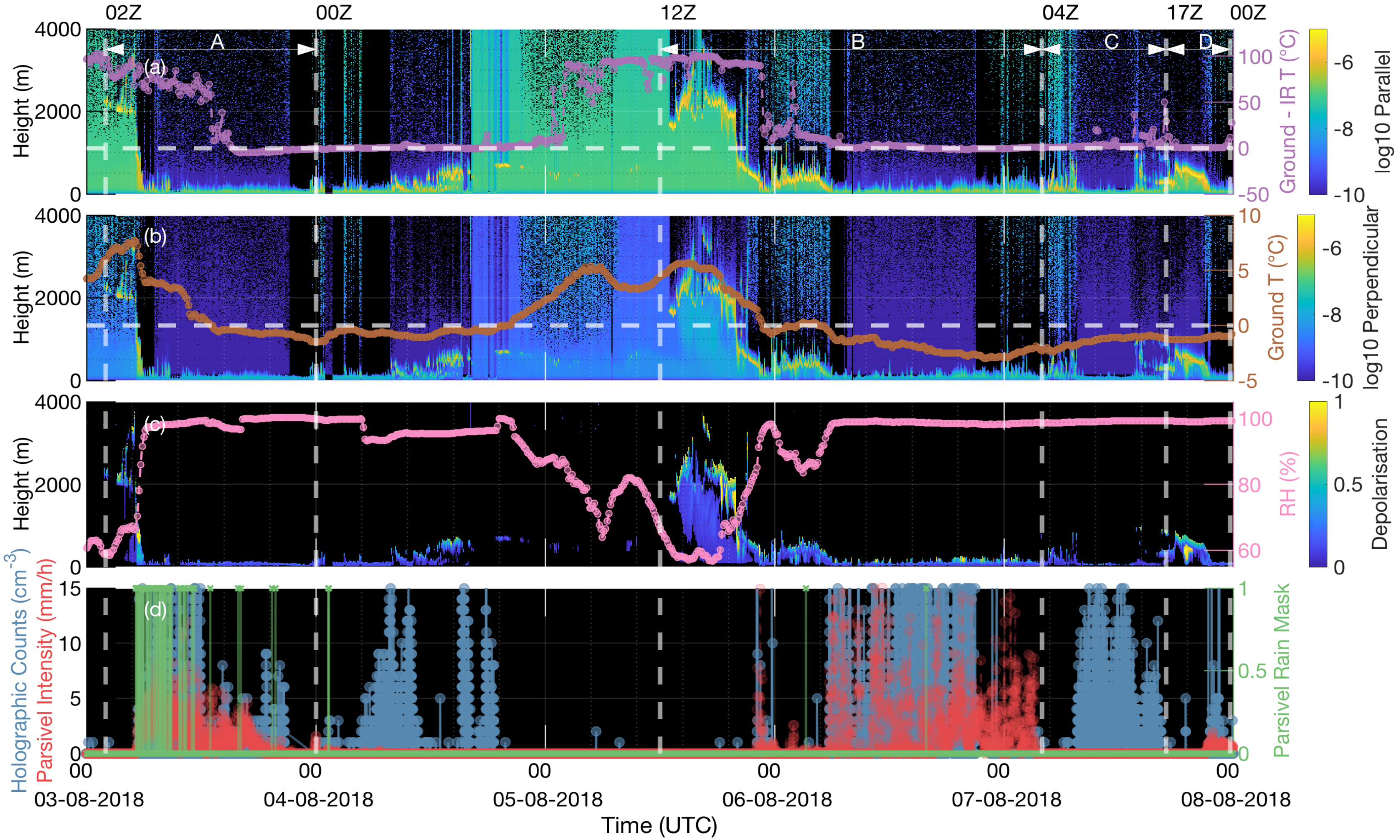

Fig. 6.8 Summary of RMAN lidar and in situ observations for the full case study period: a) parallel backscatter, b) perpendicular backscatter, c) depolarisation, and d) raw holographic microscope number density, Parsivel precipitation intensity, and Parsivel rain mask. Overlaid on the lidar plots from top to bottom are the temperature difference between that reported from the IR thermometer and ground temperature, ground temperature, and relative humidity.

parallel and perpendicularly polarised backscatter and depolarisation with height, and the bottom panel summarises the in situ observations. Overlaid on the top panel is the difference between the ground temperature and the temperature reported by the infrared thermometer. This metric is used as an indicator of when clouds are intersecting the in situ tower for which it is expected to report a temperature difference of zero. This condition is seen for cases B, C, and D which is in contrast to case A for which the difference remains large for a greater fraction of the event duration before going to zero. The ground temperature and relative humidity (RH) traces in the second and third panels indicate that cases B, C, and D were below 0 °C with high RH, whereas case A again had more variation in these parameters. The lidar is heavily attenuated by liquid cloud and precipitation and this is a further indicator of when particles are likely at ground level.

Holographic number density values are seen to fluctuate significantly between holograms, as seen in Figure 6.8 in the bottom panel. Statistically significant number densities can be reported from a single hologram, provided a sufficient number of particles are sampled to give reasonable Poisson counting uncertainties. Number densities reported in the following case analysis sections are 1-minute averaged to provide a more stable metric to compare against the other instruments which are also 1-minute averaged. This matter is discussed in greater detail in Section 6.5.

The holographic particle size distributions, accumulated over the whole period of each case, for the case A, case B, and case C events are shown in Figure 6.9. From these distributions there appear to be clear differences in each of the case events. Case B has the widest distribution which has been cropped in this figure to a value of 300 microns for ease of viewing but extends significantly out to particles of around 800 microns in diameter. This is in contrast to case C which has the narrowest distribution centred on approximately 14 microns. The width of the case A distribution sits between these extreme cases. In all cases the abrupt cutoff at 7 microns is a limitation of the automated analysis method used for particle detection and sizing. Improvements to this algorithm should allow higher resolution observations in future but is outside the scope of this work.

A more qualitative, yet still useful, check of the atmospheric conditions comes from the webcam footage, as indicated by the sample images in Figure 6.10. The top images were taken during case B, with precipitation seen impacted on the camera lens in Figure 6.10a and streaks of advected particles seen during the night in Figure 6.10b. This is in contrast to the view during case C in Figure 6.10c which has significantly reduced visibility compared with the other events. A clear day is shown for reference in Figure 6.10d.

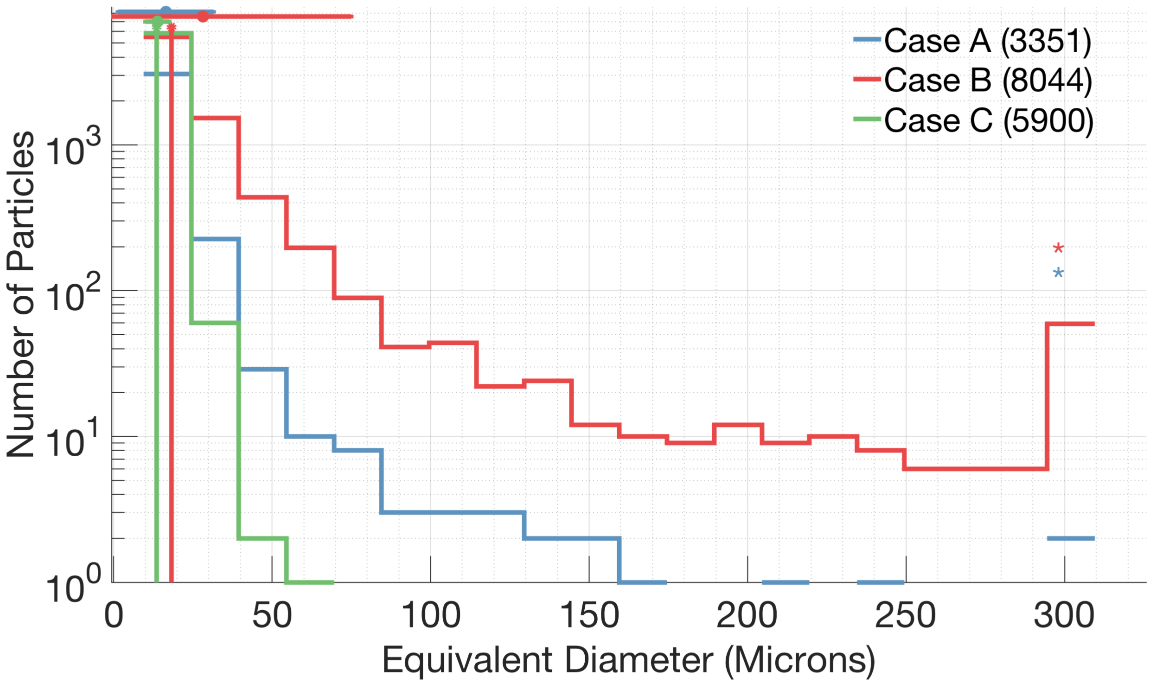

Fig. 6.9 Holographic particle size distributions for the case A, case B, and case C events identified in Figure 6.7. Error bars indicate the mean and standard deviations of each histogram, and the stem plots indicate the median values. The number of particles contributing to each histogram is shown in the legend. The star above the far-right column signifies that this column includes contributions from all data points with value larger than or equal to the bin range. The bin width for all histograms is 15 microns.

6.4.1 Individual Case Analysis

A more detailed analysis of each of the case events identified in Figure 6.7 will now be presented, with the aim of classifying the various atmospheric conditions using the holographic observations. Automated holographic observations were quality controlled for each event through intensive manual analysis. This approach consisted of going through each individual hologram, identifying particle candidates by eye, and hand tracing polygons around the in focus particles within the reconstructed 3D images. This process is slow and so not every hologram could be studied in this way. Instead, representative samples of holograms in key time intervals of the events were focussed on. There are many smaller particles that can be missed by eye that the automated algorithm can more reliably detect and so this validation method is more targeted towards the size and shape measurements, rather than number densities, for which the automated observations are considered more reliable. This manual validation process is discussed in greater detail in Section 3.6.3.

(a) 2018/08/06 03:30:03 UTC

(b) 2018/08/06 13:45:01 UTC

(c) 2018/08/07 02:15:01 UTC

(d) 2018/08/08 23:30:04 UTC

Fig. 6.10 Collocated webcam views of the instrument platform over case events B and C. a) Water droplets on the camera lens in high visibility, b) streaks of advected particles during the night, c) water droplets on the camera lens in low visibility, and d) clear conditions.

The manual quality-control process provides a reliable dataset for validating the automated observations in this case period. As this period encompassed a diverse range of atmospheric conditions, it is anticipated that this will serve as a calibration process, alongside observations from the other instruments, so that in future automated holographic observations can be interpreted without the need for this manual verification. The manual dataset is also of use for training of machine learning based particle classification methods.

6.4.1.1 Case A

A representative selection of manually extracted holographic particle images for the case A event is shown in Figure 6.11a with 200 micron scale bars overlaid. A mixture of cloud droplets as well as small, spherical rain droplets are found. A population of large irregularly-shaped particles are observed starting from 10Z, coinciding with when the BASTA

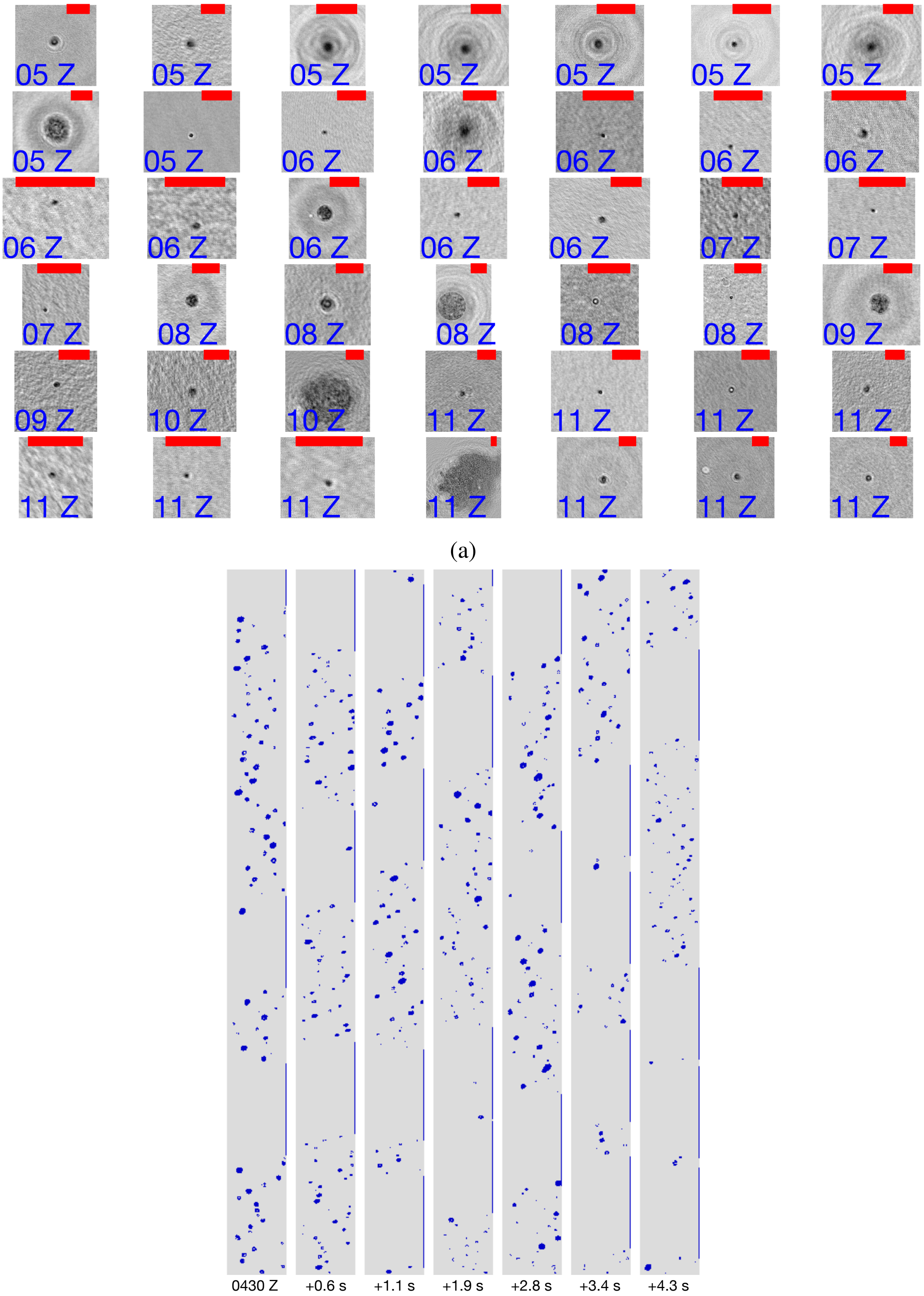

(a)

(b)

Fig. 6.11 Representative particle images for the August 3rd case A event from the a) C^2HOM–S and b) PIP. Particle detection times are indicated in the bottom-left corner of each holographic image and holographic scale bars have a fixed width of 200 microns. The width of each column of PIP data indicates the width of the sampling area which is 6.2 mm. The time of the first particle detection by the PIP is shown underneath the first column of PIP observations and the subsequent number of seconds relative to this first detection are shown under each additional column.

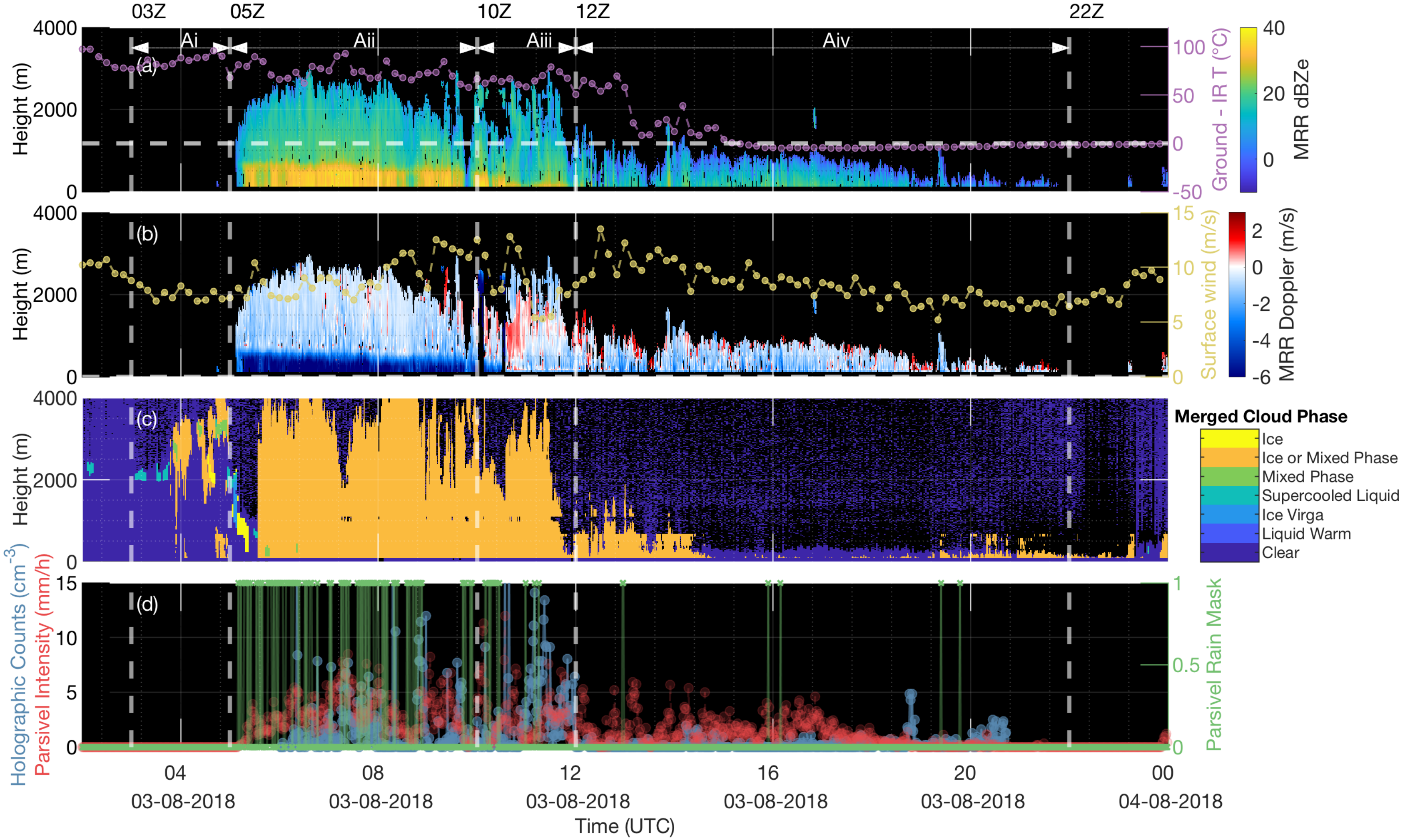

Fig. 6.12 Summary of radar and in situ observations during the August 3rd case event. a) MRR reflectivity, b) MRR Doppler velocity, c) Merged BASTA + RMAN cloud phase determination, and d) Holographic microscope number density, Parsivel precipitation intensity, and Parsivel rain mask.

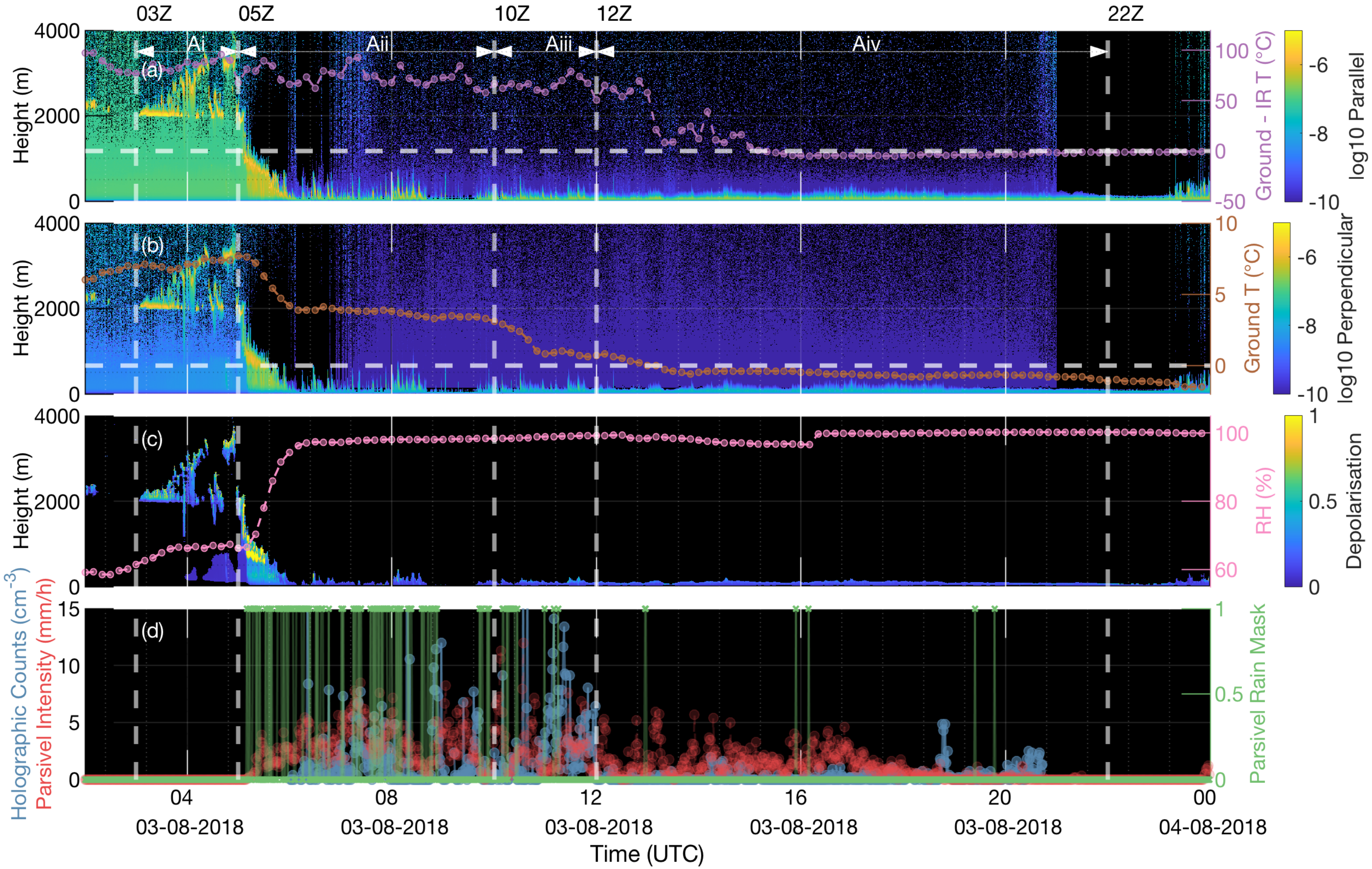

Fig. 6.13 Summary of RMAN lidar and in situ observations during the August 3rd case event. a) Parallel polarised backscatter, b) Perpendicularly polarised backscatter, c) Depolarisation, and d) Holographic microscope number density, Parsivel precipitation intensity, and Parsivel rain mask. Overlaid on the lidar plots from top to bottom are the temperature difference between that reported from the IR thermometer and ground temperature, ground temperature, and relative humidity.

radar returns dropped due to icing. From 12Z onwards the particle number density drops significantly and mostly small droplets are again seen.

The particle images can be compared to those from the collocated PIP 2D imaging probe. A representative summary of images are presented in Figure 6.11b which broadly agree with the particle types seen by the holographic microscope. It was decided that the PIP would not be used for quantitative observations due to known limitations relating to out-of-focus particles, the use of correction methods developed for airborne rather than ground-based installations, and potential particle shattering on the probe inlets (Y. Huang, private communication). It is noted that the latter issue can be more easily corrected in the holographic observations as a shattered particle can be rejected based on an anomalously large number of particles suddenly entering the sampling volume which is one of the key advantages of this technique and has been applied in this analysis.

Both instruments report a mixture of small and irregularly-shaped particles, with a lower number density of large irregularly-shaped particles. Crude quantitative comparisons between the instruments can be made by noting that the width of the PIP sampling area is 6.2 mm and it can be seen that there are a number of particles up to around 100 microns, as also reported by the holographic microscope, though these are not well focussed given that 100 microns is the minimum resolved particle diameter for the PIP.

A more detailed summary of case A is provided in Figure 6.12 and 6.13. The top two panels of Figure 6.12 show the MRR reflectivity and Doppler velocities, respectively, and the third panel gives the cloud phase classification based on a combination of BASTA and lidar observations. Figure 6.13 provides a summary of lidar observations, similar to that shown in Figure 6.8 for the full case period. Both of these figures will be implicitly referred to in the following discussion.

The event begins in the region annotated as Ai with lidar observations of a multi-layered cloud system at heights of approximately 2 km and 3.5 km. The depolarisation is consistently low, and high values seen at the top of the returns are likely due to attenuation and multiple scattering of the lidar as it is extinguished by liquid layers since the radar instruments, which are more sensitive to larger ice crystals, do not see returns during this time. Observations on the ground are not reported during this time by the in situ sensors.

The region marked as Aii begins with the appearance of ground level backscatter seen by the lidar and radar instruments along with a sudden rise in the relative humidity and a drop in ground temperature. Despite this drop, the ground temperature remains above 0 °C and the IR temperature difference remains large, suggesting that a cloud has not passed through the tower and rather that this may be a rain event.

This interpretation is further supported by the radar observations which indicate a significant increase in radar reflectivity, coinciding with a large negative Doppler signal, up to a height of approximately 500 m. This is not a typical bright band feature, for which the radar returns would be expected to be relatively high at the melting layer and quickly decrease in value towards the ground due to a reduction in number density of rain droplets as the fall velocity increases [314]. It is possible that the melting layer was too close to the ground to see the subsequent reduction in reflectivity, but in either case, it is suggestive that rain was falling during this time.

This event is seen more prominently in the MRR observations than the BASTA observations, as expected since the lower frequency will be less attenuated during a rain event. The lidar remains heavily attenuated during this time, which is also expected during heavy rain, and the Parsivel rain mask is consistently high during this period. It is during this time that the most intense in situ observations are reported on the ground and only spherical droplets are seen by the holographic microscope, consistent with rain.

The beginning of region Aiii, starting at 10Z, marks a clear transition in the characteristics of this event. A weakening of the bright-band feature is seen in the MRR reflectivity and this coincides with significant fluctuation and positive-going components in the Doppler signal. Throughout all periods the cloud phase classification is mixed phase, suggesting a population of both ice and water droplets from which rain and snow can be formed. During this time the holographic microscope and PIP report large, irregularly shaped particles at a lower number density than the droplets. All observations are consistent with a short-lived snowfall event, perhaps produced as a product of the convective conditions within this part of the cloud. During this time the temperature drops rapidly towards 0 °C, indicative of the colder conditions required for ice and snow formation.

Region Aiv sees a sudden disappearance of the rain feature in the radar reflectivity, a negative Doppler velocity that is smaller in magnitude, and a drop in the IR temperature difference towards zero. Significantly fewer counts are reported by the holographic microscope and Parsivel during this time. The detection of particles by the Parsivel suggests that this is a period of significantly lighter rain following the main event in the previous sections. There is a brief data drop out from the holographic microscope from 22Z to 24Z as the hard drive was being prepared to be swapped out. Following this period the Parsivel does not see counts whereas the holographic microscope does and the lidar is still attenuated at ground level, as seen in Figure 6.8. Breaks in the low-level layer seen in the lidar coincide with reductions in counts in the holographic microscope until this feature fully dissipates at approximately 18Z on August 4th. This is suggestive of a low layer of cloud following the rain event that the Parsivel was unable to resolve due to the small particle sizes.

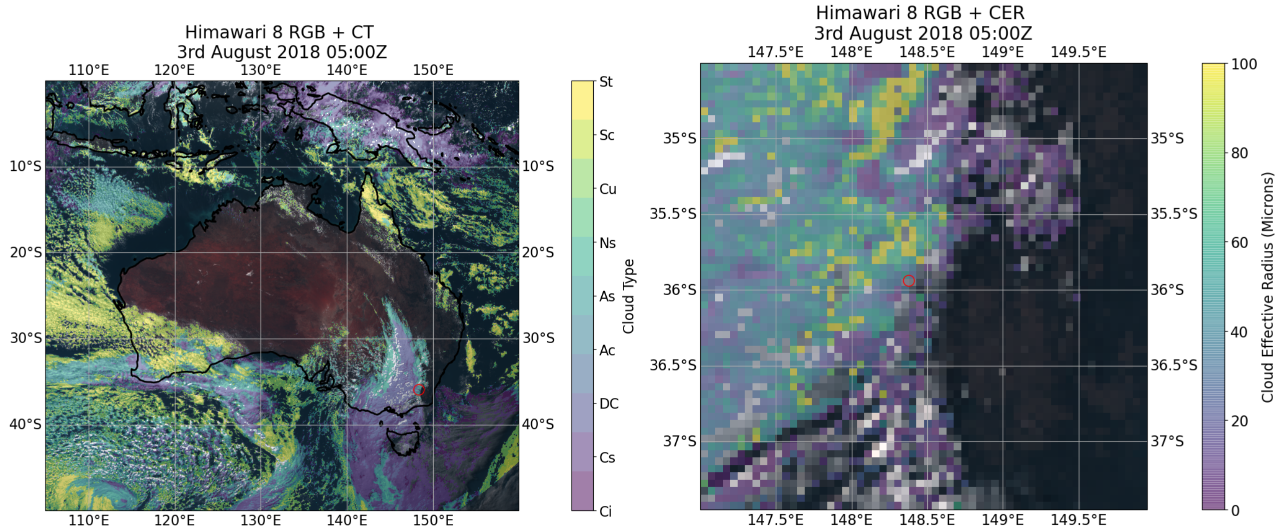

(a) (b)

Fig. 6.14 HIMAWARI-8 retrieval of a) Cloud Type (CT) and b) Cloud Effective Radius (CER), during the August 3rd case A event. The red circle indicates the position of the observation tower.

The microphysical observations can be compared with the large-scale observations of the HIMAWARI-8 satellite imager from 05Z at the start of case A. Figure 6.14a shows the cloud type classification over the wider region. It is apparent that a large-scale frontal system is passing over the field site, indicated by the red circle, during this time. The system consists of both high and mid level cloud, as indicated by the lidar observations during Ai, but no low-level clouds are reported, in further support of this being a rain event detected on the ground rather than a cloud. The retrieved Cloud Effective Radius (CER) values are shown in Figure 6.14b. A mixture of both small particles and smaller regions of large particles are observed. This is consistent with the sudden change in dynamics of the event observed in Aiii as this appears to be a rather inhomogeneous cloud system.

6.4.1.2 Case B

A representative summary of the ice crystals measured by the C^2HOM–S for case B are shown in Figure 6.15a and PIP images are in Figure 6.15b. An abundance of large, irregularly shaped particles were observed by both instruments with a mean diameter of approximately 200 microns for the holographic observations. Needle particles with a significantly lower number density were also detected with maximum dimensions as high as approximately 800 microns. A population of small droplets and irregular particles was seen by both instruments

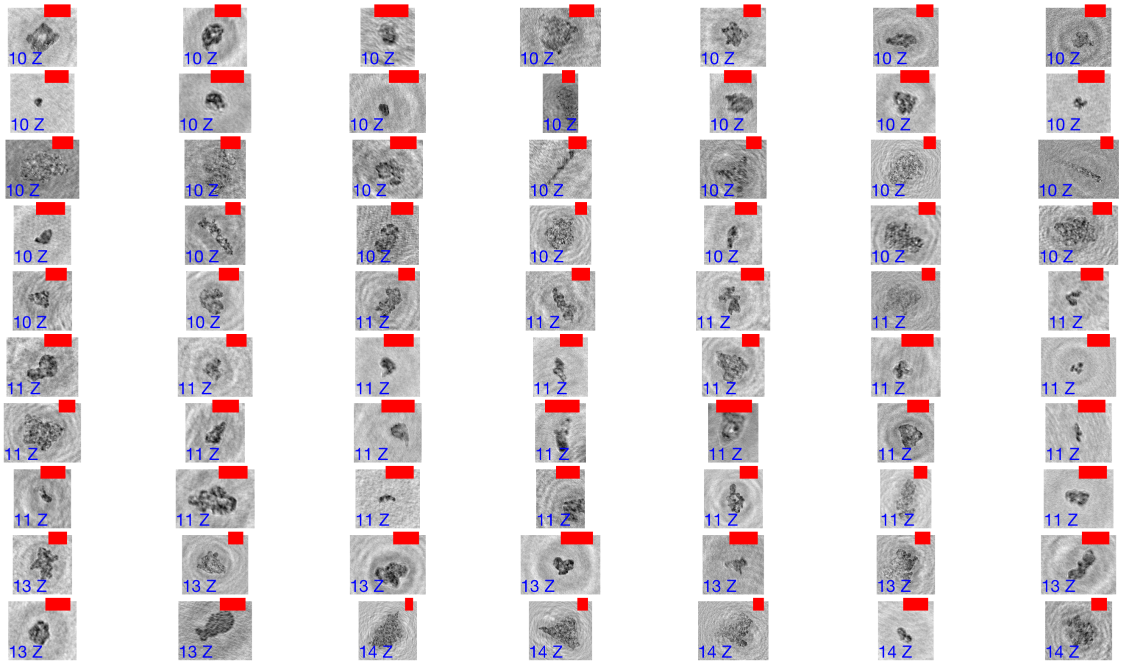

(a)

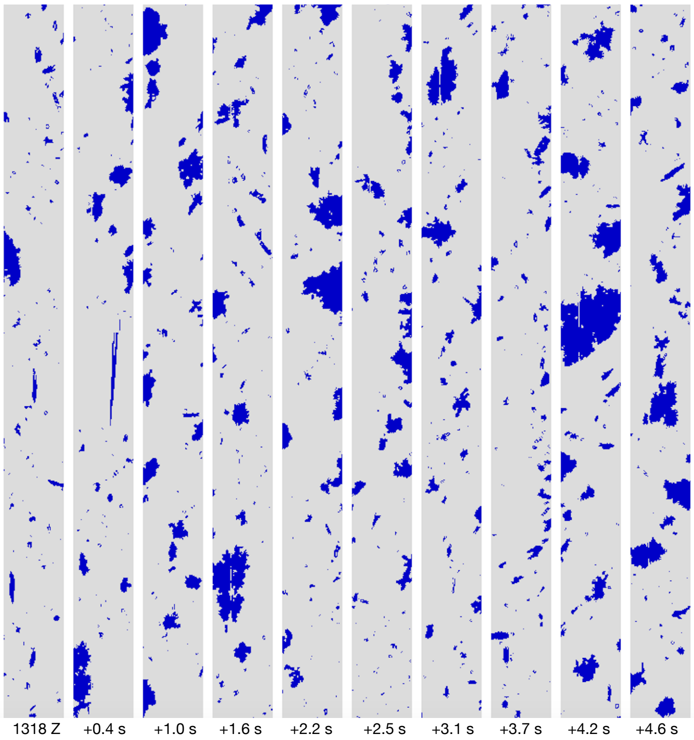

(b)

Fig. 6.15 Representative particle images for the August 6th case B event from the a) C^2HOM–S and b) PIP. Particle detection times are indicated in the bottom-left corner of each holographic image and holographic scale bars have a fixed width of 200 microns. The width of each column of PIP data indicates the width of the sampling area which is 6.2 mm. The time of the first particle detection by the PIP is shown underneath the first column of PIP observations and the subsequent number of seconds relative to this first detection are shown under each additional column.

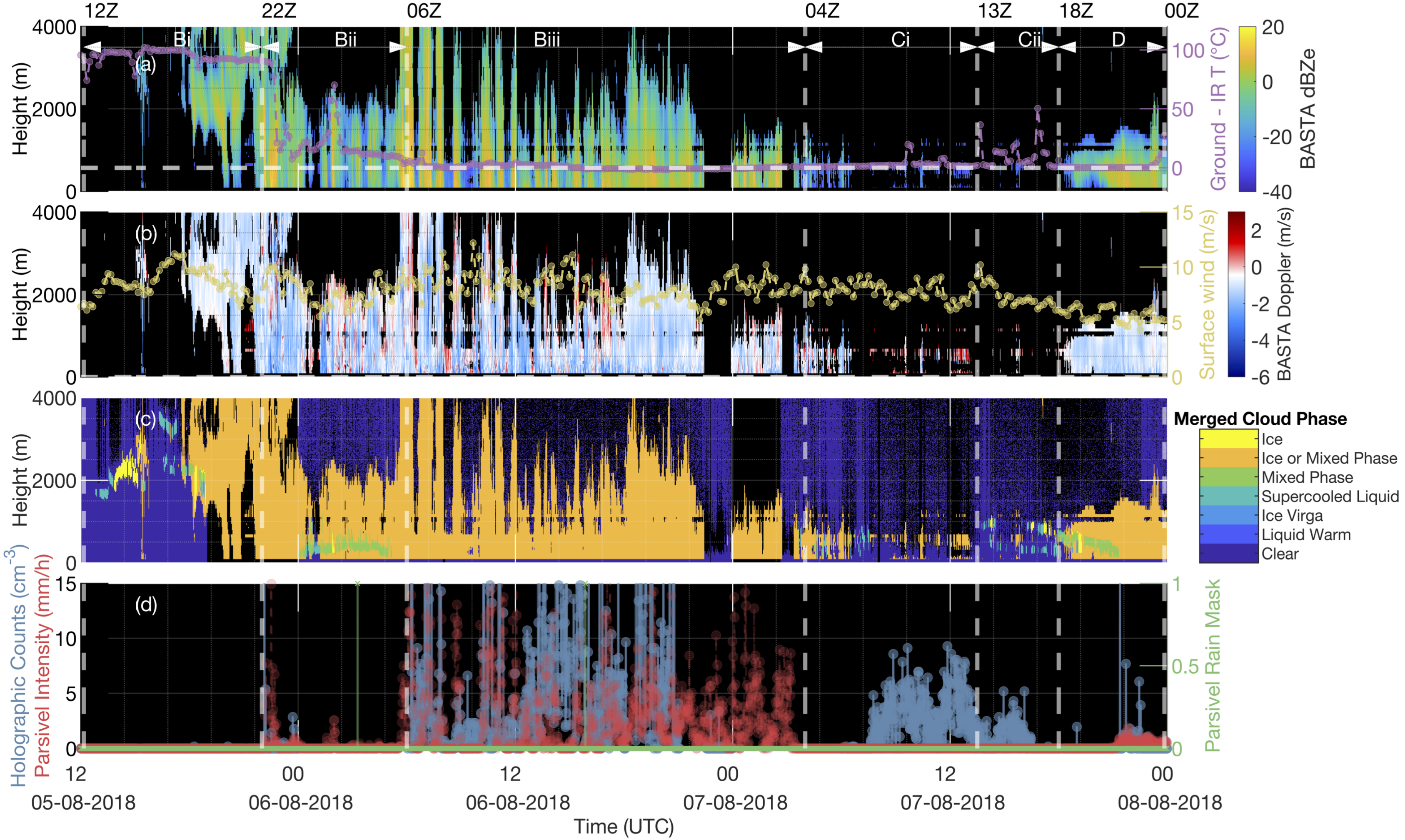

Fig. 6.16 Summary of radar and in situ observations during the August 6th case event. a) BASTA reflectivity, b) BASTA Doppler velocity, c) Merged BASTA + RMAN cloud phase determination and d) Holographic microscope number density, Parsivel precipitation intensity and Parsivel rain mask.

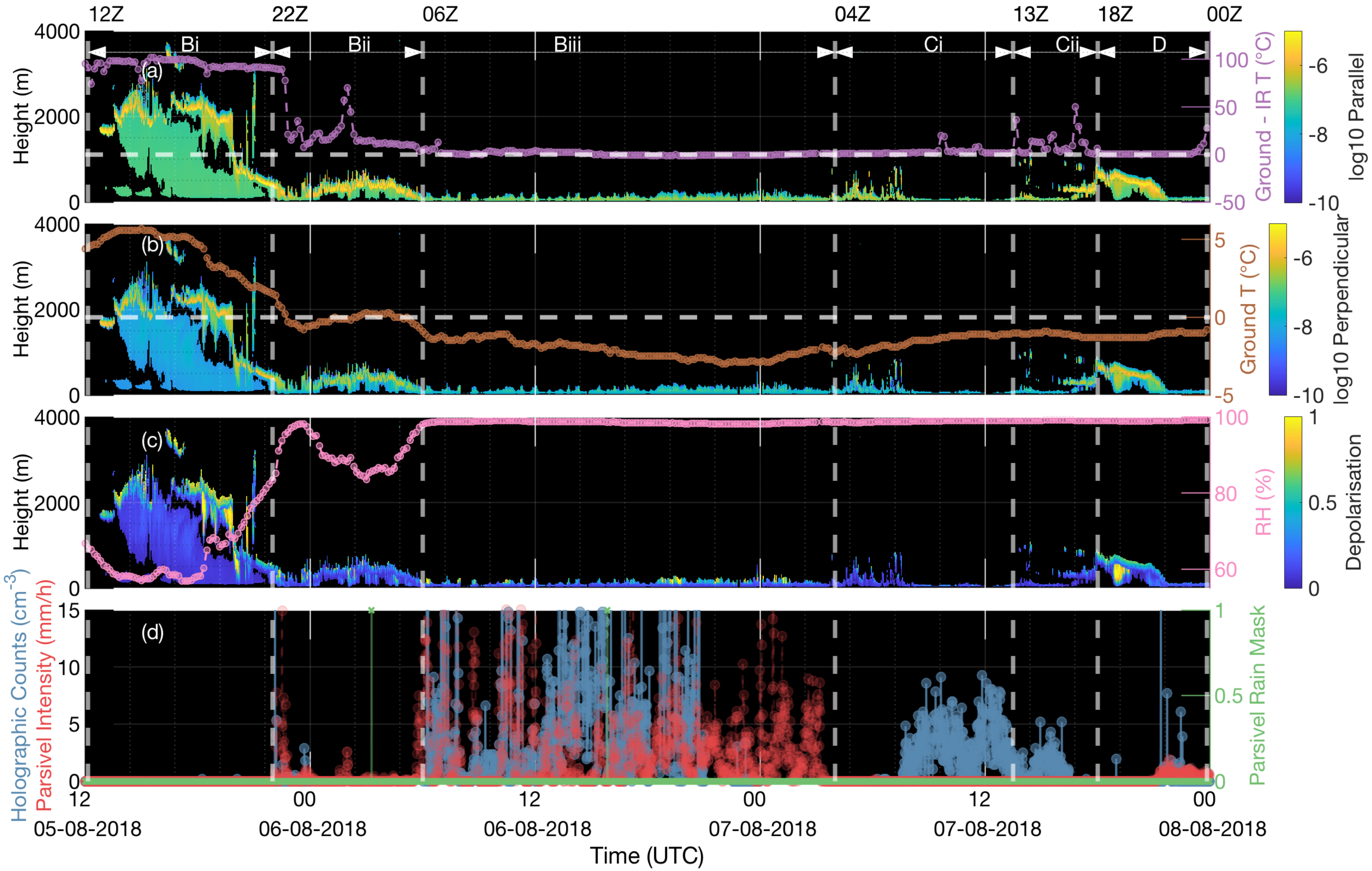

Fig. 6.17 Summary of RMAN lidar and in situ observations during the August 6th case event. a) Parallel polarised backscatter, b) Perpendicularly polarised backscatter, c) Depolarisation and d) Holographic microscope number density, Parsivel precipitation intensity and Parsivel rain mask. Overlaid on the lidar plots from top to bottom are the temperature difference reported from the IR thermometer and ground, ground temperature and relative humidity.

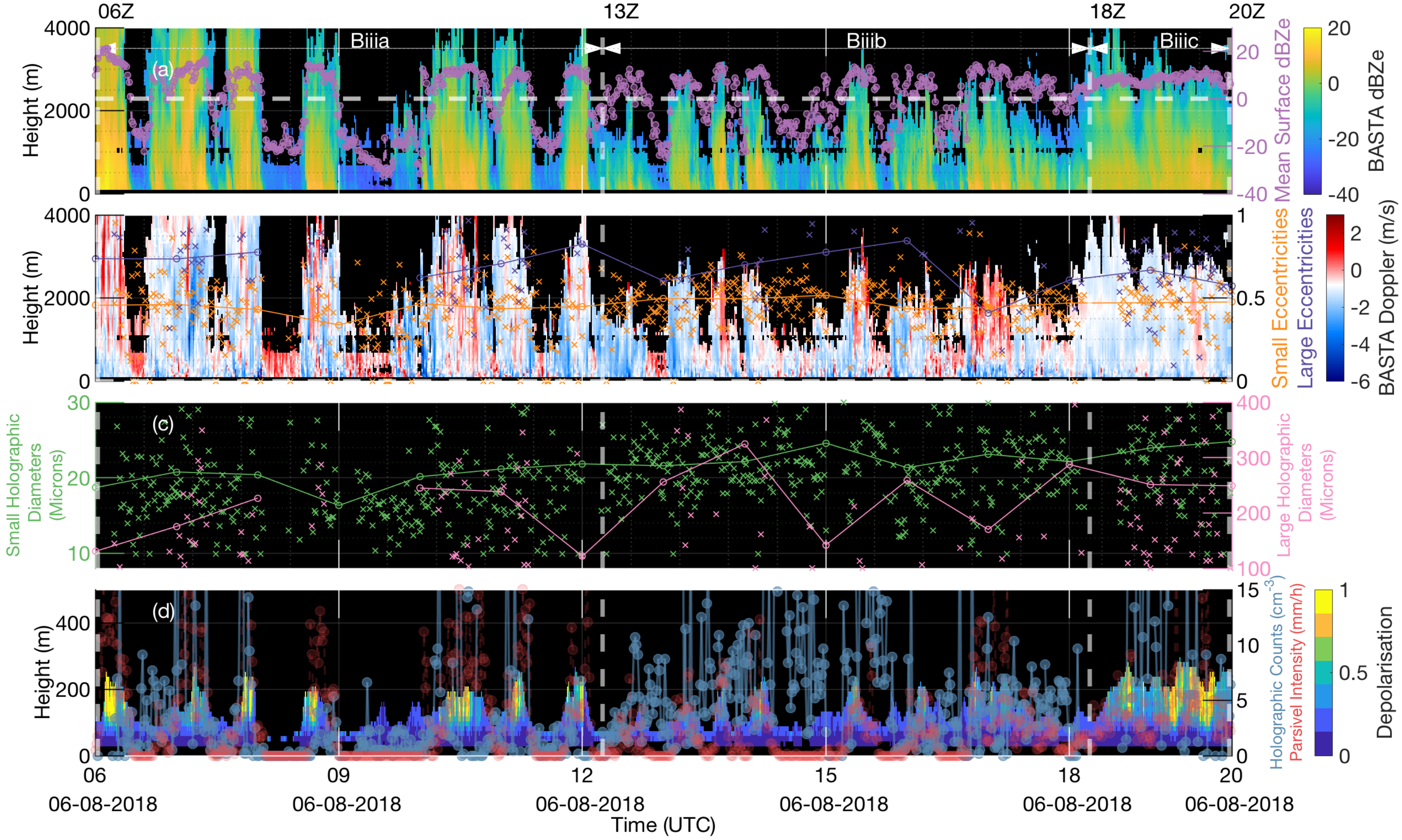

Fig. 6.18 Summary of key microphysical observations during the August 6th Biii sub event. a) BASTA reflectivity, b) BASTA Doppler velocity and holographic eccentricities for large (>100 microns) and small (<100 microns) particles, c) Holographic diameters for large (>100 microns) and small (<100 microns) particles and d) Holographic microscope number density, Parsivel precipitation intensity and depolarisation.

throughout the event and the PIP observed a significant fraction of particles with sizes up to the horizontal size limit of approximately 6 mm, indicating snow or very large ice crystals.

The larger particles were detected in bursts, whereas the smaller particles were present for the entirety of the event, as shown in Figure 6.4. The mean particle size reported by the Parsivel decreases steadily over the course of the event. Concurrently, the holographic hourly running mean diameter for large particles increases from approximately 150 to 250 microns. The running mean diameter for small particles increases by approximately 10 microns during this time and is a more statistically significant observation given that many more particles of small size were measured and since the observations are expected to follow Poisson counting statistics.

Case B is summarised more thoroughly in Figure 6.16 and Figure 6.17 which display the same parameters as described in the case A section. Multiple layers of mid-level cloud are seen by the lidar during the Bi region, most notably including a low-level cloud at a height of 1 km appearing around 21Z. No particles are measured on the ground during this time and consistently the IR temperature difference remains high and RH is low.

The low-level cloud feature is seen to descend to ground level which marks the beginning of region Bii. This coincides with the onset of in situ particle detections, a drop in ground temperature below 0 °C, the IR temperature difference going to zero, and an increase to 100 % RH – all consistent with a cloud feature. In situ particle detections are seen for only a short duration and then the cloud feature is seen to rise above ground in the lidar observations, corresponding to a drop in RH, before descending back to ground again with a rise in RH and further in situ observations. Such agreement demonstrates that the holographic microscope is reliably sampling cloud systems as they pass through the ground-level sampling volume.

Region Biii features consistent particle detections throughout the event by the in situ instruments along with a sub-zero temperature that is potentially suitable for ice formation. Note that the holographic counts are zero from 00Z as these data have been discarded due to the sunlight saturation filtering. The lidar is fully attenuated at surface level throughout the event and the RH and IR temperature difference also confirm that there is a persistent cloud layer at the ground. The BASTA & lidar cloud phase algorithm reports mixed phase conditions for the entirety of this event.

Figure 6.18 presents a summary of the microphysical processes during this period. The BASTA reflectivity and Doppler velocity are shown in the top two panels with the ground-to-100 m averaged reflectivity overlaid in purple. Significant variation is seen in these properties in both time and height, suggestive of patchy multi-cellular clouds. Regions of particularly dense cloud are identified in regions Biiia and Biiic, primarily by the larger BASTA reflectivities in cloud cells that extend up to around 4 km in altitude. This is supported by the correlation between the large lidar depolarisation values within these cells and increases in particle counts from the in situ instruments. This is likely not due to the presence of ice, as the regions of high depolarisation are only at the top of the returns, but rather is consistent with an increase in the number density of cloud particles that leads to multiple scattering and attenuation of the lidar beam.

Time periods of stronger reflectivity coincide with the bursts of ice crystals measured by the holographic microscope, as shown in the third panel. Given the mean size of approximately 200 microns for the large particles, it is not immediately clear whether these correspond to falling snow or a mixed phase cloud. Doppler velocities in these regions are consistently negative near the ground, though weaker than for the rain event in case A, and no bright band feature is detected. Fall velocities of up to a few m s^{-1} are consistent with the interpretation of falling snow rather than rain or hail [315, 316]. The webcam reports streaking particles with high visibility and visible snow on the ground, and the Parsivel size distribution extends significantly up to 10 mm.

For these reasons it is suggested that this is a snow event; however, the persistent presence of small spherical particles throughout suggests that there is also an embedded cloud at ground level consisting of small ice crystals and supercooled water droplets. The lack of high-altitude returns and insufficient number densities to induce multiple scattering in the lidar returns in region Biiib support the inference that this observation period is solely of the embedded mixed phase cloud. Clouds in the other regions have greater vertical extent, allowing more time for the falling ice crystals to grow and reach the ground as large snow flakes.

The automated holographic eccentricities for large and small particles are overlaid on the second panel. The ice crystals have consistently larger eccentricities than the mostly spherical water droplets that make up the small particle category, though small irregularly-shaped ice crystals are also seen. The eccentricity of the spherical water droplets has a consistent value of around 0.5, whereas the ice crystals show more variation indicative of the greater variety of possible ice crystal shapes. Such separation between these populations gives hope that this simpler metric can be used to automatically classify the shape characteristics, despite not going to zero for spheres as might intuitively be expected. Regardless of this result, it is likely that a more sophisticated metric encompassing other geometric properties will be required for reliable classification in future.

As identified earlier, a 10 micron increase in mean diameter is observed for the supercooled water droplets along with a 100 micron increase for the ice crystals over the course of this event. This coincides with a 100 micron decrease in the mean size of particles measured by the Parsivel – with sizes in the range of roughly 300 microns to 10 mm – from approximately 900 to 800 microns. This occurs over a span of approximately 14 hours over which time the temperature steadily decreases by a few degrees.

A potential explanation for the observed particle size variations is outlined as follows. As the multi-cellular cloud system moves over the field site, progressively older clouds, which have had more time for particles to grow and subsequently fall to the ground as snow, are measured. It is plausible therefore that the mean diameter of large particles, seen by the Parsivel, should decrease over time as the largest particles are removed from the cloud as precipitation. Whilst this is happening, the particles within the low-level mixed phase cloud continue to grow due to conditions permitting simultaneous growth of ice and liquid droplets – as opposed to those in which the parasitic Wegener–Bergeron–Findeisen (WBF) ice crystal growth process [317] is favoured – in the <300 micron size range observed by the holographic microscope. The temperature varies between approximately -1 °C and -3 °C, and an abundance of supercooled water droplets was observed over this time. Such conditions are suited to the growth of water droplets by condensation, and the formation of large snow particles via riming and aggregation [39, 74]; consistent with the predominantly irregularly-shaped ice crystals observed.

Whilst the WBF process is commonly observed in mixed phase clouds, it has been identified that such clouds can persist for hours and even days beyond the predictions of the underlying theory [77]. The mechanism for simultaneous growth of droplets and ice crystals has been shown possible under certain thermodynamic conditions which can be stated as a required lower limit on the updraft velocities [78]. Using the mean ice crystal number density of 0.3 cm^{-3} and the mean diameter of 200 microns, the vertical velocity necessary is of the order of a few m s^{-1}. Vertical velocities of this magnitude are seen throughout the event in the Doppler velocity returns. The cloud event is observed by all instruments for at least 14 hours, consistent with the interpretation that this persistent event is not driven by the WBF mechanism. The observed snowfall lends further support to this conclusion as falling ice is removed from the cloud layer which diminishes its ability to compete with the supercooled water droplets for water vapour. This interpretation is consistent with that of previous observations of mixed phase clouds over a mountainous region, with mixed phase clouds persisting for up to 8 hours in some cases [318].

The synoptic conditions can be inferred from the HIMAWARI-8 cloud type retrievals shown in Figure 6.19a. A large-scale frontal system is seen on the bottom right of this figure that has recently passed over the field site. The field site instruments appear to be sampling a low-level system of post-frontal cloud cells over this time. This can be seen more clearly in the zoomed view of Figure 6.19b showing the Cloud Effective Radius (CER) retrieval. A large-scale population of particles with a small effective radius, consistent with a low-level

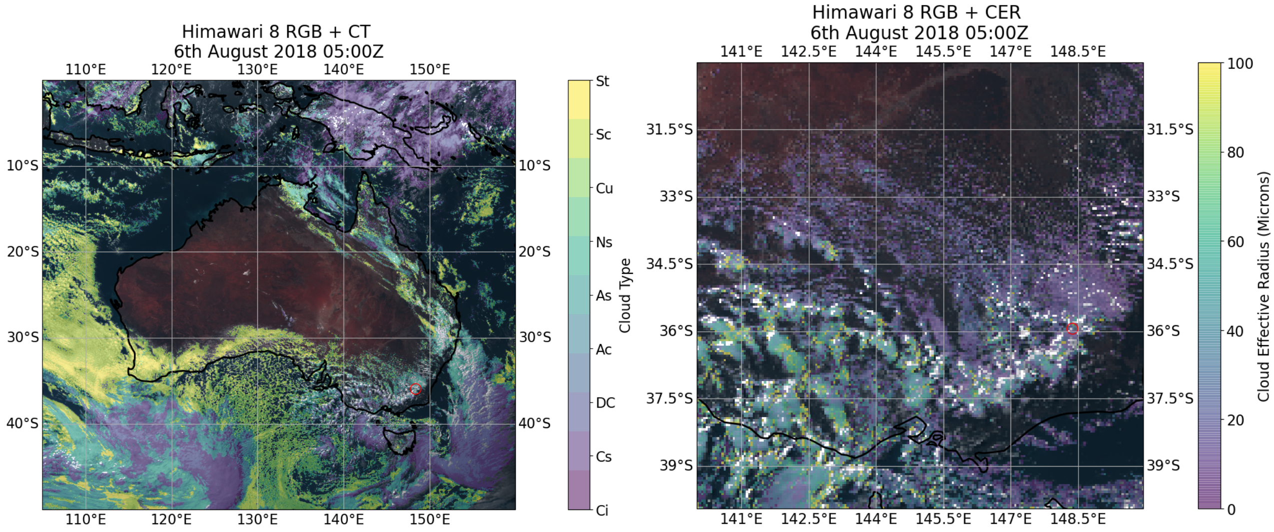

(a) (b)

Fig. 6.19 HIMAWARI-8 retrieval of a) Cloud Type (CT) and b) Cloud Effective Radius (CER), during the August 6th case B event. The red circle indicates the position of the observation tower.

cloud, is identified along with patchy regions of enhanced particle sizes, suggestive of larger ice crystal formation. These observations are consistent with the previous interpretation of a low-level mixed phase cloud with regions of enhanced ice crystal number density and falling snow.

The interpretation depends on the key assumption that cells within this larger-scale system were formed at a similar time and that individual cells are representative of a larger-scale system with comparable microphysics. The former assumption was supported by inspection of the HIMAWARI-8 imagery over multiple days and noting the persistence of the cloud system as it passed over the field site. The assumption that each cell has a comparable microphysical history is harder to test and quite likely to not hold given the complexity of the processes involved. The observation of a statistically significant and linear increase in droplet size from cell to cell throughout all cells passing over the field site lends some support to this interpretation, but it is not enough to be conclusive.

It should also be noted that significantly fewer ice crystals were detected than water droplets and the observed increase in particle diameter may not be significant within the bounds of Poisson counting uncertainties. Given these limitations, it is not possible to conclusively show that this interpretation of the cloud evolution is correct but the inferences drawn from this unique suite of instruments should be of use in guiding future investigations of this kind. Applying this style of analysis to more cloud events in the dataset should allow more statistically significant results about the nature of cloud evolution to be inferred, but this remains the topic of future investigations.

6.4.1.3 Case C and Case D

A representative summary of C^2HOM–S and PIP particle images for case C is shown in Figure 6.20. A noticeable decrease in the mean particle diameter to approximately 20 microns is observed relative to that found in previous events, though notably the population of small particles is consistent with those measured in case B, as can be seen in Figure 6.9 for diameters less than approximately 30 microns. The PIP is less suited to the measurement of small particles – with a reported resolution of 100 microns – but general agreement is found between the instruments. Spherical particles are predominantly observed, though irregularly-shaped particles, that cannot be reliably classified due to the resolution limits of both instruments, were also seen.

Observations from the other key instruments are summarised in Figure 6.16 and Figure 6.17. The region annotated as Ci begins with the embedded mixed phase cloud – as identified in case B – ascending slightly above ground height, as seen in the lidar returns. This coincides with the end of in situ particle detections, before the cloud descends again along with a subsequent onset of particle observations by the holographic microscope. The population of mostly spherical particles with a mean diameter of approximately 20 microns are well below the size resolution limit of the Parsivel and, given the sub-zero temperature, appear to indicate a cloud consisting of supercooled water droplets and a lower number density of small irregularly-shaped ice crystals. The BASTA reflectivities are significantly lower in value and patchier than seen in case B which is further consistent with the end of falling snow and a reduction in number density of large particles in the low-level cloud.

Region Cii starts with a reduction in the holographic number densities coinciding with the appearance of a multi-layered, relatively low depolarisation feature, in the lidar returns. The reduction in droplet number density should coincide with a decrease in cloud optical depth, so this association is expected. This is further consistent with the variation seen in the IR temperature difference over this time, as the IR thermometer measures the temperatures of layers of cloud at different heights through the patchy low-level cloud.

In region D the low-level cloud has fully dissipated and holographic counts go to zero. The multi-layered cloud feature is consistent with a supercooled liquid upper layer together with a region of ice crystals below, as based on the respective low and high depolarisation of these features. The high depolarisation in the region of ice crystals is not interpreted as multiple scattering since the depolarisation decreases above this feature whilst the lidar backscatter signals remains relatively strong, suggesting that the beam has not been signif-

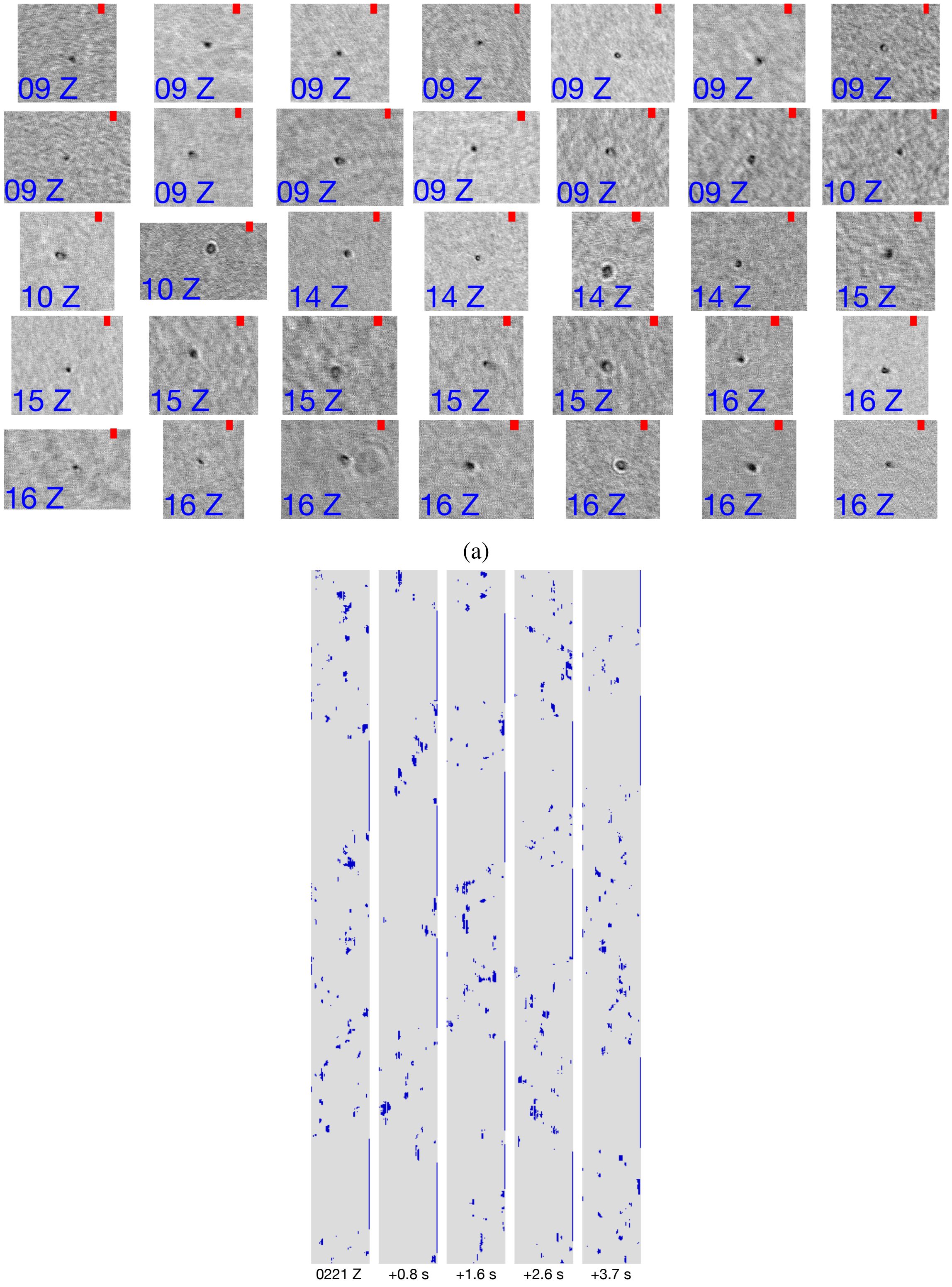

(a)

(b)

Fig. 6.20 Representative particle images for the August 7th case C event from the a) C^2HOM–S and b) PIP. Particle detection times are indicated in the bottom-left corner of each holographic image and holographic scale bars have a fixed width of 200 microns. The width of each column of PIP data indicates the width of the sampling area which is 6.2 mm. The time of the first particle detection by the PIP is shown underneath the first column of PIP observations and the subsequent number of seconds relative to this first detection are shown under each additional column.

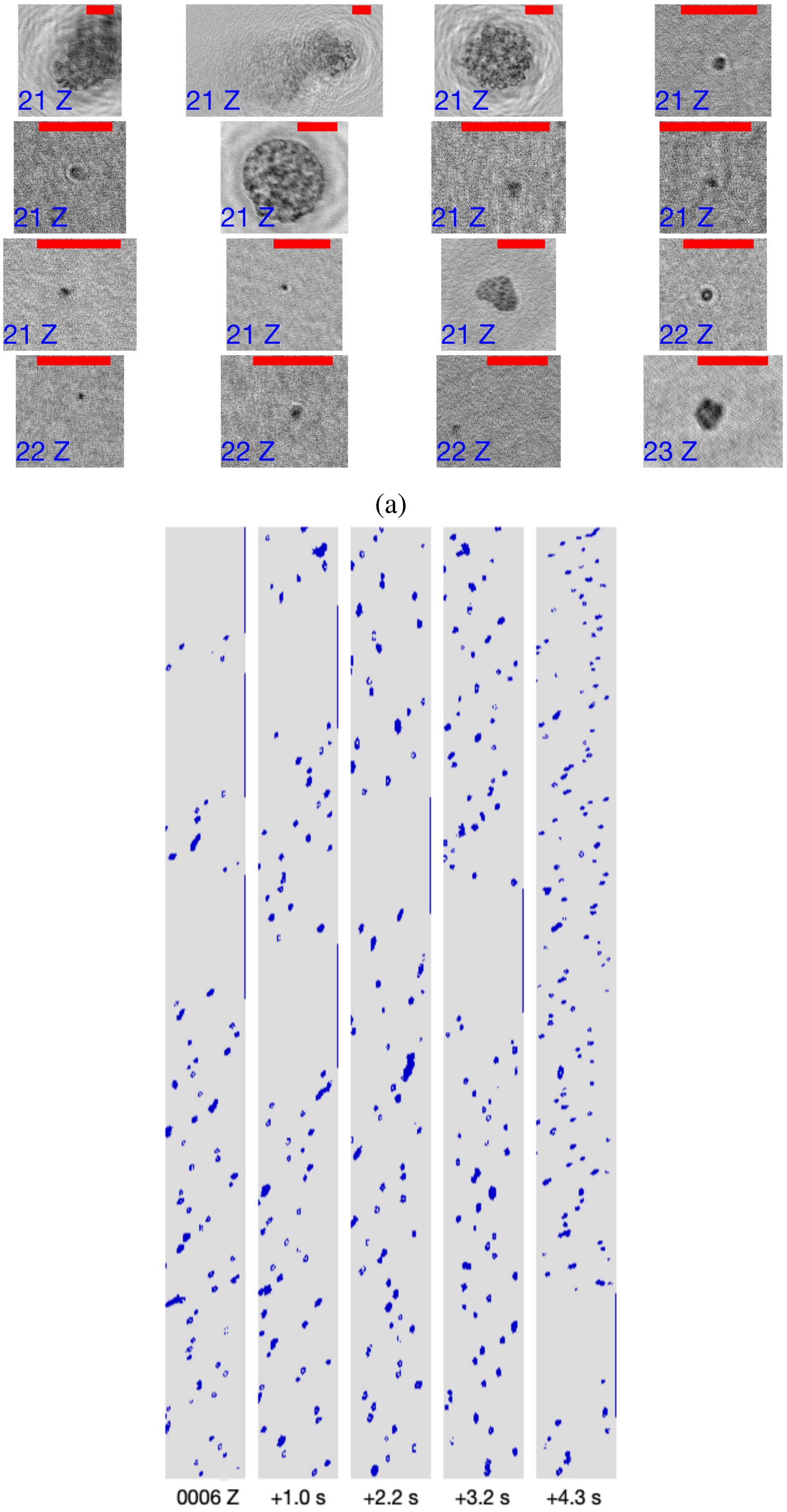

(a)

(b)

Fig. 6.21 Representative particle images for the August 8th case D event from the a) C^{2}HOM–S and b) PIP. Particle detection times are indicated in the bottom-left corner of each holographic image and holographic scale bars have a fixed width of 200 microns. The width of each column of PIP data indicates the width of the sampling area which is 6.2 mm. The time of the first particle detection by the PIP is shown underneath the first column of PIP observations and the subsequent number of seconds relative to this first detection are shown under each additional column.

icantly attenuated. A very small number of particles are seen reaching the ground by the holographic microscope while this feature persists; however, it appears that most of the falling ice crystals sublimate before reaching the in situ sensors.

The final stage of case D shows a lowering of the lidar returns to ground level and a coincident detection of particles by the C^2HOM–S, PIP, and Parsivel instruments with sizes ranging from approximately 20 microns up to a few millimetres. The particle images are summarised in Figure 6.21 and are identified to be a mixture of small supercooled water droplets and large irregularly-shaped particles. Number density and precipitation intensity are significantly lower than that seen in the case B event, perhaps indicative of the lost available water content from the previous heavy snowfall. Given the prevalence of supercooled liquid water through this event, it is suggested that these large ice particles were formed through the processes of riming and aggregation. The mean surface temperature during this time was approximately -1 °C, in the regime for which ice crystals become sticky [39, 74], which is further consistent with this interpretation.

The large-scale HIMAWARI-8 retrievals of Cloud Type are shown in Figure 6.22a. A significantly patchier cloud system is observed than that seen during case B, which indicates the dissipation of the cloud during this event and is in distinct contrast to the previous relatively high number densities and consistent falling snow. The combined cases present a consistent view of a post-frontal low-level cloud system dissipating over time. The cloud type is uniformly assigned as low-level stratiform, consistent with the low-level cloud interpretation. This is further supported by the CER retrievals in Figure 6.22b which uniformly report particle diameters of approximately 20 microns, in agreement with the holographic observations throughout the event.

6.5 Holographic Classification of Events

Based on the in-depth analysis of the case studies outlined in the previous sections, it is now of interest to consider how the C^2HOM–S observations may be used for one of the principle motivations; the calibration and validation of remote sensing microphysical inversion algorithms and climate models. Effort has been made in the study of these cases to incorporate all collocated observations to provide a detailed summary of the different atmospheric events. It is intended that such observations will form the basis for look-up tables to automatically interpret holographic field observations for future campaigns, with the goal of classifying events without the need for extensive manual analysis or comparison to such a wide range of other instruments.

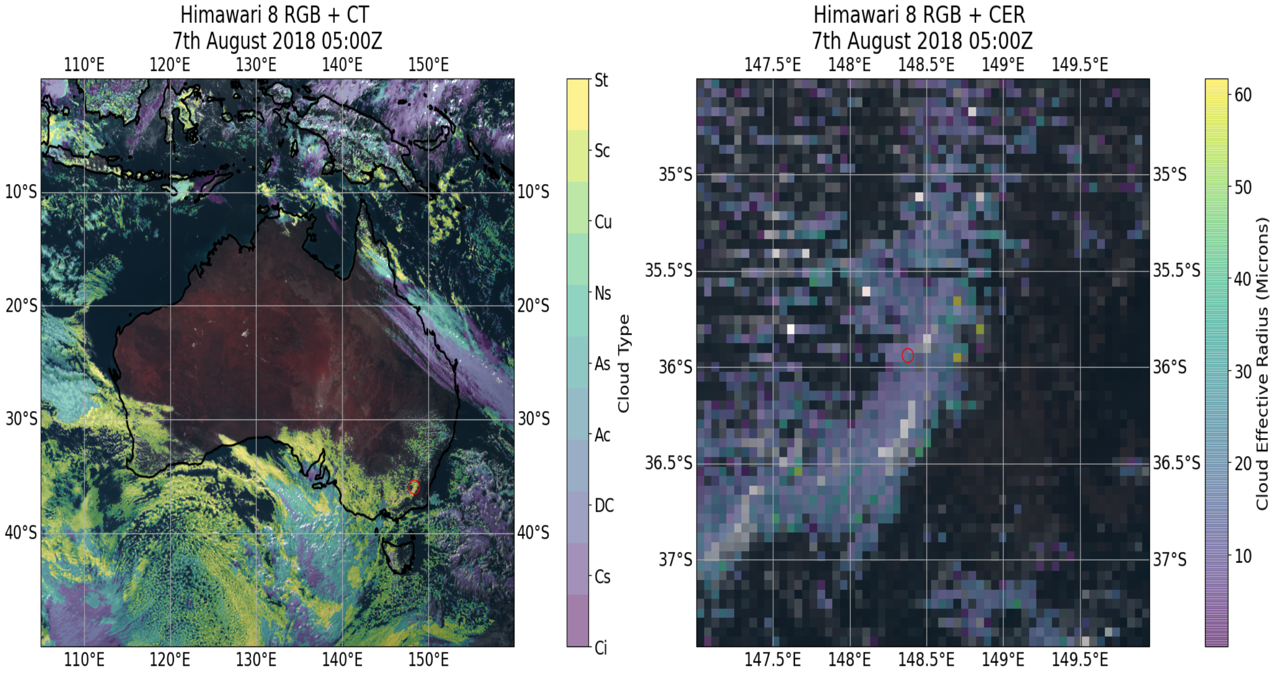

(a) (b)

Fig. 6.22 HIMAWARI-8 retrieval of a) Cloud Type (CT) and b) Cloud Effective Radius (CER), during the August 7th case C event. The red circle indicates the position of the observation tower.

The case study region included weather events that – through synthesis of observations from all instruments – have been classified as follows: (i) a rain event on August 3rd (case A), (ii) a snowfall event with an embedded mixed phase cloud starting on August 6th (case B), (iii) a non-precipitating mixed phase cloud in the middle of August 7th (case C), and (iv) a mixed phase cloud with light snowfall on August 8th (case D). A more statistically significant database of events should be compiled for more widely applicable results in future; however, these results are still of interest for a preliminary investigation into the feasibility of classifying such atmospheric events based solely on holographic observations.

The key holographic observables that are automatically extracted by the current algorithm are the particle number density, the equivalent diameter of a fitted ellipse, and the eccentricity of this ellipse. The particle number density varies significantly between holograms, as shown in Figure 6.23 for the case B event. Previous holographic studies have revealed large variations in cloud mixing at the centimetre scale [57] consistent with those observed in this campaign. Such variability may indicate turbulent mixing and entrainment of dry air with fewer cloud particles contained. A more stable metric is desired for reliable cloud classification that is still sensitive to the dynamic variability in these parameters over the

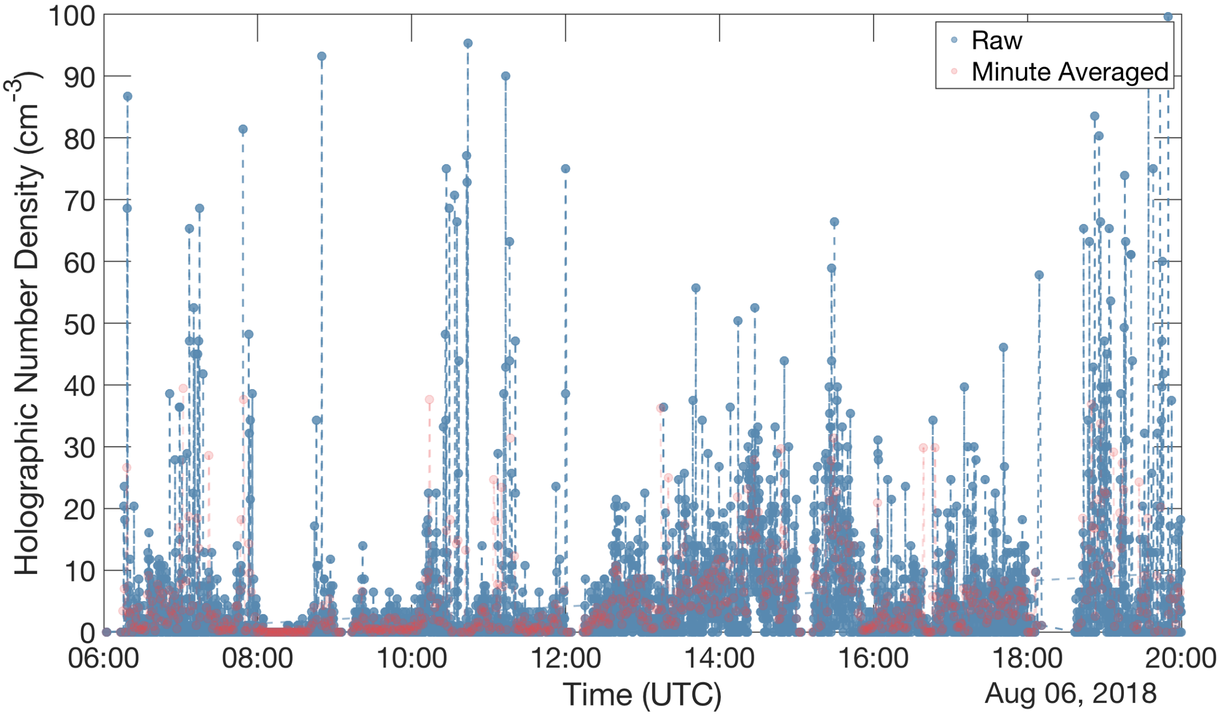

Fig. 6.23 Time series of holographic number density during a subset of the case B event. Raw observations sampled at a rate of 0.1 Hz are shown in blue and the 1-minute averaged data are overlaid in red.

duration of an event. The 1-minute average of the holographic observables was chosen for this investigation.

Clouds in this region are frequently influenced by air masses originating from the Southern Ocean [312]. Previous aircraft observations of Southern Ocean cloud particle number densities in this region have been shown to be on the order of 10 - 40 cm^{-3} [319, 320]. This is consistent with the raw number densities shown in Figure 6.23, but it is noted that the 1-minute averaged values are consistently lower than expected. This is due in part to the biases of the automated technique, as discussed in Chapter 3, but may also be representative of the inherent variability of inhomogeneous cloud mixing at small scales. Measurements of particle diameter are significantly more stable, as seen in Figure 6.18, and are consistent with the mean value of around 25 microns reported in the previous aircraft campaigns.

Despite these lower than expected mean number density values, the relative variation of this parameter is considered here to be more relevant for the classification of weather events. This is demonstrated in Figure 6.24a which shows a scatter plot of the three key holographic observables over three different atmospheric events, as indicated by the marker

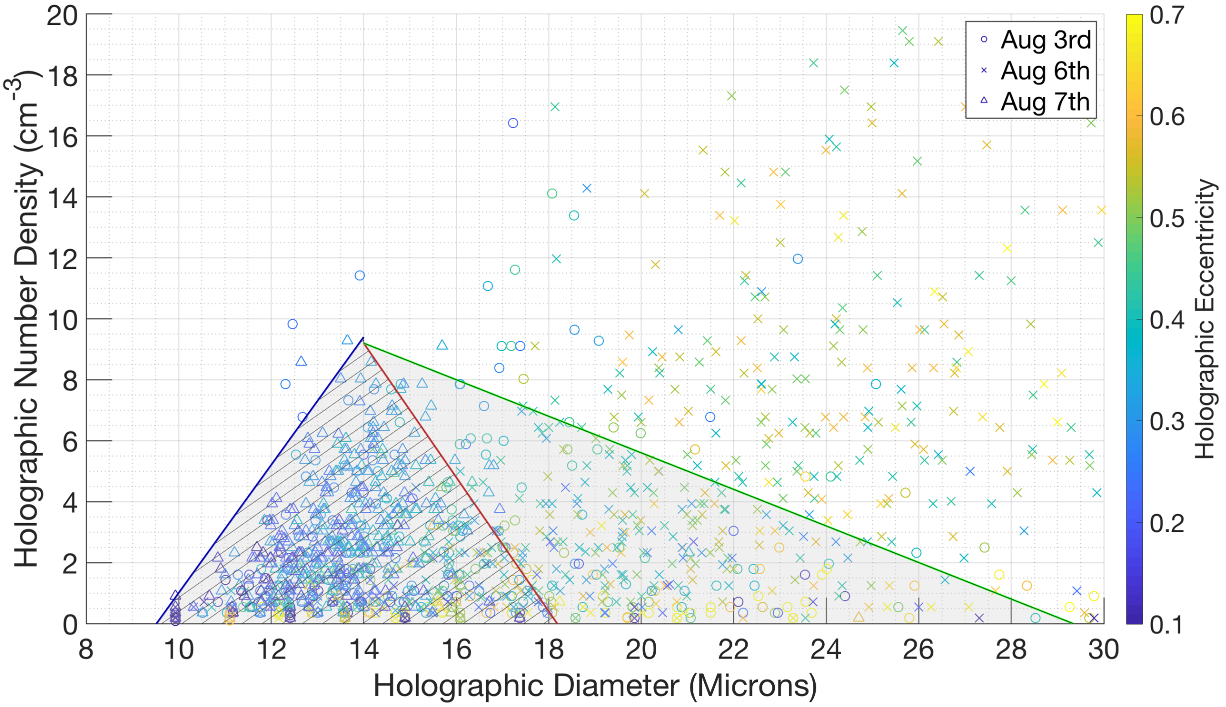

(a)

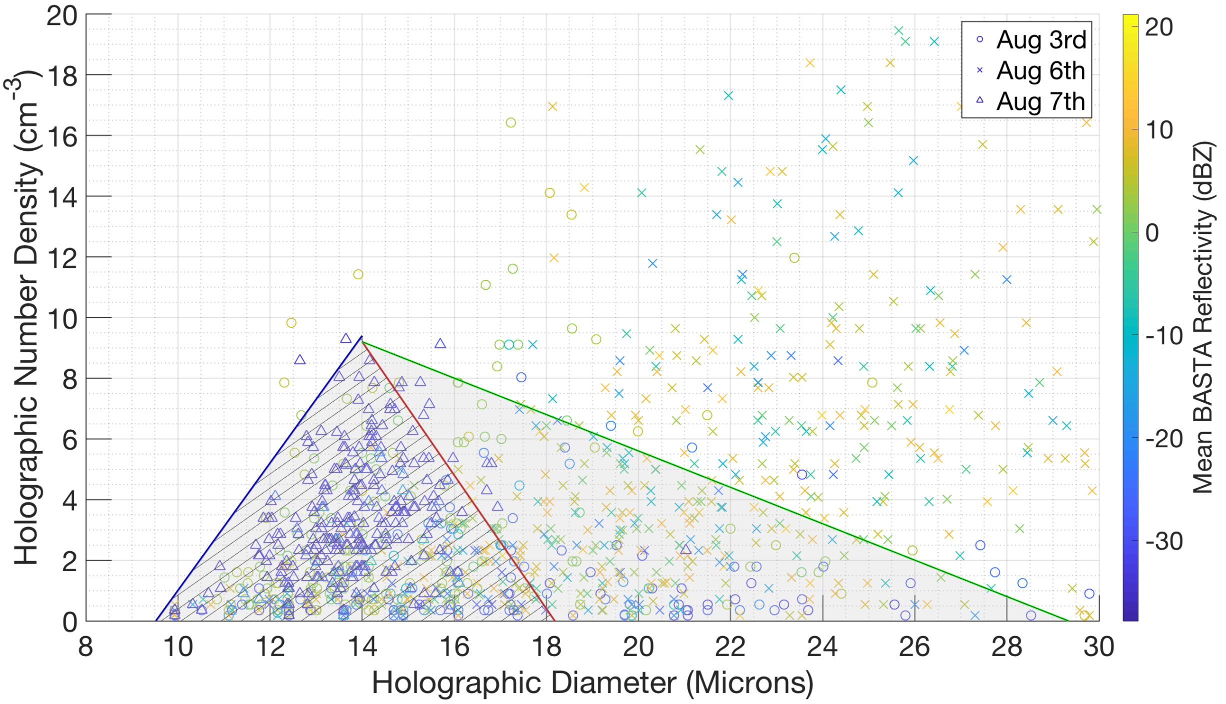

(b)

Fig. 6.24 Scatter plots of the key holographic observables for three different atmospheric events, as indicated by the shape of the plotted symbols. The colour axis designates a) the holographic eccentricity and b) the mean BASTA surface reflectivity metric. Regions are shaded to designate the parameter spaces associated with each event.

symbols. Regions of parameter space that may be used to distinguish between these events are indicated via shading.

Measurements from the August 7th mixed phase cloud event are seen to cluster tightly within the shaded region with hatching. This region has the smallest particle diameters, number densities, and eccentricities, as expected for a cloud consisting primarily of spherical supercooled water droplets. This region is in contrast to the unshaded area of the plot which predominantly consists of observations from the August 6th mixed phase cloud and falling snow event. On this scale it is seen that some observations from other events lie within this region but it is important to note that the zoomed view of the plot shown here contains the majority of observations from the other events, whereas those for the snow event extend significantly out over the size and number density axes by an order of magnitude more than shown here. When this greater parameter space is considered, a clear distinction can be made between the cloud event and the cloud coinciding with falling snow.

The August 3rd rain event is mostly contained within the shaded region and lies between these two extreme cases. A key point of distinction for this event is that whilst the mean diameters are significantly larger than those for the cloud event, the mean number densities do not go much higher than around 15 cm^{-3} and are mostly within the bounds of the shaded region.

Another way to discriminate between events is to use the mean eccentricity. Eccentricities for the cloud event are distinctly smaller than those for both the snow and rain events. The largest eccentricities are seen for the snow event, as expected due to the predominantly irregularly shaped particles seen during case B. This separation can be used to overcome some of the ambiguity between events in the region with hatching for which observations from all events are seen.

Figure 6.24b shows a similar scatter plot except the colour axis now shows the mean BASTA reflectivity from ground up to 100m in altitude. The BASTA observations for each event can be discriminated, based on their values within the holographic classification regions. Reflectivity values in the parameter space associated with the cloud event are the lowest, those for the rain event are also low – as expected due to attenuation of the 95 GHz radar frequency – yet noticeably higher, and reflectivities for the snow event have dramatically larger values, as expected due to the strong dependence on particle size. Such a distinction is also found when the BASTA Doppler velocity is compared. Distinguishing precipitation from low-lying cloud is a current challenge for radar-based microphysical studies and so comparisons of this kind may prove useful in future for the development of look-up tables for interpreting remote sensing observations.

It is again noted that this is only a preliminary investigation into classification of atmospheric events using holographic observations. More case studies of intensive field observations should be included into this database for this classification method to be applied more broadly to other times and parts of the world. An improved approach would incorporate a climatology of events from different times of the year and at different parts of the world, but this is necessarily beyond the scope of this project. It is encouraging to see that even with a limited set of case studies included here, the classification method does appear to have potential for unattended operation in future. This has been tested for the full set of observations in this campaign but a comprehensive analysis remains the topic of future work. It is also noted that these observations should prove useful for the training of neural network-based approaches to classification of weather events.

Other potential improvements to the methods are identified based on the limitations of the current design of the C^2HOM–S instrument, as discussed in more detail in Chapter 3. The eccentricity parameter does not go to zero for spherical particles due to the ambiguity in fitting an ellipse to an imperfectly focussed and pixelated particle image. A more sophisticated shape metric that includes other observables, such as the particle projected area and perimeter, is desired. A separate treatment between small and large particles, as discussed in the previous sections, would allow more sophisticated classification of events. An increased sampling volume for the instrument would also be beneficial as significantly more observations could be assigned to a given event type with a coinciding improvement in accuracy as this method is governed by Poisson counting statistics.

6.5.1 BARRA Comparison

A preliminary evaluation of the BARRA reanalysis, introduced in Section 5.4, is presented for the August 3rd rain event in Figure 6.25. The 1-minute averaged holographic number density and Parsivel precipitation intensity are compared with the BARRA-R large-scale precipitation scheme. The combination of observations from these instruments provides a sensitivity to particles with sizes ranging from approximately 7 microns up to 25 mm which covers most sizes of precipitation. The BARRA-R precipitation is reported as the amount of rain in kg m^{-2} per 10-minute model time step and convection is handled independently between grid points. The closest model grid cell to the field site was used, which was centred at 35.9295°S, 148.3810°E with a width of 1.5 km.

The C^2HOM–S and Parsivel instruments, along with all others discussed in the previous sections, report the onset of rain at approximately 0530Z and the rain component of the event lasts for approximately 5 hours. It is seen here that the large-scale BARRA-R precipitation scheme shows the onset of the event approximately 2 hours later, with a duration of only

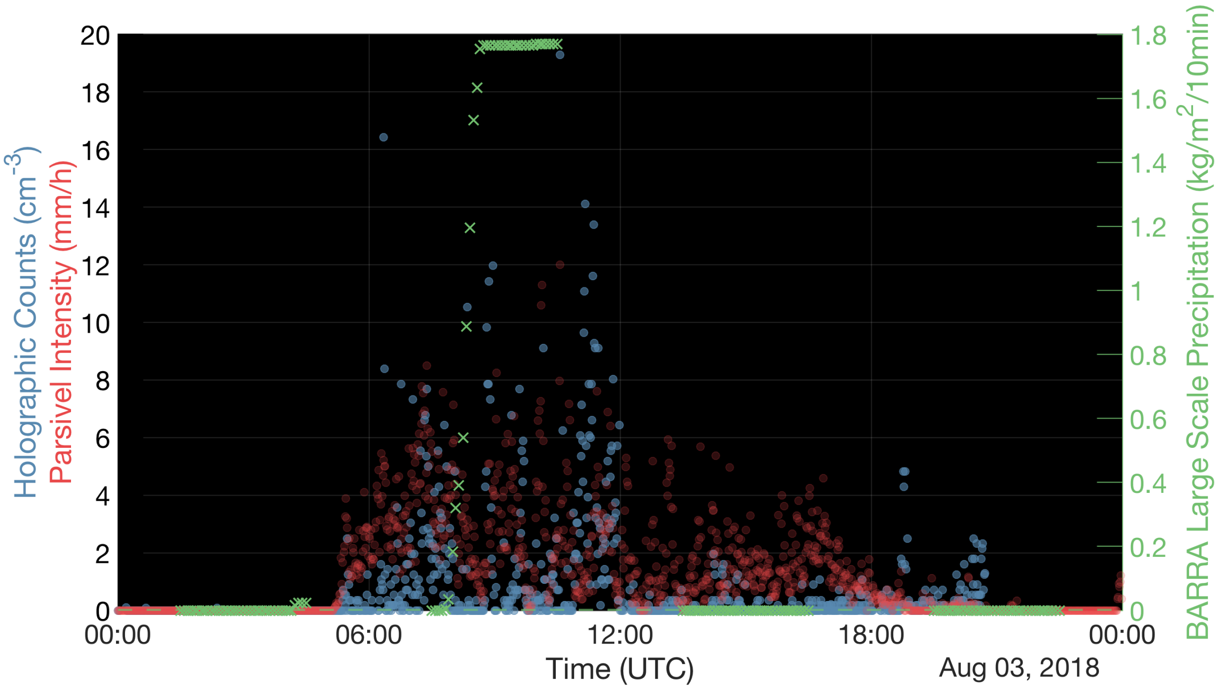

Fig. 6.25 Comparison between in situ C^2HOM–S and Parsivel observations and the BARRA-R precipitaion metric during the August 3rd case study.

3 hours. The end of the event indicated by the BARRA-R reanalysis at around 10Z agrees reasonably well with the conclusion of the rain component of the event, as reported by the instruments. The reanalysis does not report any snow during this event, in disagreement with the instruments which report light snow between around 10Z and 12Z.

A more detailed summary of BARRA outputs during case A, including those from the higher-resolution BARRA-SY reanalysis, which uses a dynamics-based convection scheme, is shown in Figure 6.26. The top two panels show the height profiles of BARRA-SY cloud ice and liquid content, respectively, with heights provided relative to the field site altitude. The bottom panel shows BARRA-SY precipitation products in blue and BARRA-R precipitation in red.

A high-altitude ice cloud is reported by the BARRA-SY reanalysis from around 11Z on August 2nd at approximately 8 km above the height of the observation tower. This feature could not be validated as it is outside the reliable detection range of the remote sensing instruments. Ice and liquid at lower altitudes is reported from around 05Z on August 3rd. This is broadly consistent with the mixed phase cloud observed around those times by the remote sensing instruments at an altitude of around 2 km, as shown in Figure 6.12 and 6.13.

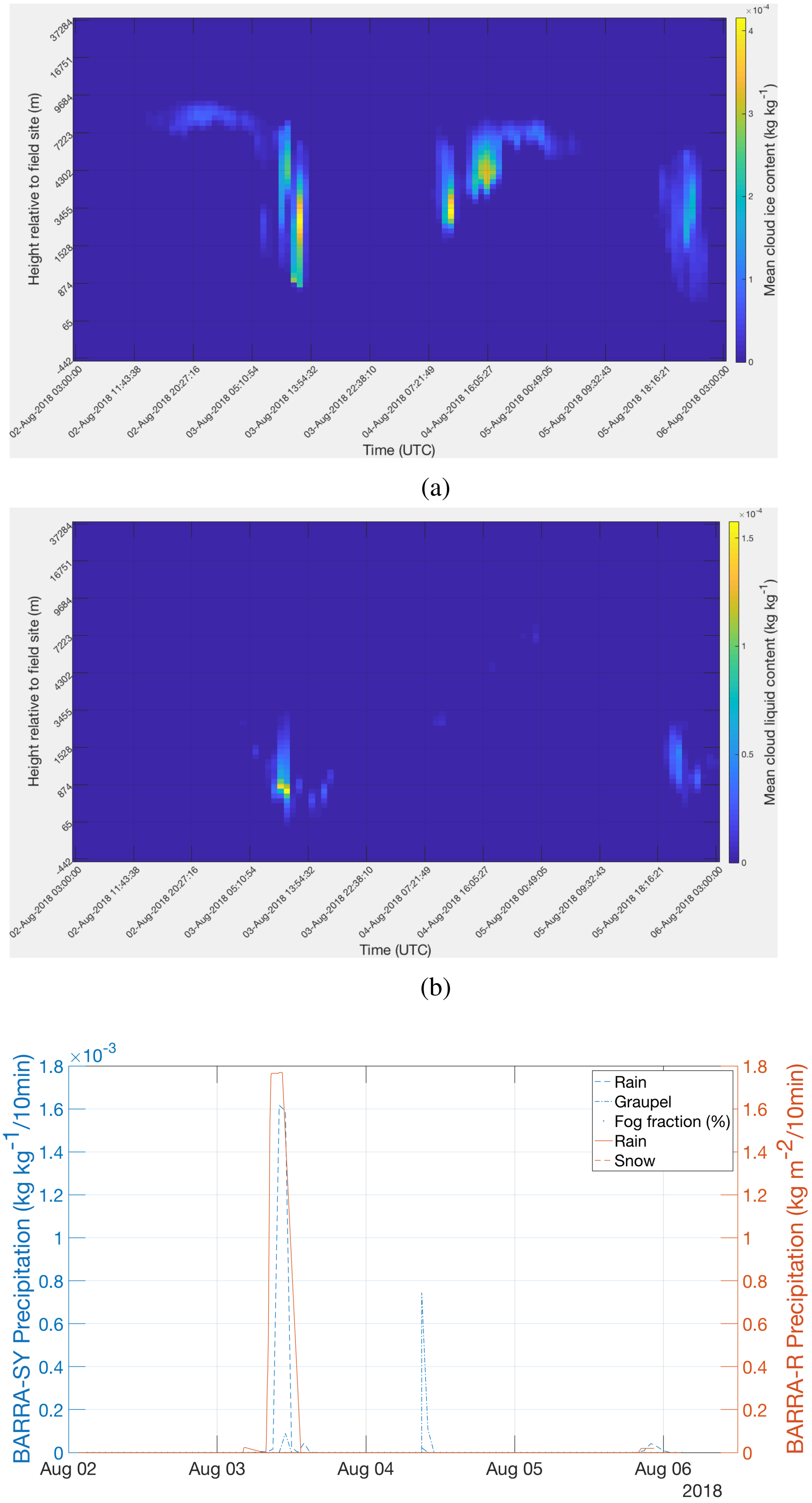

(a)

(b)

(c)

Fig. 6.26 Summary of key outputs from the BARRA reanalyses during the case study period discussed in the previous sections. Time series are shown for the vertical profiles of BARRA-SY a) mean cloud ice content and b) mean cloud liquid content. A time series of the column-summed precipitation metrics for both reanalyses is shown in c).

As discussed above, the onset of the precipitation event following this cloud feature is delayed in the reanalysis outputs by around 2 hours. An increase in lower-altitude ice and liquid water content coincides with rain reported by both reanalyses at approximately 0730Z. It is interesting to note that the BARRA-SY scheme does report a small amount of graupel around the time of measured snow at 12Z, whereas the BARRA-R scheme does not report snow, suggesting that the BARRA-SY scheme is performing more accurately than the large-scale BARRA-R precipitation scheme for this event. This is as expected for the higher-resolution dynamics-based convection and microphysics scheme.

Neither of the reanalyses reliably model the aftermath of this event, which included light rain seen by the Parsivel and holographic microscope up to approximately 20Z, and surface level cloud observations from the holographic microscope up to 16Z on August 4th. An unusual spike in BARRA-SY scheme rain and graupel is reported during the time of holographic cloud detections on August 4th but this is not seen by the Parsivel, suggesting a misclassification by the model of the low-level cloud as a precipitation event.

This brief comparison demonstrates the potential for holographic observations to be used for calibration and validation of climate models such as the BARRA reanalyses. For this particular case it is seen that the model gets the broad features of the event correct but is wrong in many of the specifics. A more quantitative analysis of this kind that compares the atmospheric event classification, number density of particles, and thermodynamic phase partitioning over all of the measured events during the campaign would allow more statistically significant conclusions to be drawn as to potential biases in these models.

6.6 Polarsonde Observations

The aim of the previous sections has been to validate the C^{2}HOM–S instrument using reliable field-tested instruments, as well as to investigate the potential of this instrument for automated classification of weather events. The Polarsonde is also an experimental instrument requiring validation and so was not included in the previous sections. Preliminary results from this instrument are presented now in an attempt to interpret these observations based on what has been learnt from the other instruments over the case study period.

The key observables of the Polarsonde are the parallel and perpendicular backscatter components in the Lin90 and Lin45 polarisation channels, as defined in Chapter 5. A scatter plot of the Lin90 observations for the August 3rd rain event is shown in Figure 6.27 with observations colour coded by time of measurement. Three distinct clusters of observations are identified corresponding to different times through the event. The ellipses that bound these

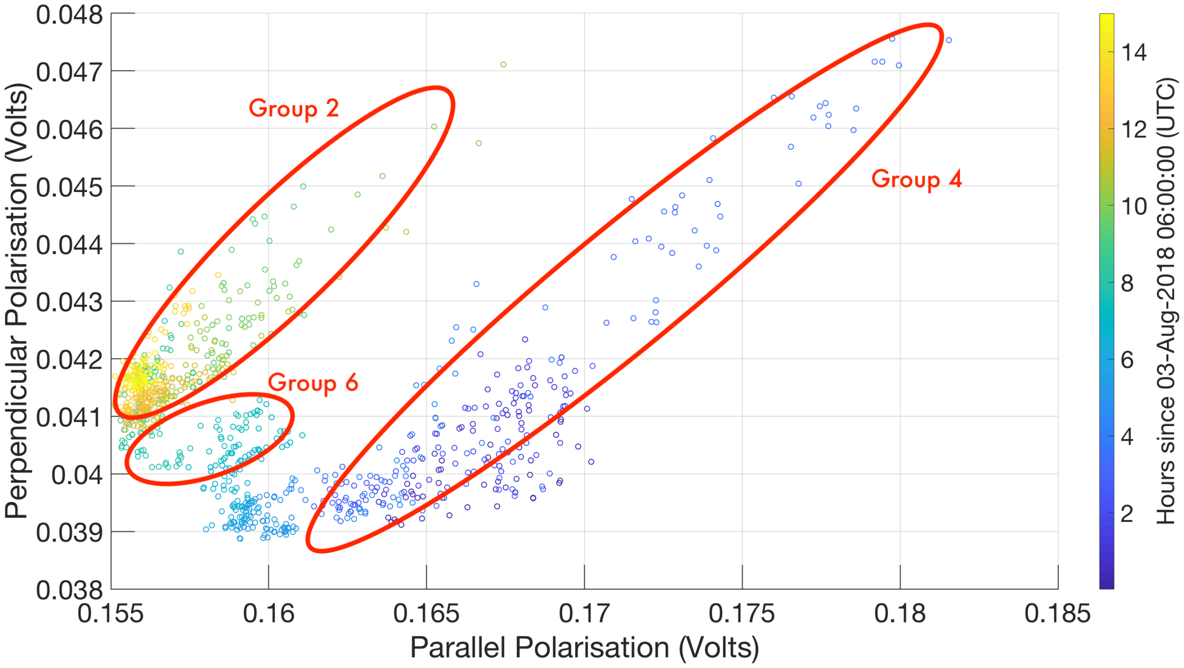

Fig. 6.27 Polarsonde Lin90 backscatter components colour-coded by time of measurement during the August 3rd rain event. Red ovals indicate main clusters of observations through the case study.

regions are seen to have a decreasing parallel component and an increasing perpendicular component over the course of the event.

To further highlight the variation of the Polarsonde returns through this event, a selection of points from each of the labelled ellipses are plotted as a function of time in Figure 6.28a along with the raw backscatter in each polarisation component. This view more readily demonstrates that different dynamic stages of the rain event are associated with specific clusters in the polarisation scatter plot. The lowest depolarisation values are seen at the start of the event when predominantly spherical rain droplets were measured. The onset of snow during this event occurred at approximately 12Z and is indicated by the BASTA surface reflectivity metric in Figure 6.28b, since the accumulated/melted snow caused a significant attenuation of the beam. This transition coincides with a cluster of Polarsonde observations with a higher perpendicular backscatter component, as expected for aspherical snow particles.

The final cluster on the scatter plot has the highest depolarisation value, yet occurs at a time when the rain and snow event had concluded and a cloud of predominantly spherical water droplets was measured by the C^{2}HOM–S instrument, though a smaller population of aspherical ice crystals were also measured. An important question to consider is whether this high depolarisation is a consequence of the small population of ice crystals, or whether this

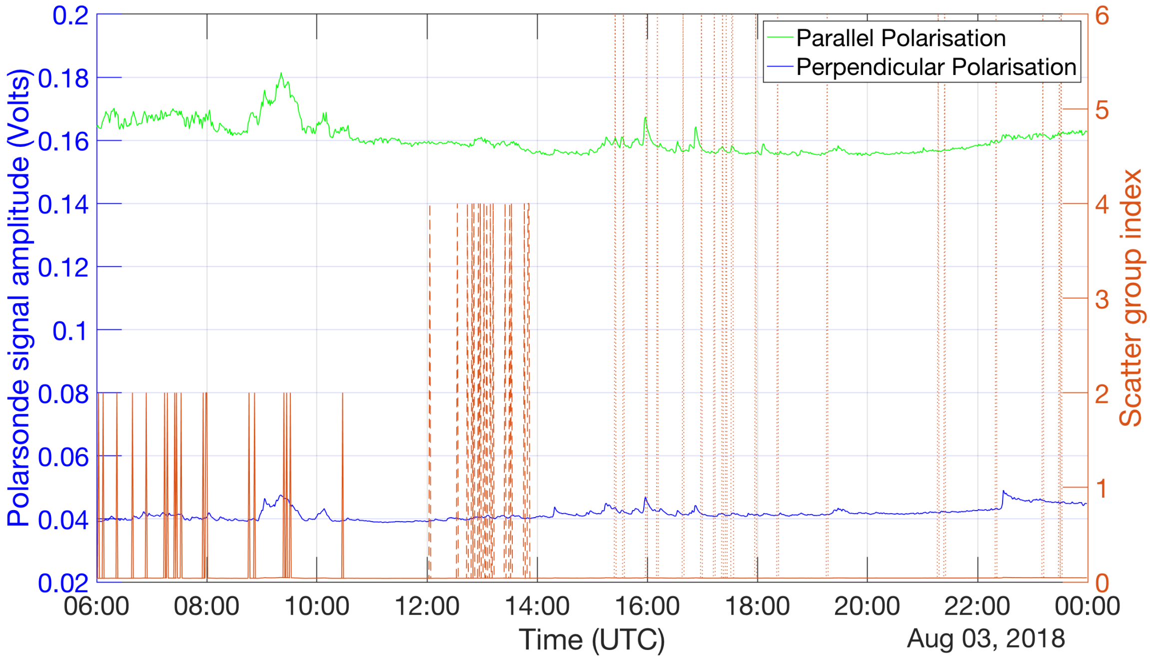

(a)

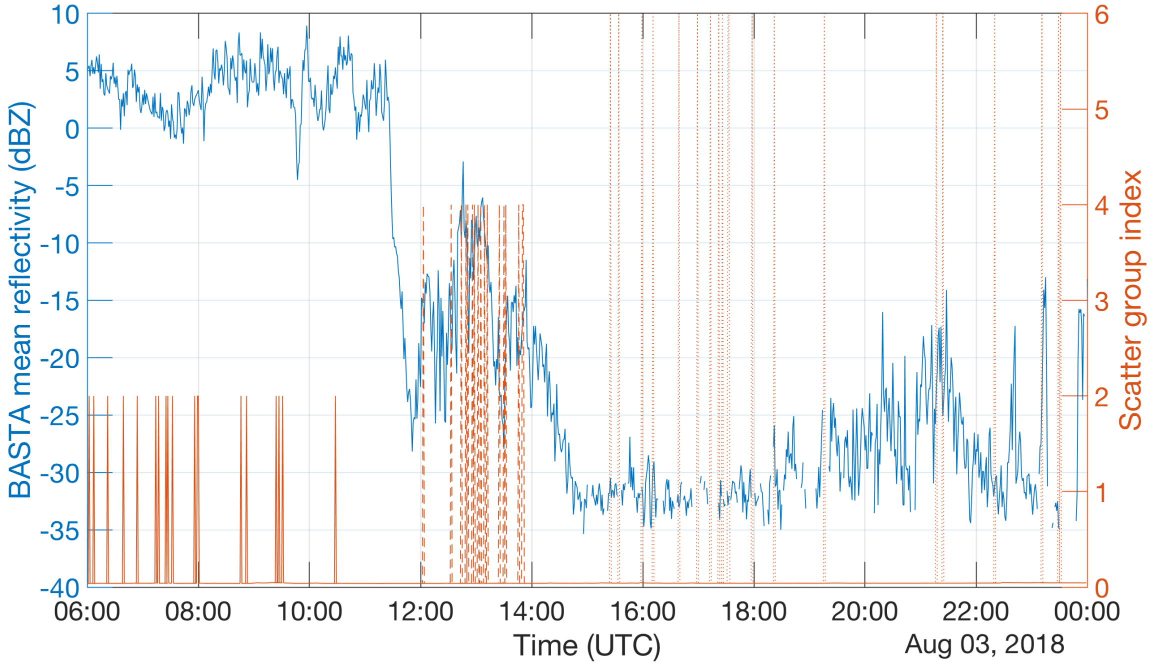

(b)

Fig. 6.28 a) Polarsonde backscatter components with vertical lines corresponding to times of data points within a given grouping defined in Figure 6.27. b) Grouping indices and mean BASTA reflectivity up to 100m above ground.

demonstrates a key limitation of relying solely on the depolarisation metric for particle shape for a fixed installation of this instrument in the field.

The contradictory observation of increasing depolarisation with increasing sphericity of particles for this case is hypothesised to be a result of accumulation of liquid and dirt on the Polarsonde sampling window. Following the precipitation event, it is expected that drops would impact the windows and, given the high relative humidity throughout the event, condensation on the window is also expected. The combination of these processes will produce a complicated scattering surface directly in front of the LEDs and photodiodes, and therefore an ambiguous backscatter signal is expected. It is also important to note that the Polarsonde instrument is sensitive to aerosols as well as cloud particles and this introduces a further ambiguity into the interpretation of backscatter and depolarisation observations.

Given these ambiguities, it is of interest to investigate other potential metrics to attempt to automatically infer particle shape properties with this instrument. It is expected that observations of aspherical particles should produce significant backscatter in both the parallel and perpendicular Lin90 channels, whereas spherical particles mostly return parallel backscatter. The correlation between the parallel and perpendicular backscatter was therefore considered as a classification metric. The Pearson correlation coefficient between backscatter components is calculated using a moving sampling window. A 5-minute window length was chosen to give a trade off between including a significant number of observations for the correlation calculation and preserving the temporal variation within an event. This metric is shown in Figure 6.29 in green with the in situ counting observations overlaid for the case period.

The fine detail of microphysical variation reported by the other instruments is not captured by this metric; however, it does appear useful in classifying more broadly between atmospheric events. A mean correlation coefficient of approximately 0.3 was found for both the rain event in case A and the mixed phase cloud event in case C. This is in contrast to the lower values of approximately 0 during times of no observed cloud or precipitation. Whilst the metric does not offer reliable discrimination between types of event, it does appear to vary consistently with variations in the in situ counts. It is therefore interesting to note the brief increase in correlation beginning at approximately 00Z on August 5th. There were no corresponding surface observations by the other instruments at this time and may therefore be indicative of an air mass consisting of aerosols with more aspherical shapes than at other times.

The correlation-based metric may prove useful, alongside others, in the interpretation of aerosol contributions, but is considered unreliable for classification between different types of atmospheric events. To this end, a different metric was developed based on the variance in the

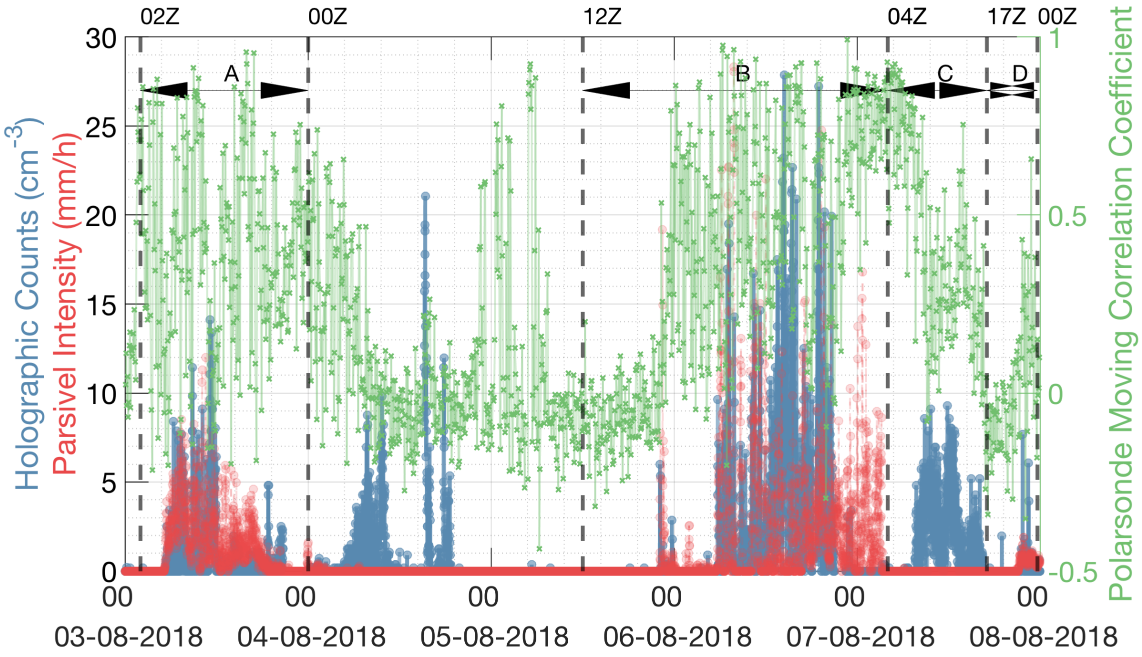

Fig. 6.29 Moving correlation coefficient between perpendicular and parallel Polarsonde polarisation channels. Overlaid are the holographic counts and Parsivel intensities for the case study duration.

signal. The rationale is that whilst water and dirt may accumulate on the sampling window and bias the mean backscatter, the variance of the signal should be less affected. Observation of airborne aspherical particles should coincide with fluctuating backscatter and high variance in both channels, whereas spherical particles should coincide with predominantly parallel backscatter fluctuations only.

It was experimentally determined that inclusion of both the Lin90 and Lin45 signals produced a more reliable classification with this metric. The Polarsonde variance-based metric (β_{PS}) is defined hereafter by the following equation:

$$\beta_{PS} = \left(\frac{I_{90}^{\perp}}{I_{90}^{\parallel}}\right)\left(\frac{\frac{\sigma_{90}^{\perp}}{\sigma_{90}^{\parallel}}}{\frac{\sigma_{45}^{\perp}}{\sigma_{45}^{\parallel}}}\right) = \frac{I_{90}^{\perp} \quad \sigma_{90}^{\perp} \quad \sigma_{45}^{\parallel}}{I_{90}^{\parallel} \quad \sigma_{90}^{\parallel} \quad \sigma_{45}^{\perp}}, \tag{6.3}$$

where the letter I is used to denote backscatter amplitude, σ is windowed variance, and the super and sub scripts identify the polarisation component and channel, respectively.

Raw backscatter observations were averaged on a 1-minute basis to reduce the impact of noise. A window size of 30 minutes was found to provide the best compromise between

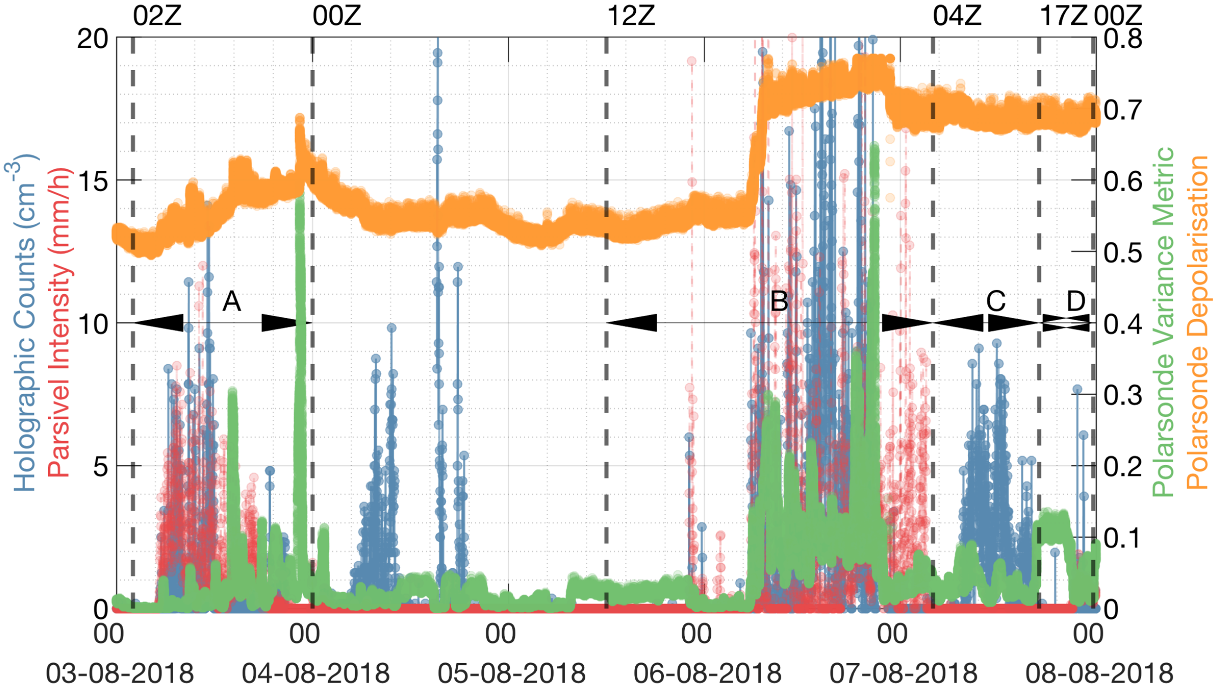

Fig. 6.30 Polarsonde Variance Metric and depolarisation for the case study period. Overlaid are the holographic number densities and Parsivel intensities for reference.

including enough points to calculate the variance and capturing the temporal variability of the event. The depolarisation and variance ratios were normalised before taking the product to produce a metric that ideally varies between zero, for spherical particles, and one, for aspherical particles. The Polarsonde variance-based metric is plotted alongside the in situ observations in Figure 6.30. The depolarisation is also plotted to emphasise the limitations of this metric for classifying events and will be compared for each of the case events.

Fluctuation in β_{PS} is seen from the onset of rain during case A, whereas the depolarisation does not show such a clear indication of an event. The β_{PS} metric reports a low value of approximately 0 during this time, consistent with the mostly spherical water droplets. The depolarisation is seen to steadily rise over the course of this event and it is not clear at what value to define the cut-off between spherical and aspherical particles since this metric does not go to zero due to the time varying and unconstrained accumulation of particles on the sampling window. The mean value of β_{PS} increases to approximately 0.05 following the onset of measured snow at approximately 12Z, as expected for aspherical irregularly shaped particles.

It is notable that β_{PS} stays at this value for the period following precipitation up to around 00Z on August 4th, similar to what was seen in the depolarisation metric. As this metric should be less influenced by accumulation of particles on the sampling window, this lends support to the interpretation that the elevated depolarisation was indeed due to the small population of ice crystals in the subsequently observed cloud. The β_{PS} metric is seen to drop to 0 at approximately 00Z on August 5th, directly following the last observed cloud particles by the C^{2}HOM–S instrument and is suggestive of clear air which may have aerosols of spherical shape. An increase in the mean β_{PS} back to approximately 0.05 is seen at around 08Z on August 5th. This is notably during a time of clear air reported by the other instruments and coincides with when the correlation-based Polarsonde metric also noted a change in the backscatter conditions. This lends further support to a change in the aerosol population at this time towards a distribution with more aspherical particles.

The β_{PS} metric drops back to zero around August 6th 00Z, coinciding with the onset of particle detections during the case B event. This was at a time when the cloud layer was seen to ascend in the lidar signals, shown in Figure 6.17, and a corresponding drop was seen in the RH. It is proposed that this metric may be able to track the changes in the air mass as the cloud lifts above the field instruments during this time. Such variations are also seen in the depolarisation, though the unconstrained mean component again makes this more challenging to interpret.

With the onset of large falling snow particles at around 0530Z, β_{PS} reaches a consistently large mean value of approximately 0.1 before dropping back to around 0.05 for the dissipating mixed phase cloud observed in case C and case D, consistent with the cloud observations following case A. An interesting rise in this metric back to around 0.1 is also reported between the end of the cloud in case C and the beginning of snow in case D. Such a large rise at a time of no cloud or precipitation observations may again indicate a significant increase in the asphericity of aerosols over this time.

A preliminary investigation of the Polarsonde variance metric has been presented in this section. It is important to note that there were no other instruments that could directly measure aerosol properties at ground during the campaign and so interpretations regarding aerosol distributions remain speculative. Despite this limitation, it is seen that the Polarsonde variance metric approach, along with the depolarisation and correlation-based methods, provides a more complete understanding of the Polarsonde observations. Future investigations should attempt to quantitatively associate the value of this metric with classes of atmospheric events and measured particle shapes, perhaps as reported by the C^{2}HOM–S instrument. Ideally the instrument would be deployed alongside other instruments that are sensitive to aerosols, as well as cloud and precipitation particles.

6.7 Summary

This chapter presents the results of field deployment of the C^2HOM–S and Polarsonde instruments alongside other more extensively validated instruments in the Australian Snowy Mountains. The C^2HOM–S instrument was found to automatically produce particle size observations consistent with those reported by the PIP and Parsivel instruments for the size ranges that all instruments could reliably resolve. Particle number density and size measurements were consistent with those from previous field campaigns in the surrounding region, though the number densities were notably low. A key limitation of this study is that the particle number density observations could not be directly compared with a cloud sampling instrument suited for the detection of small particles, such as the Cloud Droplet Probe (CDP) [270] or Cloud and Aerosol Spectrometer with Polarization (CASPOL) [321] instruments. It is possible that the low number density observations indicate a previously unidentified sampling bias of this instrument and future studies alongside these cloud instruments would help to resolve this matter.

Reconstructed particle images agreed well with those reported by the PIP instrument and shape metrics allowed discrimination between spherical and aspherical particles under a number of cases. It is expected that a more sophisticated shape metric, including properties such as the particle projected area and perimeter, will be necessary to improve the classification capability of this metric. Intensive manual analysis of holographic observations was carried out and demonstrated that the automated retrievals were performing reliably. Such observations should prove useful for the training of automated classification methods based on a neural network approach rather than the morphological method currently employed.

A range of atmospheric events including rain, snow, and mixed phase cloud were summarised in detail for all instruments. Good agreement between the times of low-level cloud and precipitation seen by the C^2HOM–S instrument, and BASTA, MRR, and RMAN remote sensing instruments was seen for all events. A number of mixed phase cloud events were identified by this instrument and not the Parsivel, highlighting the advantage of this instrument for measuring both cloud and precipitation events. This investigation led to the demonstration of the capability of the C^2HOM–S instrument to automatically classify these events based solely on the holographic observables of particle number density, size, and shape metric. This method appears to be performing reliably when applied to all events measured during this campaign, but a statistical investigation of this performance remains the topic of future work.

A persistent mixed phase cloud event was studied in detail using all available instruments. A growth in the population of both supercooled liquid water droplets and irregularly-shaped ice crystals was seen over the approximately 14 hour duration of this event. It was suggested

– based on the removal of large ice particles via snow and suitable updraft velocities – that this event was within the regime for which the WBF process was not expected to dictate the microphysics and instead permitted the growth of both ice and water droplets. This interpretation was limited by the assumption of homogeneity between cloud cells within a large-scale system and limited ice crystal measurements, and so the interpretation remains speculative for this case. A more statistically significant investigation into the frequency with which clouds follow the WBF mechanism in this region should be possible by applying this method to the other events throughout this campaign, but is beyond the scope of this project. Such observations are of particular interest in this region given the importance of mixed phase clouds in the supply of key national water and energy resources via the collocated Snowy Hydro project.

A brief demonstration of the utility of the C^2HOM–S instrument for validation of remote sensing microphysical inversion algorithms and climate models was presented. Reflectivity and Doppler measurements from the BASTA radar were seen to be associated with distinct atmospheric events identified by the C^2HOM–S instrument. This may be of particular relevance to the discrimination of low-lying cloud from precipitation by remote sensing instruments which is a current limitation of these techniques. The BARRA-R and BARRA-SY reanalyses were evaluated for a rain event case study and found to under predict the duration of the event and had a delay in the onset of the event of a few hours. The higher-resolution dynamics-based BARRA-SY microphysics scheme was seen to better model the thermodynamic phase partitioning of the case events, but significant disagreement was seen on the details of these events. An analysis of which events are particularly challenging to model and a statistical assessment of model biases incorporating all measured events in this campaign remains the topic of future work.

The Polarsonde observations were consistent with those from other instruments for the case studies investigated. It was determined that discrimination between spherical and aspherical particles based solely on depolarisation, for a fixed installation of this instrument, was unreliable due to the potential for ambiguous backscatter from dirt and water on the sampling window. New metrics were proposed to reduce this ambiguity based on the correlation between backscatter components and the signal variance. It was found that such metrics provided a more complete understanding of the microphysical variations of both cloud and precipitation particles and potentially also for aerosols. Application of these metrics to the full campaign observations may allow independent assessment of the thermodynamic phase of cloud, precipitation, and aerosols, but this is also beyond the scope of this project.

Chapter 7

Holographic Cloud Particle Observations from an Untethered Balloon

7.1 Introduction

The Compact Cloud-particle HOlographic Microscope – Balloon (C^2HOM–B) and Polarsonde instruments were launched into cloud on a weather balloon from a site north-east of Adelaide, South Australia, in August 2020. The instruments were deployed along with meteorological and tracking sensors, and the payload was retrieved on landing. This is the first time a holographic sensor has been launched on an untethered balloon, to the author's knowledge.

Holographic observations on a weather balloon allow the vertical profiling of cloud microphysical parameters, including the cloud particle number density, size, and shape properties. Due to the cost and weight of previous holographic instruments, vertically-resolved cloud observations have been obtained via more expensive methods such as aircraft campaigns or with tethered balloon systems. Each method has advantages and disadvantages, as discussed in Chapter 2, but a key advantage of the untethered balloon method is that it is significantly less expensive than aircraft campaigns, and not limited to the heights, sites, and meteorological conditions that are suited to tethering.

To allow deployment with an untethered balloon, the C^2HOM–B was designed to be light weight and inexpensive, such that the risk of losing the instrument was not cost prohibitive. A discussion of the design of this instrument is provided in Chapter 3. As this launch was the first of its kind, the primary goal was to assess the performance of the instrument under launch conditions and to determine the feasibility of the technique. Vertical profiles of in situ cloud measurements are scarce, particularly over this region, and so the observations are of

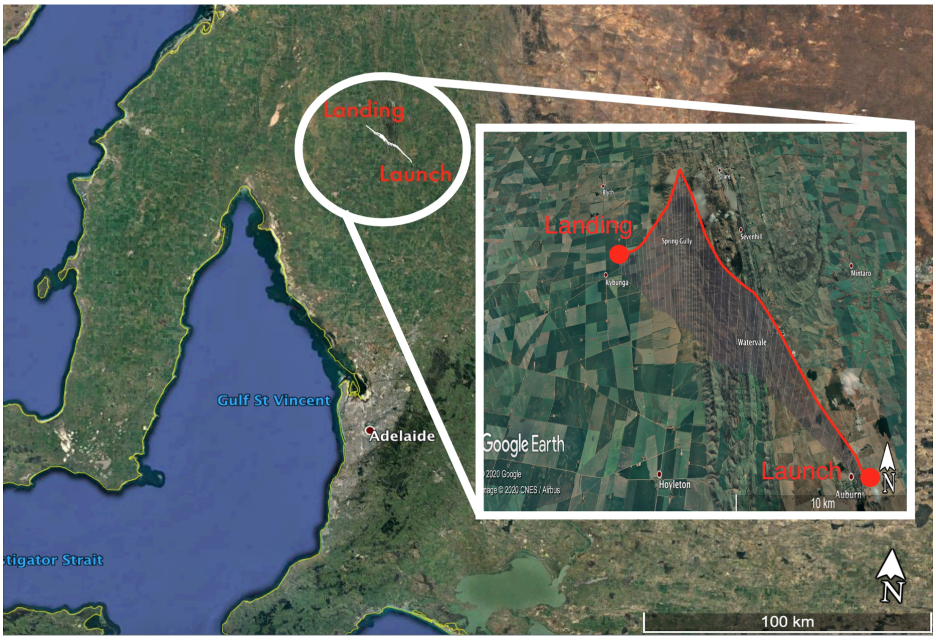

Fig. 7.1 Map of the launch location and balloon path along with the surrounding region. Image obtained from Google Earth, 2020.

further interest for applications such as validation of climate models and inversion methods for retrieving cloud microphysical measurements from remote sensing observations.

The field site and launch details are first summarised in this chapter. An overview of the holographic observations within multiple layers of cloud is then presented, along with preliminary results from the Polarsonde instrument. The chapter concludes with a comparison of the balloon observations with HYSPLIT modelling and HIMAWARI-8 satellite observations.

7.1.1 Field Site and Launch Conditions

The instruments were launched at 0155Z on the 8th of August from 34.03 °S, 138.69 °E. The launch location, at an elevation of approximately 300 m, and balloon path are shown in Figure 7.1. An average ascent rate of approximately 4 m s^{-1} was targeted and achieved by using a 500 g balloon with roughly 3 m^3 of helium. The balloon reached a maximum height of approximately 8.5 km after 30 minutes and the payload train was remotely cut down and retrieved, through use of the GPS tracking unit, approximately 20 km north-west of the launch site. A photograph of the cloud tops at the maximum launch altitude, along with launch diagnostic information, is presented in Figure 7.2a, as provided by the Amateur Radio Experimenters Group (AREG) who assisted with the launch logistics.

(a)

(b)

(c)

Fig. 7.2 a) Photograph of cloud tops at around 8500 m altitude, provided by AREG. b) Payload train before launch. From left to right: Polarsonde and Monash University data loggers, Holographic Microscope, Raspberry Pi camera and RS41 Radiosonde, parachute, and remote cut-down payload. c) Balloon in the air indicating instrument spacings.

An unbroken low-level stratus cloud was observed over the entire sky for the duration of the launch. Light rain and snow were forecasted by the Australian Bureau of Meteorology (BoM) for the nearby town of Clare in the morning and the launch was carried out during a time of no precipitation. Daily total rainfall measurements from the BoM were reported as 1.4 mm and 5.6 mm for Adelaide and Clare, respectively, and light drizzle was observed at the launch site before the balloon was launched.

The launch site is approximately 50 km from the coast and is expected to receive aerosol contributions from air masses arriving from over the ocean, as well as those coming from the continent. To reduce the risk of losing the instrument over the ocean, balloon path forecasting, incorporating Global Forecast System (GFS) wind predictions, was undertaken to select a launch day with north-eastward winds. Such conditions may have favoured air masses coming from the ocean, but as discussed in Section 7.6, HYSPLIT modelling suggests contributions to the air mass from the continent may also have impacted the aerosol properties.

7.1.2 Instrumentation Summary

A summary of the sampling considerations for each of the launched instruments is presented in this section and the assembled payload train is shown in Figure 7.2b. The C^2HOM–B and Polarsonde instruments, as described in greater detail in previous chapters, were deployed within a metre of each other at the bottom of the payload train. This spacing was chosen as a compromise between sampling similar air masses whilst not allowing the backscattered Polarsonde light to be detected on the holographic microscope camera. These instruments were suspended at a distance of approximately 9 metres from the balloon, as seen in Figure 7.2c, in an attempt to reduce the impact of the balloon on the air sampled by the microphysics instruments. Meteorological sensors were attached to the sides of the Polarsonde payload, and the radio cut-down mechanism, RS41 Radiosonde, Raspberry Pi camera, and telemetry payloads were attached from the middle of the payload train and upwards to the balloon.

7.1.2.1 C^2HOM–B

Holograms were sampled at 1-second resolution which, with an average ascent rate of around 4 m s^{-1}, corresponds to a height resolution of approximately 4 m. A spacing of approximately 7 cm between the sampling windows was chosen as a trade-off between increasing the sampling volume and limiting the amount of sunlight reaching the camera sensor. The front sampling window was approximately 50 mm from the camera sensor and this led to a maximum diffraction limited transverse resolution of around 5 microns at this

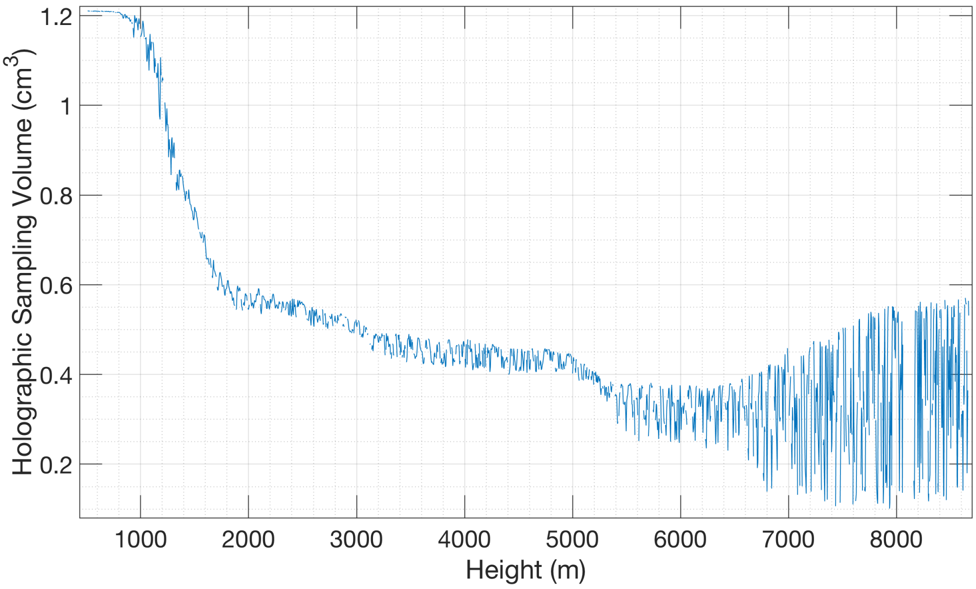

Fig. 7.3 Variation of the holographic sampling volume with height due to sunlight saturation.

end and at the position of the farther window the resolution decreased to around 11 microns, consistent with calibration measurements in the laboratory. A more complete description of this instrument was presented in Chapter 3.

This instrument configuration did not result in any sunlight saturation at ground level before the launch; however, as the balloon ascended through the clouds, more sunlight was incident on the sensor and this resulted in a significant fraction of the camera pixels becoming saturated. Inspection of the raw holograms revealed that the saturated pixels began at the bottom of the sensor and progressively higher rows of pixels became saturated as the balloon ascended. This simple progression of saturation allowed a correction to be applied to determine the effective sampling volume by subtracting the saturated pixels from the total number of pixels that lie within the spatial extent of the laser beam on the sensor.

The variation of sampling volume with height is shown in Figure 7.3 and it is seen that the maximum sampling volume at ground was approximately 1.2 cm^3 and by the maximum altitude this had reduced to only around 0.2 cm^3. The reduction in sampling volume resulted in larger uncertainties in reported number densities as these are expected to follow Poisson counting statistics. Large ice crystals were observed at the highest altitudes, yet due to the reduced sampling volume, and inherently lower number densities for ice crystals, a statistically significant number density measurement could not be obtained for these particles. Generally the number density measurements in this campaign are considered less reliable, due to the small sampling volume, and so the focus of this analysis will be on the particle size and shape measurements. This sunlight issue can be resolved in future launches by methods such as using a higher optical depth neutral density filter in front of the camera, redesigned optical baffling, or positioning the sensor further away from the instrument window.

7.1.2.2 Polarsonde

The Polarsonde was deployed in the configuration described in Chapter 5; however, due to issues from a prior deployment, the Lin45 measurements were not considered reliable and so the analysis presented in this chapter is focussed on the Lin90 measurements. Recordings were taken at 1-second intervals, with a corresponding height resolution of approximately 4 m, and no issues due to sunlight saturation were observed. Opaque black foam was placed over the photodiodes before the launch to establish the background levels, largely arising from electrical pickup from the Light Emitting Diode (LED) pulsing circuits. These backgrounds were subtracted in the subsequent analysis.

Long-term field deployments of this instrument, such as that described in Chapter 6, have revealed challenges in interpreting Polarsonde observations due to condensation and accumulation of dirt on the glass sampling window in front of the sensors and LEDs. To mitigate this problem, the glass sampling window was removed for this flight.

7.1.2.3 Meteorological Sensors

Temperature, relative humidity, and pressure were measured during the launch using a range of sensors. Two custom-built meteorological data loggers made by Monash University were attached to the Polarsonde package at the bottom of the payload train. A Bosch BME280 was used to measure relative humidity and thermocouples were used for the temperature measurements. The thermocouple used in Monash Data Logger 2 had a smaller time constant than that in the other package and hence reacted faster to temperature fluctuations. All sensors were sampled at 1-second intervals with a corresponding height resolution of about 4 m.

A Vaisala Radiosonde RS41 was deployed higher up the payload train to provide independent meteorological measurements. This instrument uses a platinum resistance thermometer to measure temperature with a reported resolution of 0.01 °C. A thin-film capacitor is used to measure relative humidity with a reported resolution of 0.1 %. Both sensors were sampled at 1-second resolution, consistent with the other instruments. This instrument was recovered from a previous launch and so measurements such as the relative humidity are considered less reliable for this reason, as discussed below.

7.1.2.4 Tracking Instruments

The position of the balloon, along with other diagnostic information, was monitored in real-time from the ground using a GPS transmitter payload and receiver antennas mounted on the chase-vehicle. The balloon path prediction, based on this data, allowed the landing zone to be targeted at a location suitable for retrieval, and not too far from the launch site such that observations of the same clouds could be made on the descent. A remotely operated cut-down mechanism was used to drop the payload train and a parachute was deployed to control the descent. No damage to the instruments was identified on landing; however, the instruments began to tumble after being cut from the balloon. This appears to have dislodged the camera trigger cable in the C^2HOM–B instrument which meant that holograms were not obtained for the descent.

An imaging payload using a Raspberry Pi camera was deployed to monitor the large-scale cloud conditions during the launch. The 6-megapixel colour images were recorded at approximately 30-second intervals, which resulted in a relatively coarse height resolution of around 120 m. These observations are therefore useful as an independent test of whether the balloon was within cloud, but the higher spatial resolution cloud particle measurements from the holographic microscope are considered to be a more reliable metric for cloud detection.

7.1.3 Meteorological Measurements

Temperatures from the three sensors are plotted in Figure 7.4 for the balloon launch. The measurements agree to within a few degrees for the majority of the launch, but key differences are noted. Significantly larger fluctuations are seen in the Monash Data Logger 1 measurements, as expected, since it had a thermocouple with a smaller time constant than the other logger. Averaging this signal over a few seconds gives a value that agrees relatively well with the raw measurements from the RS41. Monash Data Logger 2 reports systematically higher temperatures than the other loggers, suggesting an uncalibrated offset in this sensor. As the sensors do not agree within their quoted uncertainties, the temperatures were only used as an approximate measurement for this analysis and the quoted temperature values are obtained from the RS41, which is considered to be the most reliable instrument.

Temperature measurements from the RS41 suggest that the freezing level is at an altitude of approximately 1.9 km and the beginning of the tropopause is potentially seen at around 8.5 km, at the highest altitude of the ascent. The RS41 obtained observations reliably for the full launch duration, whereas the Monash Data Loggers did not take observations at temperatures below around -40 °C, likely due to a drop in the battery voltage. The RS41 temperature profiles recorded during the ascent and descent agree well at each height to

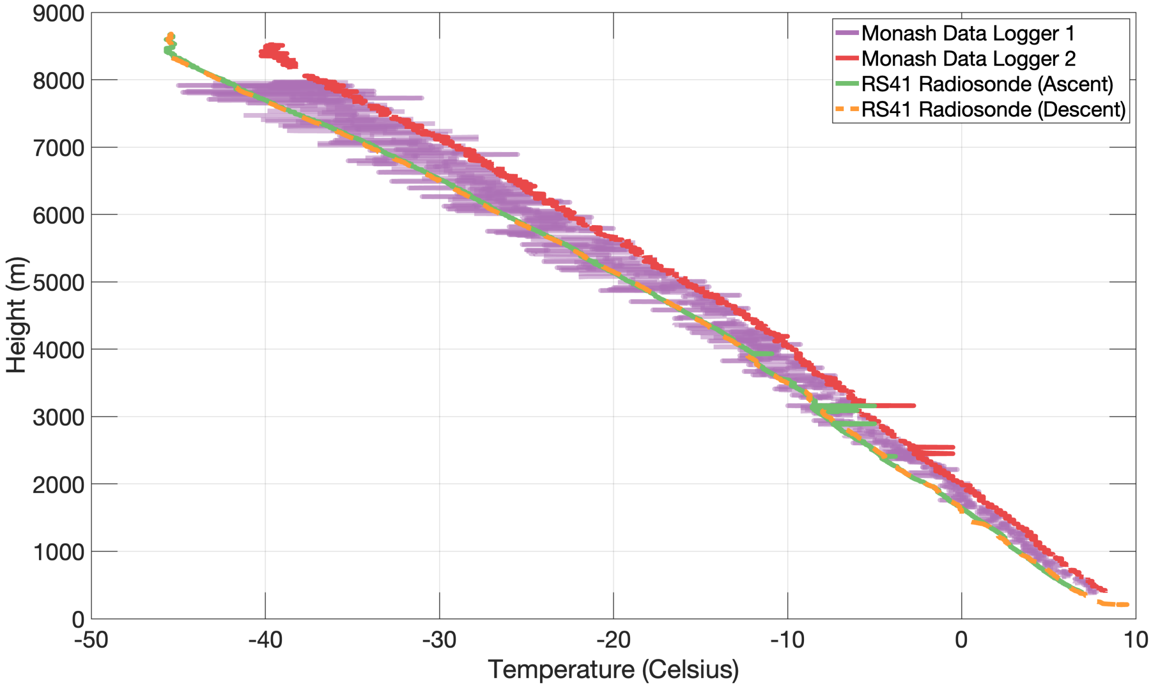

Fig. 7.4 Temperature profiles from the RS41 Radiosonde and Monash University data loggers.

within a few degrees, suggesting that the meteorological conditions were stable for the launch duration and spatial separation of around 20 km between launch location and where the instrument landed.

Relative humidity (RH) measurements are shown in Figure 7.5 for each of the sensors. Significantly different measurements are reported from each sensor in both magnitude and also in the relative signal variations. The relative variations in the RH measured by the RS41 and Monash Data Logger 2 show reasonably consistent agreement for the large-scale features seen, such as the increase in RH up to approximately 2 km, as well as the peak in RH at around 5 km. Very little consistent variation is seen in the Monash Data Logger 1 observations and so these have been excluded from the subsequent analysis.

Multiple cloud layers were observed during the launch, as discussed in the following sections, yet the measured RH does not exceed 94 % at any time during the ascent. These relatively low values may be indicative of processes such as the entrainment of drier air within the cloud due to turbulence. However, as the relative humidity is low even in the middle parts of the cloud, this is not considered the sole explanation. It is assumed here that the lower than expected values are also a result of calibration issues with the sensor. It is interesting to note that whilst the ascent measurements were relatively low, the measurements

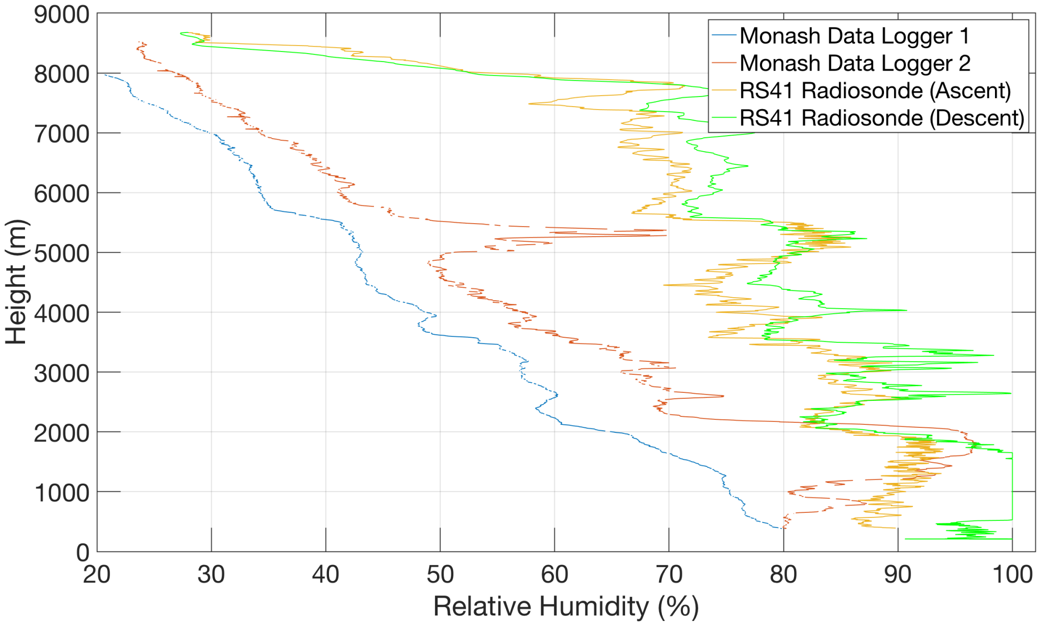

Fig. 7.5 Comparison of relative humidity profiles from the RS41 Radiosonde and Monash University data loggers.

on the descent were seen to show similar relative variations yet reached 100 % within the lowest band of cloud, seen from an altitude of around 600 m and upwards. The horizontal displacement between measurements from the ascent and descent was on the order of 20 km and visually the low-level cloud was unbroken as far as could be seen. These different values may be indicative of significant variations in the cloud water content over these spatial scales.

Due to the agreement in relative variations of the RS41 and Monash Data Logger 2 measurements, these observations are used as an independent verification of the presence of clouds. The RS41 measurements are considered to be the most reliable, due to the extensive use of this instrument for worldwide meteorological observations, and so these will be primarily referred to in this study.

7.2 Manually Analysed Holographic Data

The entire holographic dataset for the launch was manually analysed using the procedure described in Chapter 3 and this analysis procedure is briefly summarised here for reference. For each hologram, a 3D image was reconstructed, particle focus depths were identified, and a polygon was hand traced around the particle outlines. Region properties within the particle masks were then extracted, including the particle equivalent diameters and shape metrics such as the eccentricities of ellipses fitted to the polygon outlines.

This manual dataset is used to validate the automated analysis algorithm, as discussed in Chapter 3, as well as for future training of neural network-based classification methods. As noted previously, identifying the smallest particles by eye can be difficult and hence the reported number densities are expected to be lower than the true value with this method. This approach is thus primarily used to validate the automated size and shape retrievals, though it may be possible to determine a correction for the number densities based on testing alongside other cloud-sampling instruments in the future.

A 1-minute representative summary of manually analysed holographic cloud observations is presented in Figure 7.6 during a time when the balloon was within the lowest observed cloud layer. The spatial distribution of particles detected over this time is shown in the left side of the figure and no obvious sampling bias is noted. The 1-second sampling rate, which is an order of magnitude faster than that used in the Snowy Mountains field campaign discussed in Chapter 6, allows a statistically significant distribution of particles to be recorded within this cloud after approximately one minute, corresponding to a vertical sampling range of around 240 m. Further summarised observations of this kind are provided in Appendix B.

The measured particle size distribution during this time is shown in the top-right panel of Figure 7.6 and the relative particle sizes are visualised by the relative sizes of the spheres that indicate the particle positions within the sampling volume. Lognormal and gamma functions are overlaid in red and yellow, respectively, as defined in Section 6.3.1. These distributions fit the data well, as expected for a typical cloud [34], and the fit parameters are provided in the top right legend. The mean diameter is around 12 microns and the relatively low eccentricity values are consistent with the detection of a cloud of spherical water droplets. The particle images indicated that only spherical particles were observed in this cloud, confirming this interpretation.

7.2.1 Determination of Vertical Cloud Layer Extents

The vertical extent of cloud layers that the balloon passed through was determined by comparison between multiple independent sensors. The most effective method, provided the particle number density was sufficiently high, was to simply note the height at which the first, and last, cloud particles were detected by the C^2HOM–B instrument and define this as the cloud base, and top, respectively. This approach was validated by comparison with the independent measurements of relative humidity and by visual inspection of the Raspberry Pi camera images. The holographic method was preferred, except for when the number density of particles was too low to significantly detect particles, as these observations were sampled

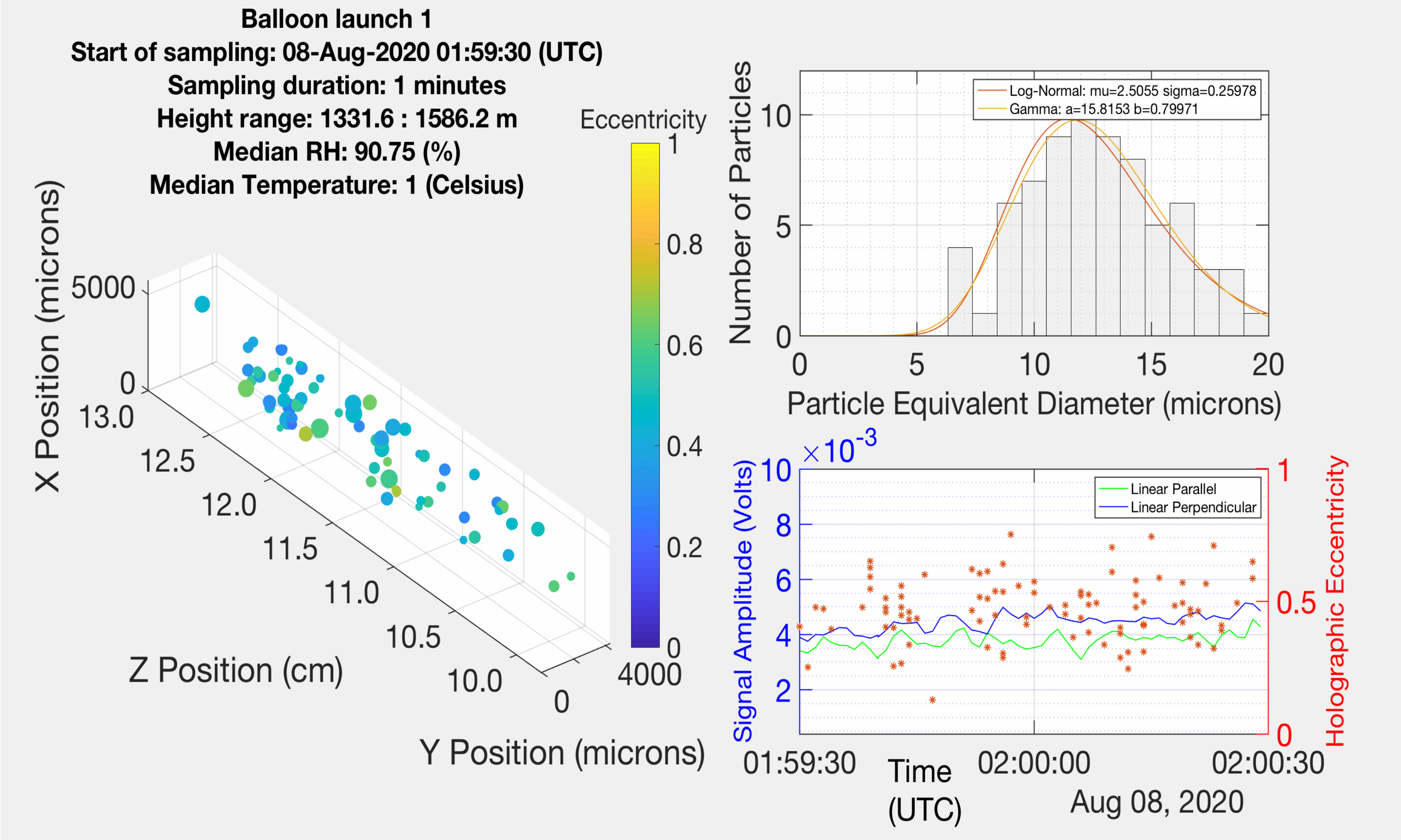

Fig. 7.6 Summary of holographic observations recorded over one minute of the launch. Particle 3D positions, size distribution, eccentricity variations, Polarsonde backscatter and median meteorological measurements are displayed. The z-axis on the 3D plot indicates the depth within the sampling volume relative to the camera sensor, and the transverse dimensions are in the plane of the camera sensor. Spheres on the 3D plot indicate the relative sizes of particles, but note that the absolute size is scaled for visibility.

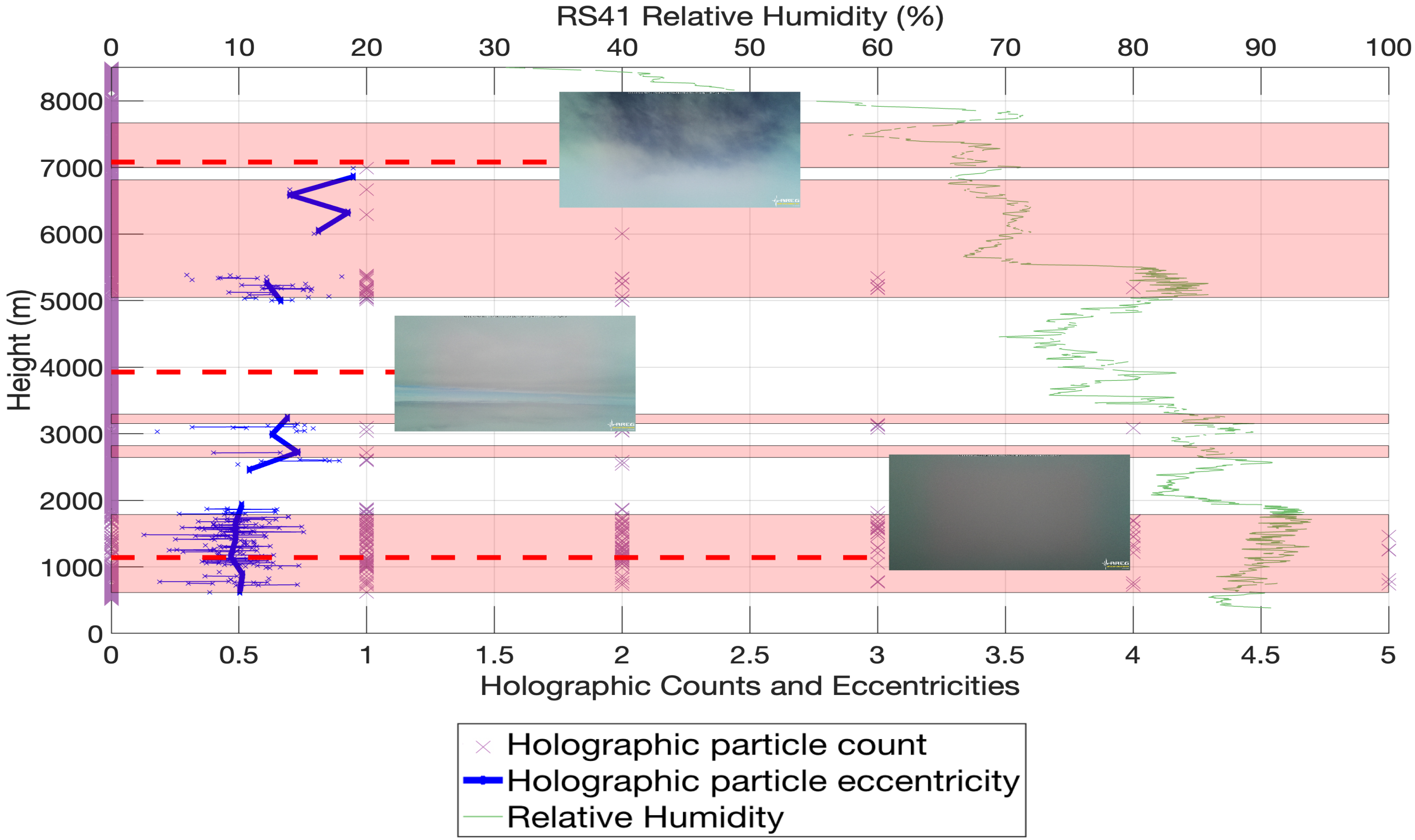

Fig. 7.7 Full vertical profile of raw and 60-second averaged particle eccentricities and raw particle counts measured by the C^2HOM–B instrument. The pink shading indicates regions for which the Raspberry Pi camera images were determined to be fully clouded. Relative humidity measurements from the RS41 are plotted for comparison.

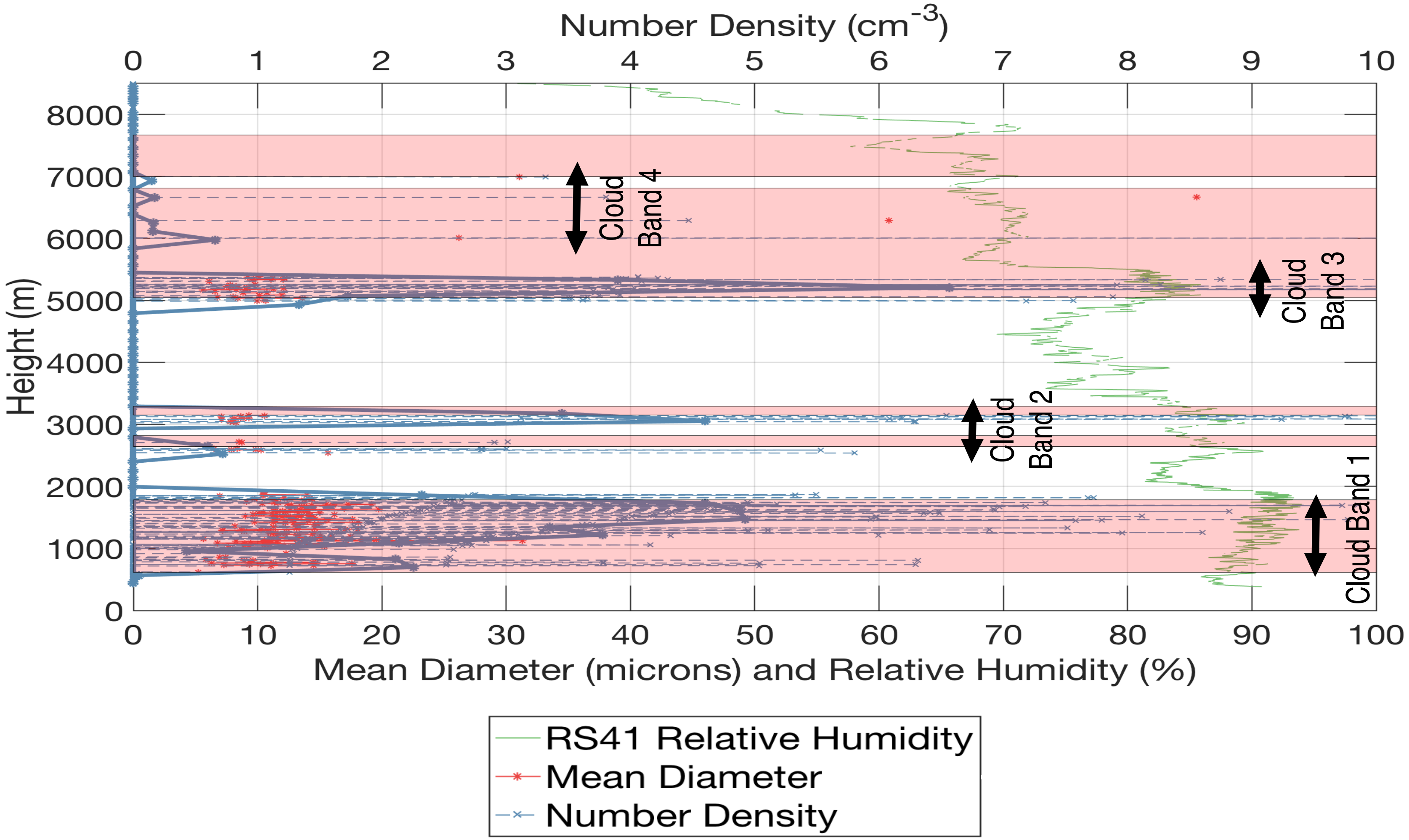

Fig. 7.8 Full vertical profile of raw and 30-second averaged particle number densities and diameters measured by the C^2HOM–B instrument. The pink shading indicates regions for which the Raspberry Pi camera images were determined to be fully clouded, and arrows denote the approximate bounds of the cloud bands determined by the holographic method. Relative humidity measurements from the RS41 radiosonde are plotted for comparison. Number density values that exceed the visible horizontal axis range have a maximum value of approximately 15 cm^{-3}.

at a vertical resolution of around 4 m, as opposed to the Raspberry Pi camera images which were obtained at vertical intervals of approximately 120 m.

A comparison between the heights of particles detected by the holographic microscope, relative humidity measurements, and Raspberry Pi camera images is shown in Figure 7.7. A sudden onset of particles at a height of around 600 m and a sharp termination in particle observations at a height of approximately 1900 m defines the extent of the lowest identified cloud band. The Raspberry Pi camera images were fully obscured by cloud for these heights and the relative humidity dropped significantly at the boundary of the cloud top, in agreement with the holographic determination of cloud extent.

No particles were identified in the height range from the top of the first cloud band up to around 2700 m in altitude. In this height range the relative humidity is seen to steadily decrease and then remain constant with height. The horizon is visible in the Raspberry Pi camera images during this time, suggesting the balloon was in a region of clear sky with cloud layers above and below. The next detection of particles at around 2700 m coincided with a peak in the relative humidity and the Raspberry Pi camera again became fully obscured by clouds. The images were brighter at this height, as more sunlight illuminated the clouds, but a clear contrast between clear sky and cloud could still be determined at the cloud boundaries, providing confidence in the holographic method of determining cloud extent.

The full vertical profiles of holographic measurements of 1-second averaged particle number density and equivalent diameter are presented in Figure 7.8. The pink shaded regions on the plot indicate heights at which the view of the Raspberry Pi camera was fully obscured by cloud and the relative humidity is included for comparison. For clouds below 4000 m there is good agreement between each method as to the extent of the cloud bands. The slight offset between the shaded region and other cloud extent metrics for the cloud bands around 3000 m is due to the coarse height resolution of the Raspberry Pi camera images. These images are recorded once every 30 seconds, as opposed to once per second for observations from the other instruments.

The vertical extents for clouds identified above 5000 m do not agree as well as for the lower clouds. In this height range the clouds were significantly more transparent, indicative of cirrus clouds, with a lower number density of primarily ice crystals. This made it more challenging to judge the extent of clouds based on the Raspberry Pi images and so the cloud extents determined by the holographic microscope were considered even more preferable in this range and tended to agree better with the measured variations in relative humidity.

Only a few particles were detected above around 6000 m and were seen to be large ice crystals with complicated shapes. Given the reduced sampling volume at these heights due to sun saturation, along with the lower number density of ice crystals, the number

Cloud Label	Base Height m	Top Height m	Thickness m	Equivalent Diameter μm	Number Density cm^{-3}
1	620	1870	1250	13 ± 4	4 ± 2
2a	2540	2720	180	9 ± 3	4 ± 1
2b	3030	3150	110	8 ± 1	7 ± 3
3	4990	5380	390	9 ± 2	6 ± 3
4	6010	6990	990	61 ± 34	–

Table 7.1 Means and standard deviations of key cloud properties measured during the launch.

density measurements from the C^{2}HOM–B instrument in this height range are not statistically significant and only observations of particle size and shape properties can be reliably obtained. Due to the small number of detected particles in the highest band of cloud, the holographic method of determining cloud extent was considered less reliable than the Raspberry Pi camera method, though both techniques were limited.

7.3 Cloud Band Comparisons

Five distinct cloud bands were identified during the ascent by the C^{2}HOM–B instrument though it is subsequently argued, due to the proximity of the clouds and similarity of particle properties, that the cloud bands labelled as 2a and 2b are better treated as a single patchy band of cloud. The key holographic measurements for each of the identified cloud bands are summarised in Table 7.1 and will be individually discussed in more detail in the following subsections.

7.3.1 Cloud Band 1

The lowest identified cloud band had a base height of approximately 620 m above mean sea level and a thickness of around 1250 m. Visual observations from the ground suggested that this was an unbroken low-level stratus cloud covering the entire sky. No precipitation was observed during the balloon flight, but light drizzle was observed earlier in the day at the launch site. The cloud feature persisted for multiple hours and it is believed that the same layer of cloud was detected on the ascent and descent of the balloon, based on the similarity of the RS41 temperature and relative humidity profiles seen in Figure 7.4 and Figure 7.5.

The temperature decreased steadily from around 5 °C at the cloud base to -1 °C at the cloud top. Manually analysed holographic images indicated that only spherical water droplets

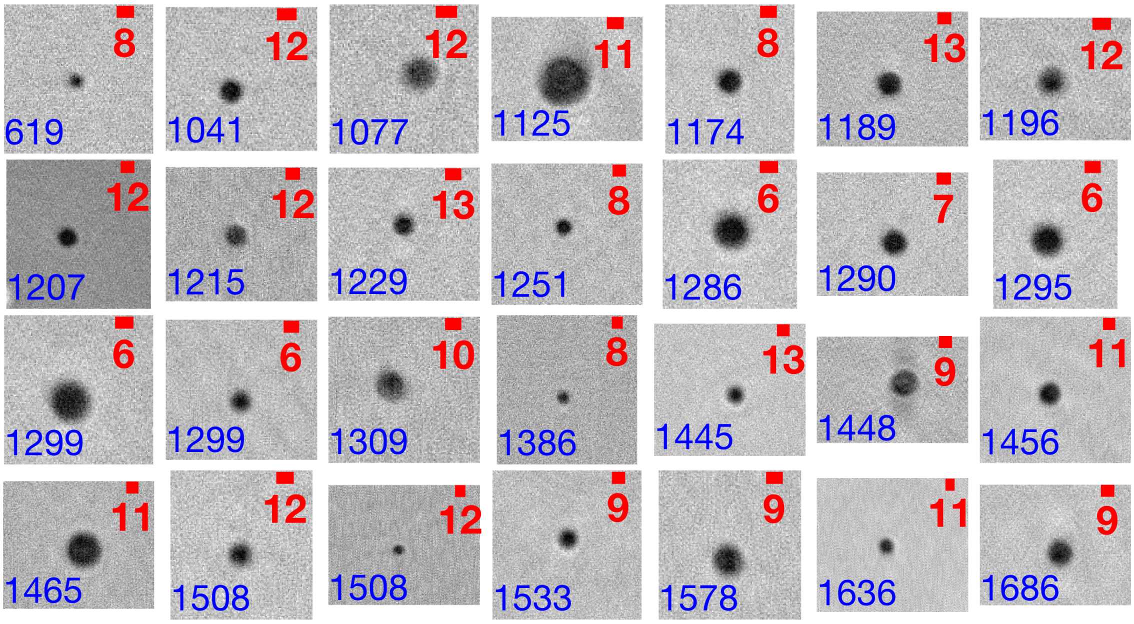

Fig. 7.9 Representative particle images in the first band of cloud ranging from around 620 m to 1870 m. Heights of the detected particles are shown in the bottom-left corner of each image in units of metres. Scalebar units are in microns and note the differing scale for each image due to depth-dependent optical magnification.

were present, as summarised in Figure 7.9. This suggests that this was a warm cloud, as defined in Chapter 2. A linear increase with height in the mean particle diameter is observed from around 9 microns to 13 microns between cloud base and top, as seen in Figure 7.8 and the eccentricity values are consistently low, supporting the visual classification of spherical particles.

The absolute number density measurements are considered less reliable, as noted previously, due to the relatively small sampling volume of this instrument, yet it is still interesting to discuss the relative variation in number density with height within the cloud. To compensate for the reduced sampling volume, it is useful to consider the 30-second averaged number density measurements shown in Figure 7.8 rather than the raw 1-second sampled observations. This averaging corresponds to a height resolution of approximately 120 m, though it is noted that similar general trends are also seen at averaging scales of just a few meters.

The number density shown in Figure 7.8 is first observed to increase and then decrease over a height range of around 500 m from cloud base. It then increases again to an overall maximum at around 1700 m before decreasing rapidly towards the cloud top at around 1800 m. Small-scale variations in cloud particle number density such as these have been observed in prior cloud observation campaigns using a holographic imager [57, 187] and may be indicative of small-scale inhomogeneities within the cloud due to processes such as turbulence and entrainment of dry air. Such high-resolution observations are a unique capability of holographic instruments and future balloon launches of this kind should prove useful in increasing the availability of measurements of small-scale cloud variability, as required for climate and weather modelling [322].

The effective sampling volume was manually calculated at a range of heights to test whether the automated method to determine the reduction in effective sampling volume due to sunlight saturation effects was not significantly influencing the number density observations. A relatively small component of the variation in number density due to the automated sunlight correction was noted; however, the majority of the variation was also seen in the raw particle counts, shown in Figure 7.7, suggesting that this variability was due to physical variations in the cloud particle distribution rather than a sampling bias. Furthermore, the sunlight issue caused a monotonic decrease in the sampling volume with height and hence cannot explain the change from an increase to a decrease in number density observed in certain parts of the cloud. Such variations are expected to be linked to physical processes such as the variability in the vertical wind velocity due to turbulence [323]. A preliminary comparison with the vertical velocity of the balloon has been undertaken that suggests a possible connection, though a rigorous investigation into this matter remains the topic of future work.

The relative humidity measured at cloud base was approximately 86 % and increased steadily up to around 92 % at cloud top, after which the relative humidity dropped sharply. The observed increase of relative humidity and decrease in temperature with height is consistent with adiabatic cloud theory [34]. All measurements on the ascent were less than 100 %, though it is noted that a consistent relative humidity of 100 % was measured within the cloud band on the descent. The lower relative humidity measured may, therefore, indicate either the entrainment of drier air into this cloud layer [324] or a calibration issue with the sensor since water droplets were measured throughout the cloud band.

The mean particle diameter measured within this cloud was relatively small, with a maximum of around 13 microns, and light drizzle was observed before the cloud was sampled, but not during the launch. The earlier drizzle would tend to remove the largest particles from the cloud and is consistent with the observation of only a few particles larger than 20 microns in diameter. The diameter at which growth by coalescence is expected to become more effective than condensation is approximately 40 microns [48] and so these observations are consistent with a warm cloud growing primarily by condensation. Adiabatic cloud theory predicts that the number density will be largest at cloud base when droplets are activated and then remain constant with height up to at least a few hundred metres above cloud base. The particle diameter is expected to increase with height over this height range as particles within rising air parcels grow by condensation [34].

The holographic measurements of number density and particle diameter suggest a deviation from the adiabatic cloud theory. Whilst particle diameter is seen to increase with height, as expected, the droplet number density has a double-peaked variation with height. Such deviations from adiabaticity have been observed in previous in situ aircraft campaigns [267, 325] as well as in a campaign using a holographic imager on a tethered balloon [187]. The latter campaign also observed a low-level stratus cloud with non-adiabatic properties and a lower than expected number density, as in this case.

Non-adiabatic variations in number density are seen throughout the vertical extent of the cloud which may indicate the presence of significant turbulence and entrainment of dry air throughout the cloud, and is consistent with the relatively low relative humidity measurements throughout the cloud. Significant turbulence may be expected to produce larger particle sizes through increased droplet collisions and coalescence, yet only small particles were detected. It is therefore possible that growth by condensation and coalescence in a turbulent environment was responsible for the light drizzle observed earlier in the day and the aftermath of this process was recorded during the launch, during which time the inhomogeneities in cloud structure persisted but the largest particles had been removed [326]. It is also possible, as in the tethered balloon campaign mentioned above, that the relatively low number densities observed are due to undersampling of the smallest cloud droplets, found at cloud base, for sizes below the resolution limit of this instrument of around 5 microns. Further launches incorporating sensors that can resolve small particles would help to address this question and improve understanding of these small-scale microphysical processes.

7.3.2 Cloud Band 2

The next band of cloud was observed with a base height of approximately 2500 m above mean sea level. Clouds above the lowest layer could not be seen by eye from the ground and so the cloud type classification is based on the Raspberry Pi camera images, cloud base altitude, and thickness. Two distinct stratus cloud bands were identified with a vertical separation of only around 300 m. A representative summary of particle images from both cloud bands is shown in Figure 7.10. No distinct differences in particle diameters and shapes were seen between the bands, and hence they are classified as a single nimbostratus cloud band with a small region of clear air separating the cloud masses.

The particle images shown in Figure 7.10 are ordered by detection time and it is noted that a few larger spherical particles were identified towards the lower cloud base. Aside from these particles, the cloud consisted mostly of irregularly shaped ice crystals with a mean

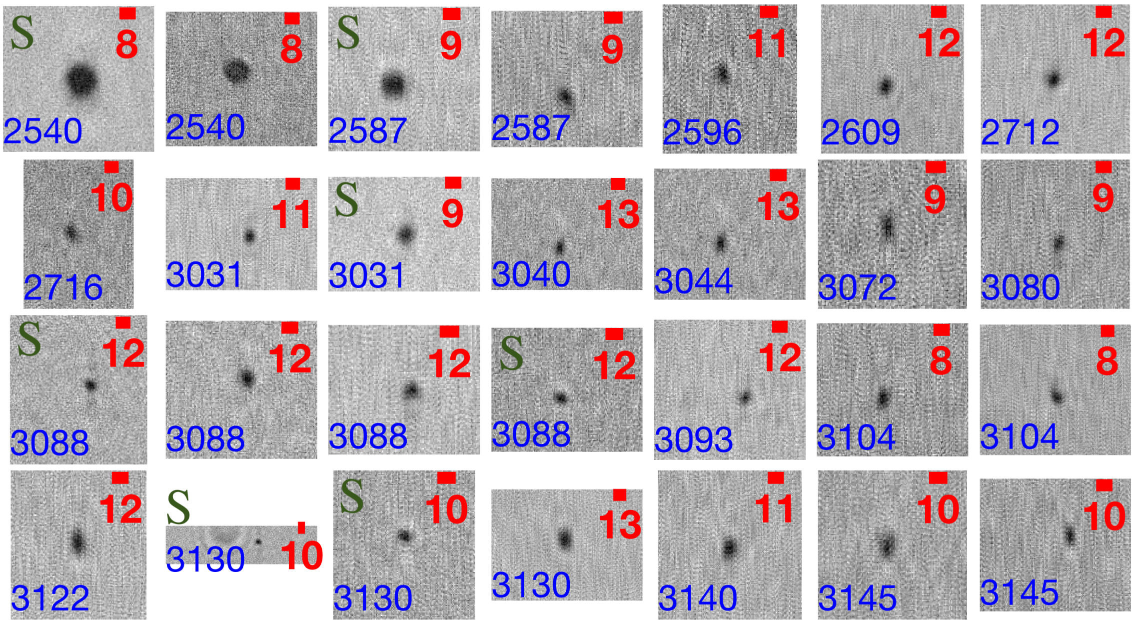

Fig. 7.10 Representative particle images in the middle patchy bands of cloud ranging from around 2540 m to 3150 m. Heights of the detected particles are shown in the bottom-left corner of each image in units of metres. Scalebar units are in microns and note the differing scale for each image due to depth-dependent optical magnification. Particles considered more likely to have a symmetric shape are indicated by a green S.

diameter of 9 microns, smaller than that seen in Cloud Band 1. These particles are at the lower resolution limit of the C^2HOM–B instrument and so specific particle habits cannot be identified; however, a noticeable increase in the mean eccentricity is noted within this cloud band, as shown in Figure 7.7, which supports the classification of primarily aspherical ice crystals. A significant number of particles have a relatively low eccentricity value that could be interpreted as a population of spherical supercooled water droplets, but such a claim is speculative due to the resolution constraints in measuring such small particles. Particles that are considered more likely to have a symmetric shape, based on visual inspection and their eccentricity, are labelled with a green S in Figure 7.10, and the other particles are considered to be more irregularly shaped.

The temperature within the cloud ranges from approximately -5 °C at cloud base to -8 °C at cloud top, suitable for the formation of ice crystals. Previous in situ field observations and laboratory studies suggest that ice crystals within this temperature range are likely to be mostly irregularly shaped with a preference for columns [71], as indicated in Figure 2.2. Whilst an unambiguous habit could not be assigned to the detected particles, the observed increase in mean eccentricity is consistent with the detection of columnar particles. It is important to note that a limitation of this instrument, as with any in-line holographic imager, is that the orientation of the particles cannot be simply deduced. It is therefore possible that hexagonal ice crystals were being viewed on their side. However, given that none of the observed particles were noticeably hexagonal, this interpretation is considered unlikely.

The vertical profile of cloud particle number density, as seen in Figure 7.8, shows that each cloud mass is relatively thin, each no greater than 200 m in thickness, limiting the investigation into number density variability. The relative humidity peaks within each of the cloud masses and sharply drops within regions of clear air. Despite each cloud mass exhibiting similar particle properties and relative humidity values, it is interesting to note that the number density measured in the lower-altitude cloud mass is significantly lower than that in the higher altitude cloud mass. This general feature was observed in Cloud Band 1 and may also be a sign of processes such as the entrainment of drier air within the cloud. A few larger spherical particles were identified at cloud base, but there were not enough such detections to conclusively determine whether this cloud band may also have produced large enough particles to fall in the light drizzle that was observed earlier in the day.

7.3.3 Cloud Band 3

A higher band of altostratus cloud was identified by the holographic detection of particles and by inspection of the Raspberry Pi camera images. As with each of the lower cloud bands, a sharp rise and fall in relative humidity is noted within this height region. The cloud base height inferred from both methods was comparable with the holographic method indicating a height of approximately 4990 m above sea level, yet a significant discrepancy is seen for the cloud top heights. The holographic height estimate coincides better with the sharp drop in the relative humidity. A subtle break in the cloud is noted in a single camera image at a corresponding height. This suggests that a region of clear air of no thicker than around 200 m separates the lower cloud layer, denoted as Cloud Band 3, from the upper Cloud Band 4, with significantly different microphysics. As a significant number of particles was detected in the lower cloud, and due to the coincident feature in the relative humidity, the holographic cloud height determination method is favoured here with a reported cloud thickness of approximately 390 m.

The temperature decreased from -19 °C to -22 °C within this cloud band. In this temperature regime it is expected that the growth of plate ice crystals should be preferred over columns, as summarised in Figure 2.2, whilst the majority of particles should still be irregularly shaped [71]. The variation in habit with temperature is less pronounced for clouds with lower relative humidities and smaller particles, such as those seen in this campaign. It is

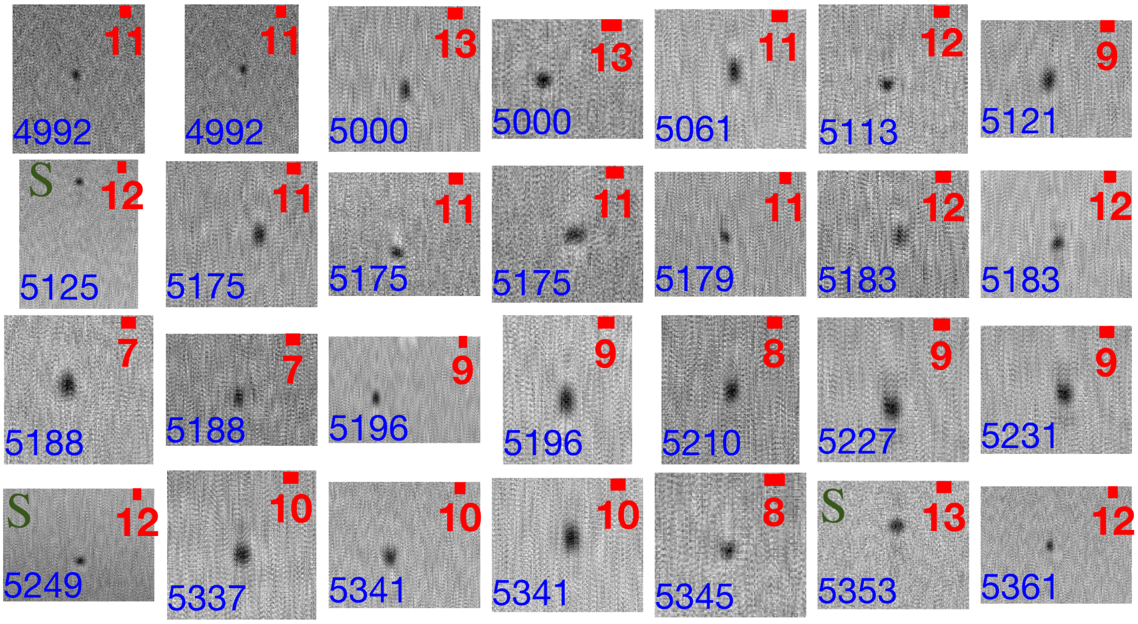

Fig. 7.11 Representative particle images in the middle patchy bands of cloud ranging from around 4990 m to 5380 m. Heights of the detected particles are shown in the bottom-left corner of each image in units of metres. Scalebar units are in microns and note the differing scale for each image due to depth-dependent optical magnification. Particles considered more likely to have a symmetric shape are indicated by a green S.

therefore perhaps not surprising that the particle sizes and images, as shown in Figure 7.11, look similar to those seen in Cloud Band 2.

The 1-minute averaged particle eccentricity is slightly smaller for this cloud band than for Cloud Band 2, as seen in Figure 7.7. This may be indicative of the expected shift towards more symmetrical hexagonal habits; however, as with the previous cloud band, the resolution of the images is such that this cannot be reliably inferred. An instrument with improved resolution, through the use of either a larger camera sensor or magnification optics, should allow such small particle habits to be classified in future field campaigns.

The number density profile is shown in Figure 7.8. As with the previous cloud bands, the absolute number densities are not considered as reliable as the sizes, yet the relative variation is still of interest. This is particularly so for this cloud band since the effective sampling volume had reduced to only 0.4 cm^3 at this altitude. Despite this limitation, a clear trend of increasing particle count and number density is observed with altitude, as with the lower stratus clouds, up to around 5200 m. No large ice crystals were identified, but the abundance of such small particles at this altitude is noteworthy.

7.3.4 Cloud Band 4

The highest altitude cloud band encountered during the launch was identified from the Raspberry Pi images with a base height of around 5850 m. Only five particles were detected within the entire cloud band by the holographic microscope, with the first identified at an altitude of 6010 m. Since the number density of particles was too low to be reliably sampled holographically, the cloud extent must be inferred from the Raspberry Pi images and relative humidity variation. The images indicate that the cloud uniformly becomes more transparent with height, allowing more sunlight to reach the camera sensors, up to an altitude of around 6500 m. Above this altitude the optical thickness throughout the cloud becomes significantly more variable, with patches of embedded clear air also noted in the images. The highest particle was detected at an altitude of 6990 m and the images indicated that the balloon had fully exited the cloud at an altitude of around 7800 m. The relative humidity measurements show variations that are consistent with this determination of cloud extent. From the base of this cloud layer up to the altitude at which the cloud optical thickness became more variable, around 6500 m, the cloud is classified as cirrostratus. Above this height the less uniform spatial extent and wispy morphology are more characteristic of a cirrus cloud.

Despite the proximity to the lower altostratus cloud layer, this band of cloud exhibits distinctly different large-scale structures, as well as dramatically different microphysics. This contrast in microphysics is primarily noted from the particle images, as shown in Figure 7.12. No small ice crystals were detected, and the mean particle equivalent diameter increased by an order of magnitude from 8 microns to 61 microns. This was the first time such large ice crystals were detected during the flight and the mean eccentricity was highest in this cloud band, as expected for the more asymmetrical particle shapes. The reason for the dramatic shift in microphysics between such proximate cloud bands is not currently understood and remains a topic for future investigation.

The temperature decreased steadily with altitude from -26 °C at cloud base to -34 °C at the height of the highest detected particle. The stratiform nature of the cloud band suggests that convection was not playing a dominant role in the cloud evolution. Such non-convective clouds that are colder than around -30 °C are designated as in situ cirrus, as opposed to anvil cirrus, following the terminology outlined in a recent review of in situ measurements of cirrus particle habits [69]. More than half of the particle mass in such clouds was determined in this review to be in the form of rosettes. Of the few particles detected in this cloud band, the particle shown in the bottom left of Figure 7.12 is classified as a budding rosette and, therefore, is consistent with this conclusion. The other particles are classified as bullets and irregular, which are identified as dominant habits for this cloud type and range of particle diameters.

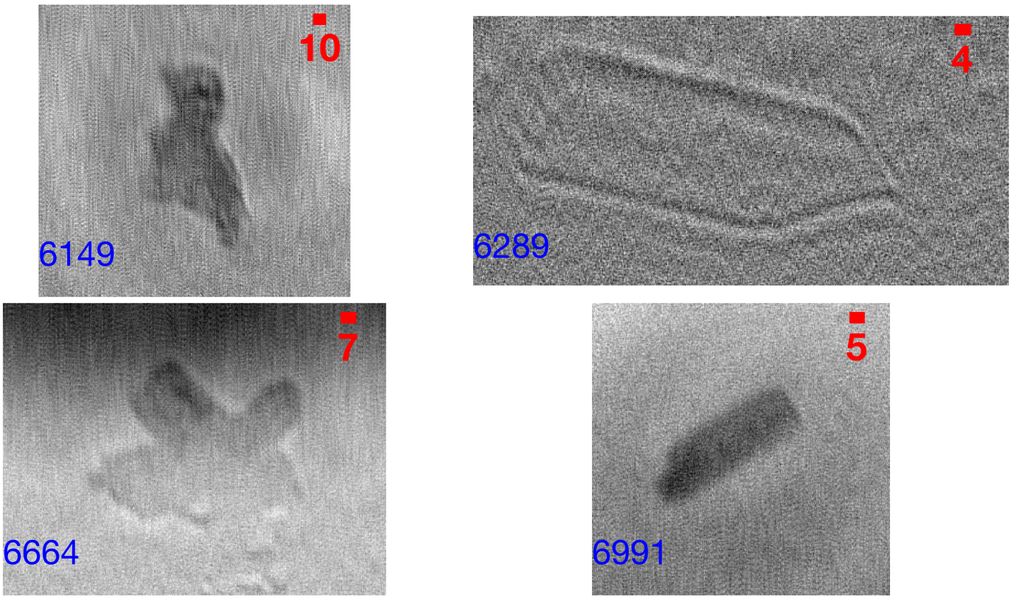

Fig. 7.12 Representative particle images in the thin top band of cloud ranging from around 6010 m to 6990 m. Heights of the detected particles are shown in the bottom-left corner of each image in units of metres. Scale bar units are in microns and note the differing scale for each image due to depth-dependent optical magnification.

The bullet ice crystal shown in the top right of Figure 7.12 is significantly more transparent than any of the other particles observed during the launch. Previous in situ cirrus observations suggest that the majority of column and bullet rosette particles are hollow within these clouds [327]. It is thus speculated that this was a hollow particle based on the transparency. Notable variations within the particle extent in both the amplitude and phase of the reconstruction are identified, and it is further speculated that such variations may allow properties of the internal particle structure to be measured, such as variations in refractive index and surface roughness. Laboratory measurements of hollow crystals should be undertaken alongside Monte Carlo modelling, using the method described in Section 4.6, to determine the feasibility of such an approach. If such a technique is indeed plausible, future launches of a holographic instrument with a larger sampling volume may significantly improve the understanding of these particles, which are currently under-constrained in climate models.

7.4 Comparison with Previous Observations

The key observables to compare with other campaigns are the cloud particle equivalent diameter and number density, which are summarised in Table 7.1 for each of the cloud bands. There are very few in situ cloud measurements in the South Australian region to compare the observations from this campaign with. Air masses originating from the nearby Southern Ocean region contribute significantly to South Australian weather systems [312], and in recent years this region has been the focus of intensive in situ observation campaigns [46, 319, 328–330]. It is therefore of interest to compare the balloon measurements with the Southern Ocean measurements, though complete agreement is unlikely; for example, due to the enhanced impact of continental aerosols over South Australia. Such differing aerosol conditions are investigated in Section 7.6 with HYSPLIT modelling.

In situ aircraft observation campaigns within Southern Ocean clouds have revealed that the cloud droplet number density is strongly seasonal, with significantly lower values measured during winter [328, 331]. Wintertime flights have been undertaken north-west of Tasmania during the SOCEX-I experiment in 1993 [319], and south of Tasmania, as part of the HIPPO campaign [329] in which a cloud with unusually large droplet number density was detected [332], and more recently in an intensive campaign between 2013 - 2015, referred to hereafter as A17 [330]. A major aircraft campaign, the Southern Ocean Cloud Radiation Aerosol Transport Experimental Study (SOCRATES), was most recently undertaken in this region in 2018 [46]. However, flights were undertaken in summertime and hence are not as directly comparable with results from this wintertime balloon launch.

The particle size distributions obtained for all particles detected during the balloon launch, and those within each stratus cloud band, are summarised in Figures 7.13a and 7.13b, respectively. Both lognormal and gamma distributions, as defined in Section 6.3.1, fit well to the particle size distribution of all particles, and within each cloud band. These distributions are expected to fit well for a typical cloud [34] and the fit parameters are provided in the legend of Figure 7.13a. The size distributions within cloud bands 2 and 3 are similar in shape with both ranging between around 5 microns and 15 microns. This similarity is perhaps not surprising given the similarity in particle images, but is still noteworthy given that the bands were separated in altitude by around 1850 m.

The size distribution for Cloud Band 1 is significantly wider than those of the other bands, and more particles were detected overall. Light drizzle was observed before the launch, but not during, and in Section 7.3.1 it was argued that the measurements within Cloud Band 1 of a relatively low number density, variable number density with height, and an increase in particle diameter with height were consistent with the observation of a non-adiabatic cloud in a post-drizzling state. Recent investigations into maritime clouds suggest that drizzle can

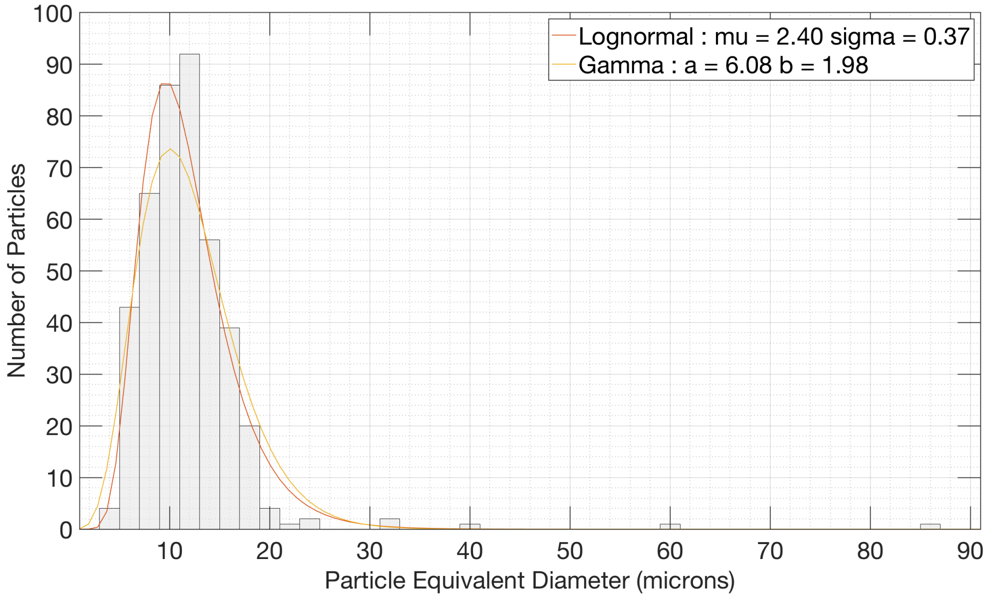

(a)

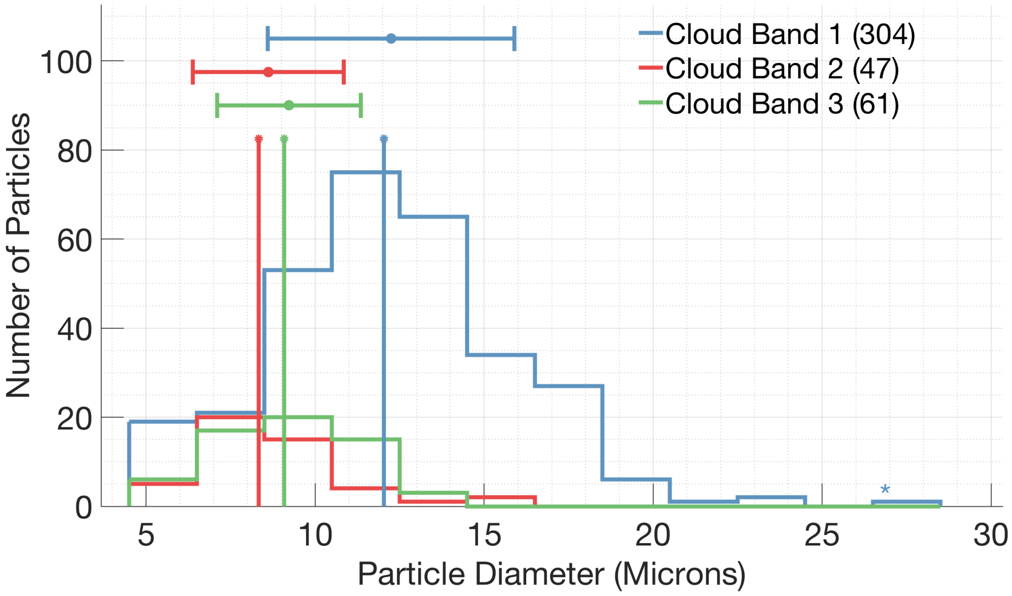

(b)

Fig. 7.13 Particle size distributions for a) all manually identified particles detected during the launch, and b) particles within each band of stratus cloud. Error bars indicate the mean and standard deviations of each histogram, and the stem plots indicate the median values. The number of particles contributing to each histogram is shown in the legend. The star above the far-right column signifies that this column includes contributions from all data points with value larger than or equal to the bin range. The bin width for both plots is 2 microns.

reduce the cloud droplet number density by a factor of 2-3 [326, 333]. A17 reported that particle diameter increased with height for non-drizzling cases, consistent with adiabatic cloud theory, but deviations from this theory were seen for drizzling clouds. Clouds detected in both the A17 and SOCEX-I campaigns with a number density less than 45 cm^{-3} were speculated to similarly be in a state of post-drizzling, and those authors also attributed this post-drizzling state to be the cause of observed deviations from adiabatic cloud theory. The wider size distribution measured within this cloud band, compared with the higher altitude clouds, further supports this interpretation.

The SOCEX-I experiment consisted of 5 wintertime flights north-west of Tasmania, one of which also observed clouds with particle diameter and number density profiles similar to that seen in the holographic balloon launch. Particle diameters from this campaign ranged between 21.6 μm and 29.4 μm, and number densities ranged between 10 cm^{-3} and 40 cm^{-3}. The A17 campaign consisted of 20 flights south of Tasmania under a range of synoptic conditions. The reported average number density for liquid clouds was 40 ± 41 cm^{-3} and the average diameter was 22.8 ± 6.0 μm. Nearly 50 % of the liquid clouds from this campaign were intermittently drizzling, and it was identified that drizzling clouds had significantly larger droplet diameters than the overall average. Number densities were mostly similar for drizzling and non-drizzling clouds, with the exception of a few extreme cases.

The mean diameter, as summarised in Table 7.1, measured within each stratus cloud band in this campaign varied between 8 ± 1 μm and 13 ± 4 μm, and the mean number density varied between 4 ± 1 cm^{-3} and 7 ± 3 cm^{-3}. In each case the uncertainty is quantified by the standard deviation. The diameter measurements agree within uncertainty with those measured within non-drizzling clouds in A17 [334], yet they are outside the range of values reported in SOCEX-I. The number density measurements are within the uncertainty bounds reported in A17, but only Cloud Band 3 is within the range of values measured in SOCEX-I.

The lack of agreement between the balloon measurements and those from SOCEX-I can potentially be explained by the significant variability of cloud microphysical properties and the fact that only 5 flights were carried out for that campaign. It is, however, noted that the number densities measured in the balloon launch are anomalously low and are possibly a sign of limitations of the C^2HOM–B instrument. Clouds with number densities below 10 cm^{-3} and comparable particle diameters have been measured in the Southern Ocean [335], and other parts of the world [336, 337], in what are referred to as Ultra Clean Layer (UCL) clouds. These UCL clouds are notably optically thin and, therefore, this explanation is considered unlikely for this experiment where clouds below the highest cloud band appeared optically thick by visual assessment. The sources of potential sampling biases for this instrument are discussed further in Chapter 3, but it is expected that such sampling issues can be resolved in future launches by increasing the sampling volume of the instrument and by resolving the sunlight saturation issue.

The comparison of balloon observations can be extended to Southern Ocean cloud observations from remote sensing instruments as part of intensive shipborne campaigns (Clouds Aerosols Precipitation Radiation and atmospheric Composition Over the SoutheRN ocean (CAPRICORN) [338] and Measurements of Aerosols, Radiation and Clouds over the Southern Ocean (MARCUS) [46]), as well as the previously mentioned summertime aircraft flights during SOCRATES [46]. A recent review of observations from each of these campaigns [293] reveals that clouds with number densities as low as those measured in this balloon launch occur with significant frequency over this region. The question as to whether such clouds could have optical depths as great as those seen in this launch remains the topic of future investigation.

The launch observations have so far been compared to those from field campaigns over the nearby Southern Ocean due to a lack of previous in situ cloud measurements in South Australia. Such a comparison is inherently challenging as clouds over the continent are expected to differ significantly from those over the Southern Ocean for a number of reasons, for example, due to the closer proximity to continental aerosol sources. It is therefore of interest to compare the balloon measurements with those from a general review of in situ measurements within stratus clouds [232]. This comparison is displayed for mean particle diameter in Figure 7.14a. The mean particle diameters measured in this launch are in the lower range for marine clouds and the upper range for continental clouds. These intermediate values may be as a result of the proximity of the launch site to both coastal and continental regions. This possibility will be investigated further in Section 7.6. The number density comparison is shown in Figure 7.14b and it is again noted that the measurements from this launch are at the very lower limit of those seen in previous campaigns.

7.5 Comparison with Polarsonde and Wind Observations

The primary Polarsonde observables are the parallel and perpendicularly polarised backscatter components in the Lin90 and Lin45 channels, as defined in Chapter 5. As noted previously, the Lin45 measurements were not considered reliable for this launch and so the following discussion is focussed on the Lin90 measurements. The instrument records backscatter from both cloud particles and aerosols [65], and so a key challenge in interpreting these observations is in separating the component of the signal due to each of these populations of particles. The Polarsonde is in the early stages of field testing and so analysis of Polarsonde

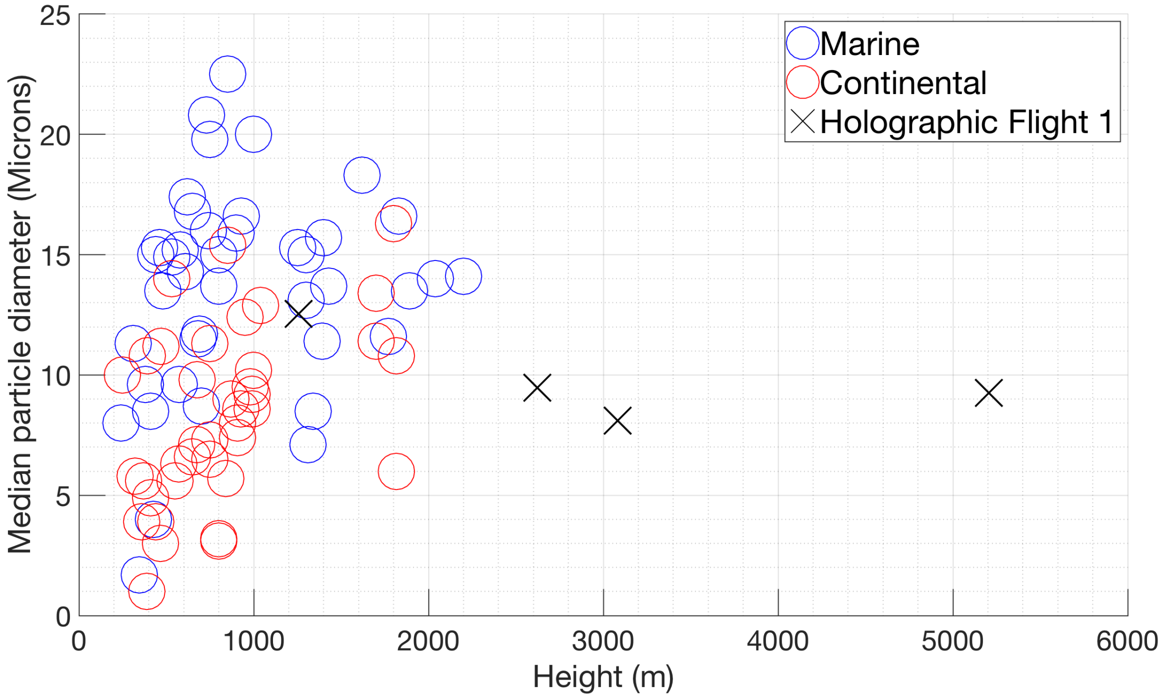

(a)

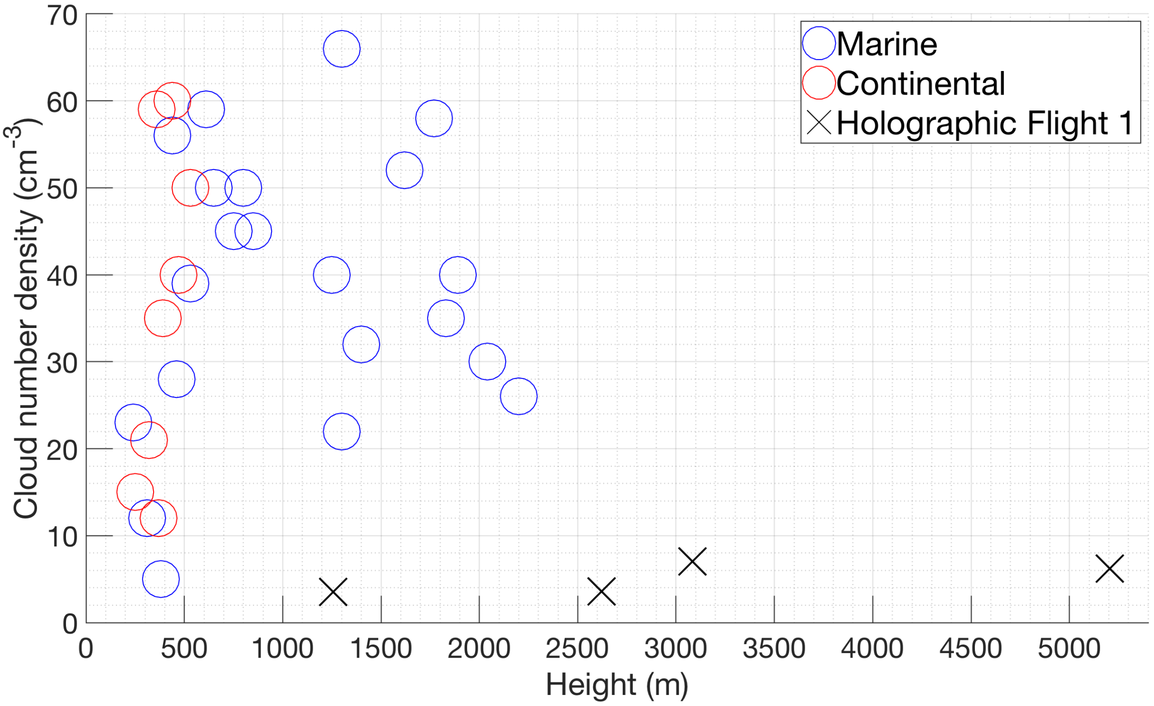

(b)

Fig. 7.14 Mean particle diameters (a) and number densities (b) measured in each cloud band during this launch compared to those for stratus clouds in the literature (Miles, 2000). Note the cropped vertical scale on the number density plot to clearly show the low values measured in the balloon launch.

observations was a secondary goal of the launch, and collocated holographic observations of particle properties should prove useful in interpreting and calibrating this instrument.

It was identified in Chapter 6 that the depolarisation can be a misleading metric under certain conditions, for example due to condensation and accumulation of dirt on the sampling window in front of the sensors and LEDs. These issues are avoided in this campaign as the Polarsonde did not have a protective cover glass and the balloon launch was relatively short in duration. Issues due to the impaction of water droplets directly onto the optical components are still possible, but no obvious spiking in the signal was identified that would indicate this impaction had occurred. Therefore, the Lin90 depolarisation is considered reliable for this field campaign. The Polarsonde variance-based metric, defined in Chapter 6 as an alternative metric for determining particle shape properties, is not used here as it depends on signals from the Lin45 channels which were not considered reliable for the Polarsonde deployed in this field campaign.

The vertical profiles of the Polarsonde Lin90 backscatter components for each polarisation channel and the Lin90 depolarisation are shown in Figure 7.15. These can be directly compared with the holographic number density profile and cloud extents determined by the Raspberry Pi camera. The balloon velocity components were calculated using the GPS position measurements and are also plotted for comparison. It is assumed that whilst the balloon will not be a perfect tracer of the ambient winds, the meridional and zonal balloon motions should provide a reasonable indication of the variations in these wind components [339, 340].

This assumption is supported by the similarities in the vertical wind profiles retrieved by the Buckland Park VHF Stratosphere Troposphere (ST) radar [341] over the same observation period, as shown in Figure 7.16. This comparison is not ideal as the radar was approximately 70 km away from the launch site, but the reasonable agreement shows that the balloon velocities are at least somewhat realistic. This methodology is supported by the findings of a previous intensive field campaign in this region to evaluate the ST radar performance as compared with radiosonde observations [340, 342]. Reasonably good agreement was reported in this study between wind measurements derived from radiosondes launched from sites separated by 36 km, and between the wind profiles derived from the ST radar and sonde-derived wind profiles. The vertical velocity is assumed to be dominated by the balloon's buoyancy and is relatively constant at around 4 m s^{-1} for the ascent. It may still be possible to extract some sense of the vertical velocity perturbations due to turbulence, but this remains the topic of future research.

A steady increase with height in both the Lin90 parallel and perpendicular components is observed within Cloud Band 1, and both signals begin to decrease at the cloud top. It is

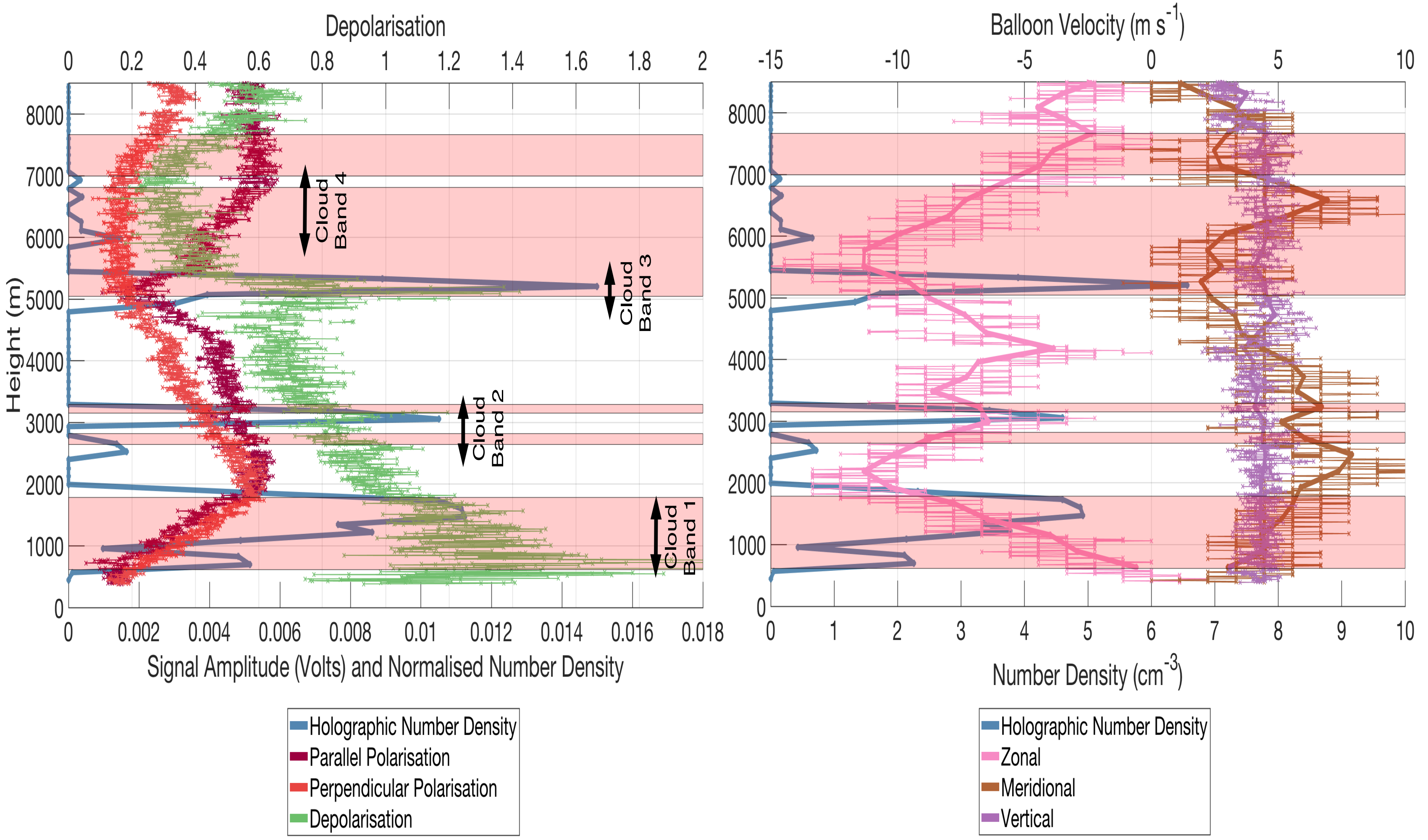

Fig. 7.15 Vertical profiles of the (left) Polarsonde Lin90 backscatter signals and Lin90 depolarisation and (right) balloon velocity components. These profiles are compared with the vertical profile of 30-second averaged holographic number density. Note that the holographic number density profile on the left-hand figure has been normalised to match the scale of the Polarsonde signal variations. Pink shaded regions indicate cloud bands identified by the Raspberry Pi Camera method, and arrows denote the approximate bounds of the cloud bands determined by the holographic method.

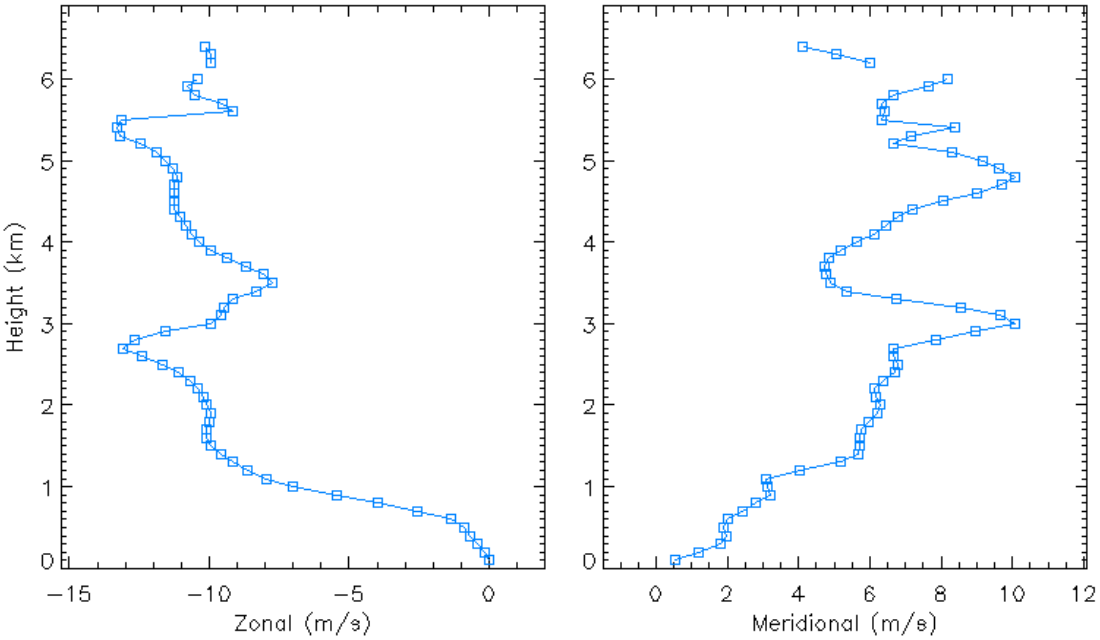

Fig. 7.16 Wind profile of horizontal wind components retrieved by the Buckland Park VHF ST radar during the launch.

tempting to attribute this increase to the observed increase in cloud droplet diameter and number density within this cloud, as this would tend to increase the backscattering efficiency; however, since only a gradual decrease in backscatter is seen above cloud top, the majority of this signal must be associated with aerosol. Therefore, it is argued that within this region, the Polarsonde observations are primarily a tracer of the aerosols. This interpretation is supported by the low cloud particle number densities reported by the holographic microscope throughout the flight, and is not unexpected given the high backscattering efficiency for nanometer-scale aerosol particles. Subtle variations in the signal are noted that coincide with variability in the cloud droplet number density, but this appears to be a very small component of the overall signal, and the task of separating these contributions remains the subject of future work.

The unscaled Lin90 depolarisation was relatively high throughout the launch and an average value of around 1.3 was recorded within Cloud Band 1. These high values are consistent with a population of irregularly shaped aerosols. Comparing with the previous observations, this suggests a population of aspherical aerosols within Cloud Band 1 that increased in either number density, size, or both, with altitude. This is interpreted as the growth of aerosols via condensation that are smaller than the roughly 2 micron diameter resolution limit of the holographic microscope.

The zonal and meridional velocities are observed to increase in magnitude with height within Cloud Band 1. A sharp reversal in these trends is identified around the cloud top and both velocities begin to decrease in magnitude with height. A coinciding reversal from increasing to decreasing backscatter with altitude is noted in the Lin90 components. This transition coincides with a trend of decreasing Lin90 depolarisation with height, consistent with a gradual shift towards a population of aerosols that are more spherical on average. It is proposed that this change in aerosol population, coinciding with the wind trend reversal, is indicative of aerosol mixing with an air mass of differing origin to that seen in the lowest cloud band. This theory is investigated further in Section 7.6 using HYSPLIT modelling. The fact that this trend is largely unaffected by the presence of Cloud Band 2 lends further support to the inference that the Polarsonde signals are mostly dominated by aerosol rather than cloud particle contributions in this region.

The rate of decrease with altitude of both the Lin90 components increases a few hundred metres below the base of Cloud Band 3, coinciding with another reversal in the zonal velocity trend. A greater decrease is seen in the parallel component than the perpendicular component and this causes a significant increase in the depolarisation within the cloud band. The parallel component sharply increases above the top of Cloud Band 3, whereas the perpendicular component remains relatively constant with height beyond this point. Since this change in trend begins below the cloud base, this feature is still considered to be associated with aerosols, though the sharp transition at cloud top suggests that the aerosols are strongly coupled with the cloud particles in this case. Even aside from the sharp depolarisation increase, the mean depolarisation at these heights is still relatively large with a mean value of around 0.5, indicative of a population of aerosols that are irregularly shaped, though still more spherical than those seen in Cloud Band 1.

A potential explanation for the sharp change in parallel backscatter within Cloud Band 3 is presented as follows. Irregularly shaped ice crystals were detected within this cloud by the C^2HOM–B instrument, and it is assumed that they were formed from the population of non-spherical aerosols detected by the Polarsonde. This aerosol population is likely different to that found within Cloud Band 1, as supported by HYSPLIT modelling presented in Section 7.6, and it is suggested that they are suitable Ice Nucleating Particles (INP) from which the ice crystals can grow. A reduction in the total aerosol number density occurs as the aerosols are converted to ice crystals and a corresponding decrease in parallel backscatter is observed, since the Polarsonde is more sensitive to aerosols. The perpendicular component is seen to remain constant throughout cloud bands 3 and 4, and this is proposed to be due to the significant perpendicular backscatter contributions from the irregularly shaped ice crystals.

In the clear air region between cloud bands 3 and 4, the parallel backscatter value jumps sharply back to the clear air value seen previously at an altitude of around 4000 m, and then remains constant with height. Coinciding with the detection of particles in Cloud Band 4, the parallel backscatter begins to increase again until the height of the last detected particle. This increase is suggested to be due to a decreasing ice crystal number density with height and it is supposed that this corresponded to an increase in aerosols as they became liberated via the sublimation of ice crystals, and hence an increasing parallel backscatter. Above the altitude at which the last ice crystal was detected, and the clouds became more transparent in the Raspberry Pi camera images, the perpendicular backscatter is seen to also increase back to the clear air value, and this is assumed to also be a sign that the aerosol number density was increasing, since no more cloud particles were being nucleated and existing particles were decreasing in size due to the reducing supersaturation. A departure from the zonal velocity trend is seen at the top of Cloud Band 4, further suggesting the potential link between variations in the wind profile, cloud formation, and aerosol mixing.

This balloon launch represents the first time in which holographic microscope and Polarsonde observations have been compared through a full vertical profile into clouds. The insights gained from this campaign are necessarily preliminary in nature, but motivate future observations of this kind to better understand the underlying cloud-aerosol processes. Future observations alongside additional cloud-sensing instruments should help in assessing alternative interpretations of these observations. The link between Polarsonde backscatter and balloon velocity seems clear, but this could instead, for example, be an indication of horizontal cloud inhomogeneities as the balloon moves through different parts of the cloud. The mostly smooth variation in the signals with height tends to support the former argument, but it is hard to conclude unambiguously. Further launches and calibration studies alongside aerosol instruments should be carried out to better constrain these complicated relationships, but it appears clear that there is the potential for these measurements to be used in quantifying both cloud particle and aerosol microphysics at a relatively low cost, as compared to aircraft campaigns.

7.6 HYSPLIT Back Trajectory Analysis

HYbrid Single-Particle Lagrangian Integrated Trajectory (HYSPLIT) [343] is a modelling system that allows the computation of air parcel trajectories. This tool can be used with a meteorological model to determine the sources of a given air mass through the computation of back trajectories [344]. HYSPLIT was used in this work to investigate the previously discussed hypothesis that air masses of differing origin and composition could explain some of the variations in C^2HOM–B and Polarsonde observations.

HYSPLIT back trajectories computed from four significant altitudes are shown in Figure 7.17. To avoid issues due to sensitivity to the initial conditions, the model was operated in meteorological grid ensemble mode in which the 3D meteorological model dataset was shifted by one grid point in each dimension, resulting in 24 independent back trajectories per model run. The Global Data Assimilation System (GDAS) meteorological model was used at a grid resolution of 1 degrees and back trajectories were computed over a time-span of 72 hours. The model was run for a few hours either side of the launch time and the outputs were seen to be largely consistent with each other.

It was noted in Section 7.4 that the mean particle diameter measurements within the stratus cloud layers were on the boundary between those for marine and continental clouds. The number density values were low, a property more typical of marine clouds which also tend to have larger diameters [34]. The back trajectories around the height of Cloud Band 1 are shown in Figure 7.17a, and it is seen that a significant contribution to this air mass has come from the Southern Ocean, as postulated earlier. Some tracks at this altitude come from the north and the majority of all tracks pass over the continent for some amount of time. This mixing of marine and continental aerosol sources may explain the diameter values that would be considered small for a marine cloud.

Above an altitude of around 2000 m, a reversal in the wind and Polarsonde backscatter trends was identified. It was proposed that this was an indication of a change in the aerosol population due to mixing with an air mass of a different origin from that below this height. A clear transition can be seen in the origin of the back trajectories as a function of height, as shown in Figure 7.17b. Around this altitude there are no longer trajectories coming from the Southern Ocean and instead the sources are solely continental, largely from the north-eastern areas of Australia. The decreasing, yet still large, Lin90 depolarisation values around these altitudes would suggest that these continental aerosols are more spherical on average than those from the lower heights, but still irregularly shaped.

The cloud particles detected in cloud bands 2 and 3 were similar in shape, size, and number density, despite being separated by around 2000 m in altitude. Over this height range there does not appear to be a significant change in the back trajectories, in that they are still solely of continental origin, as shown in Figure 7.17c. The similar air masses are consistent with the similarity in the cloud bands, though it is interesting to note that at this altitude the trajectories are originating more from the west, rather than the lower ones which came from the east.

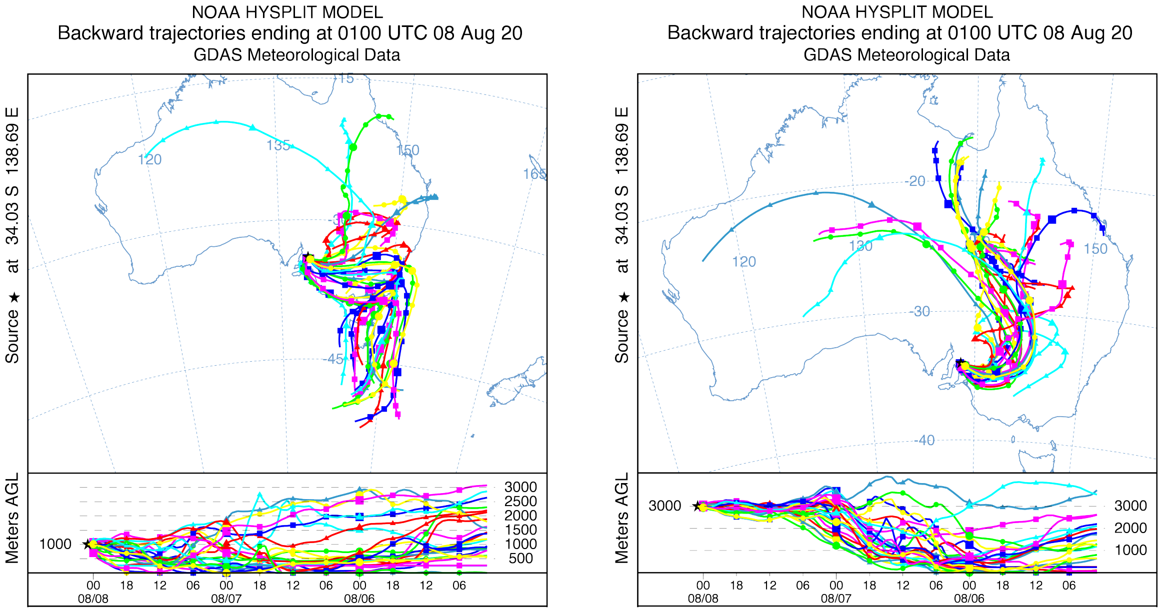

(a) 1000 m (b) 3000 m

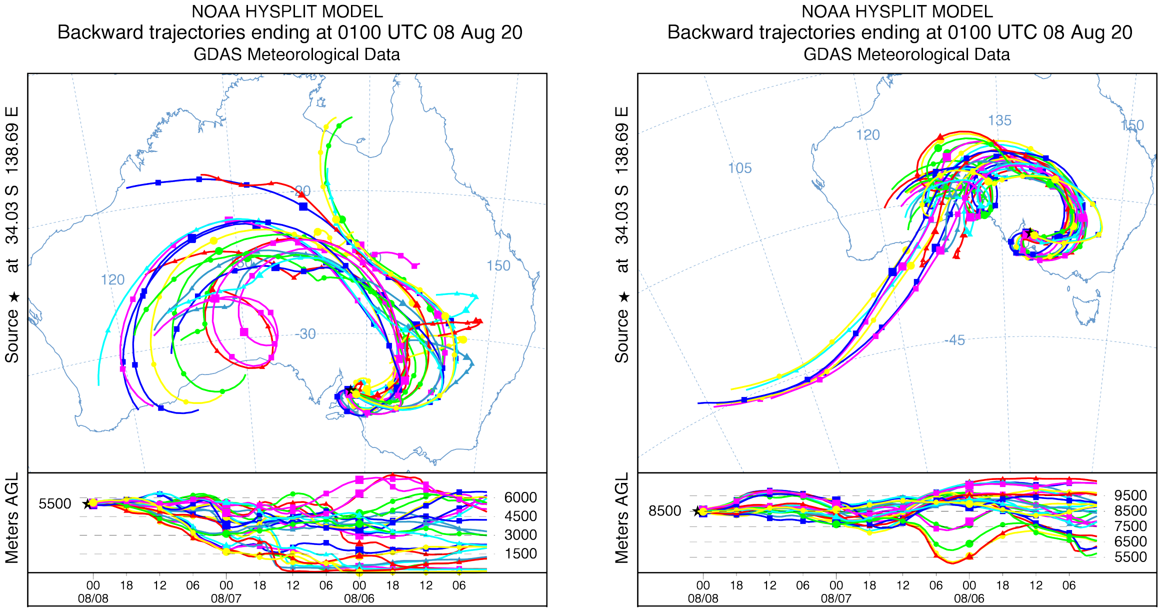

(c) 5500 m (d) 8500 m

Fig. 7.17 HYSPLIT back trajectories computed from a targeted height of a) 1000 m, b) 3000 m, c) 5500 m, and d) 8500 m.

A substantial and abrupt change in the cloud particle properties, Polarsonde backscatter signals, and winds was identified above the top of Cloud Band 3 from an altitude of around 5500 m and upwards. A band of cirrus cloud with significantly large and aspherical particles was observed, coinciding with a reversal in the wind trends and a significant decrease in the Lin90 depolarisation and backscatter trends with height. The back trajectories in this altitude region are still predominantly of continental origin, yet a significant proportion are now seen to come from the Southern Ocean again, in this case from the west, as shown in Figure 7.17d.

Source attribution of aerosols, aerosol composition, and the role of aerosols in cloud formation are complicated topics, and difficult to constrain with a simplified approach as was used here. The purpose of this investigation was, therefore, to highlight the potential connections that may exist between these observations as motivation for a more comprehensive investigation in the future. Multiple balloon launches from a range of spatially distributed locations would be of particular interest to attempt to measure the spatial variations of these properties at a range of scales, from kilometres down to millimetres.

7.7 HIMAWARI-8 Comparison

The in situ balloon observations can be directly compared to HIMAWARI-8 satellite retrievals of Cloud Type (CT), Cloud Effective Radius (CER), Cloud Top Height (CTH), and Cloud Top Temperature (CTT). HIMAWARI-8 data used in this study was obtained for 0230Z at which time the balloon was at approximately the maximum altitude of the launch. The satellite data products have a spatial resolution of 0.05 degrees and are described further in Chapter 5.

The HIMAWARI-8 Cloud Type retrieval is shown in Figure 7.18a in the region surrounding the launch site. Significant spatial variation in the retrieved CT is observed, which is consistent with the multi-layer cloud system detected during the launch. A large-scale stratus cloud layer is seen, along with more localised regions of nimbostratus and altostratus, as well as a thin cirrus layer adjacent to the launch site. Large uncertainties are expected for satellite retrievals from multi-layer clouds [297], but it is encouraging that each of these cloud types was also identified by the in situ instruments. It is assumed in this case that the reported cloud types are representative of the highest altitude cloud layer within a pixel since information predominantly comes from the cloud top [292].

Contiguous regions of each cloud type are identified in the area surrounding the launch site, and so it is further assumed that spatially averaged properties of the cloudy pixels surrounding the launch site will be representative of the cloud layers directly above the launch site that are obscured by the highest altitude clouds in the satellite retrievals. Pixels

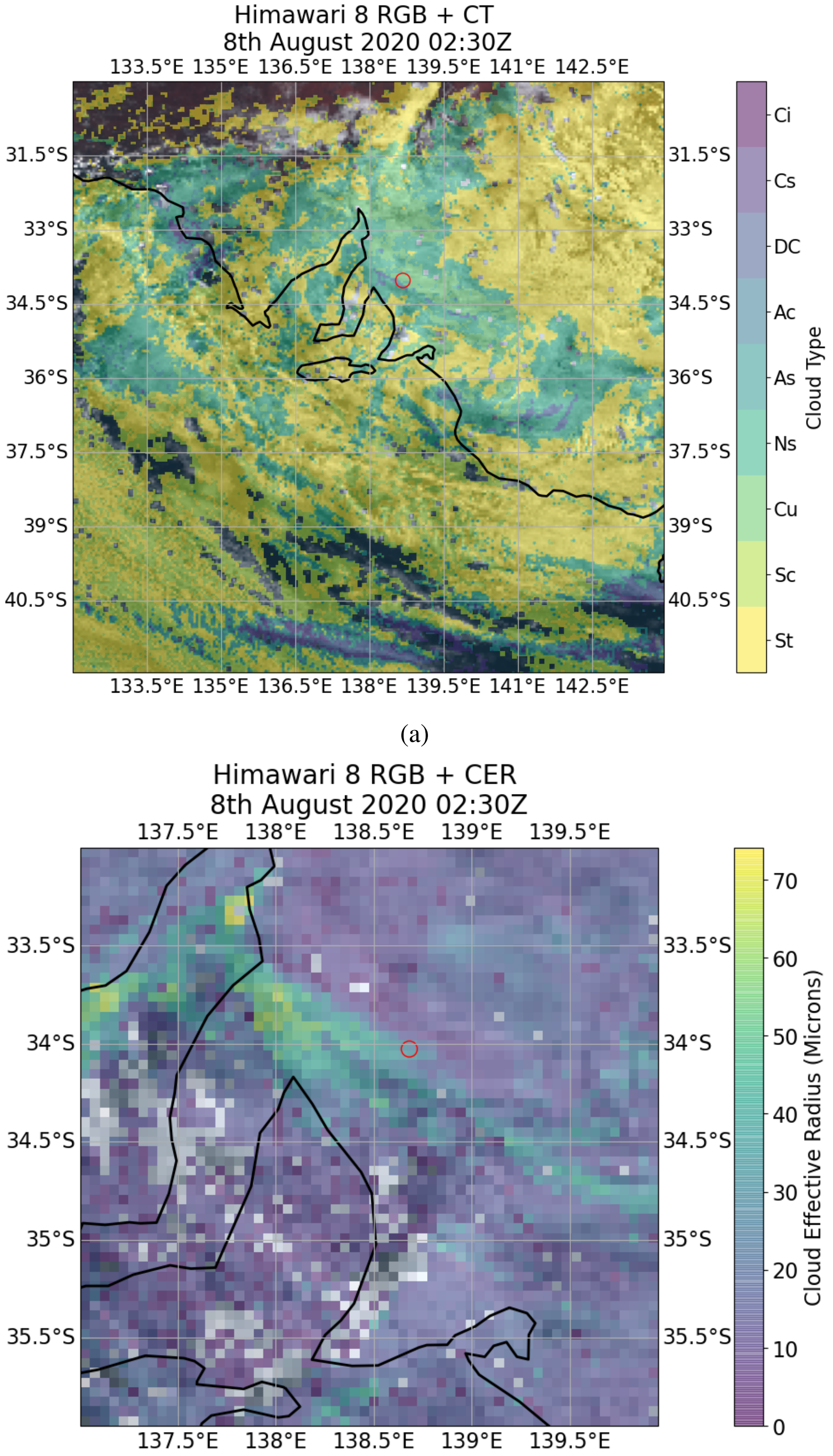

(a)

(b)

Fig. 7.18 HIMAWARI-8 retrieval of a) Cloud Type (CT) and b) Cloud Effective Radius (CER), during the launch. The red circle indicates the location of the launch site.

within a 3 x 3 degree region surrounding the field site were averaged within three broad height ranges, as masked by the CTH. Low-level clouds were defined to have a CTH in the height range below 2 km, mid-level clouds were in the range from 2 km to 6 km and high-level clouds were above 6 km. These ranges were chosen to be consistent with the altitudes at which distinct cloud types were identified from the launch observations. The spatial region used to compute the averaged values is displayed in Figure 7.18b which shows the retrieved CER. Small particle sizes are seen in the low-level and mid-level stratus clouds surrounding the launch site with larger values identified within the high-level cirrus cloud, consistent with that measured in the launch. All five of the cloud bands identified in the launch, as defined in Section 7.2.1, are compared here to maximise the number of comparisons.

A summary of the statistical comparison between in situ and HIMAWARI-8 measurements of CTH, Cloud Effective Diameter (CED), and CTT is presented in Table 7.2. The in situ balloon determination of CTH and CTT was based on the holographic method of identifying the height of the highest detected particle within a cloud band. The uncertainty with this method is difficult to quantify as it is dependent on the number density of particles, and the instrument is not sensitive to particles smaller than around 5 microns. The latter issue is not expected to be a significant problem in this case since such small particles are expected around the cloud bases rather than the tops. The CTH and CTT are rounded to a lower precision to attempt to account for this ambiguity.

Complete agreement is not expected between the in situ and satellite observations since significant spatial variability is possible over the large satellite averaging area, but the ranges of values can still be compared to determine potential biases in the HIMAWARI-8 retrievals. HIMAWARI-8 measurements, along with the holographic CED measurements, are therefore quoted as a mean and standard deviation within a given cloud band rather than as the standard error in the mean values. It is assumed that the in situ measurements are more reliable and that disagreement in results is an indication of biases due to limitations in the remote sensing technique.

The CTH and CTT comparisons of greatest interest are for the lowest and highest cloud bands, since the mid-level height range encompasses three distinct stratus layers of differing heights. For Cloud Band 1 the mean HIMAWARI-8 CTH is 340 m lower than that identified by the C^2HOM–B instrument and does not encompass the holographic value within one standard deviation from the mean. If a larger uncertainty of around 100 m is adopted for the holographic CTH method then the observations do agree within the uncertainty. The HIMAWARI-8 CTT agrees well with the RS41 value for this cloud band.

A similar underestimation of the CTH is seen in Cloud Band 4, with a larger difference of 610 m in this case. The C^2HOM–B value does not lie within two standard deviations

	Cloud Base Height	Cloud Top Height			Cloud Effective Diameter			Cloud Top Temperature		
	m	m			μm			°C		
Cloud Label	C^2HOM–B	C^2HOM–B	HIMAWARI	Diff.	C^2HOM–B	HIMAWARI	Diff.	RS41	HIMAWARI	Diff.
1	620 ± 10	1870 ± 10	1534 ± 307	–340	13 ± 4	26 ± 8	13	-1.3 ± 0.1	-1.5 ± 1.8	–0.2
2a	2540 ± 10	2720 ± 10	3849 ± 1018	1130	9 ± 3	32 ± 11	23	-6.3 ± 0.1	-12.5 ± 5.5	–6.2
2b	3030 ± 10	3150 ± 10	3849 ± 1018	700	8 ± 1	32 ± 11	24	-8.6 ± 0.1	-12.5 ± 5.5	–3.9
3	4990 ± 10	5380 ± 10	3849 ± 1018	–1530	9 ± 2	32 ± 11	23	-21.9 ± 0.1	-12.5 ± 5.5	9.4
4	6010 ± 10	6990 ± 10	6383 ± 270	–610	61 ± 34	52 ± 32	–9	-33.6 ± 0.1	-28.3 ± 2.1	5.3

Table 7.2 Comparison between cloud properties measured during the launch and by the HIMAWARI-8 satellite. Means and standard deviations are specified for each cloud parameter within the cloud bands identified by the C^2HOM–B instrument. Differences are specified as the holographic value subtracted from the HIMAWARI-8 value.

of the HIMAWARI-8 value for this cloud band. An overestimation in CTT of 5.3 °C is found for the HIMAWARI-8 retrieval and the C^2HOM–B value does not lie within the range of HIMAWARI-8 measurements. In all cases, the 95 % confidence intervals of the measured values do not overlap, suggesting that these biases may be significant. These results are consistent with a recent HIMAWARI-8 comparison [292] with Clouds, Aerosols, Precipitation, Radiation, and Atmospheric Composition over the Southern Ocean (CAPRICORN) shipborne observations [338] and the CALIPSO satellite [345] over the Southern Ocean, which also identified a low bias in CTH for warm liquid clouds and a tendency to misclassify lower-level clouds as cirrus.

The HIMAWARI-8 retrievals of CED can be compared for all height ranges, due to the similarity in the particle size distributions for each of the mid-level cloud bands. At mid-level and low-level heights the HIMAWARI-8 retrievals significantly overestimate the CED, whereas a smaller underestimation is noted for the high-altitude cirrus layer. Similarly large biases were identified in individual SOCRATES aircraft flights over the Southern Ocean [346], though the overall determined biases were significantly smaller. This large variability in cloud properties highlights the need for further balloon launches to significantly increase the availability of in situ microphysical measurements.

7.8 Summary

A world-first untethered balloon launch of a holographic microscope into clouds was undertaken and the preliminary findings are summarised in this section. Multiple bands of stratus and cirrus cloud were detected by the C^2HOM–B instrument, as independently validated by the collocated RS41 radiosonde measurements, Raspberry Pi camera images, and Polarsonde observations. The detected clouds were determined to be a warm low-level stratus cloud consisting solely of water droplets, a mid-level stratus clouds composed of small ice crystals, and a high-altitude cirrus layer of larger ice crystals with significantly more complicated particle morphologies.

Measured particle diameters for ice crystals and water droplets were compared with and found to be consistent with previous in situ measurements for these cloud types, with a focus on comparing with measurements from the surrounding Southern Ocean region from which a significant component of the observed air mass was believed to originate. The measured number densities were particularly small and whilst similar values have been measured previously, particularly in the Southern Ocean region, it is possible that this may indicate a potential sampling bias. Future launches should be carried out alongside independent cloud sampling instruments to test this interpretation, but it is expected that such a limitation could be overcome in future by increasing the instrument sampling volume through the use of a larger camera sensor and by improved optical filtering to avoid sunlight saturation issues.

The vertical profiles of particle diameter and number density revealed significant deviations from adiabatic cloud theory, most notably within the warm low-level stratus cloud. Such deviations are consistent with observations reported in previous field campaigns using holographic imagers. The low-level cloud was in a post-drizzling state during the launch and such conditions have previously been linked with non-adiabaticity. The variability in number density may also be indicative of the entrainment of drier air within the cloud as a result of small-scale turbulent processes. Such processes are not well understood currently and significantly more observations of this kind are required for better representations within climate and meteorological models.

A secondary focus of the launch was to use collocated holographic measurements to assist with the interpretation of Polarsonde observations. Significant height variability in the Polarsonde backscatter signals was identified and it was argued that this may be due to aerosol mixing with air masses of differing origin. The variability in aerosol properties was linked with changes in the vertical wind profile, as approximately traced by the balloon velocity, and with the cloud layers identified by the holographic microscope. Additional balloon launches of these instruments alongside other cloud and aerosol instrumentation should be undertaken to better understand the nature of these potential connections.

HYSPLIT back-trajectory modelling was undertaken to support the discussion of aerosol variations with height. A clear transition was identified from air masses originating from the Southern Ocean at low altitudes, to continental sources at higher altitudes. This mixing of continental and oceanic air masses may account for the observations of mean particle diameters that were at the boundary between those expected for continental and marine clouds. Heights at which the trajectory origins were found to significantly change were associated with changes in the trends in vertical profiles of Polarsonde observations, consistent with the interpretation that this instrument is mostly sensitive to aerosols rather than cloud particles for the low number density clouds observed during this launch. Cost-effective measurements of aerosol and cloud properties from the presented instruments should prove useful in addressing open questions in cloud physics, such as the nature of cloud-aerosol interactions and the connection with processes such as small-scale turbulence.

A preliminary comparison between the in situ cloud observations and remote retrievals from the HIMAWARI-8 imaging satellite was presented. These early results suggest significant biases in the satellite retrievals of Cloud Top Height, Cloud Effective Diameter, and Cloud Top Temperature, consistent with recent reports from the SOCRATES and CAPRICORN observation campaigns over the Southern Ocean. Routine launches of holographic instruments would allow a drastic increase in the availability of cloud microphysical measurements, as required for robust calibration and validation of remote sensing methods.

Chapter 8

Conclusion

8.1 Thesis Summary

This thesis describes the development and field deployment of two new instruments based on the principle of digital holography: the Compact Cloud-particle HOlographic Microscope – Surface (C^2HOM–S), and the C^2HOM – Balloon (C^2HOM–B). These instruments have been designed to be low cost and light weight to address the long-standing problem of limited in situ observations of cloud microphysical processes. A lack of such cloud observations has been identified as the leading source of uncertainty in climate and weather models, complicates the prediction of extreme weather events and aviation hazards, such as aircraft icing, and has implications for the quality of ground-based astrophysical observations.

The developed instruments open up the potential for cloud microphysical observations over wide areas, through deployment of a network of these low-cost instruments, as well as for routine vertical profiles from untethered balloons. To the authors knowledge, these instruments uniquely offer these low-cost holographic observation capabilities and the development and demonstration of these instruments should be considered the primary contribution arising from this work. Auxiliary tools and automated analysis methods have also been developed in this work to support the operation and future development of holographic instruments in general.

The over-arching contributions arising from this work are broadly summarised as follows:

- Development and field testing of two new holographic instruments, one of which sufficiently light weight ($\sim$1.5 kg) so as to be deployed on an untethered weather balloon or Unmanned Aerial Vehicle (UAV).
- Development of methods for autonomous and robust operation of holographic instruments under field conditions.

- Development of numerical simulation software (Monte-carlo Holographic Imager Simula-Tion (MHIST)) for assessment of automated holographic analysis methods and design of holographic instruments.

- Development of two automated holographic analysis methods, one of which (DoubleNSigma) tested on field data, and the other (Complex LOngitudinal Gradient (CLOG)) tested using MHIST.

- Demonstration of autonomous operation of the C^{2}HOM–S instrument for multiple months in the Australian Snowy Mountains. Automated observations were consistent with those from significantly heavier and more expensive gold-standard instruments within their overlapping sensitivity ranges.

- Detailed analysis of representative cloud and precipitation case studies from a unique multi-instrumented field campaign within the Australian Snowy Mountains. The holographic observations from this campaign provided unique insights into the microphysical processes occurring within a range of atmospheric events, including a persistent Mixed Phase Cloud (MPC).

- Investigation of potential biases in the Bureau of Meteorology Atmospheric high-resolution Regional Reanalysis for Australia (BARRA) reanalysis outputs of precipitation onset and duration, as compared with observations from the Snowy Mountains field campaign.

- Unique in situ holographic observations obtained from a world-first untethered balloon launch of a holographic microscope through clouds. Observations provided insight into the nature of warm and cold cloud processes at the micro-scale.

- Investigation of potential biases in HIMAWARI-8 satellite retrievals of Cloud Top Height (CTH), Cloud Effective Diameter (CED), and Cloud Top Temperature (CTT), through comparison with holographic observations from the balloon launch.

- Development of new methods for the analysis of Polarsonde observations and improvements in the interpretation of these observations through detailed comparisons with the developed holographic instruments.

- Generation of an extensive manually-analysed dataset of holographic observations from both field campaigns, of use for validating automated analysis methods.

These conclusions and contributions are elaborated on in greater detail within the relevant chapter summaries of this thesis.

8.2 Future Work

Demonstration of the low-cost and light-weight holographic instruments developed in this work opens the door to many exciting opportunities in future. The field testing of these instruments also identified areas in which the instruments can be further improved. A summary of this future work is described in this section.

The capability to deploy many versions of the C^2HOM–S instrument in a network of ground-based towers allows for a range of interesting experiments to be conducted. For example, deployment of holographic instruments over a large area within a mountainous region would allow the tracking of microphysical parameters within cloud systems as they evolve over time. Sensors placed up-wind, down-wind, and on top of a mountain peak could provide insight into orographic impacts on precipitation formation. Integration of these instruments into existing networks of automated weather stations operated by national meteorological organisations could allow for routine assimilation of cloud, fog, and precipitation microphysical observations, for use in climate and weather modelling. Application of this technology to the observation of other particulates is also being investigated, such as pollen and mining dust.

C^2HOM–S observations of representative case events covering a range of atmospheric conditions were compared with those from remote sensing instruments in the Snowy Mountains field campaign. It was found that holographic observations could be used to distinguish between cloud, snow, and rain events based on particle number density, size, and shape measurements. Classifications of this kind should be applied to larger datasets from additional field campaigns to determine the range of applicability of these findings. Additional comparisons should be made with observations from remote sensing instruments with the goal of improving the reliability of remote sensing retrievals of microphysical parameters. Further comparisons with climate and reanalysis models should also be undertaken to evaluate their performance.

The C^2HOM–B instrument is light weight enough to be deployed on an untethered balloon and low cost enough that loss of the instrument is not cost prohibitive. Routine balloon launches of the instrument at key locations around the world would allow for long-term climatological observations of cloud microphysical parameters that currently cannot be provided by aircraft campaigns due to their significant costs. Balloon launches of the instrument would be of particular interest in regions that are unsuited to balloon tethering, such as over the ocean from a ship where in situ cloud observations are particularly lacking. An experiment of particular interest would be to launch multiple balloons, dropsondes, or UAVs into a thunderstorm. Such storm systems are too dangerous to fly a research aircraft into and observations could be made up to the tropopause, well beyond the heights that can be sampled by tethered balloon systems, providing unique insight into the underlying processes that remain poorly understood.

The holographic instruments developed in this work have been found to operate reliably and autonomously under laboratory and field conditions for multiple months. This testing has also identified key areas in which the instruments can be further improved, such as the relatively small sampling volumes. The sampling volumes of both instruments are most constrained by their small camera sensors and the relatively slow Raspberry Pi computers used for onboard processing. Upgraded versions of both of these components have been identified that would allow an increase in sampling volume of multiple orders of magnitude, without significantly adding to the cost or weight of the instruments. Such upgrades should be undertaken for the next generation of instruments to provide statistically significant results over shorter observation periods. This is of particular interest for the understanding of small-scale turbulent processes which occur over small temporal and spatial scales.

Measurements of particle sizes and shapes from the C^2HOM–S instrument were found in the Snowy Mountains field campaign to be consistent with those from the collocated Parsivel and PIP instruments, within the overlapping size ranges that each instrument was sensitive to. The number density measurements from both holographic instruments in the Snowy Mountains and balloon launch field campaigns were found to be consistently low. Arguments were proposed in the relevant chapters to account for this, though it remains possible that these low values indicate an unconstrained bias in the instruments. Future field campaigns should be undertaken alongside reliable cloud observation instruments capable of resolving the same range of particle sizes, shapes, and number densities to determine the extent of this potential bias. If such a bias is found to be present, observations of this kind may allow for a systematic calibration factor to be determined to correct existing observations.

Holographic observations were compared in this work with those from Polarsonde instruments and new methods were presented for the analysis of Polarsonde observations. Application of these methods to other Polarsonde datasets is recommended, particularly when combined with the insights gained through comparison with holographic observations in this work. The Polarsonde appears to be particularly sensitive to aerosols, rather than cloud particles, and follow-up studies alongside aerosol measurement instruments would be useful in further calibrating and validating this low-cost device.

Plans have been made for the development of more sophisticated holographic instruments that are still suitably light weight and cost effective. Multi-wavelength systems could be developed to allow nanometre-scale observations by utilising the phase information encoded within holograms. A system of mirrors surrounding the sampling volume could be implemented to allow particle observations from multiple angles to extract full 3D information, rather than the front-on view currently provided by the in-line holographic geometry. This would be particularly useful for the observation of ice crystals with complicated shapes, such as aggregates.

An upgraded system could also be designed with multiple laser pulses recorded within a single hologram acquisition. This should allow for simultaneous measurements of the 3D trajectories of cloud particles within the sampling volume. Such observations could provide unique insights into poorly understood processes such as Secondary Ice Production (SIP) and collisional growth mechanisms.

Upgrades to the mounting designs of the instruments should be pursued. The weight of the current instruments is currently dominated by the metal structure on which the electro-optical components are mounted. It was believed that this would be required for maintaining optical stability, but ongoing laboratory testing suggests that 3D-printed components can provide sufficient strengths at a fraction of the weight. The current weight of the C^2HOM–B instrument is around 1.5 kg and this could be significantly reduced in future in this way, opening the potential for deployment on smaller UAVs and balloons with less helium.

Issues regarding sunlight saturation of the camera sensor were encountered in both field deployments discussed in this thesis. Subsequent redesigns to the optical baffling and positioning of optical components appears to have resolved this issue and such design changes should be incorporated into future upgraded instruments.

Two automated holographic analysis methods (DoubleNSigma and CLOG) were developed and tested in this work using field observations and the MHIST simulation software. The utility of both methods was identified from this preliminary testing, but more detailed tests should be undertaken in future to better constrain the biases and limitations of such approaches. Automated methods based on neural networks should also be pursued and it is expected that the extensive manually analysed datasets produced in this work should be particularly valuable for this application.

Further efforts should be made towards extending the MHIST simulation software to incorporate an N-body simulation of particles interacting under turbulent and electromagnetic forces. Comparison of the synthetic holograms generated under certain turbulent conditions with field observations could allow for the development of methods to automatically extract measurements of turbulence parameters using holographic instruments. Such observations are particularly challenging to obtain with current instruments and would prove a significant step towards the understanding of such processes and their role in climatological predictions.

A method (Resolution Enhanced Digital HOlography using Poisson's Spot (REDHOPS)) was proposed in this work for the automated retrieval of particle surface roughness and refractive index properties using holographic observations and the MHIST software. The method could be retroactively applied to existing holographic datasets to significantly increase the observations of these parameters that cannot currently be measured in situ within clouds. This approach has not yet been tested and so follow up studies of this kind are strongly recommended. If found to be effective, the combination of this approach with the low-cost instruments presented in this work would allow for routine measurements of these parameters. The predictions of climate and weather models are highly sensitive to these parameters and such observations would represent a significant contribution to this field.

References

[1] Hamblyn, R. *Clouds: Nature and Culture* (Reaktion Books Ltd, London, UK, 2017), first edn.

[2] King, M. D. *et al.* Spatial and Temporal Distribution of Clouds Observed by MODIS Onboard the Terra and Aqua Satellites. *IEEE Transactions on Geoscience and Remote Sensing* **51**, 3826–3852 (2013).

[3] Mace, G. G. Cloud properties and radiative forcing over the maritime storm tracks of the Southern Ocean and North Atlantic derived from A-Train. *Journal of Geophysical Research Atmospheres* **115**, 1–26 (2010).

[4] Forster, P. *et al.* The Earth's Energy Budget, Climate Feedbacks, and Climate Sensitivity. In Masson-Delmotte, V. *et al.* (eds.) *Climate Change 2021: The Physical Science Basis. Contribution of Working Group I to the Sixth Assessment Report of the Intergovernmental Panel on Climate Change*, chap. 7 (Cambridge University Press, Cambridge, UK, 2021).

[5] Hao, Z., Singh, V. P. & Xia, Y. Seasonal Draught Prediction: Advances, Challenges, and Future Prospects. *Reviews of Geophysics* **56**, 108–141 (2018).

[6] Morrison, H. *et al.* Confronting the Challenge of Modeling Cloud and Precipitation Microphysics. *Journal of Advances in Modeling Earth Systems* **12** (2020).

[7] Seneviratne, S. I. *et al.* Weather and Climate Extreme Events in a Changing Climate. In Masson-Delmotte, V. *et al.* (eds.) *Climate Change 2021: The Physical Science Basis. Contribution of Working Group I to the Sixth Assessment Report of the Intergovernmental Panel on Climate Change*, chap. 11 (Cambridge University Press, Cambridge, UK, 2021).

[8] Dai, A. Drought under global warming: a review. *WIREs Climate Change* **2**, 45–65 (2011).

[9] Bruintjes, R. T. A Review of Cloud Seeding Experiments to Enhance Precipitation and Some New Prospects. *Bulletin of the American Meteorological Society* **80**, 805–820 (1999).

[10] Ryan, B. F. & King, W. D. A Critical Review of the Australian Experience in Cloud Seeding. *Bulletin of the American Meteorological Society* **78**, 239–254 (1997).

[11] Flossmann, A. I. *et al.* Review of advances in precipitation enhancement research. *Bulletin of the American Meteorological Society* **100**, 1465–1480 (2019).

[12] Friedrich, K. *et al.* Quantifying snowfall from orographic cloud seeding. *PNAS* **117**, 5190–5195 (2020).

[13] Rasmussen, R. M. *et al.* Evaluation of the Wyoming Weather Modification Pilot Project (WWMPP) using two approaches: Traditional statistics and ensemble modeling. *Journal of Applied Meteorology and Climatology* **57**, 2639–2660 (2018).

[14] Gultepe, I. *et al.* A Review of High Impact Weather for Aviation Meteorology. *Pure and Applied Geophysics* **176**, 1869–1921 (2019).

[15] AON. Weather, Climate & Catastrophe Insight (2020 Annual Report). Tech. Rep., AON plc (2020).

[16] Adams-Selin, R. D. & Ziegler, C. L. Forecasting Hail Using a One-Dimensional Hail Growth Model within WRF. *Monthly Weather Review* **144**, 4919–4939 (2016).

[17] Fovell, R. G. & Su, H. Impact of cloud microphysics on hurricane track forecasts. *Geophysical Research Letters* **34**, 1–5 (2007).

[18] Kaltenegger, L. How to Characterize Habitable Worlds and Signs of Life. *Annual Review of Astronomy and Astrophysics* **55**, 433–485 (2017).

[19] Hahn, J. *et al.* Impact of aerosols and adverse atmospheric conditions on the data quality for spectral analysis of the H.E.S.S. telescopes. *Astroparticle Physics* **54**, 25–32 (2014).

[20] Nolan, S. J., Pühlhofer, G. & Rulten, C. B. Detailed studies of atmospheric calibration in imaging Cherenkov astronomy. *Astroparticle Physics* **34**, 304–313 (2010).

[21] Pecimotika, M. *et al.* Performance of the Cherenkov Telescope Array in the presence of clouds. In *Proceedings of Science*, 1–15 (2021).

[22] Acharya, B. S. *et al.* Science with the Cherenkov Telescope Array. Tech. Rep., Cherenkov Telescope Array (2017). URL https://arxiv.org/abs/1709.07997. arXiv:arXiv:1709.07997v1.

[23] Lang, T. J. *et al.* THE SEVERE THUNDERSTORM ELECTRIFICATION AND PRECIPITATION STUDY. *Bulletin of the American Meteorological Society* 1107–1126 (2004).

[24] Dwyer, J. R. & Uman, M. A. The physics of lightning. *Physics Reports* **534**, 147–241 (2014).

[25] Smith, D. M. *et al.* A terrestrial gamma ray flash observed from an aircraft. *Journal of Geophysical Research* **116**, 1–10 (2011).

[26] Dwyer, J. R. *et al.* Positron clouds within thunderstorms. *Journal of Plasma Physics* **81**, 1–17 (2015).

[27] Alexander, M. J., Beres, Jadwiga, H. & Pfister, L. Tropical stratospheric gravity wave activity and relationships to clouds. *Journal of Geophysical Research* **105**, 22299–22309 (2000).

[28] Shaw, R. A. PARTICLE-TURBULENCE INTERACTIONS IN ATMOSPHERIC CLOUDS. *Annual Review of Fluid Mechanics* **35**, 183–227 (2003).

[29] Schneider, T. *et al.* Climate goals and computing the future of clouds. *Nature Climate Change* **7**, 3–5 (2017).

[30] Ueno, Y., Hyodo, M., Yang, T. & Katoh, S. Intensified East Asian winter monsoon during the last geomagnetic reversal transition. *Scientific Reports* **9**, 1–8 (2019).

[31] Duplissy, J. *et al.* Global atmospheric particle formation from CERN CLOUD measurements. *Science* **354**, 1119–1124 (2016).

[32] Frisinger, H. H. *The History of Meteorology: to 1800* (American Meteorological Society, Boston, Massachusetts, 1983), 2 edn.

[33] Kreidenweis, S. M., Petters, M. & Lohmann, U. 100 Years of Progress in Cloud Physics, Aerosols, and Aerosol Chemistry Research. *Meteorological Monographs* **59**, 1–72 (2018).

[34] Pruppacher, H. R. & Klett, J. D. *Microphysics of Clouds and Precipitation* (Springer Dordrecht, Heidelberg, 2010), second edn.

[35] Lohmann, U., Lüönd, F. & Mahrt, F. *An Introduction to Clouds: From the Microscale to Climate* (Cambridge University Press, 2016), first edn.

[36] Connolly, P. J. *et al.* Aircraft observations of the influence of electric fields on the aggregation of ice crystals. *Quarterly Journal of the Royal Meteorological Society* **131**, 1695–1712 (2005).

[37] Heymsfield, A. *et al.* Toward Improving Ice Water Content and Snow-Rate Retrievals from Radars . Part II: Results from Three Wavelength Radar–Collocated In Situ Measurements and CloudSat–GPM–TRMM Radar Data. *Journal of Applied Meteorology and Climatology* **57**, 365–389 (2018).

[38] Li, J.-C. & Picart, P. *Digital Holography* (ISTE Ltd, London, 2012), first edn.

[39] Houze Jr., R. A. *Cloud Dynamics* (Elsevier Inc., 2014), second edn.

[40] Rogers, R. R. & Yau, M. K. *A Short Course in Cloud Physics* (Elsevier Science, 1989), third edn.

[41] Korolev, A. V. & Mazin, I. P. Supersaturation of Water Vapor in Clouds. *Journal of the Atmospheric Sciences* **60**, 2957–2974 (2003).

[42] Grabowski, W. W. & Wang, L.-p. Growth of Cloud Droplets in a Turbulent Environment. *Annual Review of Fluid Mechanics* **45**, 293–324 (2013).

[43] Prabha, T. V. *et al.* Microphysics of Premonsoon and Monsoon Clouds as Seen from In Situ Measurements during the Cloud Aerosol Interaction and Precipitation Enhancement Experiment (CAIPEEX). *Journal of the Atmospheric Sciences* **68**, 1882–1901 (2011).

[44] Does, M. V. D., Knippertz, P., Zschenderlein, P., Harrison, R. G. & Stuut, J.-B. W. The mysterious long-range transport of giant mineral dust particles. *Science Advances* **4**, 1–8 (2018).

[45] Boucher, O. *Atmospheric Aerosols* (Springer France, 2015), first edn.

[46] McFarquhar, G. M. *et al.* Observations of clouds, aerosols, precipitation, and surface radiation over the Southern Ocean: An overview of CAPRICORN, MARCUS, MICRE and SOCRATES. *Bulletin of the American Meteorological Society* 1–92 (2020).

[47] Delene, D. J. & Deshler, T. Vertical profiles of cloud condensation nuclei above Wyoming. *Journal of Geophysical Research* **106**, 579–588 (2001).

[48] Jonas, P. R. Turbulence and cloud microphysics. *Atmospheric Research* **40**, 283–306 (1996).

[49] Cooper, W. A., Lasher-Trapp, S. G. & Blyth, A. M. The Influence of Entrainment and Mixing on the Initial Formation of Rain in a Warm Cumulus Cloud. *Journal of the Atmospheric Sciences* **70**, 1727–1743 (2013).

[50] Feingold, G., Cotton, W. R., Kreidenweis, S. M. & Davis, J. T. The Impact of Giant Cloud Condensation Nuclei on Drizzle Formation in Stratocumulus: Implications for Cloud Radiative Properties. *Journal of the Atmospheric Sciences* **56**, 4100–4117 (1999).

[51] Pope, F. D. Pollen grains are efficient cloud condensation nuclei. *Environmental Research Letters* **5**, 1–6 (2010).

[52] Johnson, D. B. The Role of Giant and Ultragiant Aerosol Particles in Warm Rain Initiation. *Journal of the Atmospheric Sciences* **39**, 448–460 (1982).

[53] Barekzai, M. & Mayer, B. Broadening of the Cloud Droplet Size Distribution due to Thermal Radiative Cooling: Turbulent Parcel Simulations. *Journal of the Atmospheric Sciences* **77**, 1993–2010 (2020).

[54] Devenish, B. J. *et al.* Droplet growth in warm turbulent clouds. *Quarterly Journal of the Royal Meteorological Society* **138**, 1401–1429 (2012).

[55] Baker, M. B., Corbin, R. G. & Latham, J. The influence of entrainment on the evolution of cloud droplet spectra: I. A model of inhomogeneous mixing. *Quarterly Journal of the Royal Meteorological Society* **106**, 581–598 (1980).

[56] Lehmann, K., Siebert, H. & Shaw, R. A. Homogeneous and Inhomogeneous Mixing in Cumulus Clouds: Dependence on Local Turbulence Structure. *Journal of the Atmospheric Sciences* **66**, 3641–3659 (2009).

[57] Beals, M. J. *et al.* Holographic measurements of inhomogeneous cloud mixing at the centimeter scale. *Science* **350**, 87–90 (2015).

[58] Lü, Q. *et al.* Trajectory and velocity measurement of a particle in spray by digital holography. *Applied Optics* **48**, 7000–7007 (2009).

[59] Pruppacher, H. R. & Pitter, R. L. A Semi-Empirical Determination of the Shape of Cloud and Rain Drops. *Journal of the Atmospheric Sciences* **28**, 86–94 (1971).

[60] Blanchard, D. C. & Spencer, A. T. Experiments on the Generation of Raindrop-Size Distributions by Drop Breakup. *Journal of the Atmospheric Sciences* **27**, 101–108 (1970).

[61] Lasher-Trapp, S. G., Cooper, W. A. & Blyth, A. M. Broadening of droplet size distributions from entrainment and mixing in a cumulus cloud. *Quarterly Journal of the Royal Meteorological Society* **131**, 195–220 (2005).

[62] Tinsley, B. A., Rohrbaugh, R. P. & Hei, M. Electroscavenging in clouds with broad droplet size distributions and weak electrification. *Atmospheric Research* **59-60**, 115–135 (2001).

[63] Proud, S. R. & Bachmeier, S. Record-Low Cloud Temperatures Associated With a Tropical Deep Convective Event. *Geophysical Research Letters* **48**, 1–8 (2021).

[64] Rosenfeld, D. & Woodley, W. L. Deep convective clouds with sustained supercooled liquid water down to -37.5 °C. *Letters to Nature* **405**, 440–442 (2000).

[65] Hamilton, M., Alexander, S. P., Protat, A., Siems, S. & Carpentier, S. Polarimetric backscatter sonde observations of southern ocean clouds and aerosols. *Atmosphere* **11**, 1–20 (2020).

[66] Hoose, C. & Möhler, O. Heterogeneous ice nucleation on atmospheric aerosols: A review of results from laboratory experiments. *Atmospheric Chemistry and Physics* **12**, 9817–9854 (2012).

[67] Engelstaedter, S., Tegen, I. & Washington, R. North African dust emissions and transport. *Earth-Science Reviews* **79**, 73–100 (2006).

[68] Kanji, Z. A. *et al.* Overview of Ice Nucleating Particles. *Meteorological Monographs* **58**, 1–33 (2017).

[69] Lawson, R. P. *et al.* A Review of Ice Particle Shapes in Cirrus formed In Situ and in Anvils. *Journal of Geophysical Research: Atmospheres* **124**, 10049–10090 (2019).

[70] Murray, B. J. *et al.* Trigonal ice crystals in earth's atmosphere. *Bulletin of the American Meteorological Society* **96**, 1519–1531 (2015).

[71] Bailey, M. P. & Hallett, J. A Comprehensive Habit Diagram for Atmospheric Ice Crystals : Confirmation from the Laboratory , AIRS II , and Other Field Studies. *Journal of the Atmospheric Sciences* **66**, 2888–2899 (2009).

[72] Järvinen, E. *et al.* Additional global climate cooling by clouds due to ice crystal complexity. *Atmospheric Chemistry and Physics* **18**, 15767–15781 (2018).

[73] Planche, C., Wobrock, W. & Flossmann, A. I. The continuous melting process in a cloud-scale model using a bin microphysics scheme. *Quarterly Journal of the Royal Meteorological Society* **140**, 1986–1996 (2014).

[74] Hobbs, P. V., Chang, S. & Locatelli, J. D. The Dimensions and Aggregation of Ice Crystals in Natural Clouds. *Journal of Geophysical Research* **79**, 2199–2206 (1974).

[75] Korolev, A. *et al.* Mixed-Phase Clouds : Progress and Challenges. *Meteorological Monographs* **58**, 5.1–5.50 (2017).

[76] Findeisen, W. Die kolloidmeteorologischen Vorgänge bei der Niederschlagsbildung (translated and edited by Volken, E., A.M. Giesche, S. Brönnimann. – Colloidal meteorological processes in the formation of precipitation. Meteorol. Z. 24, (2015)). *Meteorol. Z.* **24**, 121–133 (1938).

[77] Morrison, H. *et al.* Resilience of persistent Arctic mixed-phase clouds. *Nature Geoscience* **5**, 11–17 (2011).

[78] Korolev, A. Limitations of the Wegener-Bergeron-Findeisen mechanism in the evolution of mixed-phase clouds. *Journal of the Atmospheric Sciences* **64**, 3372–3375 (2007).

[79] Vignon, É. *et al.* Challenging and Improving the Simulation of Mid-Level Mixed-Phase Clouds Over the High-Latitude Southern Ocean. *Journal of Geophysical Research: Atmospheres* **126**, 1–21 (2021).

[80] Heymsfield, A. J. *et al.* Contributions of the Liquid and Ice Phases to Global Surface Precipitation: Observations and Global Climate Modeling. *Journal of the Atmospheric Sciences* **77**, 2629–2648 (2020).

[81] Kumjian, M. R. & Lombardo, K. A Hail Growth Trajectory Model for Exploring the Environmental Controls on Hail Size: Model Physics and Idealized Tests. *Journal of the Atmospheric Sciences* **77**, 2765–2791 (2020).

[82] Korolev, A. & Leisner, T. Review of experimental studies of secondary ice production. *Atmospheric Chemistry and Physics* **20**, 11767–11797 (2020).

[83] Auer Jr, A. H., Veal, D. L. & Marwitz, J. D. Observations of Ice Crystal and Ice Nuclei Concentrations in Stable Cap CLouds. *Journal of the Atmospheric Sciences* **26**, 1342–1343 (1969).

[84] Mossop, S. C. Production of secondary ice particles during the growth of graupel by riming. *Quarterly Journal of the Royal Meteorological Society* **102**, 45–57 (1976).

[85] Lauber, A. *et al.* Continuous secondary-ice production initiated by updrafts through the melting layer in mountainous regions. *Atmospheric Chemistry and Physics* **21**, 3855–3870 (2021).

[86] Field, P. R. *et al.* Secondary Ice Production - current state of the science and recommendations for the future. *Meteorological Monographs* **58**, 1–20 (2017).

[87] Grabowski, W. W. *et al.* Modeling of Cloud Microphysics: Can We Do Better? *Bulletin of the American Meteorological Society* 655–672 (2019).

[88] Igel, A. L., Igel, M. R. & van den Heever, S. C. Make it a double? Sobering results from simulations using single-moment microphysics schemes. *Journal of the Atmospheric Sciences* **72**, 910–925 (2015).

[89] Shaw, R. A. Particle-Turbulence Interactions in Atmospheric Clouds. *Annual Review of Fluid Mechanics* **35**, 183–227 (2003).

[90] Franklin, C. N., Vaillancourt, P. A., Yau, M. K. & Bartello, P. Collision Rates of Cloud Droplets in Turbulent Flow. *Journal of the Atmospheric Sciences* **62**, 2451–2466 (2005).

[91] Lynn, B. H. *et al.* Spectral (Bin) Microphysics Coupled with a Mesoscale Model (MM5). Part I: Model Description and First Results. *Monthly Weather Review* **133**, 44–58 (2005).

[92] Khain, A. P. *et al.* Representation of microphysical processes in cloud-resolving models: Spectral (bin) microphysics versus bulk parameterization. *Reviews of Geophysics* **53**, 247–322 (2015).

[93] Xue, L. *et al.* Idealized simulations of a squall line from the MC3E field campaign applying three bin microphysics schemes: Dynamic and thermodynamic structure. *Monthly Weather Review* **145**, 4789–4812 (2017).

[94] Dziekan, P., Waruszewski, M. & Pawlowska, H. University of Warsaw Lagrangian cloud model (UWLCM) 1.0: A modern large-eddy simulation tool for warm cloud modeling with Lagrangian microphysics. *Geoscientific Model Development* **12**, 2587–2606 (2019).

[95] Igel, A. L. & van den Heever, S. C. The Importance of the Shape of Cloud Droplet Size Distributions in Shallow Cumulus Clouds. Part II: Bulk Microphysics Simulations. *Journal of the Atmospheric Sciences* **74**, 259–273 (2017).

[96] Morrison, H. & Gettelman, A. A New Two-Moment Bulk Stratiform Cloud Microphysics Scheme in the Community Atmosphere Model, Version 3 (CAM3). Part I: Description and Numerical tests. *Journal of Climate* **21**, 3642–3659 (2008).

[97] Lawson, R. P. & Baker, B. Improvement in Determination of Ice Water Content from Two-Dimensional Particle Imagery. Part I: Image-to-Mass Relationships. *Journal of Applied Meteorology and Climatology* **45**, 1282–1290 (2006).

[98] Erfani, E. & Mitchell, D. L. Developing and bounding ice particle mass- and area-dimension expressions for use in atmospheric models and remote sensing. *Atmospheric Chemistry and Physics* **16**, 4379–4400 (2016).

[99] Finlon, J. A. *et al.* A novel approach for characterizing the variability in mass-dimension relationships: Results from MC3E. *Atmospheric Chemistry and Physics* **19**, 3621–3643 (2019).

[100] Yang, P. *et al.* On the Radiative Properties of Ice Clouds : Light Scattering , Remote Sensing , and Radiation Parameterization. *Advances in Atmospheric Sciences* **32**, 32–63 (2015).

[101] Baran, A. J. *et al.* A self-consistent scattering model for cirrus. II: The high and low frequencies. *Quarterly Journal of the Royal Meteorological Society* **140**, 1039–1057 (2014).

[102] Yi, B. *et al.* Influence of ice particle surface roughening on the global cloud radiative effect. *J. Atmos. Sci.* **70**, 2794–2807 (2013).

[103] Yang, P. *et al.* Spectrally Consistent Scattering , Absorption, and Polarization Properties of Atmospheric Ice Crystals at Wavelengths from 0.2 to 100 microns. *Journal of the Atmospheric Sciences* **70**, 330–347 (2013).

[104] Gettelman, A. *et al.* High Climate Sensitivity in the Community Earth System Model Version 2 (CESM2). *Geophysical Research Letters* **46**, 8329–8337 (2019).

[105] Vial, J., Dufresne, J. L. & Bony, S. On the interpretation of inter-model spread in CMIP5 climate sensitivity estimates. *Climate Dynamics* **41**, 3339–3362 (2013).

[106] Zelinka, M. D. *et al.* Causes of Higher Climate Sensitivity in CMIP6 Models. *Geophysical Research Letters* **47**, 1–12 (2020).

[107] Lohmann, U. & Roeckner, E. Influence of cirrus cloud radiative forcing on climate and climate sensitivity in a general circulation model. *Journal of Geophysical Research* **100**, 16305 (1995).

[108] Kay, J. E. *et al.* Exposing global cloud biases in the Community Atmosphere Model (CAM) using satellite observations and their corresponding instrument simulators. *Journal of Climate* **25**, 5190–5207 (2012).

[109] Neale, R. *et al.* Description of the NCAR community atmosphere model (CAM 5.0). Tech. Rep., NCAR (2010).

[110] Loeb, N. G. *et al.* Clouds and the Earth'S Radiant Energy System (CERES) Energy Balanced and Filled (EBAF) top-of-atmosphere (TOA) edition-4.0 data product. *Journal of Climate* **31**, 895–918 (2018).

[111] Chubb, T. H., Jensen, J. B., Siems, S. T. & Manton, M. J. In situ observations of supercooled liquid clouds over the Southern Ocean during the HIAPER Pole-to-Pole Observation campaigns. *Geophysical Research Letters* **40**, 5280–5285 (2013).

[112] Kay, J. E. *et al.* Global Climate Impacts of Fixing the Southern Ocean Shortwave Radiation Bias in the Community Earth System Model (CESM). *Journal of Climate* **29**, 4617–4636 (2016).

[113] Sun, Z. & Shine, K. P. Parameterization of ice cloud radiative properties and its application to the potential climatic importance of mixed-phase clouds. *Journal of Climate* **8**, 1874–1888 (1995).

[114] Schuddeboom, A. *et al.* Cluster-Based Evaluation of Model Compensating Errors : A Case Study of Cloud Radiative Effect in the Southern Ocean. *Geophysical Research Letters* **46** (2019).

[115] Bodas-Salcedo, A., Williams, K. D., Field, P. R. & Lock, A. P. The Surface Downwelling Solar Radiation Surplus Over the Southern Ocean in the Met Office Model: The Role of Midlatitude Cyclone Clouds. *Journal of Climate* **25**, 7467–7486 (2012).

[116] Frey, W. R. & Kay, J. E. The influence of extratropical cloud phase and amount feedbacks on climate sensitivity. *Climate Dynamics* **50**, 3097–3116 (2018).

[117] Noh, Y. J. *et al.* Satellite - Based Detection of Daytime Supercooled Liquid - Topped Mixed - Phase Clouds Over the Southern Ocean Using the Advanced Himawari Imager Journal of Geophysical Research : Atmospheres. *Journal of Geophysical Research : Atmospheres* **124**, 2677–2701 (2019).

[118] Bamber, J. L. & Aspinall, W. P. An expert judgement assessment of future sea level rise from the ice sheets. *Nature Climate Change* **3**, 424–427 (2013).

[119] Marotzke, J. *et al.* Climate research must sharpen its view. *Nature Climate Change* **7**, 89–91 (2017).

[120] Hitz, S. & Smith, J. Estimating global impacts from climate change. *Global Environmental Change* **14**, 201–218 (2004).

[121] Nunez, S., Arets, E., Alkemade, R., Verwer, C. & Leemans, R. Assessing the impacts of climate change on biodiversity: is below 2 °C enough? *Climatic Change* **154**, 351–365 (2019).

[122] Stith, J. L. *et al.* 100 Years of Progress in Atmospheric Observing Systems. *Meteorological Monographs* **59**, 2.1–2.55 (2018).

[123] Grosvenor, D. P. *et al.* Remote Sensing of Droplet Number Concentration in Warm Clouds: A Review of the Current State of Knowledge and Perspectives. *Reviews of Geophysics* **56**, 409–453 (2018).

[124] Baumgardner, D. *et al.* Cloud Ice Properties: In Situ Measurement Challenges. *Meteorological Monographs* **58**, 1–23 (2017).

[125] Yang, P. *et al.* A review of ice cloud optical property models for passive satellite remote sensing. *Atmosphere* **9**, 1–31 (2018).

[126] Huang, Y. *et al.* Evaluating himawari-8 cloud products using shipborne and CALIPSO observations: Cloud-top height and cloud-top temperature. *Journal of Atmospheric and Oceanic Technology* **36**, 2327–2347 (2019).

[127] Han, Q., Rossow, W., Welch, R., White, A. & Chou, J. Validation of Satellite Retrievals of Cloud Microphysics and Liquid Water Path Using Observations from FIRE. *Journal of the Atmospheric Sciences* **52**, 4183–4195 (1995).

[128] Wu, D. L., Lambert, A., Read, W. G., Eriksson, P. & Gong, J. MLS and CALIOP Cloud Ice Measurements in the Upper Troposphere: A Constraint from Microwave on Cloud Microphysics. *Journal of Applied Meteorology and Climatology* **53**, 157–165 (2014).

[129] Böckmann, C. *et al.* Aerosol lidar intercomparison in the framework of the EARLINET project. 2. Aerosol backscatter algorithms. *Applied Optics* **43**, 977–989 (2004).

[130] Alexander, S. P. & Protat, A. Vertical Profiling of Aerosols With a Combined Raman-Elastic Backscatter Lidar in the Remote Southern Ocean Marine Boundary. *Journal of Geophysical Research : Atmospheres* **124**, 12107–12125 (2019).

[131] Fernald, F. G. Analysis of atmospheric lidar observations: some comments. *Applied Optics* **23**, 652–653 (1984).

[132] Ansmann, A. *et al.* Combined Raman Elastic-Backscatter LIDAR for Vertical Profiling of Moisture, Aerosol Extinction, Backscatter and LIDAR ratio. *Applied Physics B* **28**, 18–28 (1992).

[133] Hicks-Jalali, S. *et al.* A Raman lidar tropospheric water vapour climatology and height-resolved trend analysis over Payerne, Switzerland. *Atmospheric Chemistry and Physics* **20**, 9619–9640 (2020).

[134] Noel, V., Winker, D. M., McGill, M. & Lawson, P. Classification of particle shapes from lidar depolarization ratio in convective ice clouds compared to in situ observations during CRYSTAL-FACE. *Journal of Geophysical Research* **109**, 1–13 (2004).

[135] Noel, V., Chepfer, H., Ledanois, G., Delaval, A. & Flamant, P. H. Classification of particle effective shape ratios in cirrus clouds based on the lidar depolarization ratio. *Applied Optics* **41**, 4245–4257 (2002).

[136] Weitkamp, C. *Lidar; Range-Resolved Optical Remote Sensing of the Atmosphere* (Springer Science+Business Media Inc., New York, 2005).

[137] Hogan, R. J., Illingworth, A. J., O'Connor, E. J. & Poiares Baptista, J. P. Characteristics of mixed-phase clouds. II: A climatology from ground-based lidar. *Quarterly Journal of the Royal Meteorological Society* **129**, 2117–2134 (2003).

[138] Mace, G. G. & Protat, A. Clouds over the Southern Ocean as observed from the R/V investigator during CAPRICORN. Part I: Cloud occurrence and phase partitioning. *Journal of Applied Meteorology and Climatology* **57**, 1783–1803 (2018).

[139] Battaglia, A. *et al.* Spaceborne Cloud and Precipitation Radars: Status, Challenges, and Ways Forward. *Reviews of Geophysics* **58**, 1–59 (2020).

[140] Delanoë, J. *et al.* BASTA: A 95-GHz FMCW Doppler radar for cloud and fog studies. *Journal of Atmospheric and Oceanic Technology* **33**, 1023–1038 (2016).

[141] Sassen, K., Wang, Z., Khvorostyanov, V. I., Stephens, G. L. & Bennedetti, A. Cirrus Cloud Ice Water Content Radar Algorithm Evaluation Using an Explicit Cloud Microphysical Model. *Journal of Applied Meteorology* **41**, 620–628 (2002).

[142] Wang, Z., Heymsfield, G. M., Li, L. & Heymsfield, A. J. Retrieving optically thick ice cloud microphysical properties by using airborne dual-wavelength radar measurements. *Journal of Geophysical Research* **110**, 1–13 (2005).

[143] Ryzhkov, A. V. & Zrnic, D. S. *Radar polarimetry for weather observations* (Springer Nature Switzerland AG, 2019), first edn. URL https://www.springer.com/gp/book/9783030050924.

[144] Westbrook, C. D., Illingworth, A. J., O'Connor, E. J. & Hogan, R. J. Doppler lidar measurements of oriented planar ice crystals falling from supercooled and glaciated layer clouds. *Quarterly Journal of the Royal Meteorological Society* **136**, 260–276 (2010). arXiv:0906.0701.

[145] Min, Q. & Duan, M. Simultaneously retrieving cloud optical depth and effective radius for optically thin clouds. *Journal of Geophysical Research* **110**, 1–8 (2005).

[146] Marchand, R., Mace, G. G., Ackerman, T. & Stephens, G. Hydrometeor detection using Cloudsat - An earth-orbiting 94-GHz cloud radar. *Journal of Atmospheric and Oceanic Technology* **25**, 519–533 (2008).

[147] Baum, B. A. *et al.* Improvements in shortwave bulk scattering and absorption models for the remote sensing of ice clouds. *Journal of Applied Meteorology and Climatology* **50**, 1037–1056 (2011).

[148] Kuma, P. *et al.* Evaluation of Southern Ocean cloud in the HadGEM3 general circulation model and MERRA-2 reanalysis using ship-based observations. *Atmospheric Chemistry and Physics* **20**, 6607–6630 (2020).

[149] Platnick, S. *et al.* The MODIS cloud products: Algorithms and examples from terra. *IEEE Transactions on Geoscience and Remote Sensing* **41**, 459–473 (2003).

[150] Forster, L., Davis, A. B., Diner, D. J. & Mayer, B. Toward Cloud Tomography from Space Using MISR and MODIS: Locating the "Veiled Core" in Opaque Convective Clouds. *Journal of the Atmospheric Sciences* **78**, 155–166 (2021). arXiv:1910.00077.

[151] Korolev, A., Emery, E. & Creelman, K. Modification and Tests of Particle Probe Tips to Mitigate Effects of Ice Shattering. *Journal of Atmospheric and Oceanic Technology* **30**, 690–708 (2013).

[152] Lawson, R. P. Effects of ice particles shattering on the 2D-S probe. *Atmospheric Measurement Techniques* **4**, 1361–1381 (2011).

[153] Jackson, R. C. & McFarquhar, G. M. An assessment of the impact of antishattering tips and artifact removal techniques on bulk cloud ice microphysical and optical properties measured by the 2D cloud probe. *Journal of Atmospheric and Oceanic Technology* **31**, 2131–2144 (2014).

[154] Field, P. R., Heymsfield, A. J. & Bansemer, A. Shattering and particle interarrival times measured by optical array probes in ice clouds. *Journal of Atmospheric and Oceanic Technology* **23**, 1357–1371 (2006).

[155] Korolev, A. & Isaac, G. A. Shattering during sampling by OAPs and HVPS. Part I: Snow particles. *Journal of Atmospheric and Oceanic Technology* **22**, 528–542 (2005).

[156] McFarquhar, G. M. *et al.* Processing of Ice Cloud In Situ Data Collected by Bulk Water, Scattering, and Imaging Probes: Fundamentals, Uncertainties, and Efforts toward Consistency. *Meteorological Monographs* **58**, 11.1–11.33 (2017).

[157] Rango, A. *et al.* Rime and graupel: Description and characterization as revealed by low-temperature scanning electron microscopy. *Scanning* **25**, 121–131 (2003).

[158] Tape, W. *Atmospheric Halos* (American Geophysical Union, Washington, D.C., 1994).

[159] Schmitt, C. G. & Heymsfield, A. J. The Size Distribution and Mass-Weighted Terminal Velocity of Low-Latitude Tropopause Cirrus Crystal Populations. *Journal of the Atmospheric Sciences* **66**, 2013–2028 (2009).

[160] Magee, N. *et al.* Captured Cirrus Ice Particles in High Definition. *Atmospheric Chemistry and Physics Discussions* 1–27 (2020).

[161] McFarquhar, G. M. & Heymsfield, A. J. Parameterization of Tropical Cirrus Ice Crystal Size Distributions and Implications for Radiative Transfer: Results from CEPEX. *Journal of the Atmospheric Sciences* **54**, 2187–2200 (1997).

[162] Jensen, J. B. *et al.* The Giant Nucleus Impactor (GNI)—A System for the Impaction and Automated Optical Sizing of Giant Aerosol Particles with Emphasis on Sea Salt. Part I: Basic Instrument and Algorithms. *Journal of Atmospheric and Oceanic Technology* **37**, 1551–1569 (2020).

[163] Dye, J. E. & Baumgardner, D. Evaluation of the Forward Scattering Spectrometer Probe. Part I: Electronic and Optical Studies. *Journal of Atmospheric and Oceanic Technology* **1**, 329–344 (1984).

[164] Baumgardner, D. *et al.* Cloud Ice Properties: In Situ Measurement Challenges. *Meteorological Monographs* **58**, 9.1–9.23 (2017).

[165] Hergert, W. & Wriedt, T. *The Mie Theory: Basics and Applications* (Springer-Verlag Berlin Heidelberg, 2012), first edn.

[166] Baumgardner, D. *et al.* The cloud particle spectrometer with polarization detection (CPSPD): A next generation open-path cloud probe for distinguishing liquid cloud droplets from ice crystals. *Atmospheric Research* **142**, 2–14 (2014).

[167] Um, J. *et al.* Dimensions and aspect ratios of natural ice crystals. *Atmospheric Chemistry and Physics* **15**, 3933–3956 (2015).

[168] Cotton, R. *et al.* The ability of the small ice detector (SID-2) to characterize cloud particle and aerosol morphologies obtained during flights of the FAAM BAe-146 research aircraft. *Journal of Atmospheric and Oceanic Technology* **27**, 290–303 (2010).

[169] Johnson, A., Lasher-Trapp, S., Bansemer, A., Ulanowski, Z. & Heymsfield, A. J. Difficulties in early ice detection with the small ice Detector-2 HIAPER (SID-2H) in maritime cumuli. *Journal of Atmospheric and Oceanic Technology* **31**, 1263–1275 (2014).

[170] Lance, S. Coincidence Errors in a Cloud Droplet Probe (CDP) and a Cloud and Aerosol Spectrometer (CAS), and the Improved Performance of a Modified CDP. *Journal of Atmospheric and Oceanic Technology* **29**, 1532–1541 (2012).

[171] Knollenberg, R. G. The Optical Array: An Alternative to Scattering or Extinction for Airborne Particle Size Determination. *Journal of Applied Meteorology* **9**, 86–103 (1970).

[172] Kuhn, T. & Heymsfield, A. J. In Situ Balloon-Borne Ice Particle Imaging in High-Latitude Cirrus. *Pure and Applied Geophysics* **173**, 3065–3084 (2016).

[173] O'Shea, S. *et al.* Characterising optical array particle imaging probes: Implications for small-ice-crystal observations. *Atmospheric Measurement Techniques* **14**, 1917–1939 (2021).

[174] Vaillant De Guélis, T. *et al.* Study of the diffraction pattern of cloud particles and the respective responses of optical array probes. *Atmospheric Measurement Techniques* **12**, 2513–2529 (2019).

[175] Korolev, A. Reconstruction of the sizes of spherical particles from their shadow images. Part I: Theoretical considerations. *Journal of Atmospheric and Oceanic Technology* **24**, 376–389 (2007).

[176] Lawson, R. P. *et al.* The 2D-S (Stereo) Probe: Design and Preliminary Tests of a New Airborne, High-Speed, High-Resolution Particle Imaging Probe. *Journal of Atmospheric and Oceanic Technology* **23**, 1462–1477 (2006).

[177] Abdelmonem, A. *et al.* PHIPS-HALO: The airborne Particle Habit Imaging and Polar Scattering probe - Part 1: Design and operation. *Atmospheric Measurement Techniques* **9**, 3131–3144 (2016).

[178] Fugal, J. P. & Shaw, R. A. Cloud particle size distributions measured with an airborne digital in-line holographic instrument. *Atmospheric Measurement Techniques Discussions* **2**, 659–688 (2009).

[179] Khmaladze, A., Kim, M. & Lo, C.-m. Phase imaging of cells by simultaneous dual-wavelength reflection digital holography. *Optics Express* **16**, 900–911 (2008).

[180] Jackson, R. C. *et al.* An Assessment of the Impact of Antishattering Tips and Artifact Removal Techniques on Cloud Ice Size Distributions Measured by the 2D Cloud Probe. *Journal of Atmospheric and Oceanic Technology* **31**, 2567–2590 (2014).

[181] Conway, B. J., Caughey, S. J., Bentley, A. N. & Turton, J. D. Ground-based and airborne holography of ice and water clouds. *Atmospheric Environment* **16**, 1193–1207 (1982).

[182] Desai, N. *et al.* Vertical Variation of Turbulent Entrainment Mixing Processes in Marine Stratocumulus Clouds Using High-Resolution Digital Holography. *Journal of Geophysical Research: Atmospheres* **126**, 1–16 (2021).

[183] Thompson, B. J. Holographic particle sizing techniques. *Journal of Physics E: Scientific Instruments* **7**, 781–788 (1974).

[184] Raupach, S. M. F., Vössing, H. J., Curtius, J. & Borrmann, S. Digital Crosed-beam holography for in situ imaging of atmospheric ice particles. *Journal of Optics A: Pure and Applied Optics* **8**, 796–806 (2006).

[185] Henneberger, J., Fugal, J. P., Stetzer, O. & Lohmann, U. HOLIMO II: A digital holographic instrument for ground-based in situ observations of microphysical properties of mixed-phase clouds. *Atmospheric Measurement Techniques* **6**, 2975–2987 (2013).

[186] Beck, A., Henneberger, J., Schöpfer, S., Fugal, J. & Lohmann, U. HoloGondel: In situ cloud observations on a cable car in the Swiss Alps using a holographic imager. *Atmospheric Measurement Techniques* **10**, 459–476 (2017).

[187] Ramelli, F., Beck, A., Henneberger, J. & Lohmann, U. Using a holographic imager on a tethered balloon system for microphysical observations of boundary layer clouds. *Atmospheric Measurement Techniques* **13**, 925–939 (2020).

[188] Fugal, J. P., Schulz, T. J. & Shaw, R. A. Practical methods for automated reconstruction and characterization of particles in digital in-line holograms. *Measurement Science and Technology* **20**, 075501 (2009).

[189] Schlenczek, O. *Airborne and Ground-based Holographic Measurement of Hydrometeors in Liquid-phase, Mixed-phase and Ice Clouds*. PhD Thesis, Universitätsbibliothek Mainz (2018).

[190] Touloupas, G., Lauber, A., Henneberger, J., Beck, A. & Lucchi, A. A convolutional neural network for classifying cloud particles recorded by imaging probes. *Atmospheric Measurement Techniques* **13**, 2219–2239 (2020).

[191] Egerer, U., Gottschalk, M., Siebert, H., Ehrlich, A. & Wendisch, M. The new BELUGA setup for collocated turbulence and radiation measurements using a tethered balloon: First applications in the cloudy Arctic boundary layer. *Atmospheric Measurement Techniques* **12**, 4019–4038 (2019).

[192] Mazzola, M., Busetto, M., Ferrero, L., Viola, A. P. & Cappelletti, D. AGAP: an atmospheric gondola for aerosol profiling. *Rend. Fis. Acc. Lincei* **27**, 105–113 (2016).

[193] Magono, C. & Tazawa, S. Design of “Snow Crystal Sondes”. *Journal of the Atmospheric Sciences* **23**, 618–625 (1966).

[194] Miloshevich, L. M. & Heymsfield, A. J. A Balloon-Borne Continuous Cloud Particle Replicator for Measuring Vertical Profiles of Cloud Microphysical Properties : Instrument Design , Performance , and Collection Efficiency Analysis. *Journal of Atmospheric and Oceanic Technology* **14**, 753–768 (1997).

[195] Cirisan, A. *et al.* Balloon-borne match measurements of midlatitude cirrus clouds. *Atmospheric Chemistry and Physics* **14**, 7341–7365 (2014).

[196] Murakami, M., Matsuo, T., Nakayama, T. & Tanaka, T. Details of Cloud Particle Video Sonde. *Journal of the Meteorological Society of Japan* **65**, 803–809 (1987).

[197] Takahashi, T. Near Absence of Lightning in Torrential Rainfall Producing Micronesian Thunderstorms. *Geophysical Research Letters* **17**, 2381–2384 (1990).

[198] Boussaton, M. P., Coquillat, S., Chauzy, S. & Gangneron, F. A New Videosonde with a Particle Charge Measurement Device for In Situ Observation of Precipitation Particles. *Journal of Atmospheric and Oceanic Technology* **21**, 1519–1531 (2004).

[199] Waugh, S. M. *et al.* A Balloonborne Particle Size , Imaging , and Velocity Probe for in Situ Microphysical Measurements. *Journal of Atmospheric and Oceanic Technology* **32**, 1562–1580 (2015).

[200] Waugh, S. M., Zeigler, C. L. & MacGorman, D. R. In Situ Microphysical Observations of the 29 – 30 May 2012 Kingfisher, OK, Supercell With a Balloon-Borne Video Disdrometer. *Journal of Geophysical Research: Atmospheres* **123**, 5618–5640 (2018).

[201] Waugh, S. M., Ziegler, C. L. & MacGorman, D. R. In Situ Microphysical Observations of a Multicell Storm Using a Balloon - Borne Video Disdrometer During Deep Convective Clouds and Chemistry. *Journal of Geophysical Research : Atmospheres* **56**, 1–27 (2020).

[202] Ward, S. M., Deshler, T. & Hertzog, A. Quasi-Lagrangian measurements of nitric acid trihydrate formation over Antarctica. *Journal of Geophysical Research: Atmospheres* **119**, 245–258 (2014).

[203] Takahashi, T., Sugimoto, S., Kawano, T. & Suzuki, K. Microphysical Structure and Lightning Initiation in Hokuriku Winter Clouds. *Journal of Geophysical Research: Atmospheres* **124**, 13156–13181 (2019).

[204] Chambers, T. E. *A Digital Holographic Imager for Cloud Microphysics Studies* (MPhil Thesis, University of Adelaide, 2017).

[205] Chambers, T. E., Hamilton, M. W. & Reid, I. M. A low-cost digital holographic imager for calibration and validation of cloud microphysics remote sensing. *Proc. of SPIE* **10001**, 1–10 (2016).

[206] Gabor, D. A NEW MICROSCOPIC PRINCIPLE. *Nature* **161**, 777–778 (1948).

[207] Gabor, D. Microscopy by reconstructed wave-fronts. *Proc. R. Soc. Lond.* **197**, 454 –487 (1949).

[208] Gabor, D. Microscopy by Reconstructed Wave Fronts: II. *Proc. Phys. Soc.* **64**, 449–469 (1951).

[209] Bragg, W. L. A New Type of X-Ray Microscope. *Nature* **143**, 678 (1939).

[210] Lichte, H. & Lehmann, M. Electron holography — basics and applications. *Reports on Progress in Physics* **71** (2008).

[211] Harp, G. R. *et al.* Primary Beam and Dish Surface Characterization at the Allen Telescope Array by Radio Holography. *IEEE Transactions on Antennas and Propagation* **59**, 2004–2021 (2011).

[212] Faridian, A. *et al.* Nanoscale imaging using deep ultraviolet digital holographic microscopy. *Optics Express* **18**, 14159 (2010).

[213] Tegze, M. & Faigel, G. X-ray holography with atomic resolution. *Letters to Nature* **380**, 49–51 (1996).

[214] Korecki, P., Korecki, J. & Slezak, T. Atomic Resolution Gamma-ray Holography Using the Mössbauer Effect. *Physical Review Letters* **79**, 3518–3521 (1997).

[215] Maynard, J. D., Williams, E. G. & Lee, Y. Nearfield acoustic holography : I. Theory of generalized holography and the development of NAH. *The Journal of the Acoustical Society of America* **78**, 1395–1413 (1985).

[216] Fujita, J., Mitake, S. & Shimizu, F. Interferometric Modulation of an Atomic Beam by an Electric Field : A Phase Hologram for Atoms. *Physical Review Letters* **84**, 4027–4030 (2000).

[217] Lindsey, C. & Braun, D. C. BASIC PRINCIPLES OF SOLAR ACOUSTIC HOLOGRAPHY. *Solar Physics* **192**, 261–284 (2000).

[218] Schawlow, A. L. & Townes, C. H. Infrared and Optical Masers. *Physical Review* **112**, 1940–1949 (1958).

[219] Leith, E. N. & Upatnieks, J. Reconstructed Wavefronts and Communication Theory. *Journal of the Optical Society of America* **52**, 1123–1130 (1962).

[220] Denisyuk, Y. N. Photographic reconstruction of the optical properties of an object in its own scattered radiation field. *Soviet Physics Doklady* **7**, 543 (1962).

[221] Leith, E. N. & Upatnieks, J. Wavefront Reconstruction with Diffused Illumination and Three-Dimensional Objects. *Journal of the Optical Society of America* **54**, 1295–1301 (1964).

[222] Schnars, U. & Jüptner, W. Direct recording of holograms by a CCD target and numerical reconstruction. *Applied optics* **33**, 179–181 (1994).

[223] Garcia-Sucerquia, J. *et al.* Digital in-line holographic microscopy. *Applied Optics* **45**, 836–850 (2006).

[224] Kaikkonen, V. A., Molkoselkä, E. O. & Mäkynen, A. J. A rotating holographic imager for stationary cloud droplet and ice crystal measurements. *Optical Review* **27**, 205–216 (2020).

[225] Raupach, S. M. F. Cascaded adaptive-mask algorithm for twin-image removal and its application to digital holograms of ice crystals. *Appl. Opt.* **48**, 287–301 (2009).

[226] Zhang, Y., Pedrini, G., Osten, W. & Tiziani, H. J. Whole optical wave field reconstruction from double or multi in-line holograms by phase retrieval algorithm. *Optics Express* **11**, 3234–3241 (2003).

[227] Liu, G. & Scott, P. D. Phase retrieval and twin-image elimination for in-line Fresnel holograms. *Journal of the Optical Society of America A* **4**, 159–165 (1987).

[228] Sheng, J., Malkiel, E. & Katz, J. Digital holographic microscope for measuring three-dimensional particle distributions and motions. *Applied optics* **45**, 3893–3901 (2006).

[229] Cartwright, S., Dunn, P. & Thompson, B. Particle sizing using far -field holography: new developments. *Optical Engineering* **19**, 727–733 (1980).

[230] Goodman, J. W. *Introduction to Fourier Optics* (McGraw-Hill, New York, 1996), second edn.

[231] Collier, R. J., Burkhardt, C. B. & Lin, L. H. *Optical Holography* (Academic Press, New York, 1971).

[232] Miles, N. L., Verlinde, J. & Clothiaux, E. E. Cloud droplet size distributions in low-level stratiform clouds. *Journal of the Atmospheric Sciences* **57**, 295–311 (2000).

[233] Schnars, U. & Jueptner, W. *Digital Holography* (Springer-Verlag Berlin Heidelberg, 2005), 1 edn.

[234] Born, M. & Wolf, E. *Principles of Optics* (Cambridge University Press, 1999), 7 edn.

[235] Saleh, B. E. A. & Teich, M. C. *Fundamentals of Photonics* (John Wiley & Sons, New York, 1991).

[236] Autodesk. Autodesk CFD (2020).

[237] Kim, M. K. Principles and techniques of digital holographic microscopy. *SPIE Reviews* **1**, 018005 (2010).

[238] Dubois, F., Schockaert, C., Callens, N. & Yourassowsky, C. Focus plane detection criteria in digital holography microscopy by amplitude analysis. *Optics Express* **14**, 5895–5908 (2006).

[239] Kemppinen, O., Heinson, Y. & Berg, M. Quasi-three-dimensional particle imaging with digital holography. *Applied Optics* **56** (2017).

[240] Khanam, T., Rahman, M. N., Rajendran, A., Kariwala, V. & Asundi, A. K. Accurate size measurement of needle-shaped particles using digital holography. *Chemical Engineering Science* **66**, 2699–2706 (2011).

[241] Otsu, N. A Threshold Selection Method from Gray-Level Histograms. *IEEE Transactions on Systems, Man and Cybernetics* **20**, 62–66 (1979).

[242] Canny, J. A Computational Approach to Edge Detection. *IEEE Transactions on Pattern Analysis and Machine Intelligence* **6**, 679–698 (1986).

[243] Cuche, E., Marquet, P. & Depeursinge, C. Aperture apodization using cubic spline interpolation: application in digital holographic microscopy. *Optics Communications* **182**, 59–69 (2000).

[244] Dubois, F., Monnom, O., Yourassowsky, C. & Legros, J.-C. Border processing in digital holography by extension of the digital hologram and reduction of the higher spatial frequencies. *Applied Optics* **41**, 2621–2626 (2002).

[245] Raupach, S. M. F. Observation of interference patterns in reconstructed digital holograms of atmospheric ice crystals. *Journal of Atmospheric and Oceanic Technology* **26**, 2691–2693 (2009).

[246] Min, J. *et al.* Dual-wavelength slightly off-axis digital holographic microscopy. *Applied Optics* **51**, 191 (2012).

[247] Mann, C. J., Bingham, P. R., Paquit, V. C. & Tobin, K. W. Quantitative phase imaging by three-wavelength digital holography. *Optics express* **16**, 9753–9764 (2008).

[248] Aiello, L. *et al.* Green's formulation for robust phase unwrapping in digital holography. *Optics and Lasers in Engineering* **45**, 750–755 (2007).

[249] Palacios, F., Goncalves, E., Ricardo, J. & Valin, J. L. Adaptive filter to improve the performance of phase-unwrapping in digital holography. *Optics Communications* **238**, 245–251 (2004).

[250] Xie, Y., Yang, P., Kattawar, G. W., Minnis, P. & Hu, Y. X. Effect of the inhomogeneity of ice crystals on retrieving ice cloud optical thickness and effective particle size. *Journal of Geophysical Research* **114**, 1–12 (2009).

[251] Reisinger, T., Leufke, P. M., Gleiter, H. & Hahn, H. On the relative intensity of Poisson's spot. *New Journal of Physics* **19** (2017).

[252] Tang, G., Panetta, R. L., Yang, P., Kattawar, G. W. & Zhai, P.-W. Effects of ice crystal surface roughness and air bubble inclusions on cirrus cloud radiative properties from remote sensing perspective. *Journal of Quantitative Spectroscopy and Radiative Transfer* **195**, 119–131 (2017).

[253] Hamilton, M. Optical design of low-cost polarimetric back-scatter sondes. *Applied Optics* **57** (2018).

[254] Löffler-Mang, M. & Joss, J. An optical disdrometer for measuring size and velocity of hydrometeors. *Journal of Atmospheric and Oceanic Technology* **17**, 130–139 (2000).

[255] Yuter, S. E., Kingsmill, D. E., Nance, L. B. & Löffler-Mang, M. Observations of precipitation size and fall speed characteristics within coexisting rain and wet snow. *Journal of Applied Meteorology and Climatology* **45**, 1450–1464 (2006).

[256] Battaglia, A., Rustemeier, E., Tokay, A., Blahak, U. & Simmer, C. PARSIVEL snow observations: A critical assessment. *Journal of Atmospheric and Oceanic Technology* **27**, 333–344 (2010).

[257] Tokay, A., Wolff, D. B. & Petersen, W. A. Evaluation of the New Version of the Laser-Optical Disdrometer, OTT Parsivel2. *Journal of Atmospheric and Oceanic Technology* **31**, 1276–1288 (2014).

[258] Raupach, T. H. & Berne, A. Correction of raindrop size distributions measured by Parsivel disdrometers, using a two-dimensional video disdrometer as a reference. *Atmospheric Measurement Techniques* **8**, 343–365 (2015).

[259] Park, S. G., Kim, H. L., Ham, Y. W. & Jung, S. H. Comparative evaluation of the OTT PARSIVEL2 using a collocated two-dimensional video disdrometer. *Journal of Atmospheric and Oceanic Technology* **34**, 2059–2082 (2017).

[260] Liu, X., He, B., Zhao, S., Hu, S. & Liu, L. Comparative measurement of rainfall with a precipitation micro-physical characteristics sensor, a 2D video disdrometer, an OTT PARSIVEL disdrometer, and a rain gauge. *Atmospheric Research* **229**, 100–114 (2019).

[261] Ji, L. *et al.* Raindrop size distributions and rain characteristics observed by a PARSIVEL disdrometer in Beijing, Northern China. *Remote Sensing* **11** (2019).

[262] Kruger, A. & Krajewski, W. F. Two-dimensional video disdrometer: A description. *Journal of Atmospheric and Oceanic Technology* **19**, 602–617 (2002).

[263] Thurai, M., Bringi, V. N., Petersen, W. A. & Gatlin, P. N. Drop shapes and fall speeds in rain: Two contrasting examples. *Journal of Applied Meteorology and Climatology* **52**, 2567–2581 (2013).

[264] Uijlenhoet, R. & Sempere Torres, D. Measurement and parameterization of rainfall microstructure. *Journal of Hydrology* **328**, 1–7 (2006).

[265] Baumgardner, D., Jonsson, H., Dawson, W., O'Connor, D. & Newton, R. The cloud, aerosol and precipitation spectrometer: A new instrument for cloud investigations. *Atmospheric Research* **59-60**, 251–264 (2001).

[266] Knollenberg, R. G. The Optical Array: An Alternative to Scattering or Extinction for Airborne Particle Size Determination. *Journal of Applied Meteorology* **9**, 86–103 (1970).

[267] Patade, S., Shete, S., Malap, N., Kulkarni, G. & Prabha, T. V. Observational and simulated cloud microphysical features of rain formation in the mixed phase clouds observed during CAIPEEX. *Atmospheric Research* **169**, 32–45 (2016).

[268] Fu, Y. & Lei, H.-C. Aircraft observation of cloud microphysical characteristics of pre-stratiform-cloud precipitation in Jiangxi Province. *Atmospheric and Oceanic Science Letters* **10**, 364–371 (2017).

[269] Klotz, B. W. & Uhlhorn, E. W. Improved Stepped Frequency Microwave Radiometer Tropical Cyclone Surface Winds in Heavy Precipitation. *Journal of Atmospheric and Oceanic Technology* **31**, 2392–2408 (2014).

[270] Lance, S., Brock, C. A., Rogers, D. & Gordon, J. A. Water droplet calibration of the Cloud Droplet Probe (CDP) and in-flight performance in liquid , ice and mixed-phase clouds during ARCPAC. *Atmospheric Measurement Techniques* **3**, 1683–1706 (2010).

[271] Black, R. A. & Hallett, J. Rain Rate and Water Content in Hurricanes Compared with Summer Rain in Miami , Florida. *Journal of Applied Meteorology and Climatology* **51**, 2218–2235 (2012).

[272] Cui, C., Dong, X., Wang, B. & Yang, H. Phase Two of the Integrative Monsoon Frontal Rainfall Experiment (IMFRE-II) over the Middle and Lower Reaches of the Yangtze River in 2020. *Advances in Atmospheric Sciences* **38**, 346–356 (2021).

[273] Huggins, A. W. *et al.* The snowy precipitation enhancement research project: A description and preliminary results. *The Journal of Weather Modification* **40**, 28–53 (2008).

[274] Gurganus, C. & Lawson, P. Laboratory and flight tests of 2D imaging probes: Toward a better understanding of instrument performance and the impact on archived data. *Journal of Atmospheric and Oceanic Technology* **35**, 1533–1553 (2018).

[275] Heymsfield, A. J. & Parrish, J. L. A Computational Technique for Increasing the Effective Sampling Volume of the PMS Two-Dimensional Particle Size Spectrometer. *Journal of Applied Meteorology* **17**, 1566–1572 (1978).

[276] Protat, A. & McRobert, I. Three-dimensional wind profiles using a stabilized shipborne cloud radar in wind profiler mode. *Atmospheric Measurement Techniques* **13**, 3609–3620 (2020).

[277] Lhermitte, R. Attenuation and Scattering of Millimeter Wavelength Radiation by Clouds and Precipitation. *Journal of Atmospheric and Oceanic Technology* **7**, 464–479 (1990).

[278] Kollias, P. *et al.* Millimeter-wavelength radars: New Frontier in Atmospheric Cloud and Precipitation Research. *Bulletin of the American Meteorological Society* 1608–1624 (2007).

[279] Dupont, J. C. *et al.* Evaluation of fog and low stratus cloud microphysical properties derived from in situ sensor, cloud radar and SYRSOC algorithm. *Atmosphere* **9**, 1–19 (2018).

[280] Gultepe, I. *et al.* Fog research: A review of past achievements and future perspectives. *Pure and Applied Geophysics* **164**, 1121–1159 (2007).

[281] Toledo, F. *et al.* Absolute calibration method for frequency-modulated continuous wave (FMCW) cloud radars based on corner reflectors. *Atmospheric Measurement Techniques* **13**, 6853–6875 (2020).

[282] Ewald, F. *et al.* Calibration of a 35 GHz airborne cloud radar: Lessons learned and intercomparisons with 94 GHz cloud radars. *Atmospheric Measurement Techniques* **12**, 1815–1839 (2019).

[283] Löffler-Mang, M., Kunz, M. & Schmid, W. On the performance of a low-cost K-band Doppler radar for quantitative rain measurements. *Journal of Atmospheric and Oceanic Technology* **16**, 379–387 (1999).

[284] Protat, A. *et al.* The Latitudinal Variability of Oceanic Rainfall Properties and Its Implication for Satellite Retrievals: 1. Drop Size Distribution Properties. *Journal of Geophysical Research: Atmospheres* **124**, 13291–13311 (2019).

[285] Kneifel, S., Maahn, M., Peters, G. & Simmer, C. Observation of snowfall with a low-power FM-CW K-band radar (Micro Rain Radar). *Meteorology and Atmospheric Physics* **113**, 75–87 (2011).

[286] Walter, B., Huwald, H., Gehring, J., Bühler, Y. & Lehning, M. Radar measurements of blowing snow off a mountain ridge. *The Cryosphere* **14**, 1779–1794 (2020).

[287] Leinonen, J. *et al.* Evidence of nonspheroidal behavior in millimeter-wavelength radar observations of snowfall. *Journal of Geophysical Research Atmospheres* **117**, 1–10 (2012).

[288] Maahn, M. & Kollias, P. Improved Micro Rain Radar snow measurements using Doppler spectra post-processing. *Atmospheric Measurement Techniques* **5**, 2661–2673 (2012).

[289] Tridon, F., Van Baelen, J. & Pointin, Y. Aliasing in Micro rain radar data due to strong vertical winds. *Geophysical Research Letters* **38**, 4–7 (2011).

[290] Royer, P., Bizard, A., Sauvage, L. & Thobois, L. Validation protocol and intercomparison campaigns with the R-MAN 510 aerosol lidar. In *Proc. 17th International Symposium for the Advancement of Boundary Layer Remote Sensing*, 1 (2014).

[291] Alexander, S. P. & Protat, A. Cloud Properties Observed From the Surface and by Satellite at the Northern Edge of the Southern Ocean. *Journal of Geophysical Research : Atmospheres* **123**, 443–456 (2017).

[292] Huang, Y. *et al.* Evaluating Himawari-8 Cloud Products Using Shipborne and CALIPSO Observations : Cloud-Top Height and Cloud-Top Temperature. *Journal of Atmospheric and Oceanic Technology* **36**, 2327–2347 (2019).

[293] Mace, G. G. *et al.* Southern Ocean Cloud Properties Derived From CAPRICORN and MARCUS Data. *Journal of Geophysical Research : Atmospheres* **126**, 1–23 (2021).

[294] Hu, Y. Depolarization ratio – effective lidar ratio relation : Theoretical basis for space lidar cloud phase discrimination. *Geophysical Research Letters* **34**, 6–9 (2007).

[295] Bessho, K. *et al.* An introduction to Himawari-8/9 — Japan's new-generation geostationary meteorological satellites. *Journal of the Meteorological Society of Japan* **94**, 151–183 (2016).

[296] Kawamoto, K., Nakajima, T. & Nakajima, T. Y. A global determination of cloud microphysics with AVHRR remote sensing. *Journal of Climate* **14**, 2054–2068 (2001).

[297] Hamann, U. *et al.* Remote sensing of cloud top pressure/height from SEVIRI: Analysis of ten current retrieval algorithms. *Atmospheric Measurement Techniques* **7**, 2839–2867 (2014).

[298] Zhao, L., Zhao, C., Wang, Y., Wang, Y. & Yang, Y. Evaluation of Cloud Microphysical Properties Derived From MODIS and Himawari-8 Using In Situ Aircraft Measurements Over the Southern Ocean. *Earth and Space Science* **7**, 1–18 (2020).

[299] Su, C.-H. *et al.* BARRA v1.0: The Bureau of Meteorology Atmospheric high-resolution Regional Reanalysis for Australia. *Geoscientific Model Development* **12**, 2049–2068 (2019).

[300] Davies, T. *et al.* A new dynamical core of the Met Office's global and regional modelling of the atmosphere. *Quarterly Journal of the Royal Meteorological Society* **131**, 1759–1782 (2005).

[301] Puri, K. *et al.* Implementation of the initial ACCESS numerical weather prediction system. *Australian Meteorological and Oceanographic Journal* **63**, 265–284 (2013).

[302] Su, C.-H. *et al.* BARRA v1.0: Kilometre-scale downscaling of an Australian regional atmospheric reanalysis over four midlatitude domains. *Geoscientific Model Development* **14**, 4357–4378 (2021).

[303] Wilson, D. R. & Ballard, S. P. A microphysically based precipitation scheme for the UK Meteorological Office Unifed Model. *Quarterly Journal of the Royal Meteorological Society* **125**, 1607–1636 (1999).

[304] Dee, D. P. *et al.* The ERA-Interim reanalysis: Configuration and performance of the data assimilation system. *Quarterly Journal of the Royal Meteorological Society* **137**, 553–597 (2011).

[305] Jones, D. A., Wang, W. & Fawcett, R. High-quality spatial climate data-sets for Australia. *Australian Meteorological and Oceanographic Journal* **58**, 233–248 (2009).

[306] Acharya, S. C., Nathan, R., Wang, Q. J., Su, C.-h. & Eizenberg, N. An evaluation of daily precipitation from a regional atmospheric reanalysis over Australia. *Hydrology and Earth System Sciences* **23**, 3387–3403 (2019).

[307] Ackermann, L. *et al.* Wintertime Precipitation over the Australian Snowy Mountains: Observations from an Intensive Field Campaign 2018. *Journal of Hydrometeorology* **22**, 2193–2211 (2021).

[308] Sarmadi, F., Huang, Y., Siems, S. T. & Manton, M. J. Characteristics of wintertime daily precipitation over the Australian Snowy Mountains. *Journal of Hydrometeorology* **18**, 2849–2867 (2017).

[309] Houze Jr., R. A. Orographic Effects on Precipitating Clouds. *Reviews of Geophysics* **50**, 1–47 (2012).

[310] Morrison, A. E., Siems, S. T. & Manton, M. J. On a Natural Environment for Glaciogenic Cloud Seeding. *Journal of Applied Meteorology and Climatology* **52**, 1097–1104 (2013).

[311] Osburn, L., Chubb, T., Siems, S., Manton, M. & Peace, A. D. Observations of Supercooled Liquid Water in Wintertime Alpine Storms in South Eastern Australia. *Atmospheric Research* **169**, 345–356 (2016).

[312] Chubb, T. H., Siems, S. T. & Manton, M. J. On the Decline of Wintertime Precipitation in the Snowy Mountains of Southeastern Australia. *Journal of Hydrometeorology* **12**, 1483–1497 (2011).

[313] Schober, P., Boer, C. & Schwarte, L. A. Correlation Coefficients: Appropriate Use and Interpretation. *Anasthesia & Analgesia* **126**, 1763–1768 (2018).

[314] Brast, M. & Markmann, P. Detecting the melting layer with a micro rain radar using a neural network approach. *Atmospheric Measurement Techniques* **13**, 6645–6656 (2020).

[315] Locatelli, J. D. & Hobbs, P. V. Fall speeds and masses of solid precipitation particles. *Journal of Geophysical Research* **79**, 2185–2197 (1974).

[316] Heymsfield, A., Szakáll, M., Jost, A., Giammanco, I. & Wright, R. A comprehensive observational study of graupel and hail terminal velocity, mass flux, and kinetic energy. *Journal of the Atmospheric Sciences* **75**, 3861–3885 (2018).

[317] Findeisen, W. Die kolloidmeteorologischen Vorgänge bei der Niederschlagsbildung. *Meteorol. Z.* **55**, 121–133 (1938).

[318] Lohmann, U. *et al.* Persistence of orographic mixed-phase clouds. *Geophysical Research Letters* **43**, 10,512–10,519 (2016).

[319] Boers, R., Jensen, J. B., Krummel, P. B. & Gerber, H. Microphysical and short-wave radiative structure of wintertime stratocumulus clouds over the Southern Ocean. *Quarterly Journal of the Royal Meteorological Society* **122**, 1307–1339 (1996).

[320] Ahn, E. *et al.* In situ observations of wintertime low-altitude clouds over the Southern Ocean. *Quarterly Journal of the Royal Meteorological Society* **143**, 1381–1394 (2017).

[321] Glen, A. & Brooks, S. D. A new method for measuring optical scattering properties of atmospherically relevant dusts using the Cloud and Aerosol Spectrometer with Polarization (CASPOL). *Atmospheric Chemistry and Physics* **13**, 1345–1356 (2013).

[322] Baker, M. B. & Peter, T. Small-scale cloud processes and climate. *Nature* **451**, 299–300 (2008).

[323] Wood, R. Drizzle in Stratiform Boundary Layer Clouds . Part I : Vertical and Horizontal Structure. *Journal of the Atmospheric Sciences* **62**, 3011–3033 (2005).

[324] Korolev, A. & Isaac, G. A. Relative Humidity in Liquid , Mixed-Phase , and Ice Clouds. *Journal of the Atmospheric Sciences* **63**, 2865–2880 (2006).

[325] Lim, K.-S. S. *et al.* Evaluation of long-term surface-retrieved cloud droplet number concentration with in situ aircraft observations. *Journal of Geophysical Research : Atmospheres* **121**, 2318–2331 (2016).

[326] Wood, R., Leon, D., Lebsock, M., Snider, J. & Clarke, A. D. Precipitation driving of droplet concentration variability in marine low clouds. *Journal of Geophysical Research* **117**, 1–11 (2012).

[327] Schmitt, C. G. & Heymsfield, A. J. On the Occurrence of Hollow Bullet Rosette – and Column-Shaped Ice Crystals in Midlatitude Cirrus. *Journal of the Atmospheric Sciences* **64**, 4514–4519 (2007).

[328] Boers, R., Jensen, J. B. & Krummel, P. B. Microphysical and short-wave radiative structure of stratocumulus clouds over the Southern Ocean: Summer results and seasonal differences. *Quarterly Journal of the Royal Meteorological Society* **124**, 151–168 (1998).

[329] Wofsy, S. C. HIAPER Pole-to-Pole Observations (HIPPO): fine-grained , global-scale measurements of gases and aerosols. *Philosophical transactions of the Royal Society* **369**, 2073–2086 (2011).

[330] Ahn, E. *et al.* In situ observations of wintertime low-altitude clouds over the Southern Ocean. *Quarterly Journal of the Royal Meteorological Society* **143**, 1381–1394 (2017).

[331] Mccoy, I. L. *et al.* The hemispheric contrast in cloud microphysical properties constrains aerosol forcing. *PNAS* **117**, 18998–19006 (2020).

[332] Chubb, T. *et al.* Observations of high droplet number concentrations in Southern Ocean boundary layer clouds. *Atmospheric Chemistry and Physics* **16**, 971–987 (2016).

[333] Bennartz, R. Global assessment of marine boundary layer cloud droplet number concentration from satellite. *Journal of Geophysical Research* **112**, 1–16 (2007).

[334] Ahn, E., Huang, Y., Siems, S. T. & Manton, M. J. A Comparison of Cloud Microphysical Properties Derived From MODIS and CALIPSO With In Situ Measurements Over the Wintertime Southern Ocean. *Journal of Geophysical Research: Atmospheres* **123**, 11,120–11,140 (2018).

[335] Mccoy, I. L. *et al.* Influences of Recent Particle Formation on Southern Ocean Aerosol Variability and Low Cloud Properties. *Journal of Geophysical Research : Atmospheres* **126**, 1–27 (2021).

[336] Wood, R. *et al.* Ultraclean Layers and Optically Thin Clouds in the Stratocumulus-to-Cumulus Transition . Part I : Observations. *Journal of the Atmospheric Sciences* **75**, 1631–1652 (2018).

[337] O, K.-T., Wood, R. & Bretherton, C. S. Ultraclean Layers and Optically Thin Clouds in the Stratocumulus-to-Cumulus Transition . Part II : Depletion of Cloud Droplets and Cloud Condensation Nuclei through Collision – Coalescence. *Journal of the Atmospheric Sciences* **75**, 1653–1673 (2018).

[338] Mace, G. G. & Protat, A. Clouds over the Southern Ocean as Observed from the R / V Investigator during CAPRICORN . Part I : Cloud Occurrence and Phase Partitioning. *Journal of Applied Meteorology and Climatology* **57**, 1783–1803 (2018).

[339] Haefele, A. & Ruffieux, D. Validation of the 1290 MHz wind profiler at Payerne, Switzerland, using radiosonde GPS wind measurements. *Meteorological Applications* **22**, 873–878 (2015).

[340] Dolman, B. K. & Reid, I. M. Buckland Park Stratospheric Tropospheric Profiler Intensive Observation Period Report. Tech. Rep., ATRAD Pty Ltd (2011).

[341] Dolman, B. K., Reid, I. M. & Tingwell, C. Stratospheric tropospheric wind profiling radars in the Australian network. *Earth, Planets and Space* **70**, 1–10 (2018).

[342] Dolman, B. K. & Reid, I. M. Buckland Park Boundary Layer Profiler Intensive Observation Period Report. Tech. Rep., ATRAD Pty Ltd (2011).

[343] Stein, A. F. *et al.* NOAA'S HYSPLIT ATMOSPHERIC TRANSPORT AND DISPERSION MODELING SYSTEM. *Bulletin of the American Meteorological Society* **96**, 2059–2078 (2015).

[344] Fleming, Z. L., Monks, P. S. & Manning, A. J. Review : Untangling the influence of air-mass history in interpreting observed atmospheric composition. *Atmospheric Research* **104-105**, 1–39 (2012).

[345] Winker, D. M. *et al.* The Calipso Mission: A Global 3D View of Aerosols and Clouds. *Bulletin of the American Meteorological Society* **91**, 1211–1229 (2010).

[346] Kang, L., Marchand, R. & Smith, W. Evaluation of MODIS and Himawari-8 Low Clouds Retrievals Over the Southern Ocean With In Situ Measurements From the SOCRATES Campaign. *Earth and Space Science* **8**, 1–30 (2021).

[347] Sanchez Brea, L. M. Diffractio, python module for diffraction and interference optics (2019). URL https://pypi.org/project/diffractio/.

[348] Brenner, K.-H. & Singer, W. Light propagation through microlenses: a new simulation method. *Applied Optics* **32**, 4984–4988 (1993).

[349] Ratcliffe, J. A. Some Aspects of Diffraction Theory and their Application to the Ionosphere. *Reports on Progress in Physics* **19**, 188–267 (1956).

[350] Sherman, G. C. Application of the Convolution Theorem to Rayleigh's Integral Formulas. *Journal of the Optical Society of America* **57**, 546–547 (1967).

Appendix A

Digital Holographic Imaging Theory

The theory of optical holographic imaging extends directly from the classical explanation of light as an electromagnetic wave, as described by Maxwell's equations of electromagnetism [230]. The sensors used in holography for recording wavefronts are orders of magnitude more sensitive to the electric field component and so the magnetic field component will be ignored in the following discussion. The application of cloud particle imaging entails scattering from particles significantly larger than the wavelength of light within air such that the scalar description of light is sufficiently accurate. Such a formulation describes the wave nature of light using the following expression for the electric field:

$$\begin{aligned} U(x,y,z,t) &= A\left(x,y,z\right)\cos\left(2\pi\nu t + \phi\left(x,y,z\right)\right) \\ &= \mathrm{Re}\{Ae^{i\phi}e^{i2\pi\nu t}\}, \end{aligned} \tag{A.1}$$

where A is the wave amplitude, ϕ is the phase, ν is the optical frequency, and Re denotes the real component of the complex function which will be omitted in subsequent expressions for simplicity.

Optical holographic imaging can be considered as a two-stage imaging process in which an optical wavefront is used to illuminate the objects to be imaged. An example of such a setup is shown in Figure A.1 for the interaction between an incident plane wavefront and a spherical water droplet, as simulated using the DiffractIO Python package [347] with the Wavefront Propagation Method (WPM) [348]. Figure A.1a and Figure A.1b demonstrate the disturbance of the wavefront introduced by the scattering object in intensity and phase, and Figure A.1c shows an example of the resultant interference pattern formed further along the optical axis in the transverse dimensions.

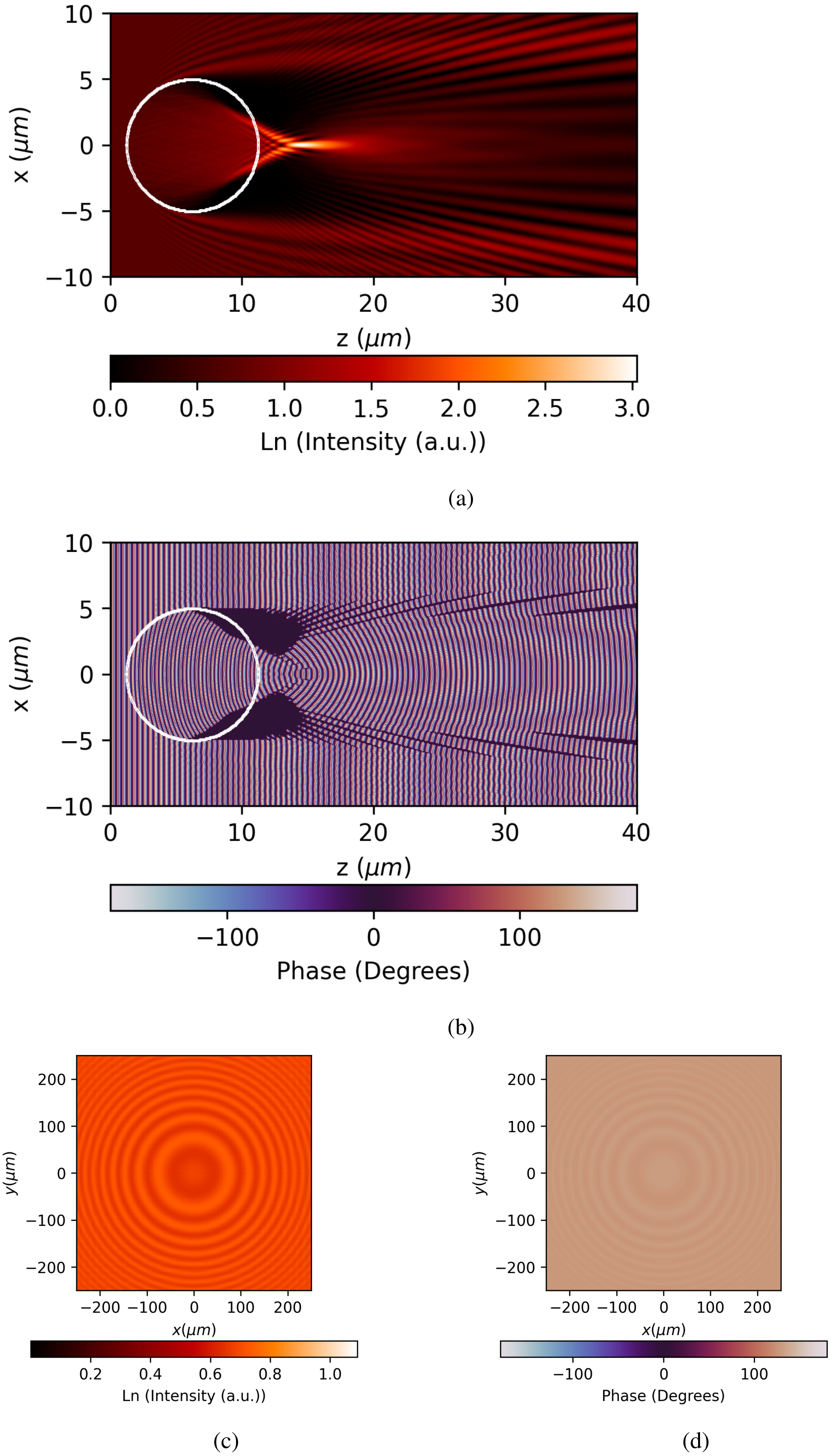

Fig. A.1 Simulated wavefront propagation demonstrating the hologram formation process for light scattering from a spherical water droplet.

A.1 Digital Holographic Recording

The interference pattern, subsequently referred to as a hologram, between the scattered light and a known reference wavefront is first recorded which encodes information about both the amplitude and the phase of the scattered wavefronts. Preservation of the amplitude and phase information in the hologram allows the subsequent reconstruction of the scattered object wavefronts at a range of depths and hence a 3D image of the original objects can be reproduced. This is in contrast to 2D imaging techniques in which only the amplitude is recorded and the shape of the wavefronts can no longer be determined.

Semiconductor camera sensors are used in digital holography to measure the optical wavefronts. The frequency of optical wavefronts is on the order of hundreds of terahertz which is orders of magnitude faster than the response time of such sensors, and so the phase of the wavefront cannot be directly measured in this way. Semiconductor sensors produce a measurable photocurrent that is proportional to the intensity of the wavefront, defined as follows:

$$I(x,y,z) = \left|U(x,y,z)\right|^2, \tag{A.2}$$

where U is the wave amplitude, as defined in Equation A.1. It is therefore necessary to encode the phase information as intensity variations via interferometric methods.

The hologram formed from the interference between coherent light scattered from an object field and a reference wavefront can be described by the following expression:

$$\begin{aligned} I &= |U_R + U_O|^2 \\ &= \left|A_R e^{i\phi_R} + A_O e^{i\phi_O}\right|^2 \\ &= A_R^2 + A_O^2 + A_O A_R e^{i(\phi_R - \phi_O)} + A_O A_R e^{i(\phi_O - \phi_R)} \\ &= A_R^2 + A_O^2 + 2A_O A_R \cos(\phi_O - \phi_R), \end{aligned} \tag{A.3}$$

where the symbols are defined according to Equation A.1 and the subscripts refer to the reference and object wavefronts, respectively. The first two terms represent a uniform background intensity that can be filtered out using Fourier methods. The final term represents a spatial intensity variation encoding information about both the amplitude and phase of the object wavefront and it is in this way that the wavefront information can be preserved.

A.2 Digital Holographic Reconstruction

The second stage of the holographic imaging method is the reconstruction of the recorded object wavefront. This is achieved in analogue holography by illumination of the hologram recorded on a transparent photographic plate by the original reference wavefront. In digital holography this process is simulated numerically using scalar diffraction theory. The wavefront transmitted by the hologram in the digital case can be described by the following expressions:

$$\begin{aligned} U_H &= A_R e^{i\phi_R} I \qquad \text{(A.4)} \\ &= A_R e^{i\phi_R}\{A_R^2 + A_O^2 + A_O A_R e^{i(\phi_R-\phi_O)} + A_O A_R e^{i(\phi_O-\phi_R)}\} \\ &= \{A_R^2 + A_O^2\}A_R e^{i\phi_R} + A_O A_R^2 e^{i2\phi_R} e^{-i\phi_O} + A_R^2 A_O e^{i\phi_O}, \qquad \text{(A.5)} \end{aligned}$$

where U_H is the wavefront transmitted by the hologram and the remaining symbols are as defined in Equation A.3. The first term in this expression represents a uniform background noise source due to the reference wavefront that can be filtered or subtracted out. The second term is proportional to the object wavefront but with a conjugated phase and is referred to as the twin image. This term is corrupted by the phase of the reference wavefront and is also treated as a noise term in the reconstruction. The final term in this expression is an exact reconstruction of the object wavefront up to a uniform multiplicative factor introduced by the reference wavefront. The extent to which the noise sources can be isolated from the object wavefront depends on the experimental configuration of the holographic imaging instrument and the properties of the objects. This matter is discussed further in Section 3.3 for the holographic instruments used in this work.

The final aspect of the digital holographic imaging method requires the propagation of the object wavefront from the hologram plane to the depth at which the image of the object comes into focus. This wavefront propagation can be rigorously described by the scalar theory of diffraction which arises from the solution of Maxwell's equations with a minimal set of reasonable assumptions. It is beyond the scope of this work to derive the results of this theory and so they will simply be stated here without derivation for reference. Readers interested in the detail of this theory are encouraged to consult the standard textbooks in this field [38, 230].

Two of the most widely used propagation methods in digital holography are referred to as the first Rayleigh-Sommerfield solution and the Angular Spectrum (AS) method [349]. It can be shown that these formulations are equivalent [350]; however, the AS method can be numerically evaluated with one fewer Fast Fourier Transform (FFT) and is thus more computationally efficient. The AS propagation method is described by the following relationship:

$$U(x,y,z) = \iint\limits_{-\infty}^{+\infty} U(x,y,0) e^{i\frac{2\pi}{\lambda}z\sqrt{1-(f_x\lambda)^2-(f_y\lambda)^2}} dxdy$$
$$= \mathrm{FFT}^{-1}\{\mathrm{FFT}\{U(x,y,0)\} e^{i\frac{2\pi}{\lambda}z\sqrt{1-(f_x\lambda)^2-(f_y\lambda)^2}}\}, \tag{A.6}$$

where $U(x,y,z)$ is the complex valued wavefront at a propagation depth of z, $U(x,y,0)$ is the wavefront recorded in the hologram plane as determined by Equation A.5, f_x and f_y are the spatial frequency coordinates, and FFT denotes the FFT operator. This expression can be evaluated efficiently due to the FFT formulation at a range of depths to reconstruct a 3D image of the scattering objects.

The depth to which a wavefront can be propagated by the AS method without introducing aliasing artefacts can be inferred by consideration of the Nyquist sampling theory. To adequately sample the function described in Equation A.6 both the object function and the exponential propagation function must obey the Nyquist constraints. The former condition imposes a resolution limit on the system, as discussed in Section 3.3, and the latter condition leads to the following constraint:

$$z \leq \frac{N\Delta x\sqrt{(N\Delta x)^2 - \lambda^2 N^2}}{\lambda N}, \tag{A.7}$$

where z is the propagation depth, N is the number of pixels per row or column on the camera sensor, Δx is the pixel size, and λ is the wavelength. This limit is around 20 mm for the instruments used in this work.

Alternate diffraction formulations must be used to propagate to larger depths whilst still satisfying the Nyquist sampling criteria. The Rayleigh-Sommerfield diffraction method is an exact approach, though it requires the computation of an additional FFT as compared with the AS method. If computational efficiency is required then the Fresnel approximation can also be used for these larger distances, but this comes at the cost of accuracy. Each of these methods have been implemented and tested in the software developed for use in this work under a range of laboratory and field conditions. Laboratory testing with calibration particles approximating cloud particles and Monte Carlo based modelling undertaken in this work suggests that in practice the AS method can be used significantly beyond this depth limit for reliable amplitude reconstructions.

Appendix B

Summary of Holographic Balloon Observations

A summary of the holographic observations obtained during the untethered balloon launch of the Compact Cloud-particle HOlographic Microscope – Balloon (C^2HOM–B) instrument is provided in this section. Observations include all 1-minute time intervals in which particles were detected below an altitude of approximately 5.2 km. Trends in this dataset are discussed in Chapter 7.

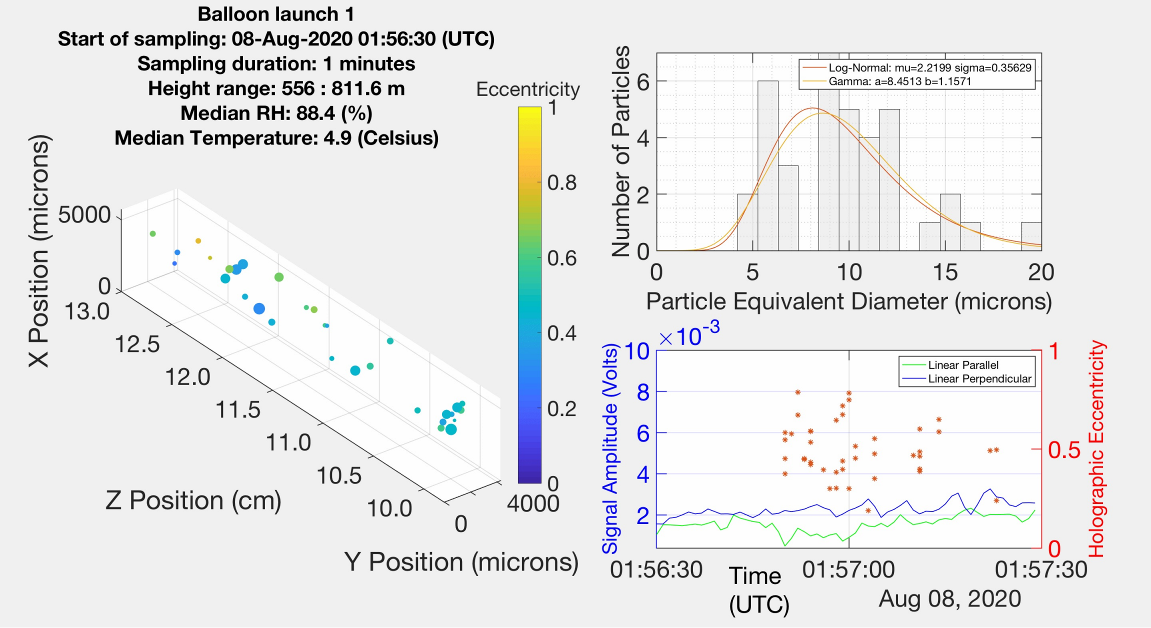

Fig. B.1 Summary of holographic observations recorded over one minute of the launch. Particle 3D positions, size distribution, eccentricity variations, Polarsonde backscatter, and median meteorological measurements are displayed. The z-axis on the 3D plot indicates the depth within the sampling volume relative to the camera sensor, and the transverse dimensions are in the plane of the camera sensor. Spheres on the 3D plot indicate the relative sizes of particles, but note that the absolute size is scaled for visibility.

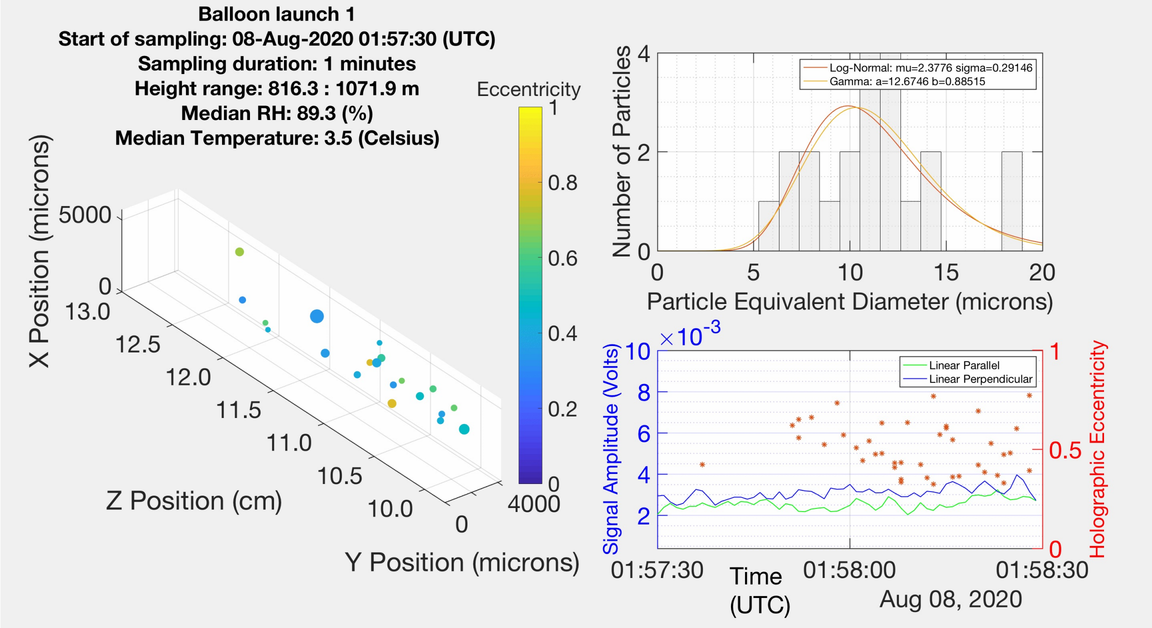

Fig. B.2 See caption in Figure B.1.

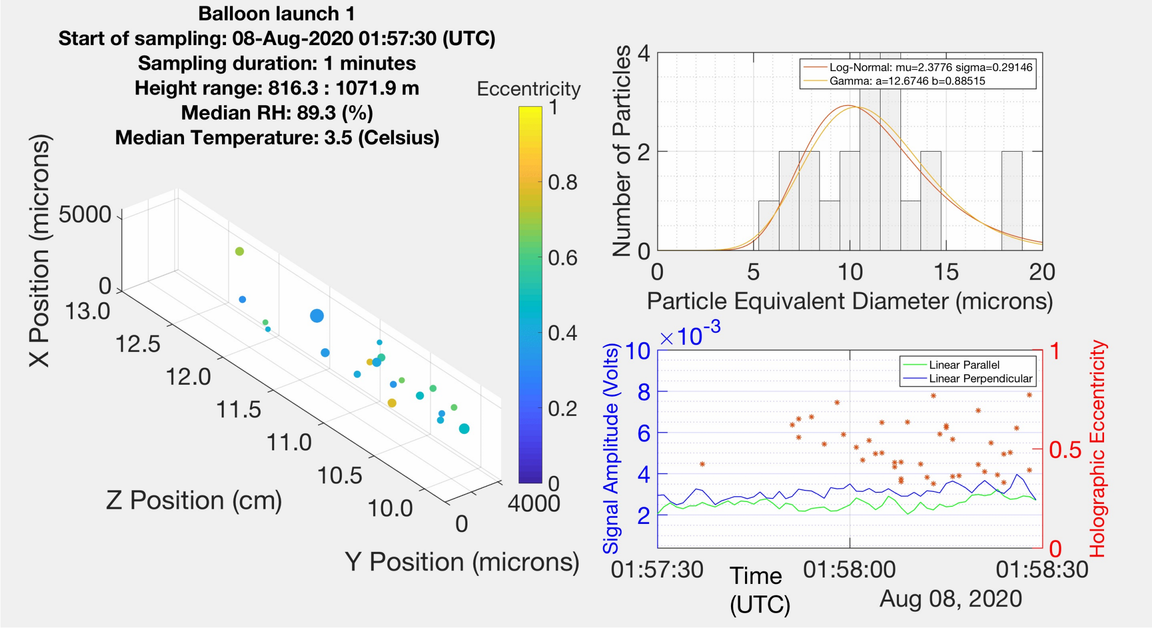

Fig. B.3 See caption in Figure B.1.

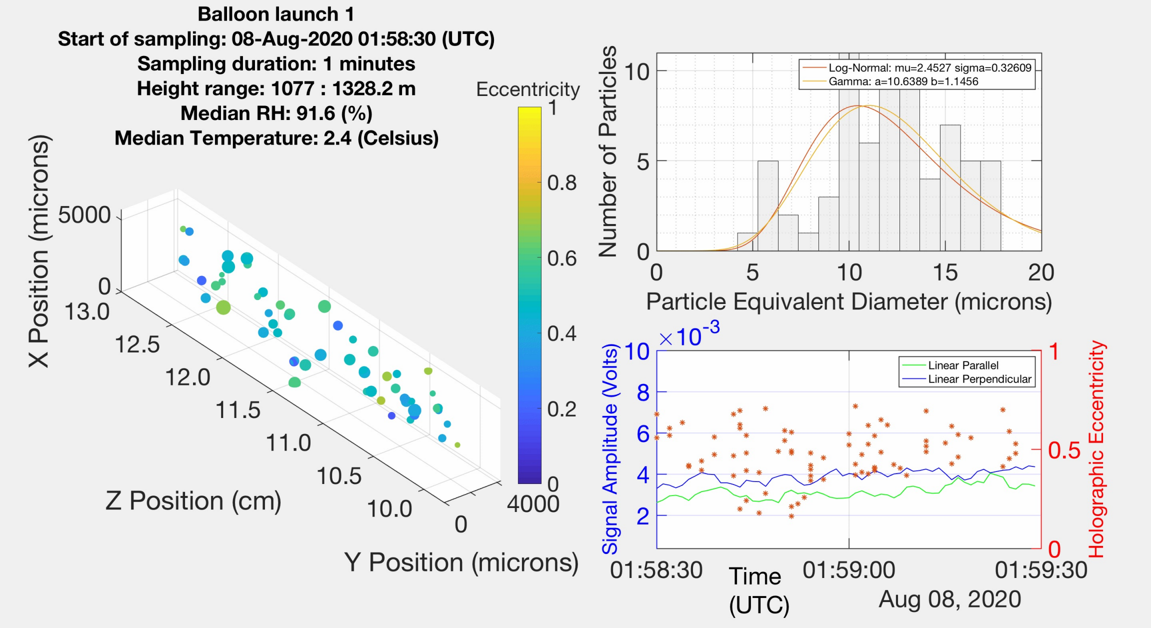

Fig. B.4 See caption in Figure B.1.

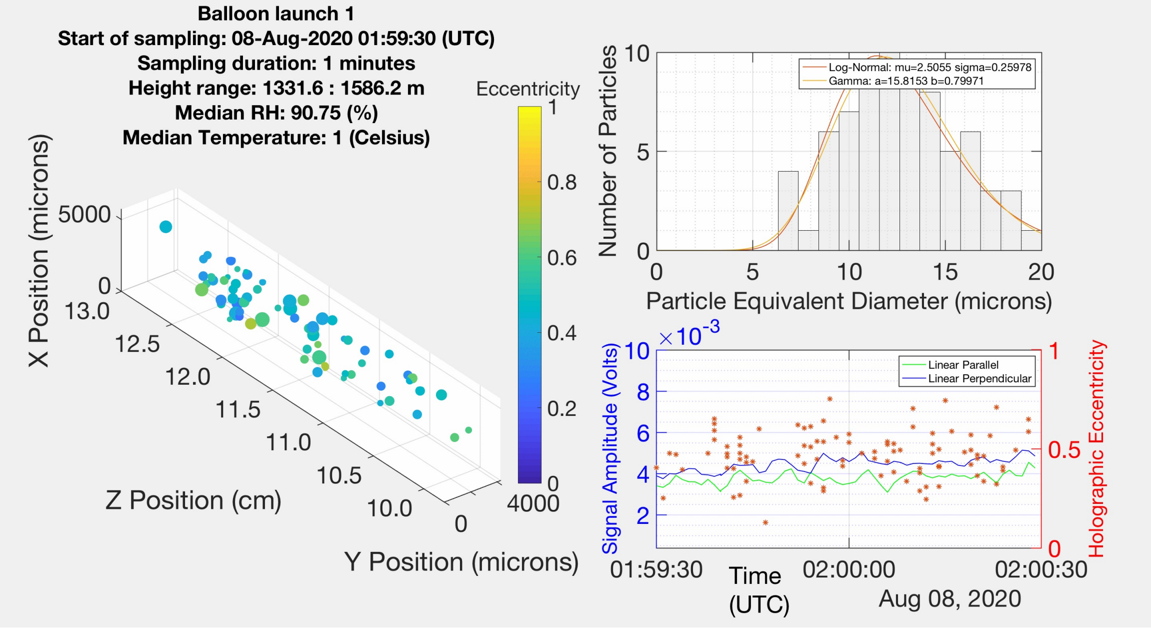

Fig. B.5 See caption in Figure B.1.

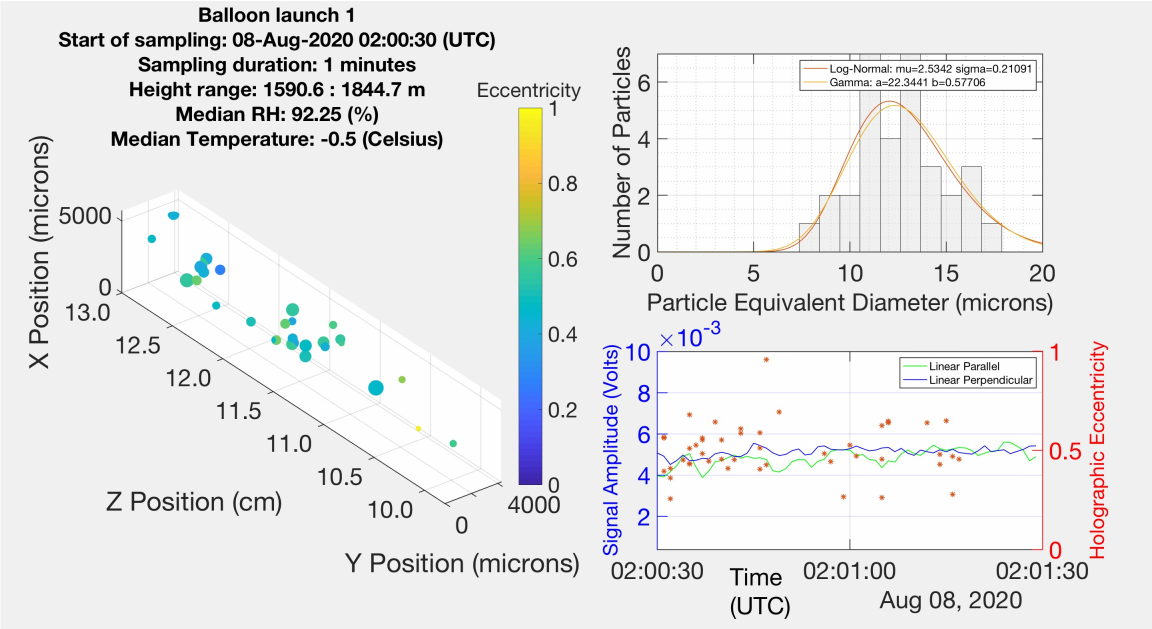

Fig. B.6 See caption in Figure B.1.

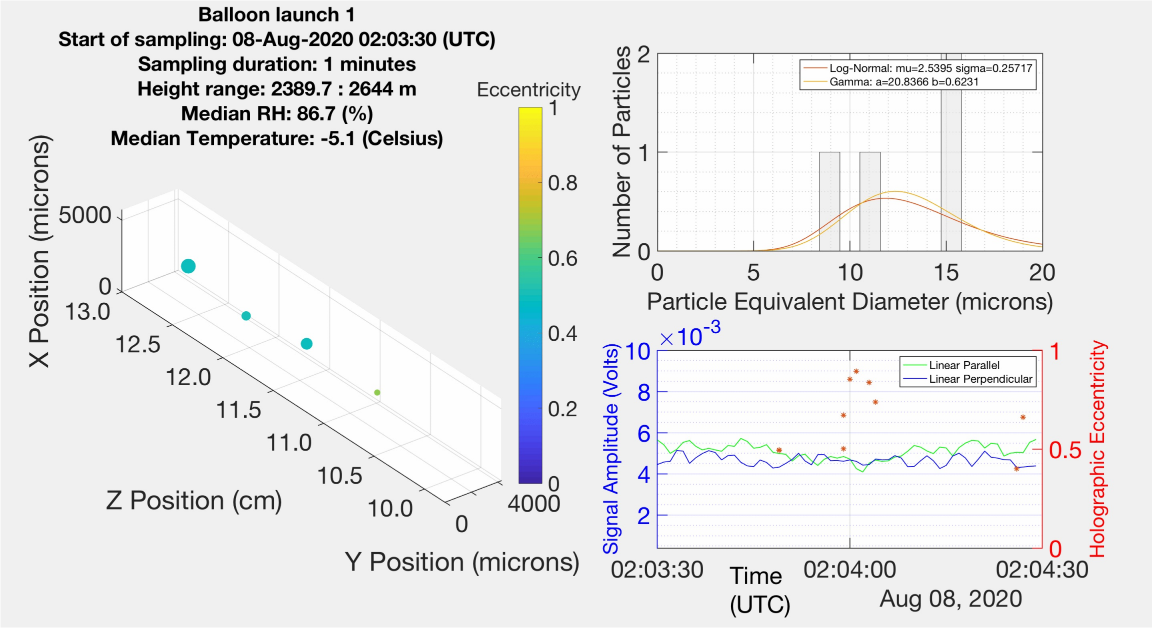

Fig. B.7 See caption in Figure B.1.

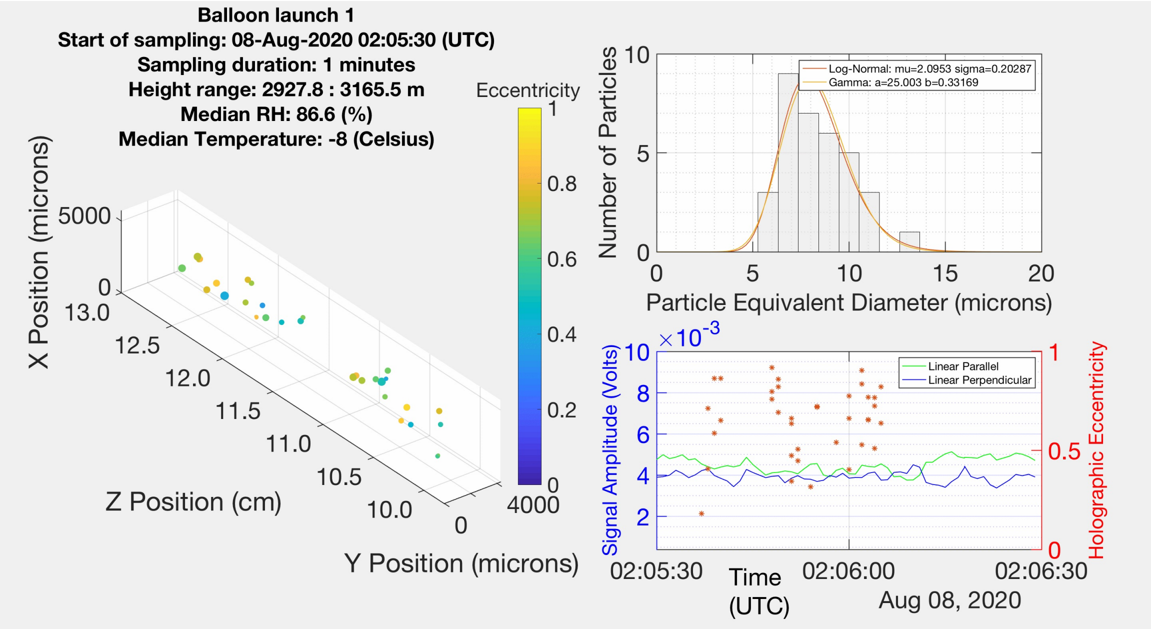

Fig. B.8 See caption in Figure B.1.

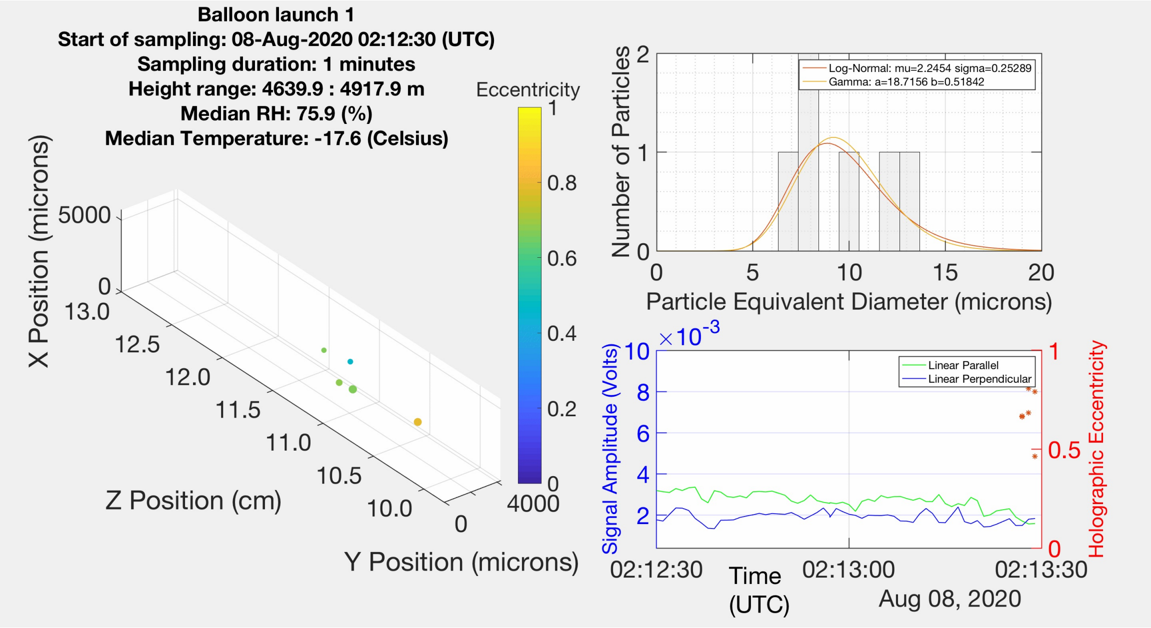

Fig. B.9 See caption in Figure B.1.

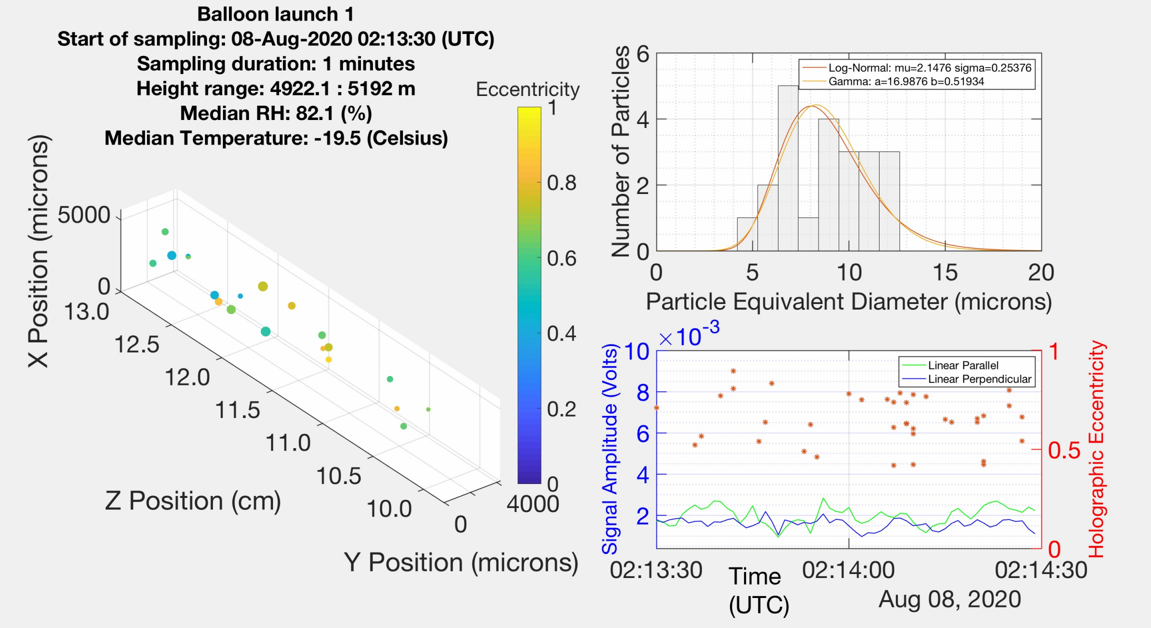

Fig. B.10 See caption in Figure B.1.